Stellingen behorende bij het proefschrift

STRAIN FIELDS IN CRYSTALLINE MATERIALS

Methods of Analysis Based on X-Ray Diffraction-Line Broadening

Jurgen van Berkum

1. A perfect standard specimen for X-ray diffraction line-profile analysis does not exist (see Chapter 1 of this thesis).

2. An interpretation of line broadening in terms of both size and dislocations is meaningful only if it is made sure that the size effect is truly due to the average crystal or grain size (see Chapters 3 and 8 of this thesis).

3. Size broadening due to a subdivision of grains into incoherently diffracting "domains" is unlikely to occur in plastically deformed specimens (see Chapters 7 and 8 of this thesis).

4. For the microstructure of a specimen, order-dependence is the most discriminating line-broadening feature.

5. Volgens de "hiërarchie der wetenschappen" van Auguste Comte (1798-1857) neemt in de volgorde wiskunde, astronomie, fysica, chemie, biologie en sociologie de beheersing van het studie-object af, maar het maatschappelijk belang toe. Anderhalve eeuw wetenschappelijke arbeid heeft aan deze hiërarchie nauwelijks iets veranderd.

6. Als studenten die zitting hebben in het bestuur van een studentenvereniging tegelijkertijd een redelijke productiviteit in hun studie moeten halen, kunnen zij hun bestuursjaar bij een latere sollicitatie met recht als een "pre" opvoeren.

7. De belangrijkste zwakte van het onderwijs in de Nederlandse taal betreft niet de *spel*vaardigheid, maar de *stel*vaardigheid van de afgeleverde leerlingen.

8. Het almaar stijgen van de normen voor hygiëne en lichaamsverzorging is slecht voor het milieu.

9. De criminalisering van drugs en doping heeft veel problemen veroorzaakt en nauwelijks problemen opgelost.

10. De benaming beeldende kunsten miskent het beeldende karakter van andere kunstvormen, zoals literatuur, muziek en ballet.

11. In alle experimentele wetenschappen wordt steeds meer gemeten om het meten. Dit is een vorm van decadentie die het einde van een eeuw niet misstaat.

STRAIN FIELDS IN CRYSTALLINE MATERIALS
Methods of Analysis Based on
X-Ray Diffraction-Line Broadening

REKVELDEN IN KRISTALLIJNE MATERIALEN
Analysemethoden Gebaseerd op
Röntgendiffractie-Lijnverbreding

Front cover: Soap-bubble model of three parallel dislocations and the associated lattice distortions [taken from Bragg, W.L. & Nye, J.F. (1947): *Proc. Roy. Soc. London* **A190**, 474-481].

CIP-DATA KONINKLIJKE BIBLIOTHEEK, DEN HAAG

Berkum, Johannes Gerardus Maria van

Strain fields in crystalline materials : methods of analysis
based on X-ray diffraction-line broadening / Johannes
Gerardus Maria van Berkum. - [S.l. : s.n.]. - Ill.
Thesis Technische Universiteit Delft. - With ref. - With
summary in Dutch.
ISBN 90-9007196-2
NUGI 812
Subject headings: X-ray diffraction / line broadening /
crystalline materials ; strain fields.

STRAIN FIELDS IN CRYSTALLINE MATERIALS
Methods of Analysis Based on X-Ray Diffraction-Line Broadening

Proefschrift ter verkrijging van de graad van doctor
aan de Technische Universiteit Delft,
op gezag van de Rector Magnificus prof. ir. K.F. Wakker,
in het openbaar te verdedigen ten overstaan van een commissie,
door het College van Dekanen aangewezen,
op maandag 13 juni 1994 te 16.00 uur

door

Johannes Gerardus Maria van Berkum,

materiaalkundig ingenieur,
geboren te Oss.

Dit proefschrift is goedgekeurd door de promotor:
prof. dr. ir. E.J. Mittemeijer

To the memory of my grandfather,
Johannes Antonius van Berkum.

A word is dead
When it is said,
Some say.

I say it just
Begins to live
That day.

(Emily Dickinson, 1830-1886)

CONTENTS

Part I. Determination of Instrumental Line Broadening

Part II. Separation of Size and Strain Broadening

Part III. Specific Models for Strain Broadening

Part IV. General Model for Strain Broadening

LIST OF PUBLICATIONS

Berkum, J.G.M. van, Delhez, R., Keijser, Th.H. de, Mittemeijer, E.J. & Mourik, P. van
Note on Relaxation of Cooling-Induced Strains in Two-Phase AlSi Alloys at Room Temperature.
Scripta Metall. Mater. **25**, 2255-2258 (1991). See Chapter 5 of this thesis.

Berkum, J.G.M. van, Delhez, R., Keijser, Th.H. de & Mittemeijer, E.J.
Characterization of Deformation Fields around Misfitting Inclusions in Solids by Means of Diffraction-Line Broadening.
Phys. stat. sol. (a) **134**, 335-350 (1992). See Chapter 4 of this thesis.

Berkum, J.G.M. van, Vermeulen, A.C., Delhez, R., Keijser, Th.H. de & Mittemeijer, E.J.
Fourier Methods for Separation of Size and Strain Broadening. Validity of the Warren-Averbach and Alternative Analyses.
Mater. Sci. Forum **133-136**, 77-82 (1993). See Chapter 2 of this thesis.

Delhez, R., Keijser, Th.H. de, Mittemeijer, E.J., Berkum, J.G.M. van, Sonneveld, E.J. & Vermeulen, A.C.
Line-Profile Analysis for Probing Structural Imperfection.
In: *Residual Stresses*, eds. Hauk, V., Hougardy, H.P., Macherauch, E. & Tietz, H.-D. (Oberursel, Germany: DGM Informationsgesellschaft), pp. 49-64 (1993).

Berkum, J.G.M. van, Vermeulen, A.C., Delhez, R., Keijser, Th.H. de, Mittemeijer, E.J.
Applicabilities of the Warren-Averbach Analysis and an Alternative Analysis for Separation of Size and Strain Broadening.
J. Appl. Cryst. In the press. See Chapter 3 of this thesis.

Berkum, J.G.M. van
Diffraction-Line Broadening Due to Lattice Distortions.
I. Order-Dependence of Line Shape and Line Width and Coherency of Diffraction.
To be published. See Chapter 7 of this thesis.

Berkum, J.G.M. van, Delhez, R., Keijser, Th.H. de & Mittemeijer, E.J.
Diffraction-Line Broadening due to Lattice Distortions.
II. Methods of Analysis: Line-Profile Decomposition Using Size and Strain Parameters *versus* Line-Profile Simulation Using a Generally Applicable Strain-Field Model.
To be published. See Chapter 8 of this thesis.

Berkum, J.G.M. van, Sprong, G.J.M., Keijser, Th.H. de, Delhez, R. & Sonneveld, E.J.
The Optimum Standard Specimen for X-Ray Diffraction Line-Profile Analysis.
To be published. See Chapter 1 of this thesis.

PREFACE

First of all, the reader should be warned. This thesis is a compilation of papers published or to be published. As a consequence, each chapter can be read apart from the others, but, on the other hand, the texts of the chapters do not link up with each other. Therefore, the reader is advised to read the General Introduction and the Summary first to sense the outline and cohesion of this thesis.

Secondly, this thesis is the precipitation of four years of scientific research. In such a period, neither a full account of all the branches in the field can be given, nor complete and everlasting recipes. Nevertheless, I hope the reader agrees that our understanding of strain broadening and the possibilities for its analysis in practice have been enhanced significantly.

Finally, I would like to acknowledge all who have contributed to this thesis in any way. In particular, Eric Mittemeijer is thanked for employing me in his group, but much more for his scientific insight and guidance, Rob Delhez for his enthusiasm and creativity and Staf de Keijser for his never-ending, but valuable comments. With Arnold Vermeulen, I have had a fruitful co-operation and a lot of fun. Further help I received from Bert Sprong, Niek van der Pers, dhr. van Lent, Ed Sonneveld, Anne Buis, Frans van Oostrum, Dick de Haan, dhr. Jansma, dhr. Colijn, dhr. Bakker, Anke Kerklaan-Koene, Liesbeth Secker-Versteegh, and all other present and former colleagues in the section FCM-2. Dr. Langford induced me to do the important measurements on deformed tungsten. Without Tamás Ungár, I would have missed an essential branch of line-profile analysis and thanks to Endre Borbély and Pista Groma I have had a fruitful and pleasant stay in Budapest. Last but not least: thanks to Ina, family and friends, who have given me the necessary diversion in the past time.

April, 1994 Jurgen van Berkum

GENERAL INTRODUCTION

I. BACKGROUND

The mechanical properties of crystalline materials are often largely determined by the presence of crystal imperfections. All crystal imperfections, including the finite sizes of the grains or crystallites of the material, give rise to broadening of (X-ray) diffraction lines. In this thesis, the attention is concentrated on imperfections that are accompanied by microstrains, *i.e.* local distortions of the crystalline lattice. Examples of such crystal imperfections are dislocations, precipitates and inclusions. It is easily understood qualitatively that microstrains induce diffraction-line broadening. The angular position of a diffraction line is related to the average distance between the lattice planes corresponding to the reflection considered (Bragg's law). Microstrains involve local deviations of such distances from the average. The corresponding parts of the specimen diffract at angular positions somewhat deviating from the average, resulting in broadening of the total line. The aim of this thesis is to develop methods for the analysis of microstrains from (X-ray) diffraction-line broadening.

The first application of line-broadening analysis concerned a determination of the crystallite size of colloidal particles by Scherrer (1918). The relation between microstrains and line broadening was firstly investigated by Dehlinger (1927) for cold rolled metals. Important theoretical progress is due to Stokes & Wilson (1942; 1944) and Bertaut (1949). Using the kinematical theory of diffraction, a complete and undisputed description of the Fourier coefficients of diffraction-line profiles broadened by finite crystallite sizes and microstrains was developed by Warren and Averbach (1950; see also Warren, 1969). Using this theoretical description, the line broadening of a given atomic arrangement can be calculated exactly.

Unfortunately, this does not imply that analysis of measured line broadening is straightforward. Methods of analysis have been proposed by Warren & Averbach (1952) and Williamson & Hall (1953) and, in spite of objections raised against these methods (see Sec. II), they are probably still the methods most frequently applied for the analysis of microstrains. In the meantime, experimental possibilities have been improved enormously. Nowadays, X-ray diffraction-line broadening can be measured precisely and reproducibly by means of commercially available instruments. Further, possibilities for (numerical) data manipulation have become almost unlimited. This, in combination with the accepted theoretical description of line broadening, makes line-broadening analysis to a potentially very powerful tool in microstructural research. It is complementary to transmission electron microscopy, because of the relatively large sampling volume, the quantitative character and the relatively small preparation effects of line-broadening analysis. At present, the main obstacle for the application of line-broadening analysis is the lack of straightforward methods for the translation of measured data to physically meaningful parameters. The methods discussed and developed in this thesis have been divided into two categories, which are called "analytical methods" and "model-based methods". The reasons for this division are explained in the following two sections.

II. ANALYTICAL METHODS

Based on the diffraction-line broadening theory, a number of methods for line-profile analysis have been developed. The development as well as the application of these methods always proceeds as indicated in the following diagram:

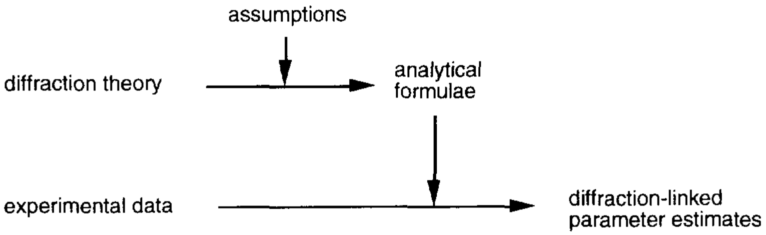

Firstly, the general theoretical description of line broadening, too complex to be used in a method of analysis itself, is translated into practicable formulae by applying simplifying assumptions. The derived formulae contain parameters that are necessarily linked closely to the diffraction theory. Secondly, using these formulae, the experimental data are translated directly to parameter values.

For some specimens, it is reasonable to assume that all broadening is due to the finite crystallite size and to discard the part describing the effect of microstrains from the theory. Then, relatively simple relations between observable quantities and parameters in the diffraction theory can be derived, that allow a detailed investigation of crystallite sizes and shapes (*e.g.* Louër *et al.*, 1983).

If microstrains are present in the material, the general description of line broadening is much more complex. The frequently applied Warren-Averbach method (1952) involves the least assumptions of the analytical methods available to analyse strain broadening or simultaneous size and strain broadening. Unfortunately, the Warren-Averbach method translates measured line broadening to parameters that still refer to the diffraction process and that are incompatible with generally adopted theories to describe the deformed solid state. The physical meaning of the size parameter in the Warren-Averbach method (and all other analytical methods), for example, has always been unclear (see *e.g.* Warren, 1959). In the Chapters 7 and 8, the concept of "size" and the meaning of the size parameter in the Warren-Averbach method are investigated. On the other hand, the Warren-Averbach parameters have the advantage that they are sufficiently general for the description of specimens with any type of crystal imperfection, whereas the use of more specific parameters is necessarily more restricted.

Another objection raised against the Warren-Averbach method is that the approximation used for the description of strain broadening is incompatible with the nature of the microstrains in a plastically deformed material and that the Warren-Averbach method therefore produces unreliable results (Wilkens, 1979; 1984). In the Chapters 2, 3, and 8 of this thesis, this second objection is investigated. Further, in the Chapters 2 and 3, a method is developed similar to the Warren-Averbach method, but based on different approximate descriptions of size and strain broadening. With the two methods together, more types of size and strain broadening can be analysed than with a single one. The selection of the appropriate method, however, requires appreciable advance knowledge about the size and strain characteristics of the specimen.

III. MODEL-BASED METHODS

A completely different approach of line-profile analysis is used in model-based methods, which are executed as indicated in the following diagram:

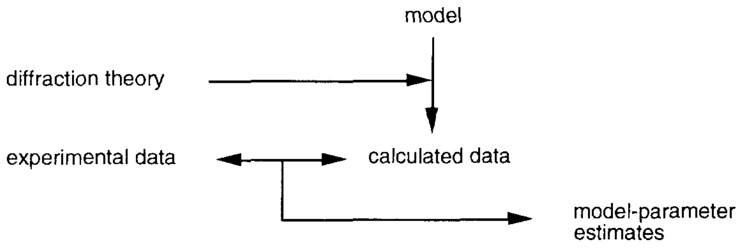

The starting point is a model that describes the essential characteristics of the microstructure of the specimen. The model contains a limited number of adjustable model parameters. Using the diffraction theory, data can be calculated (usually necessarily numerically, but without applying any approximations) that would have been obtained if the model were a real specimen. By adapting and refining the model parameters until the fit between calculated and experimental data is as good as possible, the best parameter estimates are obtained.

The main advantage of model-based methods over analytical methods is that the parameters used characterize the microstructure of the specimen directly in a physically meaningful way. A second advantage is that (virtually) no assumptions are involved in the data calculation and parameter evaluation. Obviously, substituting the true microstructure by a model is a serious assumption and, therefore, the adequacy of the model has to be judged carefully. Fortunately, in model-based methods it is relatively easy to extend or change the model in order to investigate the effects ignored in a first step. A related advantage is the flexibility in the choice of experimental data to be fitted: they may be line widths or Fourier coefficients and they may be corrected for background intensity and instrumental broadening or not (if not, these effects are included in the calculated data, if necessary by means of adjustable parameters).

A problem inherent to model-based methods is the judgment of the fit. Statistical measures for goodness-of-fit are only meaningful if the differences between the calculated and the experimental data are accidental (random), not systematic. If systematic errors dominate, which is often the case, and one cannot or does not want to extend the model, effects of the probably most important deficiencies of the model should be taken into account in the judgment of the fit. If this is impossible, parameter values should be presented with care and, preferably, with an indication of their variability.

The microstructural models used for the analysis of line broadening have been divided into two categories: models for specific types of crystal imperfections and models providing a more general description of the microstrains in a distorted specimen. In this thesis, two specific models are discussed (see Sec. III.A) and one general model is developed (see Sec. III.B).

A. Specific models for strain broadening

The first specific model concerns dislocation configurations. An accurate determination of the dislocation density and arrangement is one of the most important potential possibilities of line-broadening analysis. A first attempt of modelling the line broadening originating from the strain fields around dislocations is due to Wilson (1952); important progress is due to Krivoglaz & Ryaboshapka (1963), Wilkens (1970), Ungár *et al.* (1984) and Groma, Ungár & Wilkens (1988). The existing methods do not comply fully with the definition of model-based methods, since they make use of approximate analytical formulae for a direct translation of experimental data to parameter values. They are classified here as model-based, because their starting points are microstructural models and their parameters refer directly to these models. The existing methods are not yet widely applied because of both practical difficulties in their application and theoretical difficulties in the interpretation of their results. In Chapter 4, these methods are reviewed and compared theoretically. Further, procedures for their application in practice are developed and tested by means of widely different sets of experimental data.

The second example of a method based on a specific microstructural model concerns specimens containing misfitting inclusions. The strains in such specimens have been investigated extensively by Eshelby (1956). The misfit between the matrix and the inclusions is important for the mechanical behaviour of the material, but, to determine the value of the misfit in practice, there are only very few methods, of which X-ray diffraction-line broadening analysis is one. In Chapter 5, a model-based method is developed for the analysis of the line broadening from different AlSi alloys with very fine Si precipitates in an Al matrix. All known microstructural characteristics (*e.g.* the average precipitate size) are incorporated in the model, leaving only the misfit as an adjustable parameter. As a further illustration of the application of the method, the effect of ageing at room temperature on the misfit in AlSi alloys is investigated in Chapter 6.

B. General model for strain broadening

In addition to models for specific crystal imperfections, an attempt is made to develop a realistic and flexible model that contains the most important characteristics of microstrains in a distorted specimen in general. It is thought that the total strain field in a specimen can be considered as the superposition of many "component strain fields", induced by individual crystal imperfections, and that the distances between the imperfections and the amplitudes and widths of the component strain fields are most important for the strain broadening. The spatial distribution of the imperfections and the characteristics of their strain fields are described statistically in this model to simulate the unpredictability of the total strain field in a real specimen. Using this model, the relation between a number of line-broadening characteristics and the general strain-field characteristics is investigated (Chapter 7). The possibility of using the strain-field model in a model-based method of analysis is investigated by analysing experimental line profiles recorded from a ball-milled tungsten powder (Chapter 8).

IV. PRACTICAL CONSIDERATIONS

Although the physical interpretation of measured data is the most severe problem in line-profile analysis, the execution of the measurements and correction for unwanted experimental effects also require attention.

An important experimental problem is the correction for the line broadening inherent to the instrument. Diffractometers have been built that minimize the instrumental broadening (Wilkens & Eckert, 1964), but these are not commercially available and not (routinely) applicable to fine-grained materials (crystallite size ≲ 1μm). Moreover, they lack an important advantage of powder diffraction techniques: they do not probe many grains at once. Using conventional powder diffractometers the instrumental broadening can be measured from a standard specimen, *i.e.* a specimen that contains no lattice defects that contribute to the measured broadening. The requirements, preparation and characterization of a general purpose standard specimen are presented in Chapter 1. Once a standard specimen is available, the correction for instrumental broadening of measured line profiles is straightforward by means of well-established deconvolution procedures (Stokes, 1948; Langford, 1978).

Two other experimental complications are the unavoidable profile truncation due to a finite measurement range and overlapping of neighbouring profiles. Both topics are subject of current research of the present group (see Vermeulen *et al.*, 1992 and Sonneveld *et al.*, 1992, respectively).

V. OUTLINE

The body of this thesis starts with a practical subject: the determination of instrumental line broadening (Part I). Subsequently, a classical and a new *analytical* method of line-broadening analysis are discussed (Part II). The rest of this thesis is devoted to *model-based* methods: two specific models for strain broadening (Part III) and one general model for strain broadening (Part IV).

REFERENCES:

Bertaut, F. (1949). *C. R. Acad. Sci. Paris* **228**, 187-189, 492-494.

Dehlinger, U. (1927). *Z. Kristallogr.* **65**, 615-631.

Eshelby, J.D. (1956). *Solid State Phys.* **3**, 79-144.

Groma, I., Ungár, T. & Wilkens, M. (1988). *J. Appl. Cryst.* **21**, 47-53.

Krivoglaz, M.A. & Ryaboshapka, K.P. (1963). *Phys. Met. Metall.* **15**, 14-26.

Langford, J.I. (1978). *J. Appl. Cryst.* **11**, 10-14.

Louër, D., Auffrédic, J.P., Langford, J.I., Ciosmak, D. & Niepce, J.C. (1983). *J. Appl. Cryst.* **16**, 183-191.

Scherrer, P. (1918). *Nachr. Ges. Wiss. Göttingen*, July 26, 98-100. See also: Scherrer, P. (1920). In: R. Zsigmondy, *Kolloidchemie* (Leipzig, Germany: Otto Spamer), pp. 387-409.

Sonneveld, E.J., Delhez, R., Keijser, Th.H. de & Mittemeijer, E.J. (1992). *Mater. Sci. Forum* **79-82**, 119-124.

Stokes, A.R. (1948). *Proc. Phys. Soc. London* **61**, 382-391.

Stokes, A.R. & Wilson, A.J.C. (1942). *Proc. Camb. Phil. Soc.* **38**, 313-322.

Stokes, A.R. & Wilson, A.J.C. (1944). *Proc. Phys. Soc. London* **56**, 174-181.

Ungár, T., Mughrabi, H., Rönnpagel, D. & Wilkens, M. (1984). *Acta Metall.* **32**, 333-342.

Vermeulen, A.C., Delhez, R., Keijser, Th.H. de & Mittemeijer, E.J. (1992). *J. Appl. Phys.* **71**, 5303-5309.

Warren, B.E. (1959). *Prog. in Metal Phys.* **VIII**, 147-202.

Warren, B.E. (1969). *X-ray Diffraction* (Reading, Massachusetts: Addison-Wesley), pp. 264-268.

Warren, B.E. & Averbach, B.L. (1950). *J. Appl. Phys.* **21**, 595-599.

Warren, B.E. & Averbach, B.L. (1952). *J. Appl. Phys.* **23**, 497.

Wilkens, M. (1970). In: *Fundamental Aspects of Dislocation Theory*, NBS Spec. Publ. 317, vol. II, eds. Simmons, J.A., Wit, R. de & Bullough, R. (Washington: US Dpt. of Commerce), pp. 1195-1221.

Wilkens, M. (1979). *J. Appl. Cryst.* **12**, 119-125.

Wilkens, M. (1984). In: *Microstructural Characterization of Materials by Non-Microscopical Techniques*, eds. Hessel Andersen, N., Eldrup, M., Hansen, N., Juul Jensen, D., Leffers, T., Lilholt, H., Pedersen, O.B., Singh, B.N. (Roskilde, Denmark: Risø National Lab.), pp. 153-168.

Wilkens, M. & Eckert, K. (1964). *Z. Naturforschg.* **19 a**, 459-470.

Williamson, G.K. & Hall, W.H. (1953). *Acta Metall.* **1**, 22-31.

Wilson, A.J.C. (1952). *Acta Cryst.* **5**, 318-322.

CHAPTER 1

THE OPTIMUM STANDARD SPECIMEN FOR X-RAY DIFFRACTION LINE-PROFILE ANALYSIS

J.G.M. VAN BERKUM, G.J.M. SPRONG, TH.H. DE KEIJSER, R. DELHEZ, AND E.J. SONNEVELD
Laboratory of Materials Science, Delft University of Technology,
Rotterdamseweg 137, 2628 AL Delft, The Netherlands.

ABSTRACT

A *perfect* general purpose standard specimen for high accuracy line-profile analysis is shown to be an illusion. Balancing the partly contradictory requirements, an *optimum* standard specimen for a parafocussing diffractometer is developed. To obtain the optimum standard specimen, a 5-10 μm particle size fraction is taken from the NIST certified Si powder SRM640a, about 1.5 mg/cm^2 of this powder is uniformly deposited on a (510) oriented Si single-crystal wafer and the assembly is heat treated for 2 h at 1273 K to remove lattice imperfections. All procedures necessary are precisely given, easily applicable, and reproducing. For the present standard specimens, the random errors due to crystal statistics are quantified and shown to be acceptable for spinning specimens; the systematic errors due to residual size and transparency broadening are determined semi-empirically and can be eliminated, if desired. Thus, the proposed optimum standard specimen allows the determination of instrumental line profiles free from systematic errors and with random errors in the line width of the order of 0.001 °2θ, allowing a full use of the capacities of modern diffractometers and data evaluation procedures.

I. INTRODUCTION

In X-ray powder-diffraction analysis, there is a need for knowledge about the shape of the line profile due to the non-ideal optics of the diffraction equipment and the wavelength distribution of the radiation used. This instrumental line profile (*g* profile) depends, among other things, on the diffraction angle 2θ. A line profile measured from a structurally imperfect specimen (h profile) can be considered as the convolution of the line profile due to the imperfections (f profile) and the g profile. In line-profile analysis, either g is deconvoluted from a measured line profile h to obtain a structural line profile f, or g is convoluted with a calculated f profile to obtain a line profile that is to be compared with a measured line profile h. In principle, computer simulation of g is possible (see *e.g.* Kogan and Kupriyanov, 1992; Timmers *et al.*, 1992a). However, not all the characterizing parameters of the diffraction equipment to be used in the simulation (*e.g.* of the tube focus, Soller slits, monochromator performance, *etc.*) can be determined directly with sufficient accuracy. Therefore, a measurement of g is more precise and reliable, provided a standard specimen is available. A perfect standard specimen gives no structural broadening and no errors due to counting statistics, crystal statistics (too few diffracting crystallites), and differences in properties (*e.g.* transparency) with the specimen to be investigated. It would be ideal to have a standard specimen from the same material as the specimen to be investigated. In practice, this is seldomly achievable because of the difficulties and time involved in the preparation of such a specimen[1]. Therefore, the development of a general purpose standard is desirable. The problem of non-matching 2θ can be overcome by interpolation of the parameters describing the g profile.

Candidate materials for a standard specimen have been reviewed and LaB_6 has been determined to be an excellent one (Fawcett *et al.*, 1988). The National Institute of Standards & Technology (NIST), Gaithersburg (MD), U.S.A., has made available LaB_6 as a standard material: SRM 660. As already stated in the NIST certificate, small strains are still present in the material (see Sec. III.E). For an analysis of the highest demands, a material with less structural imperfection is wanted. Apart from the structural perfection of the material, also a warranted procedure for the preparation of an appropriate standard specimen from a powder is essential.

In view of modern developments in Rietveld analysis, profile fitting, truncation correction, analysis of marginal structural broadening, *etc.*, the error in instrumental line profiles should meet the precision of modern equipment (*e.g.* errors in the profile width of the order of 0.001 °2θ). Then problems arise. Specimens consisting of crystallites with dimensions of the order of 10 μm produce size broadening already of the order of (the desired) 0.001 °2θ. For the same specimens, the error due to crystal statistics in the integrated intensity of the measured g profile may easily exceed 1 % (Klug and Alexander, 1974). The corresponding error in the integral breadth β is about the same and thus (see Fig. 5) may easily exceed 0.001 °2θ. Larger crystallites give a smaller size broadening but a larger crystal-statistical error; for smaller

---

[1] A roughly prepared "standard" of the same material and of the same constitution as the specimen to be investigated may be useful in establishing backgrounds.

crystallites, the reverse holds. The errors due to crystal statistics may be minimized by using a thick standard specimen made from a (very) low-absorption material, but then one is confronted with extra line broadening due to specimen transparency.

Therefore, it seems impossible to produce *perfect* standard specimens for X-ray diffraction line-profile analysis. The best way out is to develop *optimum* standard specimens which allow line-profile measurements with minimum random errors due to counting and crystal statistics, and with small systematic errors due to finite crystallite size and transparency. The systematic errors of optimum standard specimens should be removable so that perfect g profiles can be obtained.

Strains are always present in the starting material. These have to be removed by heat treatment. In massive specimens, this will usually produce much grain growth, which causes bad crystal statistics. The heat treatment itself will produce strains in case of materials with anisotropic thermal expansion. Further, massive specimens may deform due to temperature gradients during cooling. For these reasons, there is a strong preference for a standard material in powdered form, although surface roughness and lateral density fluctuations may pose problems. A powder has the additional advantage that it can be used as an "internal" standard or, by mixing with a filler material, for producing standard specimens with variable transparency.

In this paper, an easily applicable, reproducing procedure is described for producing optimum standard specimens. The specimens give rise to very small broadenings, caused by crystallite size, surface roughness, and transparency that can all be corrected for. The crystal-statistical errors are small and the counting times required for small counting-statistical errors are moderate.

II. FABRICATION OF THE OPTIMUM STANDARD SPECIMEN

In this section, the reasonings are given for the choices of materials and techniques used in the production of the *optimum* standard specimen (for definition of *optimum*, see Sec. I). It was demanded that the resulting recipe should guarantee reproducibility. The conclusion was reached, and experimentally confirmed (see Secs. III and IV), that the optimum standard specimen should consist of Si particles of 5 to 10 μm diameter evenly and practically unstacked distributed over a (510) Si single-crystal wafer; to avoid lattice-imperfection broadening, this assembly had to be heat treated.

A. Starting material

With the X-ray wavelengths CuKα, CoKα, CrKα, currently used in X-ray diffraction analysis, low-absorption-coefficient materials are favourable for good crystal statistics and small effects due to extinction and surface roughness. The imminent transparency broadening with such materials can be reduced to an almost immaterial level by using a thin layer of powder (see Sec. IV.A), although part of the advantages are then lost. A general purpose standard specimen should be stable with respect to the ambient atmosphere and should give sufficient, but not too many, diffraction lines evenly distributed over the diffraction angle 2θ. Further, in view of the techniques most suitable for producing the desired particle size distribution (see Sec. II.B) and the unstacked, even distribution of the standard powder over a support (see Sec. II.C), the starting material should not be dissolvable in the fluids used. Overviewing these demands, it is almost self-evident to use Si or Ge.

Si is favoured because there are already Si powders available certified for use as a diffraction standard in the determination of lattice spacings, namely SRM 640a and 640b issued by NIST (formerly NBS), Gaithersburg (MD), U.S.A. (Hubbard, 1983). The two standard materials are practically the same; we have used SRM 640a. The powder as received is not immediately suited, because it contains a fraction of very small particles (Fawcett *et al.*, 1988) and the particles contain lattice imperfections (see Sec. II.D).

A further argument for the use of Si is the easy availability of Si single-crystal wafers as a support for the thin Si powder layer (see Sec. II.C). By using a support of the same material as the standard powder, problems are avoided evoked by interdiffusion, chemical reactions, and the difference in thermal expansion during the heat treatment for the removal of lattice imperfections.

B. Obtaining the desired particle size distribution

The particle size distribution of SRM 640a is relatively broad (see Figs. 1 and 2). There is a considerable fraction of too small particles that produce too much size broadening (see Fig. 3). Further, a number of very large particles are present that are very detrimental with respect to crystal statistics. The obvious method to obtain a narrower particle-size distribution is sedimentation in a fluid (Allen, 1990). The fluid to be used should give acceptable sedimentation times, very good wetting of the Si particles to obtain isolated particles in the fluid during sedimentation. It should also be easily removable, for example by evaporation, without leaving a residue. Taking also into account toxicity, inflammability, and availability, we ended up (rather arbitrarily) with 2-propanol. Details about the sedimentation procedure applied (which takes ~ 1 day) are given in App. A. The effects of the procedure are presented in Figs. 1 and 2.

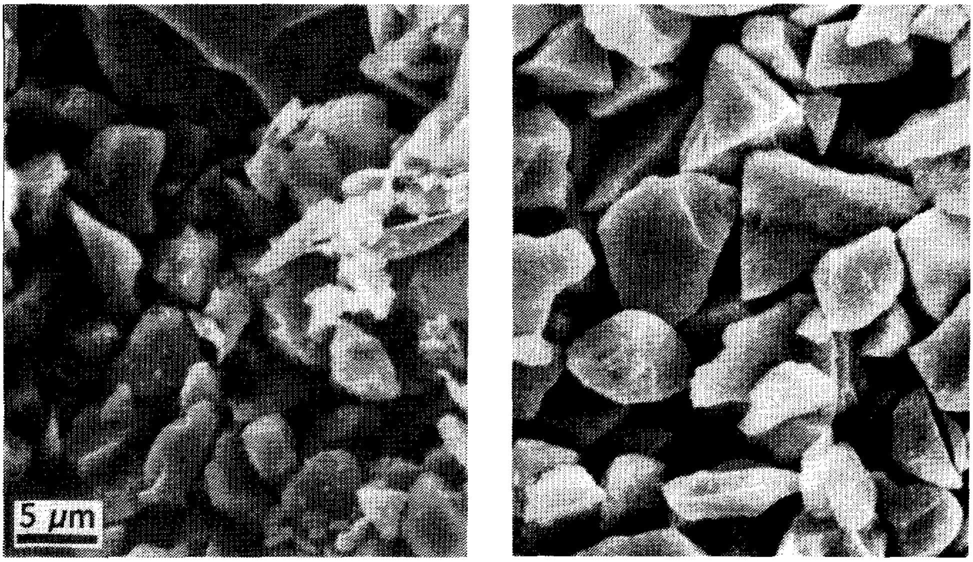

(*a*) (*b*)

Fig. 1 Scanning-electron-microscope observations (JEOL JSM-840A) of Si powder from SRM 640a, (*a*) before and (*b*) after application of the sedimentation procedure of App. I.

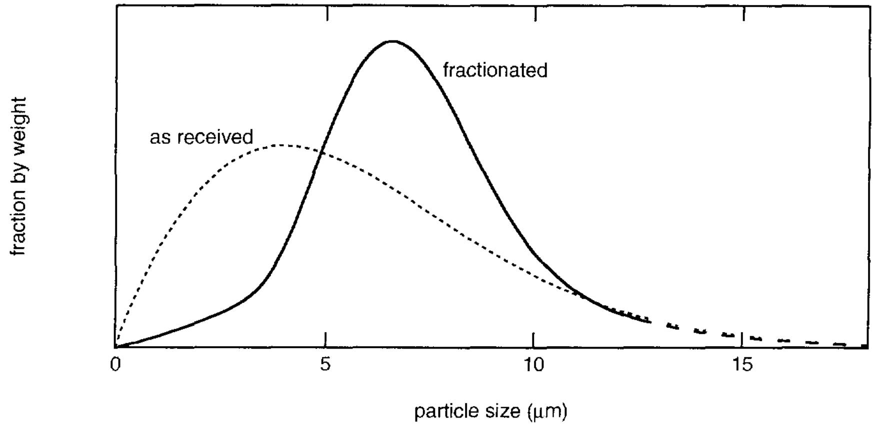

Fig. 2 Particle-size distribution of Si powder from SRM 640a, measured by a Coulter Multisizer, before (as received) and after (fractionated) application of the sedimentation procedure of App. A. The average sizes before and after the sedimentation are 5.8 and 7.2 μm, respectively. The areas under the curves are equal. The experimental data points (124 classes between 1 and 33 μm) have been fitted with analytical functions. Fractions at large sizes (>13 μm) are uncertain.

C. Mounting the powder on a support

With increasing layer thickness, *i.e.* increasing mass of Si per unit area of the support, the counting and crystal-statistical errors decrease but the broadening due to transparency increases. On the basis of experimental information (see Secs. III and IV), one may conclude that about 1.5 mg/cm^2 of Si powder, produced according to App. A, is the optimum amount for a standard specimen. Then, the "extra" transparency and size broadenings are very small and can be neglected or corrected for (see Sec. IV) and the crystal statistics and required counting times are acceptable (see Table II). For all reflections except one, errors in the integral breadth of the order of 0.001 °2θ are achieved. Of course, one can, on the basis of the same experimental information, choose for a thicker layer, *i.e.* for shorter counting times and better crystal statistics, but at the expense of a larger transparency broadening.

The particle layer should be laterally homogeneous. Sedimentation from a homogeneous suspension, followed by a complete evaporation of the fluid, is a favourable technique with again 2-propanol as a suitable fluid. As a support for the layer of Si particles, a Si single-crystal wafer, cut parallel to *e.g.* (510), is unexcelled: it gives no peaks or humps with the usual X-ray wavelengths (in the normal, Bragg-Brentano geometry) and its contribution to the background is very low (Parrish, 1980).

Surprisingly, there is no need for any additive to the suspension fluid or "glue" on the support to promote the adhesion of the Si particles to the Si wafer. The assembly remains perfectly intact during normal laboratory handling as long as the layer is not touched. The recipe for the sedimentation is given in App. A.

D. Heat treatment of the specimen

One can establish when a standard material is sufficiently free from crystal imperfections by investigating line broadening as a function of heat-treatment time: line broadening should decrease and reach a constant (= minimum) level. To confirm that the minimum has been reached, a second, higher temperature can be used.

For the present Si particles on a Si (510) wafer, a heat treatment of 2 h at 1273 K proved to be sufficient to produce the optimum standard (see Table I; the decrease for the {220} reflection after 2 h at 1273 K is not significant). In Fig. 3, the effect of this heat treatment on the integral breadth of the {220} line profile is shown.

The same heat treatment as above can be applied if one wishes to obtain loose standard powder. The powder with the desired particle-size distribution can be enclosed in a quartz glass capsule filled with Ar (0.21×10^5 Pa, purity 99.998 %). With the time and temperature indicated above and a moving capsule, sintering of the silicon particles is practically avoided.

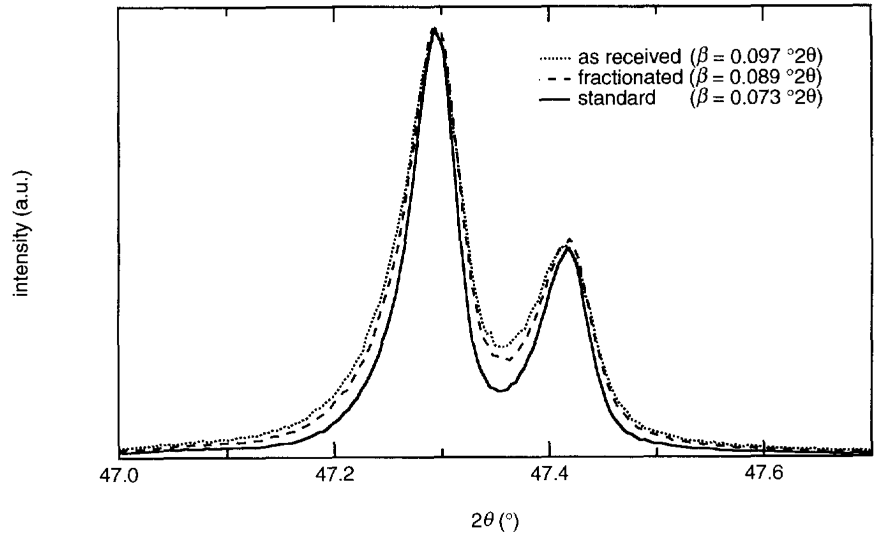

Fig. 3 The {220} line profile of Si from SRM 640a, before (as received) and after (fractionated) application of the sedimentation procedure of App. A and after 2 h at 1273 K additionally (standard). For the X-ray diffraction measurement conditions and the data evaluation, see Table II. The maximum intensities are scaled equal. The difference in line broadening between "as received" and "fractionated" is larger than what follows from the difference in size broadening calculated from the size distributions (Fig. 2). Apparently, the removed particles are structurally less perfect than the remaining ones.

Table I. The effect of heat treatment on the integral breadth β of the {220} and {531} reflections of the Si powder (1.36 mg/cm^2) on a (510) Si wafer. The heat treatments were performed in a horizontal tube furnace (internal diameter 75 mm) through which passed 20 ml/min Ar at atmospheric pressure. Before entering the furnace the Ar (99.998 %) passed subsequently a moisture filter, a charcoal filter, an oxygen filter, and a BTS column at 368 K. For the X-ray measurement conditions, the data evaluation and $\sigma_\beta^{\text{cnt.st.}}$, see Table II.

Sequent heat treatments	β (°2θ)	
	{220}	{531}
none	0.0901	0.192
2 h at 1273 K	0.0737	0.135
18.5 h at 1273 K	0.0731	0.135
4 h at 1348 K	0.0727	0.135
$\sigma_\beta^{\text{cnt.st.}}$:	0.0005	0.002

Table II. **X-Ray Diffraction Measurement Conditions, Data Evaluation and Results**

Measurement conditions: Siemens D500 diffractometer, distance focus-axis and axis-receiving slit 200.6 mm, Philips Cu tube, line focus 0.4 × 8 mm, take-off angle 6.0°, 45 kV, 30 mA, divergence slit 12.0 × 1.038 mm (= 1°), divergence and receiving scatter slits, diffracted-beam Soller slits with divergence 0.01765 (= distance between foils divided by length of foils), receiving slit 12.0 × 0.064 mm (= 0.018 °2θ), effective height of irradiated area 13 mm, diffracted-beam Johann graphite monochromator, Siemens NaI (Tl) scintillation counter, pulse height discrimination. Slits and monochromator were handled in accordance with Timmers *et al.* (1992b). Inlet temperature of the cooling water for the X-ray tube was 19.3 ± 0.3 °C. Temperature of diffractometer, specimen and ambient atmosphere was 22.5 ± 0.3 °C. The specimen was spinning (30 rpm) around an axis perpendicular to its surface. Fixed-time counting was applied.

Data evaluation: The background for a measurement range was estimated as a least-squares straight line through the first and last 20 data points and removed. The CuKα_2 component was removed according to Delhez and Mittemeijer (1975) with an α_2/α_1 intensity ratio of 0.475 (this value gave least rippling of high-angle tail of α_1 component). The peak position and intensity were estimated by least squares fitting of a parabola through the data points above 70 % of the maximum intensity. No corrections to β were applied for residual transparency and size broadening (see Sec. IV).

Results: Peak position ($2\theta_p$), integrated (I_{int}), peak (I_p) and background (I_{bg}) intensities, integral breadth (β), and standard deviations of β due to counting statistics ($\sigma_\beta^{cnt.st.}$, see App. B) and crystal statistics ($\sigma_\beta^{cryst.st.}$, see Sec. III.C) of all CuKα_1 reflections of a spinning Si standard specimen (with 1.36 mg/cm^2).

{*hkl*}	measurement range (°2θ)		step size (°2θ)	meas. time (h)	$2\theta_p$ (°2θ)	I_p*) %{111}	I_{int} %{111}	I**) from JCPDS %{111}	I_p/I_{bg}	β (°2θ)	$\sigma_\beta^{cnt.st.}$ (°2θ)	$\sigma_\beta^{cryst.st.}$ (°2θ)
111	26.7	30.2	0.006	0.5	28.423	100.0	100.0	100.0	662	0.0823	0.0005	0.0002
220	45.6	49.1	0.006	1.4	47.292	29.0	25.6	38.6	296	0.0727	0.0005	0.0003
311	54.6	58.1	0.006	3.4	56.120	11.3	10.1	18.5	111	0.0734	0.0006	0.0003
400	67.5	71.0	0.006	16.8	69.124	1.6	1.6	3.2	18	0.0813	0.0040	0.0008
331	74.5	78.5	0.006	6.8	76.373	5.0	4.9	5.4	63	0.0806	0.0009	0.0004
422	86.5	90.5	0.006	6.1	88.029	4.7	5.2	5.3	67	0.0922	0.0010	0.0006
511/333	93.0	97.5	0.008	5.8	94.952	2.1	2.6	2.5	30	0.1026	0.0024	0.0006
440	104.5	109.5	0.008	28.6	106.707	1.2	1.7	1.2	16	0.1195	0.0023	0.0013
531	112.0	117.0	0.010	17.3	114.087	1.7	2.9	2.6	19	0.1359	0.0020	0.0008
620	125.0	130.5	0.012	45.5	127.528	0.8	1.8	2.8	7	0.1800	0.0033	0.0016
533	134.5	140.0	0.014	35.8	136.878	0.9	2.3	1.0	7	0.2140	0.0036	0.0020
444	156.0	163.0	0.030	20.1	158.633	0.7	3.5	-	5	0.4119	0.0067	0.0073

*) For the {111} reflection, $I_p \approx 5\times10^3$ cps.

**) Relative intensities for finite specimen thickness (*i.e.* finite mass of Si per unit area η), calculated from intensities for infinite specimen thickness I_{hkl}^{∞} from JCPDS file 27-1402, according to $I = I_{hkl}^{\eta} / I_{111}^{\eta}$, where $I_{hkl}^{\eta} = I_{hkl}^{\infty}[1-\exp\{-2(\mu/\rho)\eta/\sin\theta_{hkl}\}]$ with (μ/ρ) = 68.7 cm^2/g and η = 0.00136 g/cm^2.

III. CHARACTERIZATION OF THE OPTIMUM STANDARD SPECIMEN

As explained in the introduction, it is impossible to produce a perfect standard specimen; only an optimum standard specimen is possible. Line profiles from an optimum standard specimen are unavoidably affected by systematic errors due to size broadening and transparency broadening and by random errors due to crystal statistics. Also errors due to counting statistics may pose problems if the small amount of standard material requires excessive counting times. In Sec. IV, it is shown that the residual size and transparency broadenings are very small and can be corrected for properly. In this section, emphasis will be on the effects of crystal statistics, required counting times, and the performance of the present standard with respect to LaB_6 (SRM 660). For an overview of measured standard line-profile parameters, see Table II.

A. X-ray diffraction and data evaluation

Full details about the equipment, measurement conditions, and data evaluation are given in Table II. To counteract effects of changes in barometric pressure and in performance of the equipment, long measurements were performed by scanning a range repeatedly and adding up data files. It is noted that the alignment procedure and the specimen mounting in the diffractometer (with Bragg-Brentano geometry) were such that the surface of the Si (510) wafer corresponds to zero specimen displacement. Since the Si powder is on top of this surface, there is always a small specimen displacement (of the order of the "average" layer thickness ~ 7 μm).

As a characterizing parameter for the broadening of the line profiles, the integral breadth β (= profile area/height) is chosen, rather than the full width at half maximum, because the latter is less sensitive to the tails of a profile.

B. Homogeneity and reproducibility

The standard specimen has a homogeneous, smooth appearance. However, at close inspection, one can distinguish concentric "rings". These probably originate from the 2-propanol evaporation process (see App. A). An attempt was made to quantify possible fluctuations in the local mass of Si per unit area by wiping away from the support the Si powder in 12 concentric rings (successively from the outside to the centre) with an area of 50 mm^2 each. From the differences in weight of the specimen before and after each wiping of a ring, it was found for three standard specimens (Ø 27 mm with about 1.6 mg/cm^2 of Si) that the relative standard deviations in the Si mass for the 12 rings were 23 %, 28 % and 32 %. The uncertainties in the measurement technique (*e.g.* ± 0.1 mg in weighing) account for about half of the observed variance, so the fluctuations are about 20 %.

To investigate the reproducibility[2] of the standard specimens with respect to the X-ray diffraction, the {220} reflections were recorded of three standard specimens with 1.26 , 1.36 and 1.36 mg/cm^2 of Si (measurement conditions and data evaluation as in Table II). The integrated intensities were 94 , 104 and 92 cps×°2θ, the peak positions were 47.297, 47.294 and 47.295 °2θ, and the integral breadths were 0.0726 , 0.0731 and 0.0721 °2θ, respectively. The fluctuations in the mass of Si per unit area observed in the wiping procedure probably account for the relatively large variations in the integrated intensities. The variation in the peak positions is very small. The variation in the integral breadths is well within the experimental error (see Table II), which shows that the heat treatment of the specimens reproduces well.

A comparison with JCPDS data (see Table II) does not indicate significant texture in the present standard specimens.

C. Crystal-statistical errors

The term "crystal statistics" indicates a sampling problem in powder diffraction: the number of diffracting crystallites is subjected to statistical variations and so are line-profile characteristics like position, integrated intensity, and integral breadth. At the moment, no straightforward method exists to determine the standard deviation $\sigma_\beta^{\text{cryst.st.}}$ in the integral breadth due to crystal statistics. To arrive at an estimate for $\sigma_\beta^{\text{cryst.st.}}$ for all reflections (with CuKα), a large number of standard specimens (a few dozens for significant results) could have been prepared and measured. This is very impracticable and another route was followed, which is described in App. C.

The method followed involves measurements of a low-angle reflection $\{h_0k_0l_0\}$ at a number of different φ settings (φ is the angle of rotation around an axis perpendicular to the specimen surface). From such a set of measurements, the relative standard deviation for a *stationary* specimen $\left(\sigma_\beta^{\text{cryst.st.}}/\beta\right)_{h_0k_0l_0}^{\text{stat}}$ is obtained. For two standard specimens, with 1.36 and 1.26 mg/cm^2 of Si, measurements (for conditions, see Table II) of the {220} reflection at 36 different φ settings (see Fig. 4) yielded on average:

$$\left(\frac{\sigma_\beta^{\text{cryst.st.}}}{\beta}\right)_{220}^{\text{stat}} = 0.041\ . \qquad (1)$$

---

[2] It was experienced that at the desired level of precision (of the order of 0.001 °2θ) the long-term stability of the diffraction equipment may play a role. Especially the X-ray tube and its stand need attention: the tube ages, the focus becomes damaged and curved, and small variations in the cooling water temperature (< 1 °C) already have measurable effects. Therefore, in line-profile analysis of the highest demands, h and g should be measured shortly after each other.

The same measurements together with a set of 36 measurements for both specimens after removal of the Soller slits from the diffractometer yielded a Soller slit factor $\gamma = 0.33$ (see App. C). Using Eqs. (C.2) through (C.5) and Eq. (1) with the focus and slit dimensions as given in Table II, the values for $\sigma_{\beta}^{\text{cryst.st.}}$ for a *spinning* specimen as given in Table II were calculated.

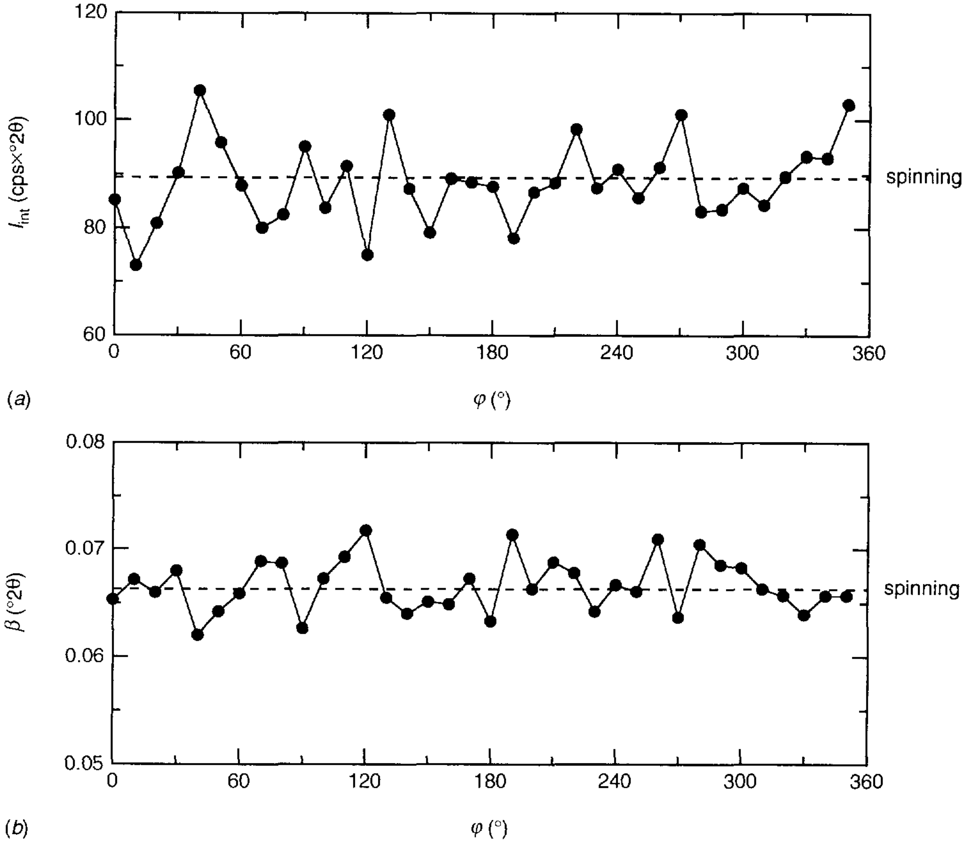

Fig. 4 The effects of crystal statistics: (*a*) the integrated intensity I_{int} and (*b*) the integral breadth β of the {220} reflection of a Si standard specimen (with 1.36 mg/cm^2 of Si) *versus* φ, *i.e.* the angle of rotation around an axis perpendicular to the specimen surface. The results for the spinning specimen are included. For the X-ray diffraction measurement conditions and the data evaluation, see Table II. The ranges were shorter than those of Table II. This evoked truncation of profiles and thus I_{int} and β being a bit too low. This is insignificant for studying crystal statistics (*i.e.* looking for differences). The standard deviations due to counting statistics (see App. B) are much smaller than the size of the dots used in the figure.

From $\sigma_{\beta}^{\text{cryst.st.}}$ in Table II, it follows that the crystal-statistical errors in the integral breadths of the g profiles are acceptable (*i.e.* of the order of 0.001 °2θ) for all reflections except {444}. With stationary specimens, the errors are 5 to 20 times larger [see Eq. (C.3)], so spinning is essential for accurate g profiles. It also follows from Table II that the crystal-statistical errors are of the same order of magnitude as the counting-statistical errors, which means that longer measurement times do not improve the accuracy of the measured g profiles very much.

Concerning crystal statistics, an additional remark has to be made. Crystal-statistical errors in I_{int} can be reduced by increasing the number of diffracting crystallites, *e.g.* by increasing the divergence slit or removing the Soller slits. However, by such measures, the errors in β are not reduced by the same factor as the errors in I_{int}, because the covariance of I_{int} and I_{p} is reduced if defocussing is increased and, therefore, the factor f in Eq. (C.1) is increased. For example, it was found experimentally that the removal of the Soller slits decreased the standard deviation of I_{int} of the {220} reflection for a stationary specimen by a factor of 1.7, whereas the standard deviation of β was *increased* by a factor of 1.8! In general, for accurate line width and shape determinations, defocussing has to be minimized also from the point of view of crystal statistics.

D. Counting times required

For the proposed standard specimen (*i.e.* ~ 1.5 mg/cm^2 of Si), the counting times needed to meet the precision demands set in Sec. I are relatively long, especially for the high angle reflections (see Table II). It is noted, however, that the measurement times given in Table II apply to diffractometer settings intended for giving very narrow instrumental line profiles. In many practical situations, even when a high precision is wanted, much shorter measurement times can be attained: one may choose for (i) a larger divergence slit, (ii) a larger receiving slit, and (iii) for a (limited) increase of the mass of Si per unit area. The first and last measure also improve crystal statistics. The last measure, however, leads to more transparency broadening (see Sec. IV.A).

E. Comparison with LaB_6 (SRM 660)

For a genuine comparison, line profiles from a Si standard and from LaB_6 (SRM 660) have been measured with the same diffractometer, thereby taking measurement conditions as equal as possible. The LaB_6 specimen was prepared analogously to the standard specimen, but without a heat treatment. The integral breadths are plotted *versus* the peak position $2\theta_{\text{p}}$ in Fig. 5. The standard deviation due to both counting statistics and crystal statistics is on average about the same for both specimens at comparable 2θ and about equal to the values given in Table II.

It is clear that the integral breadths of the standard specimen are smaller than those of LaB_6. The irregular behaviour of the LaB_6 data points originates probably from anisotropic structural broadening.

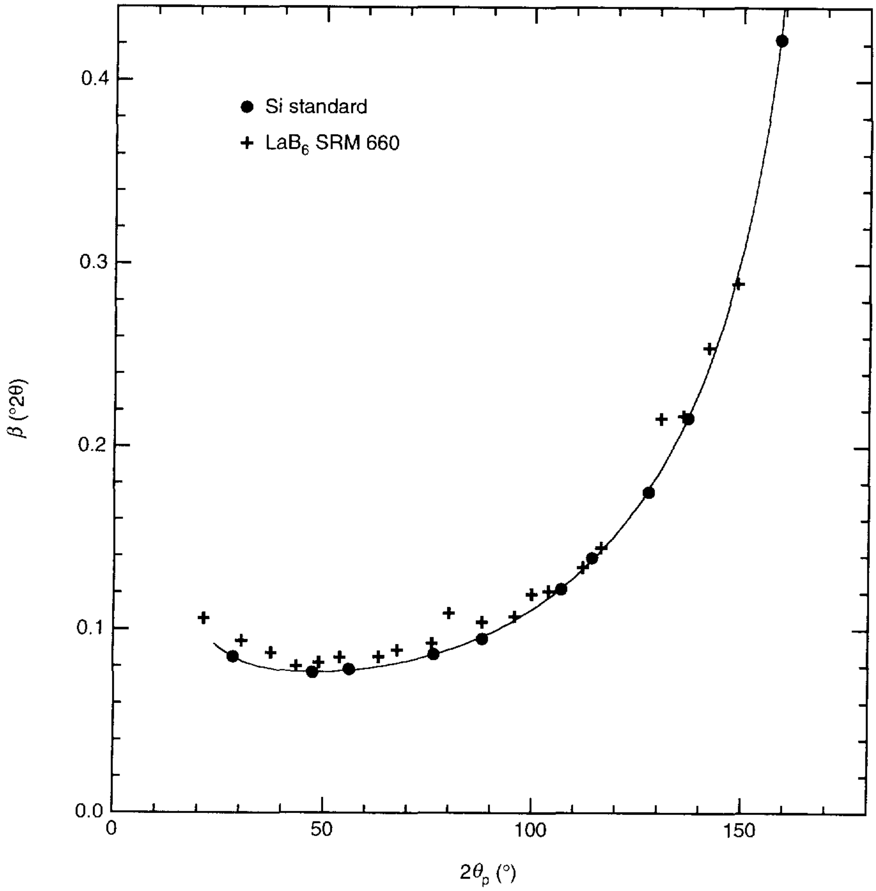

Fig. 5 The integral breadth β *versus* peak position $2\theta_p$ for a Si standard specimen (with 1.0 mg/cm^2) and an LaB_6 specimen prepared (analogously) from SRM 660 (with 0.7 mg/cm^2). The X-ray diffraction measurement conditions and the data evaluation are the same (or equivalent) for both specimens and are found in Table II. The present β for Si are slightly different from those of Table II, because it here concerns an other X-ray tube (of the same type) and, as a consequence, an other alignment.

IV. CORRECTIONS FOR RESIDUAL BROADENINGS

The line profiles from the proposed standard specimen are unavoidably slightly broadened by the transparency and the finite size of the silicon particles. The extents of these broadenings are discussed below and corrections are shown to be possible to such an amount that the remaining errors are completely negligible.

A. Residual transparency broadening

For a homogeneous layer, transparency broadening increases with layer thickness. For the present specimens, consisting of stacked irregularly shaped particles, the residual transparency broadening is very hard to describe mathematically (see Fig. 1). Therefore, an experimental approach seems more appropriate: measure line profiles from specimens with a different mass of Si per unit area η and deduce from that corrections. The experiments are not a serious problem, considering the easy and quick way in which defined specimens can be produced and that a heat treatment can be omitted in such experiments because the residual transparency broadening will be the same for annealed and not-annealed specimens.

The integral breadth β of the $\{220\}$ profile as a function of η is shown in Fig. 6. Note that, for small η, the errors are relatively large due to the effects of crystal and counting statistics. Clearly, a straight line describes sufficiently accurately the behaviour of the experimentally obtained integral breadths.

It is not completely self-evident to find the extra integral breadth due to transparency from a linear extrapolation to $\eta = 0$ of the straight line fitted to the data points. As long as the Si particles are unstacked, no matter how much of the specimen support is covered, the extra integral breadth takes (apart from shielding effects) a certain value that is determined by the particle size, regardless of η. The integral breadth starts to rise when stacking of particles starts (the straight line should only be fitted to the data points from that point on). For a guess about the mass of Si per unit area corresponding to that point, we consider a layer of two-dimensionally close-packed Si spheres with a diameter D equal to the average size of the Si particles after sedimentation (D = 7.2 µm, see Fig. 2). Such a layer corresponds with η = 1.01 mg/cm^2. For that layer, an upper bound for the integral breadth β_{tr} of the transparency profile is the integral breadth $\beta_{\mathrm{tr}}^{\mu=0}$ for a fully transparent massive layer of a thickness equal to D. If the integral breadth is set equal to the square root of the variance, then $\beta_{\mathrm{tr}}^{\mu=0}$ reads (Wilson, 1963):

$$\beta_{\mathrm{tr}}^{\mu=0} = \frac{D\cos\theta}{R\sqrt{3}}, \tag{2}$$

where R is the radius of the diffractometer and $\beta_{\mathrm{tr}}^{\mu=0}$ is in radians 2θ.

The actual increase in the integral breadth due to transparency will be smaller than $\beta_{\mathrm{tr}}^{\mu=0}$, because (i) Si is not fully transparent, (ii) a transparent layer of particles of size D gives a smaller breadth than a massive transparent layer of thickness D, and (iii) convolution of the transparency profile with the true instrumental profile, in general, causes the breadth of the resulting profile to be larger by an amount smaller than β_{tr}. For the {220} profile of a specimen with 1 mg/cm^2 of Si, the extra breadth $\Delta\beta$ due to transparency is at most $\beta_{\mathrm{tr}}^{\mu=0}$ = 0.0011 °2θ. On the basis of the extrapolated straight line in Fig. 6 for η = 1 mg/cm^2, one arrives at $\Delta\beta$ = 0.0007 °2θ. Therefore, the conclusion is reached that the linear extrapolation to η = 0, even if it is not completely justified, anyhow gives an empirical correction that is accurate to a few times 0.0001 °2θ, which is sufficient for the present instrumental profiles.

Since the effect of transparency is very small, a correction procedure like the one above will also work for other line-shape parameters as Fourier coefficients, profile fit-function parameters, *etc.*

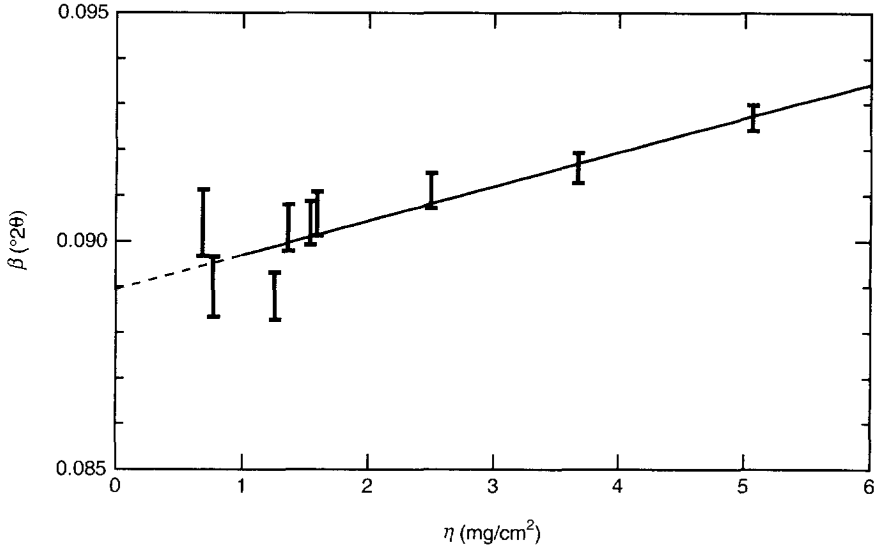

Fig. 6 The integral breadth β of the Si {220} reflection *versus* η, the mass of Si per unit area. The specimens were prepared according to Sec. II, but not heat treated. For the X-ray diffraction measurement conditions and the data evaluation, see Table II. The straight line is fitted to the data points of the specimens with η > 1 mg/cm^2. The error bars indicate the estimated uncertainty ($\pm\sigma$) due to counting statistics (see App. B) and crystal statistics (see Sec. III.C; for the effect of η, see end of App. C).

For the chosen standard specimen (*i.e.* ~ 1.5 mg/cm^2 of Si), the extra broadening of its {220} reflection due to transparency as determined from Fig. 6 is 0.0011 °2θ. For reflections at higher 2θ, the extra broadening is even less [see Eq. (2)]. Such small broadenings are comparable to or smaller than the errors due to crystal statistics and counting statistics (see Table II).

B. Residual size broadening

The residual broadening due to the finite size of the Si particles (ignoring extinction effects) is determined by the distribution $p(M)$ of column lengths M within all particles of the specimen (Warren, 1969). This distribution depends on the distributions of particle shapes and particle sizes. In the present case, only a small correction is necessary and therefore the particles are simply taken spherical with a diameter distribution $p(D)$. For spheres, $p(M)$ is obtained from $p(D)$ by (*cf.* Adler and Houska, 1979):

$$p(M) = \frac{M \int\limits_M^\infty p(D)\,\mathrm{d}D}{\int\limits_0^\infty M \int\limits_M^\infty p(D)\,\mathrm{d}D\,\mathrm{d}M} = \frac{2}{\langle D^2 \rangle} M \int\limits_M^\infty p(D)\,\mathrm{d}D, \tag{3}$$

where $\langle ... \rangle$ denotes the average. The denominator is calculated by changing the order of integration with proper adaptation of the limits of integration. The particle-size measurements performed (see Fig. 2) concern a distribution by *weight* $p_w(D)$, where D and particle size are equated. The distributions $p_w(D)$ and $p(D)$ are related by:

$$p_w(D) = \frac{1}{\langle D^3 \rangle} D^3\, p(D). \tag{4}$$

Using Eqs. (3) and (4), the average column length $\langle M \rangle$, which is used below, can be expressed in terms of particle size averages:

$$\langle M \rangle = \frac{2\,\langle D^3 \rangle}{3\,\langle D^2 \rangle} = \frac{2}{3\,\langle D^{-1} \rangle_w}, \tag{5}$$

where $\langle D^{-1} \rangle_w$ is the average of D^{-1} for the distribution $p_w(D)$.

The measured particle-size distribution (see Fig. 2) of the powder used for the standard specimen yields $\langle D^{-1} \rangle_w = 0.17\ \mu\text{m}^{-1}$, so that $\langle M \rangle = 4.0\ \mu\text{m}$.

An exact correction for the residual size broadening is possible by means of deconvolution (Stokes, 1948): divide the Fourier coefficients of the measured *g* profile by those of the size profile and synthesize from the obtained Fourier coefficients the correct *g* profile. In such a procedure, the large average column length $\langle M \rangle = 4.0$ µm (see above) allows the Fourier coefficients $A^S(L)$ of the size profile to be approximated by:

$$A^S(L) = 1 - \frac{L}{\langle M \rangle}. \tag{6}$$

By way of illustration, the effects of size broadening have been calculated for a low and a high angle reflection (see Table III). It follows that the correction of the measured integral breadths is only ~ 1.5 %.

Table III. Integral breadth β^S of the Si size profile, calculated from $\beta^S = \lambda / \langle M \rangle_V \cos\theta$ with λ = 0.1540562 nm (CuKα_1) and the volume-averaged column length $\langle M \rangle_V = \langle M^2 \rangle / \langle M \rangle = 5.4$ µm, and the decrease $\Delta\beta$ in the integral breadth of the measured g profile when it is corrected for the Si size profile by means of Stokes deconvolution using Eq. (6) with $\langle M \rangle = 4.0$ µm.

{hkl}	β^S	$\Delta\beta$	
	(°2θ)	(°2θ)	(%)
220	0.0018	0.0014	1.9
533	0.0044	0.0029	1.3

V. IN CONCLUSION

It is possible to design an optimum standard specimen for line-profile analysis that meets the precision of modern diffractometers and data-evaluation procedures. Such an optimum standard specimen can be fabricated reproducibly by means of easily applicable procedures. The optimum standard proposed comprises about 1.5 mg/cm^2 of Si powder deposited by sedimentation onto a (510) oriented Si single-crystal wafer, followed by a 2 h heat treatment at 1273 K; the Si powder used is a 5 - 10 µm fraction of the NIST (formerly NBS) Si powder SRM 640a. The precision of the integral breadth, with respect to crystal statistics (for a spinning specimen) and counting statistics (with moderate counting times), is of the order of 0.001 °2θ (for low 2θ, about 1 %; for high 2θ, about 2 %). In the as-measured profiles, systematic errors of the same magnitude are present due to "residual" size and transparency broadening. These errors, however, can be eliminated to a completely negligible level, which means that instrumental profiles can be obtained free of systematic errors.

ACKNOWLEDGEMENTS

The authors wish to thank Ir. A.C. Vermeulen and Ing. N.M. van der Pers for their support in the project and comments on the manuscript, Ir. A. Buis for scanning-electron-microscope facilities and H.L. Jansma, L.A. Peffer, and R.G. Veldpape of the Analytical Education & Research Group of Delft University of Technology for the particle-size measurements.

APPENDIX A: PREPARATION OF THE STANDARD POWDER AND A STANDARD SPECIMEN

1. Obtaining the desired particle size distribution

An overview of the procedure is given in Fig. A1. The sedimentation was carried out in graduated cylinders with a height of 235 mm (Ø 36 mm, 250 ml). The fluid used was 2-propanol (analyzed quality). Suspensions were transferred using a transfer pipet. Vibration was performed in an ultrasonic cleaning bath for 15 minutes in order to separate the silicon particles. Just before each sedimentation, the suspension was well homogenized by shaking. Evaporation of the 2-propanol from the last "sediment" was performed on a polyethene foil, because the powder is easily removed from such a foil. About 54 mass% of the basic material was retained as standard powder. Of course, if one accepts a lower overall yield, the left branch, starting after the first sedimentation, can be omitted.

The sedimentation process was found to be well described by assuming that the Si particles settle with a stationary speed v given by (*cf.* Allen, 1990):

$$v = \frac{D^2 (\rho_s - \rho_{fl})\, g}{18\, \eta} \phi, \qquad (A.1)$$

where D is the particle diameter, ρ_s (= 2.33×10^3 kg·m^{-3} for Si) and ρ_{fl} (= 0.785×10^3 kg·m^{-3} for 2-propanol) are the densities of the particles and the fluid, respectively, g (= 9.83 kg·m·s^{-2}) is the gravitation constant, η (= 2.43×10^{-3} kg·m^{-1}·s^{-1} for 2-propanol at 293 K) is the viscosity of the fluid and ϕ is a factor that accounts for, among other things, the shape of the particles. Using Eq. (A.1), a given liquid column height and sedimentation time, the fraction of the particles of a certain diameter that has reached the bottom of the cylinder can be calculated. From that and an initial particle-diameter distribution, the particle-diameter distributions in the sediments and in the suspensions can be deduced for subsequent sedimentation steps. A homogeneous suspension at the beginning of each sedimentation is assumed. The effect of the procedure described in Fig. A1 has been calculated, using the measured particle-diameter

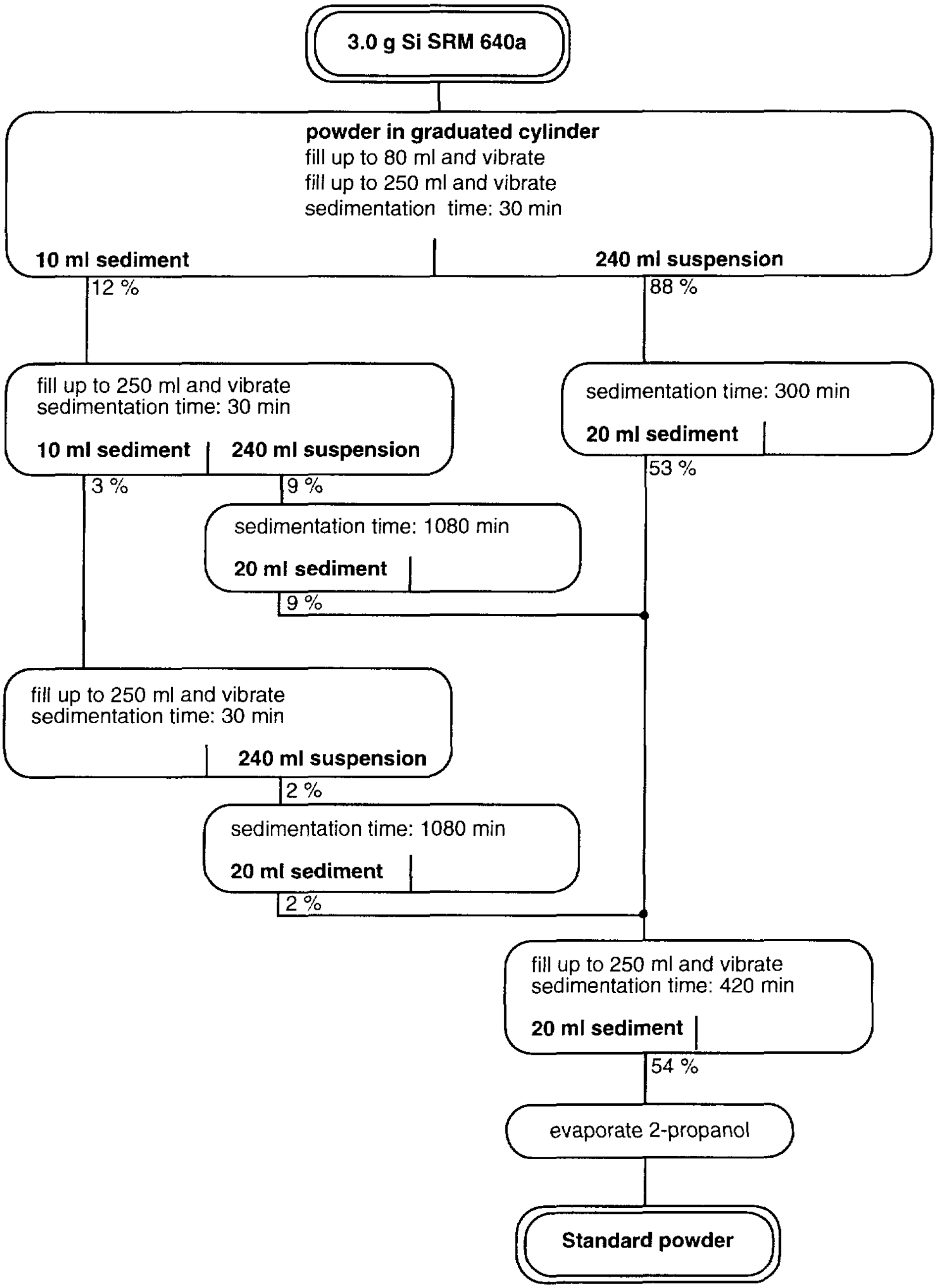

Fig. A1: Procedure for the removal of too small and too large particles. The yields (calculated, see text) after each step are given as percentages of the starting mass of Si.

distribution as given in Fig. 2. With $\phi = 1.3$, the calculated yield equals the measured one (54 %), the calculated weight-averaged diameter (7.8 μm) is a little bit larger than the measured one (7.2 μm), but the calculated overall distribution $p(D)$ after the procedure of Fig. A1 corresponds very well with the measured one.

2. Preparing a uniform thin layer on a flat support by sedimentation

A Si (510) wafer (Ø 48 mm) was used as a support. A brass ring (Ø 48 × Ø 27 × 9 mm) was put on the support. The side of the ring facing the support was polished to prevent leakage of the suspension. The support-ring assembly was placed on an electric hot plate (~ 318 K). A homogeneous suspension (vibrate, see above) of the desired amount of Si powder in 5 ml 2-propanol was poured into the ring. For the optimum standard, 9 mg of the Si powder prepared according to the procedure described in Fig. A.1 was used. During evaporation, vibrations and air turbulences are to be avoided. After removal of the ring, the formerly covered part of the support was freed from possible particles in order to avoid specimen displacement in the diffractometer.

APPENDIX B: VARIANCE IN INTEGRAL BREADTH DUE TO COUNTING STATISTICS[3]

The variances of many line-profile characteristics due to the counting-statistical errors in the observed intensities have been derived by Wilson (1967). Concerning the integral breadth β, an uncommon method of peak height determination was adopted in the derivation of the variance $\sigma^2(\beta)$. Here, $\sigma^2(\beta)$ is derived for the frequently applied parabola fit for the peak determination. The uncertainty in the parabola fit is obtained in a way analogous to that used by Kurita (1981). The following derivation holds for the integral breadth in real (=2θ) space as well as in reciprocal space.

Consider a line profile measured with a step size δ in a range T, which is taken symmetrical with respect to the position X_p of maximum net (*i.e.* after background subtraction) intensity. It is supposed that the background is linear in the range T. Then:

$$\beta \equiv \frac{\delta I_{\mathrm{int}}}{I_p} = \frac{\delta I_{\mathrm{int}}' - T I_b}{I_p' - I_b}, \tag{B.1}$$

where I_{int} and I_{int}' are the integrated intensities (in counts) with and without background correction, respectively, I_p and I_p' are the intensities (in counts) at X_p with and without

---

[3] In this appendix, $\sigma_x^{\mathrm{cnt.st.}}$ is shortened to $\sigma(x)$, *i.e.* the indication of counting statistics is omitted.

background correction, respectively, and I_b is the (interpolated) height of the background intensity (in counts) at X_p. If the measurements are sufficiently precise, $\sigma^2(\beta)$ can be calculated using Eq. (1) of Wilson (1967):

$$\frac{\sigma^2(\beta)}{\beta^2} = \frac{\sigma^2(I_{int}')}{I_{int}^2} - 2\,\frac{\sigma^2(I_{int}',I_p')}{I_{int}\,I_p} + \frac{\sigma^2(I_p')}{I_p^2} + \frac{(T-\beta)^2\,\sigma^2(I_b)}{\delta^2\,I_{int}^2}, \tag{B.2}$$

where $\sigma^2(x)$ denotes the variance of x and $\sigma^2(x,y)$ the covariance of x and y. The covariances $\sigma^2(I_{int}',I_b)$ and $\sigma^2(I_p',I_b)$ have been left out, since they are nil or very small. Intensity measurements follow Poisson statistics, *i.e.* the variance $\sigma^2(I)$ of an observed intensity of I counts is best estimated as I. Thus:

$$\sigma^2(I_{int}') = I_{int}', \tag{B.3}$$

$$\sigma^2(I_b) = \frac{I_b}{p}, \tag{B.4}$$

where p is the number of data points used to estimate a linear background (*cf.* Wilson, 1967). The quantities $\sigma^2(I_p')$ and $\sigma^2(I_{int}',I_p')$ depend on the method of peak height determination. In his calculation of $\sigma^2(\beta)$, Wilson (1967) used the average of q measurements at X_p as an estimate of I_p'. A nowadays common method for the determination of X_p and I_p is a least squares parabola fit on q intensities I_i around the maximum after background correction, where $i = 1, 2, \ldots q$. Here, the fit of the corresponding parabola $I_i' = c_0 + c_1\,x_i + c_2\,x_i^2$ to the as-measured intensities I_i' is considered (x_i is the distance to X_p). To make the error calculations not unnecessarily complicated, the fit range is taken symmetrical with respect to X_p, *i.e.* $x_i = \delta\,[i-(q+1)/2]$ and $I_p' = c_0$. Using unweighted least squares fitting, I_p' is calculated as (*e.g.* readily derived from Eq. (8.51) of Sterling & Pollack (1968), recognizing that $\Sigma x_i = \Sigma x_i^3 = 0$):

$$I_p' = \frac{\Sigma(a_4 - a_2\,x_i^2)\,I_i'}{b_2}, \tag{B.5}$$

where Σ represents summation over i from 1 to q, $a_2 = \Sigma x_i^2 = \delta^2 q(q^2-1)/12$, $a_4 = \Sigma x_i^4 = \delta^4 q(q^2-1)(3q^2-7)/240$ and $b_2 = qa_4 - a_2^2 = \delta^4 q^2(q^2-1)(q^2-4)/180$. The variance $\sigma^2(I_p')$ due to counting-statistical errors in the data points can be calculated from Eq. (B.5):

$$\sigma^2(I_p') = \Sigma\left(\frac{\partial I_p'}{\partial I_i'}\right)^2 \sigma^2(I_i') = \frac{1}{b_2^2}\,[a_4^2\,\Sigma I_i' - 2\,a_2\,a_4\,\Sigma x_i^2 I_i' + a_2^2\,\Sigma x_i^4 I_i']. \tag{B.6}$$

If the background slope is not too large, this expression can be simplified significantly by taking $I_i' \approx I_p' + c_2\,x_i^2$. If further the expressions below Eq. (B.5) are used and, in addition, the relation $a_6 = \Sigma x_i^6 = \delta^6 q(q^2-1)(3q^4-18q^2+31)/1344$, it follows:

$$\sigma^2(I_p') \approx \frac{I_p'\,a_4}{b_2} + \frac{c_2\,a_2}{b_2^2}(a_2\,a_6 - a_4^2) \approx \frac{I_p'\,a_4}{b_2} \approx \frac{9\,I_p'}{4\,q}\,. \tag{B.7}$$

The result is accurate within 8 % for $q \geq 5$. The covariance $\sigma^2(I_{int}',I_p')$ is calculated using Eq. (105) of Wilson (1967) and simplified using Eq. (B.5):

$$\sigma^2(I_{int}',I_p') = \Sigma \frac{\partial I_{int}'}{\partial I_i'}\,\frac{\partial I_p'}{\partial I_i'}\,\sigma^2(I_i') = \Sigma \frac{\partial I_p'}{\partial I_i'}\,I_i' = I_p'. \tag{B.8}$$

Substituting the expressions (B.3) for $\sigma^2(I_{int}')$, (B.4) for $\sigma^2(I_b)$, (B.7) for $\sigma^2(I_p')$ and (B.8) for $\sigma^2(I_{int}',I_p')$ into Eq. (B.2) yields:

$$\frac{\sigma^2(\beta)}{\beta^2} = \frac{I_{int}'}{I_{int}^2} - 2\,\frac{I_p'}{I_{int}\,I_p} + \frac{9\,I_p'}{4\,q\,I_p^2} + \frac{(T-\beta)^2\,I_b}{p\,\delta^2\,I_{int}^2}\,. \tag{B.9}$$

As a test for the newly derived expression (B.9) for $\sigma^2(\beta)/\beta^2$, the {211} reflection of an α-quartz specimen has been measured 40 times without touching the specimen or diffractometer. The reflection is chosen because of the symmetry of its peak, so that no systematic errors are introduced by the parabola fit. It was measured from 58.8 to 61.2 °2θ with $\delta = 0.006$ °2θ using a receiving-slit width of 0.05 °2θ. Further conditions of measurement are like in Table II. The relevant profile characteristics are: $I_{int} = 75\times10^3$ counts, $I_p' = 3.9\times10^3$ counts, $I_b = 39.9$ counts, and $\beta = 0.116$ °2θ. The number of data points used for the background estimation $p = 40$, for the parabola fit $q = 8$. The experimentally obtained relative standard deviation $\sigma(\beta)/\beta = 0.0094$ with standard error 0.0010.

Expression (B.9) predicts $\sigma(\beta)/\beta = 0.0095$, which is in very good agreement with the experiment. In principle, Eq. (63) of Wilson (1967) for $\sigma(\beta)$ does not apply to this experiment, because it does not account for the parabola fit. If it used nevertheless, one predicts $\sigma(\beta)/\beta =$ 0.0069, which is 27 % smaller than the experimental value.

APPENDIX C: VARIANCE IN INTEGRAL BREADTH DUE TO CRYSTAL STATISTICS[4]

Expressions for the standard deviation $\sigma(I_{int})$ of the integrated intensity I_{int} due to crystal statistics have been derived by Alexander, Klug & Kummer (1948) for stationary specimens and by Wolff (1958) for spinning specimens. The standard deviation $\sigma(\beta)$ in the integral breadth β depends on the standard deviations $\sigma(I_{int})$ in I_{int} and $\sigma(I_p)$ in the peak intensity I_p and on the covariance $\sigma^2(I_{int},I_p)$ of I_{int} and I_p. If the relation between $\sigma(I_{int})$ and $\sigma(\beta)$ is written as:

---

[4] In this appendix, $\sigma_x^{\mathrm{cryst.st.}}$ is shortened to $\sigma(x)$, *i.e.* the indication of crystal statistics is omitted.

$$\frac{\sigma(\beta)}{\beta} = f\,\frac{\sigma(I_{\mathrm{int}})}{I_{\mathrm{int}}}, \tag{C.1}$$

then f depends on $\sigma(I_{\mathrm{p}})$ and, in particular, on $\sigma(I_{\mathrm{int}},I_{\mathrm{p}})$. With increasing 2θ, wavelength dispersion becomes the dominant factor in instrumental line broadening. As a consequence, the width of the line profiles originating from individual crystallites, which together constitute the measured line profile, approaches, with increasing 2θ, the width of the total instrumental line profile. Therefore, $\sigma(I_{\mathrm{int}},I_{\mathrm{p}})$ increases and, consequently, f decreases with increasing 2θ.

By substituting Eq. (C.1) in Eq. (9) of Wolff (1958)[5] and assuming that f is independent of 2θ, the following relation between $\sigma_{\mathrm{X}}(\beta)$ of different reflections $\{hkl\}$ of a stationary specimen can be obtained:

$$\left(\frac{\sigma^2(\beta)}{\beta^2}\right)_{hkl}^{\mathrm{stat}} = \frac{\sin^2\theta_{hkl}}{\sin^2\theta_{h_0k_0l_0}}\,\frac{m_{h_0k_0l_0}}{m_{hkl}}\left(\frac{\sigma^2(\beta)}{\beta^2}\right)_{h_0k_0l_0}^{\mathrm{stat}}, \tag{C.2}$$

where m_{hkl} is the multiplicity factor of reflection $\{hkl\}$. If $\{h_0k_0l_0\}$ is a low-angle reflection, assuming a constant f produces "safe" (= high) estimates for $\sigma(\beta)$ of high-angle reflections. If Eq. (C.1) is substituted into Eqs. (9) and (17) of Wolff (1958), $\sigma(\beta)$ for the $\{hkl\}$ reflection of a spinning specimen can be related to $\sigma(\beta)$ for the $\{hkl\}$ reflection of a stationary specimen:

$$\left(\frac{\sigma^2(\beta)}{\beta^2}\right)_{hkl}^{\mathrm{spin}} = \frac{2.6\,w\,\sin\theta_{hkl}}{h}\left(\frac{\sigma^2(\beta)}{\beta^2}\right)_{hkl}^{\mathrm{stat}}, \tag{C.3}$$

where w and h are the width and height, respectively, of an area specifying the crystallite orientations that can contribute to the measured intensity. Here, the width w is calculated as:

$$w = \frac{1}{2}(w_{\mathrm{F}} + w_{\mathrm{S}}), \tag{C.4}$$

where w_{F} is the apparent width of the focal line and w_{S} is the width of the receiving slit. In general, w contains an additional contribution proportional to the rocking angle of the diffracting crystallites (see Wolff, 1958). For the present (nearly perfect) Si crystallites, this contribution is relatively small and it is ignored in the estimate of $\sigma(\beta)$. The height h for a diffractometer with Soller slits can be written as:

$$h = \frac{\gamma}{2}(h_{\mathrm{F}} + h_{\mathrm{S}}), \tag{C.5}$$

where h_{F} and h_{S} are the lengths of the focal line and the receiving slit, respectively, and γ accounts for the (almost 2θ independent) effect of Soller slits. Wolff (1958) did not account for

---

[5] Equations (9) and (17) of Wolff (1958) are identical to Eqs. (1) and (2) of Wolff, Taylor & Parrish (1959).

Soller slits and used Eq. (C.5) with $\gamma = 1$. Since $\sigma^2(I_{\mathrm{int}})/I_{\mathrm{int}}^2$ is inversely proportional to h [see Eq. (9) of Wolff (1958)], the factor γ can be determined experimentally as the ratio of the variances $\sigma^2(I_{\mathrm{int}})/I_{\mathrm{int}}^2$ of a certain reflection for a stationary specimen without and with Soller slits in the diffractometer, all other things being equal.

Using Eqs. (C.2) and (C.3), $\sigma(\beta)$ can be calculated for all reflections of spinning as well as stationary specimens if, for one reflection $\{h_0k_0l_0\}$ of a stationary specimen, $\sigma(\beta)$ is available. The latter can be obtained by measuring the integral breadth of the $\{h_0k_0l_0\}$ reflection of a single specimen at a number of different φ settings (φ is the angle of rotation around an axis perpendicular to the specimen surface). According to Wolff, Taylor & Parrish (1959), measurements on stationary specimens with sufficiently different (say > 1°) φ settings can be considered as independent with respect to crystal statistics. Of course, the error due to counting statistics in measurements thus performed has to be negligible with respect to the observed error due to crystal statistics.

From Eqs. (9) and (17) of Wolff (1958), it follows that crystal-statistical errors are proportional to $N_{\mathrm{eff}}^{-1/2}$, where N_{eff} is the effective number of irradiated crystallites. As long as absorption in the Si layer is small, N_{eff} is proportional to η, the mass of Si per unit area (see Alexander, Klug & Kummer, 1948) and, therefore, $\sigma(\beta)/\beta$ is proportional to $\eta^{-1/2}$. Using this, $\sigma(\beta)$ of specimens with different η can be related.

REFERENCES

Adler, T. & Houska, C.R. (1979). *J. Appl. Phys.* **50**, 3282-3287.

Alexander, L., Klug. H.P. & Kummer, E. (1948). *J. Appl. Phys.* **19**, 742-753.

Allen, T. (1990). *Particle size measurement*, 4th ed. (London: Chapman and Hall), Chap. 7.

Delhez, R. & Mittemeijer, E.J. (1975). *J. Appl. Cryst.* **8**, 609-611.

Fawcett, T.G., Crowder, C.E., Brownell, S.J., Zhang, Y., Hubbard, C., Schreiner, W., Hamill, G.P., Huang, T.C., Sabino, E., Langford, J.I., Hamilton, R. & Louër, D. (1988). *Powder Diffr.* **3**, 209-218.

Hubbard, C.R. (1983). *J. Appl. Cryst.* **16**, 285-288.

Keijser, Th.H. de & Mittemeijer, E.J. (1980). *J. Appl. Cryst.* **13**, 74-77.

Klug, H.P. & Alexander, L.E. (1974). *X-ray Diffraction Procedures*, 2nd ed. (New York: John Wiley), p. 367.

Kogan, V.A. & Kupriyanov, M.F. (1992). *J. Appl. Cryst.* **25**, 16-25.

Kurita, M. (1981). *J. Test. Eval.* **9**, 133-140.

Parrish, W. & Huang, T.C. (1980). *Accuracy in Powder Diffraction*, NBS Special Publication 567, eds. Block, S. & Hubbard, C.R. (Washington: U.S. Dpt. of Commerce), p. 98.

Pike, E.R. (1957). *J. Sci. Instr.* **34**, 355-363.

Sterling, T.D. & Pollack, S.V. (1968). *Introduction to Statistical Data Processing* (Englewood Cliffs, New York: Prentice-Hall), p. 355.

Stokes, A.R. (1948). *Proc. Phys. Soc. London* **61**, 382-391.

Timmers, J., Delhez, R., Tuinstra, F. & Peerdeman, F. (1992a). *Accuracy in Powder Diffraction II*, NIST Special Publication 846, eds. Prince, E. & Stalick, J.K. (Washington: U.S. Dpt. of Commerce), p. 217.

Timmers, J., Pers, N.M. van der, Sprong, G.J.M., Keijser Th.H. de & Delhez, R. (1992b). *Powder Diffr.* **7**, 83-88.

Warren, B.E. (1969). *X-ray Diffraction* (Reading, Massachusetts: Addison-Wesley), p. 271.

Wilson, A.J.C. (1963). *Mathematical Theory of Powder Diffractometry* (Eindhoven, The Netherlands: Centrex), p. 24.

Wilson, A.J.C. (1967). *Acta Cryst.* **23**, 888-898.

Wolff, P.M. de (1958). *Appl. Sci. Res.* **7**, 102-112.

Wolff, P.M. de, Taylor, Jeanne M. & Parrish, W. (1959). *J. Appl. Phys.* **30**, 63-69.

CHAPTER 2

FOURIER METHODS FOR SEPARATION OF SIZE AND STRAIN BROADENING

Validity of the Warren-Averbach Analysis and Alternative Analyses

J.G.M. VAN BERKUM, A.C. VERMEULEN, R. DELHEZ, TH.H. DE KEIJSER, AND
E.J. MITTEMEIJER
Laboratory of Materials Science, Delft University of Technology,
Rotterdamseweg 137, 2628 AL Delft, The Netherlands.

ABSTRACT

The validity regions of the Warren-Averbach method and an alternative size-strain separation method have been mapped. To this end, Fourier coefficients of line profiles have been simulated on the basis of physically realistic size and strain distributions. Due to the different approximations used in the methods, different classes of specimens can be analysed with sufficient accuracy. Consequently, the range of applicability of Fourier size-strain separation has been extended.

I. INTRODUCTION

Broadening of (X-ray) diffraction-line profiles is caused by non-ideal optics of the instrument, wavelength dispersion and structural imperfection of the specimen. The structural line broadening is often subdivided in size broadening and strain broadening. Size broadening is caused by finite size of "domains diffracting essentially incoherently with respect to one another" (Warren, 1959). Strain broadening is due to varying displacements of the atoms with respect to their reference lattice positions.

The classical Fourier method to separate size and strain broadening using multiple orders of reflection was developed by Warren and Averbach (WA) (1950; 1952). For the case of cold-worked metals, the WA-method yields average size values that are considerably smaller than the grain sizes of the materials under study. Such observations have been interpreted as due to some sort of a domain structure within the grains caused by the cold deformation (Warren, 1959). However, it has also been argued that the data may reflect the incompatibility of the assumptions underlying the WA-method with the nature of the strains in cold-worked metals (Williamson & Smallman, 1954; Wilkens, 1984).

Other approaches, in general equally valid, are possible. In the alternative presented here, assumptions are made that differ from those of the WA-method.

The WA-method and the alternative method are applied to simulated Fourier coefficients of structurally broadened profiles in order to compare extracted parameters with the true ones. On this basis, the validity of both methods will be discussed. In practice, *a priori* knowledge of the microstructure of the specimen can help in choosing the suitable method.

II. METHODS FOR SIZE-STRAIN SEPARATION

According to the kinematical diffraction theory, the complex Fourier coefficients $F(n,l)$ [$= A(n,l) + \mathrm{i}B(n,l)$; n = harmonic number, l = order of reflection] of a structurally broadened line profile in reciprocal space can be written as the product of real, order-independent, size coefficients $A^S(n)$ and complex, order-dependent, strain coefficients $F^D(n,l)$ [$= A^D(n,l) + \mathrm{i}B^D(n,l)$]. In the present paper, only the real (or cosine) part $A(n,l)$ [$= A^S(n)A^D(n,l)$] is considered.

If the specimen is considered to consist of columns parallel to the diffraction vector, $A^S(n)$ is determined by the column-length (size) distribution $p(j)$, where j is the column length in number of unit cells. The average column length (size), measured in unit cells, is denoted $\langle N\rangle$. Further, $A^D(n,l)$ is determined by the strain distributions $p(e_n)$ (one for each n), where e_n is the average strain over a length of n unit cells in a column. All distributions are normalized to unit area. Summarizing (Warren, 1959):

$$A^S(n) = \frac{1}{\langle N\rangle} \int_{|n|}^{\infty} (j-|n|)\, p(j)\, \mathrm{d}j, \tag{1}$$

$$A^D(n,l) = \int_{-\infty}^{\infty} p(e_n) \cos(2\pi nle_n)\, \mathrm{d}e_n. \tag{2}$$

To obtain information on $A^S(n)$ and $A^D(n,l)$ separately, at least two orders of reflection have to be measured and the l dependence of $A^D(n,l)$ has to be specified by making assumptions on $p(e_n)$.

A. The Warren-Averbach analysis

By assuming that the tails of each $p(e_n)$ decrease rapidly enough, it can be shown for $nl \ll \langle e_n^2 \rangle^{-1/2}$ that:

$$\ln[A^D(n,l)] \approx -2\pi^2 n^2 l^2 \langle e_n^2 \rangle \approx l^2 \ln[A^D(n,1)], \tag{3}$$

where $\langle e_n^2 \rangle$ is the mean squared strain. Equation (3) is exact for all values of n and l if all $p(e_n)$ are Gaussian. The original separation method of Warren and Averbach uses the form with $\langle e_n^2 \rangle$ (Warren & Averbach, 1950, 1952). Here, for the sake of comparison [see Eq. (7)] and in view of the testing procedure [see Eq. (16)], the following form of the basic equation for the WA-method is preferred:

$$\ln[A(n,l)] = \ln[A^S(n)] + l^2 \ln[A^D(n,1)]. \tag{4}$$

From plots of $\ln[A(n,l)]$ *vs.* l^2, the size Fourier coefficients are obtained from the intercepts and the first-order reflection strain Fourier coefficients are acquired from the slopes.

B. An alternative analysis

An alternative assumption on the strain distributions $p(e_n)$ may be that they are independent of n, implying that strain gradients within the columns are neglected [Stokes-Wilson approximation (Stokes & Wilson, 1944; Wilson, 1955)]. For $A^D(n,l)$, this results in [*cf.* Eq. (2)]:

$$A^D(\tfrac{n}{l},l) = A^D(n,1), \tag{5}$$

where $\frac{n}{l}$ is a whole number. If for the strain profiles all orders of reflection have the same shape and a breadth proportional to the order, Eq. (5) holds (Eastabrook & Wilson, 1952). For atomic displacements due to certain arrangements of dislocations, it can be derived that Eq. (5) holds for small n (Krivoglaz, Martynenko & Ryaboshapka, 1983; Wilkens, 1970).

By restricting the Taylor series of $\ln[A^S(n)]$ to the first term, it can be shown for $n \ll \langle N \rangle$ that:

$$\ln[A^S(\tfrac{n}{l})] \approx \frac{1}{l} \ln[A^S(n)]. \tag{6}$$

Equation (6) is exact for all n if the column length distribution obeys $p(j) = \langle N \rangle^{-1} \exp[-j/\langle N \rangle]$. Although for any distribution $p(j)$ the initial behaviour of $A^S(n)$ is described by Eq. (6), the range over which this equation is applicable depends on the shape of the distribution $p(j)$. Even in the extreme case of the delta-type distribution, representing a monodisperse system, it holds within 10% for $n \leq \frac{1}{3}\langle N \rangle$.

Using Eqs. (5) and (6), the basic equation for the alternative method becomes:

$$\ln[A(\tfrac{n}{l},l)] = \frac{1}{l}\ln[A^S(n)] + \ln[A^D(n,1)]. \tag{7}$$

From plots of $\ln[A(\frac{n}{l},l)]$ *vs.* $\frac{1}{l}$, the size Fourier coefficients are obtained from the slopes and the first-order reflection strain coefficients are acquired from the intercepts.

III. TEST PROFILES

Simulated Fourier coefficients of line profiles have been used to determine the range of applicability of the WA-method and the alternative method. As compared to experiments, simulations have the advantage that they allow comparison of the extracted size-strain data with the true data. However, one has to take care that the simulations adequately represent physical reality.

Size Fourier coefficients $A^S(n)$ are simulated by adopting a column-length distribution $p(j)$ (see Sec. III A). Strain Fourier coefficients $A^D(n,l)$ are simulated by adopting a series of strain distributions $p(e_n)$ (see Sec. III B). There are very many physically realistic shapes of size and strain distributions. Here, a class of analytical descriptions has been chosen that allow a wide variation of the shape of the distributions by varying only a few parameters. Total Fourier coefficients $A(n,l)$ [$= A^S(n)A^D(n,l)$] are calculated such that the relative contributions of size and strain broadening vary (see Sec. III C).

To approach common practice, the orders of reflection $l = 1$ and $l = 2$ have been simulated.

A. Size broadening

Since for small $|n|$ the shape of $A^S(n)$ is rather insensitive to the shape of $p(j)$ and only small $|n|$ values are involved in the tests (see Sec. IV.A), the shape of $p(j)$ is not varied. Here, the following distribution function $p(j)$ with $p(0) = p'(0) = 0$ and $p(\infty) = 0$ has been chosen (with only the average column length $\langle N \rangle$ as a parameter):

$$p(j) = \alpha(\langle N \rangle)\, j^2 \exp\left(\frac{-3j}{\langle N \rangle}\right), \quad \text{where} \quad \alpha(\langle N \rangle) = \frac{27}{2\langle N \rangle^3}. \tag{8}$$

The corresponding size Fourier coefficients for the testing, as calculated using Eq. (1), read:

$$A^S(n) = \frac{2\langle N\rangle^2 + 4\langle N\rangle|n| + 3\,n^2}{2\langle N\rangle^2}\exp\left(\frac{-3|n|}{\langle N\rangle}\right). \tag{9}$$

B. Strain broadening

Since the WA-method makes assumptions involving the shapes of the strain distributions (Williamson & Smallman, 1954; Warren, 1963, 1969; Wilkens, 1984) and the same holds for the alternative, in the simulations the shapes of all $p(e_n)$ are widely varied. The distributions $p(e_n)$ are described by physically plausible bell-shaped analytical functions. (Pseudo-)Voigt and the Pearson-VII functions are examples of tuneable shape functions with the Lorentzian and Gaussian shapes as limiting cases. Here, an important feature of such functions is the relative weight of the tails. Lorentzian distributions have long-range tails, whereas Gaussians have not. All (pseudo-)Voigtian strain distributions except for the Gaussian have an infinite second moment (mean squared strain) $\langle e_n^2\rangle$, implying an infinite amount of stored elastic energy, which is physically impossible. Here, the Pearson-VII function has been adopted for $p(e_n)$:

$$p(e_n) = \frac{\alpha(\sigma_n,m_n)}{\left[1 + \frac{1}{m_n}\left(\frac{e_n}{\sigma_n}\right)^2\right]^{m_n}}, \quad \text{where } \alpha(\sigma_n,m_n) = \frac{\Gamma(m_n)}{\sqrt{\pi m_n}\,\sigma_n\,\Gamma(m_n-\frac{1}{2})} \tag{10}$$

and σ_n is the width parameter of $p(e_n)$, m_n is the shape parameter ($m_n = 1$ for Lorentzian, $m_n = \infty$ for Gaussian), and $\Gamma(x)$ is the Gamma-function. The mean squared strain $\langle e_n^2\rangle$ [$= \sigma_n^2 m_n/(2m_n-3)$] is only finite for $m_n > \frac{3}{2}$ (see further Sec. V). The corresponding strain Fourier coefficients can be calculated using Eq. (2) and expressed in terms of the modified Bessel function $K_\nu(x)$ (Abramowitz & Stegun, 1965):

$$A^D(n,l) = \frac{2}{\Gamma(\nu)}z^\nu K_\nu(2z), \quad \text{where} \quad z = \pi\sigma_n|n|l/\sqrt{m_n} \quad \text{and} \quad \nu = m_n - \tfrac{1}{2}. \tag{11}$$

In general, both the width and the shape parameters of the distributions $p(e_n)$ will depend on n. In the present simulations the shape parameter m_n is taken independent of n, *i.e.* $m_n = m$. Usually, for fluctuating strains within the columns, the width parameter σ_n decreases with increasing $|n|$ due to the corresponding increase of the averaging distance. This is accounted for by taking (see also Adler & Houska, 1979):

$$\sigma_n = \sigma|n|^{-q}, \quad \text{with} \quad n \neq 0 \quad \text{and} \quad q \geq 0. \tag{12}$$

The value of $\frac{1}{q}$ is a measure for the "wavelength" of the fluctuations of the local strain along a column. For uniformly strained columns, no strain fluctuations occur within a column, the "wavelength" is infinite and $q = 0$. For $q = \frac{1}{2}$, the local strain changes randomly from cell to cell.

This is the case in the ideal-paracrystal model (Hosemann & Bagchi, 1962; Kulshreshtha, Dweltz & Radhakrishnan, 1971). A crystalline solid containing localized defects like dislocations, precipitates, *etc.* will exhibit strains with definitely larger wavelengths than in the ideal-paracrystal model, and therefore $q \ll \frac{1}{2}$ in those cases.

C. Relative amounts of size and strain broadening

The amounts of size and strain broadening (in reciprocal space) are characterized by the corresponding integral breadths β^S and $\beta^D_{l=1}$. The integral breadth (area divided by top height) of the size-broadened test profile depends on $\langle N\rangle$ (see Sec. III A):

$$\beta^S = \left[\sum_{-\infty}^{\infty} A^S(n)\right]^{-1} = \left[\tfrac{4}{3}\langle N\rangle\right]^{-1}. \tag{13}$$

The integral breadth of the first-order strain-broadened profile $\beta^D_{l=1}$ depends on the distribution parameters σ, m and q (see Sec. III B):

$$\beta^D_{l=1} = \left[\sum_{-\infty}^{\infty} A^D(n,1)\right]^{-1} = \frac{(\pi\sigma\sqrt{m})^{\gamma}\,\Gamma(m-\frac{1}{2})}{\gamma\,\Gamma(m-\frac{1}{2}+\frac{1}{2}\gamma)\,\Gamma(\frac{1}{2}\gamma)}\ , \quad \text{where} \quad \gamma = \frac{1}{(1-q)}\,. \tag{14}$$

A parameter r is used to characterize the relative amount of strain broadening:

$$r = \frac{\beta^D_{l=1}}{\beta^S + \beta^D_{l=1}}\,. \tag{15}$$

Thus, $r = 0$ indicates a purely size-broadened and $r = 1$ a purely strain-broadened profile.

For given values of m and q, one value of the parameter r corresponds with an infinite number of combinations of values of $\langle N\rangle$ and σ. It can be shown that the error parameter used in the testing procedure (see Sec. IV A) attains the same value for all these combinations, because the evaluation is performed on a relative scale. Therefore, with the size and strain distributions chosen, it suffices to study the quality of the separation methods as a function of only r, m and q.

IV. TEST RESULTS

A. Error parameter

In this paper, the aim of the size-strain separation methods is to obtain values for the separated size and strain Fourier coefficients from experimental coefficients $A(n,l)$. Using simulations, determination of the accuracy of the separation achieved implies comparison of obtained (separated) and simulated (true) values for the size and strain coefficients: $A^S_{\mathrm{sep}}(n)$ and $A^S_{\mathrm{true}}(n)$, and $A^D_{\mathrm{sep}}(n,1)$ and $A^D_{\mathrm{true}}(n,1)$. In practice, only coefficients up to a certain harmonic number can be determined accurately. Moreover, most physical information is deduced from $A^S(n)$ and $A^D(n,1)$ for small $|n|$. For the present simulations, the upper harmonic number n_{up} is chosen equal to $\frac{1}{2}(\beta^S+\beta^D_{l=1})^{-1}$, implying $A(n_{\mathrm{up}},l{=}1) \lesssim \frac{1}{2}$. This choice means that the comparison is performed on a relative scale. The error parameter, E, used here for characterizing the accuracy of the size-strain separation is defined as:

$$E = \frac{1}{n_{\mathrm{up}}} \int_{n=0}^{n_{\mathrm{up}}} \left| \frac{A^S_{\mathrm{sep}}(n)-A^S_{\mathrm{true}}(n)}{A^S_{\mathrm{true}}(n)} \right| \cdot \left| \frac{A^D_{\mathrm{sep}}(n,1)-A^D_{\mathrm{true}}(n,1)}{A^D_{\mathrm{true}}(n,1)} \right| \mathrm{d}n. \tag{16}$$

Perfect separation implies $E = 0$. For small deviations, E equals the mean squared relative deviation of $A^S_{\mathrm{sep}}(n)$ from $A^S_{\mathrm{true}}(n)$ and necessarily also of $A^D_{\mathrm{sep}}(n,1)$ from $A^D_{\mathrm{true}}(n,1)$, because $A^S_{\mathrm{sep}}(n)A^D_{\mathrm{sep}}(n,1) = A^S_{\mathrm{true}}(n)A^D_{\mathrm{true}}(n,1) = A(n,1)$. For instance, $E = 0.01$ means an average relative deviation of 10%.

B. Size-strain separations

The three parameters r, m and q (see Sec. III) have been assigned 21, 18 and 21 values respectively (7938 different combinations). For all (r,m,q)-combinations, the WA-separation and the alternative separation have been executed and E is evaluated numerically [*cf.* Eq. (16)], yielding E_{WA} and E_{Alt} respectively. The error parameter E can be conceived as a function in a three-dimensional space, $E(r,m,q)$. In this space, the loci of points with equal E are called iso-E-surfaces. An iso-E-surface can serve as the boundary between acceptable and unacceptable separations. Here, the iso-E-surface for $E = 0.01$ is chosen as such and drawn for the WA and the alternative method in Fig. 1, where instead of m, ranging from 1 to ∞, the quantity $\frac{1}{m}$ has been used because then the bounding values for the parameters along the axes are all finite. Since the iso-E-surfaces of the WA-method and the alternative one intersect, there are four regions: (i) acceptable separations by both the WA- and the alternative method, (ii) acceptable separation only by WA, (iii) acceptable separation only by the alternative and (iv) unacceptable separation by both methods.

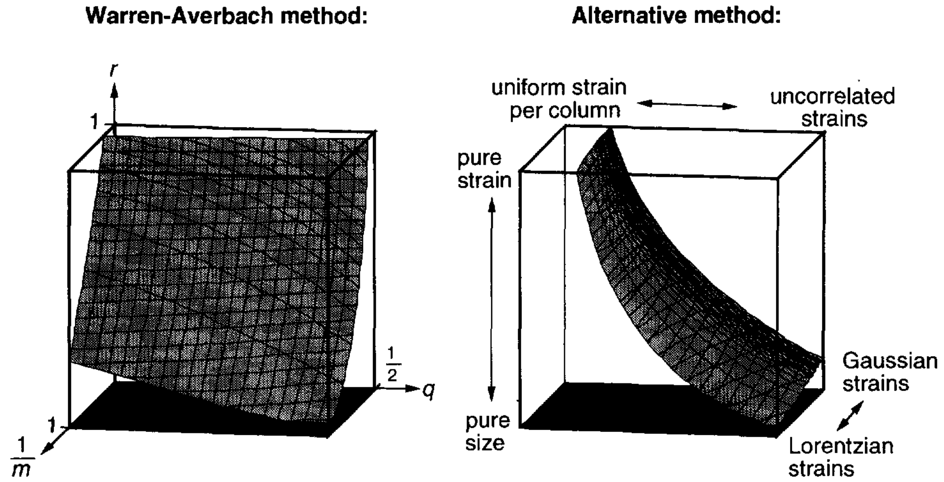

Fig. 1: Iso-E-surfaces for $E = 0.01$ for the WA-method and the alternative method in $(r, \frac{1}{m}, q)$-space. Accepted separations ($E < 0.01$, *i.e.* average relative deviation < 10 %) are found below the iso-E-surfaces.

V. DISCUSSION

As follows from Fig. 1, both the WA-method and the alternative method give acceptable results for dominant size broadening ($r \rightarrow 0$). As regards dominant strain broadening ($r \rightarrow 1$), the WA-method is insensitive to the strain-fluctuation parameter q and sensitive to the strain-distribution shape parameter m, while the reverse holds for the alternative method. This is not surprising in the light of the assumptions made in both methods. In the WA-method, it is assumed that the terms containing $\langle e_n^4 \rangle$ and higher moments are negligible in the Taylor-series expansion of $\ln[A^D(n,l)]$. The correctness of this assumption is determined by the shape of the strain distributions: the more they approach a Gaussian, the more it is justified. In the alternative method, it is assumed that $p(e_n)$ does not depend on n. This assumption is the more justified, the larger the "wavelength" of the local strain fluctuations (*i.e.* the smaller the parameter q).

In practice, advance knowledge about the specimen to be investigated is required to choose the appropriate size-strain separation method. To demonstrate this, three examples will be discussed now.

(i) *Pure size broadening* corresponds with the basal plane ($r = 0$) in Fig. 1. The WA-method yields perfect results for this case, while the alternative method yields an average relative deviation of 5 % (which was acceptable with respect to the chosen criterion). This deviation is

caused by the non-zero values of the neglected terms in the Taylor-series expansion of $\ln[A^S(n)]$ in the alternative method (see Sec. II B).

(ii) Specimens containing a single dislocation per crystallite have strain distributions with tails proportional to $|e_n|^{-3}$ (Wilson, 1955), which for the present Pearson-VII strain distributions corresponds to $m = \frac{3}{2}$ [*cf.* Eq. (10)]. Thus, within the context of the present simulations, if strain broadening is dominant in such specimens ($r \rightarrow 1$), the alternative method can yield acceptable results, depending on the q value, but the WA-method can well be inapplicable (see Fig. 1).

(iii) Specimens with uncorrelated local strains (paracrystalline disorder), for which $p(e_n)$ always tends to a Gaussian shape for increasing n (Adler & Houska, 1979), are only accessible for the alternative method if the average size is relatively small ($r \rightarrow 0$), whereas the WA-method can be correct for all sizes.

In the simulations, the Pearson-VII strain distributions $p(e_n)$ have infinitely long tails, resulting in infinite mean squared strains $\langle e_n^2 \rangle$ for $1 \leq m \leq \frac{3}{2}$ (see Sec. III B). In practice, the tails of $p(e_n)$ are finite and thus the values of $\langle e_n^2 \rangle$ are also finite. However, the maximum values of $|e_n|$ that occur in practice are so large compared to the average values, that the contributions to $A^D(n,l)$ of the surplus tails (*i.e.* beyond these maximum values) of the adopted $p(e_n)$ are generally of minor importance. Hence, the results for $m \leq \frac{3}{2}$ in Fig. 1 may be of practical interest too.

Cases of size-strain broadening have been investigated on the basis of characterization by three parameters: r (relative amount of strain broadening), m (shape of strain distributions) and q (strain fluctuations). In general, the microstructure of a real specimen cannot be described completely by only three parameters. Therefore, Fig. 1 can only be regarded as indicative for the applicability of the separation methods considered. This leaves unimpeded the recognition that the alternative method provides size-strain separation generally equivalent to the classical WA-method. The applicability regions of both methods are different and thus the alternative method and the WA-method complement each other.

VI. CONCLUSIONS

The classical Warren-Averbach method for size-strain separation on the basis of Fourier coefficients of broadened line profiles is only applicable to a finite class of specimens. This class consists of specimens with approximately Gaussian strain distributions. For other classes of specimens, alternative separation formalisms can be developed. The one elaborated here is applicable to specimens with limited strain variations inside the columns, but with no restrictions to the shapes of the distributions of the strains over the columns. Both methods are applicable to specimens with relatively little strain.

Thus, both the Warren-Averbach and the alternative method are applicable to different, partly overlapping, classes of specimens, the union of which implies an extension of the field of application of Fourier size-strain separation.

ACKNOWLEDGEMENT

Financial support by the Foundation for Fundamental Research on Matter (Stichting FOM), The Netherlands, is gratefully acknowledged (ACV).

REFERENCES

Abramowitz, M. & Stegun, I.A. (1965). *Handbook of Mathematical Functions* (New York: Dover), Chap. 9.

Adler, T. & Houska, C.R. (1979). *J. Appl. Phys.* **50**, 3282-3287.

Eastabrook, J.N. & Wilson, A.J.C. (1952). *Proc. Phys. Soc. London* **B65**, 67-75.

Hosemann, R. & Bagchi, S.N. (1962). *Direct Analysis of Diffraction by Matter* (Amsterdam, The Netherlands: North-Holland), Chap. IX.

Krivoglaz, M.A., Martynenko, O.V. & Ryaboshapka, K.P. (1983). *Phys. Met. Metall.* **55**, 1-12.

Kulshreshtha, A.K., Dweltz, N.E., & Radhakrishnan, T. (1971). *J. Appl. Cryst.* **4**, 116-124.

Stokes, A.R. & Wilson, A.J.C. (1944). *Proc. Phys. Soc. London* **56**, 174-181.

Warren, B.E. (1959). *Prog. in Metal Phys.* **VIII**, 147-202.

Warren, B.E. (1963). *Acta Metall.* **11**, 995-996.

Warren, B.E. & Averbach, B.L. (1950). *J. Appl. Phys.* **21**, 595-599.

Warren, B.E. & Averbach, B.L. (1952). *J. Appl. Phys.* **23**, 497.

Wilkens, M. (1970). *Phys. stat. sol. (a)* **2**, 359-370.

Wilkens, M. (1984). In: *Microstructural Characterization of Materials by Non-Microscopical Techniques,* eds. Hessel Andersen, N., Eldrup, M., Hansen, N., Juul Jensen, D., Leffers, T., Lilholt, H., Pedersen, O.B., Singh, B.N. (Roskilde, Denmark: Risø National Lab.), pp. 153-168.

Williamson, G.K. & Smallman, R.E. (1954). *Acta Cryst.* **7**, 574-581.

Wilson, A.J.C. (1955). *Nuovo Cimento* **1**, 277-283.

$$P_i(\Delta S) = K \sum_{L=-\infty}^{+\infty} A(L,S_i)\cos(2\pi L\Delta S) + B(L,S_i)\sin(2\pi L\Delta S), \qquad (1)^1$$

where K is (approximately) a constant, A and B are the cosine and sine Fourier coefficients and L is a distance perpendicular to the diffracting planes. In practice, L takes specific discrete values $n\Delta L$, where n is an integer and ΔL is inversely proportional to the length of the measurement range in reciprocal space. The line profile according to Eq. (1) is defined with respect to a distance S_i to the origin in reciprocal space, related to a diffraction angle $2\theta_i$ by $S_i = 2\sin\theta_i / \lambda$, where λ is the wavelength. The deviation from S_i is denoted by ΔS, where $\Delta S = 2(\sin\theta - \sin\theta_i) / \lambda$. Usually, for $2\theta_i$ the location of the centroid of the line profile is chosen. Any pair of line profiles P_1 and P_2 with $S_2 = 2S_1$ will be called a first and second order of reflection. In the present paper only the cosine Fourier coefficients $A(L,S_i)$ are considered, because usually the sine coefficients are not physically interpreted [exceptions are the work of Mittemeijer & Delhez (1978) and Ungár, Groma & Wilkens (1989)].

The profile measured from a structurally imperfect specimen can be considered as the convolution of a structurally broadened line profile with an instrumental line profile. Fourier coefficients of a measured profile are therefore the products of Fourier coefficients of the structural and the instrumental line profile. The instrumental line profile can be measured using a "standard" specimen that is (essentially) free of lattice defects. By division of Fourier coefficients of the line profiles of the imperfect and the "standard" specimen, Fourier coefficients of the structurally broadened line profile are obtained (Stokes, 1948). If no standard specimen is available, two *broadened* line profiles can be treated analogously by assigning the role of the instrumental profile to the profile with the smaller broadening. The resulting Fourier coefficients then represent the *differences* in lattice imperfection (size and strain) (Keijser & Mittemeijer, 1980). This procedure is used in Sec. IV.A.

The Fourier cosine coefficients of a structurally broadened line profile can be written as the products of order-independent size coefficients $A^S(L)$ and order-dependent strain coefficients $A^D(L,S_i)$ (superscript S for size and D for distortion). If the specimen is considered to consist of columns parallel to the diffraction vector, $A^S(L)$ is determined by the column-length (size) distribution $p(D)$, where D is the column length. The average column length (size) is denoted $\langle D \rangle$. Further, $A^D(L,S_i)$ is determined by the strain distributions $p(e_L)$ (one for each L), where e_L is the average of the true (local) strain e_0 over a length L. All distributions are normalized to unit area. In summary (Warren, 1959):

---

[1] In textbooks (e.g. Warren, 1969) the notations $P(h_3)$ and $A(n,l)$ are often used. For that notation, it is necessary to choose a unit-cell dimension a_3 in the direction of the diffraction vector. Then, $n = L/a_3$, $l = S_i a_3$ and $h_3 = (S_i+\Delta S)a_3$. We prefer the present notation for practical purposes.

$$A(L,S_i) = A^S(L)\, A^D(L,S_i), \tag{2}$$

$$A^S(L) = \frac{1}{\langle D\rangle} \int_{|L|}^{\infty} (D-|L|)\, p(D)\, \mathrm{d}D, \tag{3}$$

$$A^D(L,S_i) = \int_{-\infty}^{\infty} p(e_L) \cos(2\pi L S_i e_L)\, \mathrm{d}e_L. \tag{4}$$

To obtain information on $A^S(L)$ and $A^D(L,S_i)$ separately, at least two orders of reflection have to be measured and the L and/or S_i dependence of $A^S(L)$ and/or $A^D(L,S_i)$ has to be specified by making assumptions on $p(D)$ and/or $p(e_L)$. The latter can be done in different ways, leading to different separation methods, and in practice one must try to choose the one most suited to the specimen to be investigated.

A. The Warren-Averbach analysis

In the WA analysis, an approximation is used for the S_i dependence of $A^D(L,S_i)$. It can be shown by a Taylor-series expansion that for small L and S_i (Warren & Averbach, 1950; see App. A):

$$\ln[A^D(L,S_i)] \approx -2\pi^2 L^2 S_i^2 \langle e_L^2\rangle \approx \left(\frac{S_i}{S_1}\right)^2 \ln[A^D(L,S_1)], \tag{5}$$

where $\langle e_L^2\rangle$ is the mean squared strain. If all $p(e_L)$ are Gaussian, Eq. (5) is exact for all values of L and S_i (Warren & Averbach, 1950). The more the $p(e_L)$ deviate from being Gaussian, the smaller the range in L for which Eq. (5) is valid [see below Eq. (A.2)].

From Eq. (5) and the order-independence of $A^S(L)$, the WA analysis is derived by taking the logarithm on both sides of Eq. (2) (Warren & Averbach, 1952):

$$\ln[A(L,S_i)] = \ln[A^S(L)] - 2\pi^2 L^2 S_i^2 \langle e_L^2\rangle. \tag{6}$$

Here, for the sake of comparison with the other separation method [*cf.* Eq. (10)], the following form of the basic equation for the WA analysis is preferred:

$$\ln[A(L,S_i)] = \ln[A^S(L)] + \left(\frac{S_i}{S_1}\right)^2 \ln[A^D(L,S_1)]. \tag{7}$$

From plots of $\ln[A(L,S_i)]$ *versus* $(S_i/S_1)^2$, the size Fourier coefficients are obtained from the intercepts and the strain Fourier coefficients of the profile P_1 are acquired from the slopes. If application of the WA analysis is justified, mean squared strains $\langle e_L^2\rangle$ can be calculated from $A^D(L,S_1)$ using Eq. (5) and they can be physically interpreted in terms of $\langle e_0^2\rangle$, $\langle e_0'^2\rangle$, *etc.* using Eq. (A.3) (Turunen, Keijser, Delhez & Pers, 1983).

B. An alternative analysis

As indicated above, the WA analysis breaks down at a certain value of L if the strain distributions are not Gaussian. The breakdown may occur so early that in practice size and strain parameters become very unreliable. For this reason, an alternative analysis has been developed. This alternative analysis also breaks down at a certain L value, which can be smaller or larger than for the WA analysis due to the different approximations used. Hence, specimens for which the WA analysis is problematic may be analysed reliably by the alternative analysis and *vice versa* (Berkum, Vermeulen, Delhez, Keijser & Mittemeijer, 1993).

The first approximation used in the alternative analysis concerns the L and S_i dependences of $A^D(L,S_i)$. By expressing $A^D(L,S_i)$ in terms of the local strain e_0 and its derivatives, it can be shown that for small L the strain gradients within the columns can be neglected [this is sometimes called the Stokes-Wilson approximation, see Stokes & Wilson (1944) and Wilson (1955)]. Then, the following relation can be derived for small L and S_i (see App. A):

$$A^D(L_i,S_i) \approx A^D(L_1,S_1), \qquad \text{where } L_i = \frac{S_1}{S_i} L_1. \tag{8}$$

The smaller the average strain gradients in the columns, the larger the range in L for which Eq. (8) holds [see Eq. (A.6)]. For specimens for which the lattice spacing is constant within each grain, but varies from grain to grain (*e.g.* due to differences in composition), the strain gradients are zero, the $p(e_L)$ are independent of L and Eq. (8) is exact at least for L_1 up to the smallest grain size [*cf.* Eq. (4)]. In that case, the strain profiles of all orders of reflection have the same shape and a breadth proportional to the order (Eastabrook & Wilson, 1952).

A size-strain separation method based on Eq. (8) requires an additional equation specifying the L dependence of $A^S(L)$. For $L \ll \langle D \rangle$, the Taylor series of $\ln[A^S(L)]$ can be restricted to the first term and it can be shown that (see App. B):

$$\ln[A^S(L_i)] \approx \frac{S_1}{S_i} \ln[A^S(L_1)], \qquad \text{where } L_i = \frac{S_1}{S_i} L_1. \tag{9}$$

The range over which this equation is applicable depends on the shape of the distribution $p(D)$. It is exact for all L if the column-length distribution obeys $p(D) = \frac{1}{\langle D \rangle}\exp[-\frac{D}{\langle D \rangle}]$. Using Eqs. (2), (8) and (9), the basic equation for the alternative analysis becomes:

$$\ln[A(L_i,S_i)] = \ln[A^D(L_1,S_1)] + \frac{S_1}{S_i} \ln[A^S(L_1)], \qquad \text{where } L_i = \frac{S_1}{S_i} L_1. \tag{10}$$

From plots of $\ln[A(L_i,S_i)]$ *versus* S_1/S_i, the strain Fourier coefficients of the profile P_1 are obtained from the intercepts and the size Fourier coefficients are acquired from the slopes.

Calculation of $\langle e_L^2 \rangle$ from $A^D(L,S_1)$ obtained by this alternative analysis is not useful, because the method is designed for specimens that do not permit neglection of the influence on $A^D(L,S_i)$ of $\langle e_L^4 \rangle$, $\langle e_L^6 \rangle$, *etc.* (see App. A). In case of appropriate applications of the alternative method, $A^D(L,S_1)$ can be interpreted in terms of $\langle e_0^2 \rangle$, $\langle e_0^4 \rangle$, *etc.* by fitting the first column of terms of Eq. (A.5) to $A^D(L,S_1)$.

C. Remarks

(i) Linear versions of the analyses

It has been argued that, instead of a truncated Taylor series of $\ln[A(L,S_i)]$, simply that of $A(L,S_i)$ can be used in the WA analysis (Delhez & Mittemeijer, 1976) (see App. A):

$$A^D(L,S_i) \approx 1 - 2\pi^2 L^2 S_i^2 \langle e_L^2 \rangle \approx 1 - \left(\frac{S_i}{S_1}\right)^2 [1 - A^D(L,S_1)], \tag{11}$$

leading to the following equivalent of Eq. (7):

$$A(L,S_i) = A^S(L) - \left(\frac{S_i}{S_1}\right)^2 A^S(L)\,[1 - A^D(L,S_1)]. \tag{12}$$

From plots of $A(L,S_i)$ *versus* $(S_i/S_1)^2$, the size Fourier coefficients are obtained from the intercepts and the strain Fourier coefficients of the profile P_1 can be deduced from the slopes.

Just like Eq. (5), Eq. (11) is correct for small L and S_i. Unlike Eq. (5), no distributions $p(e_L)$ exist for which Eq. (11) holds exactly. It can be shown that the first term neglected in the derivation of Eq. (11) is always larger than the one in Eq. (5) (see App. A). This disadvantage of the WA analysis executed according to Eq. (12) is countered by an important advantage: Eq. (12) is less sensitive to the inevitable random errors in $A(L,S_i)$ due to the counting statistics in the measured profiles. Variances in Fourier coefficients $A(L,S_1)$ and $A(L,S_2)$ propagate into variances in $A^S(L)$ and $A^D(L,S_1)$ smaller by using Eq. (12) than by using Eq. (7) (see App. C).

For the alternative analysis, introduced in Sec. II.B, a comparable equivalent exists. Instead of the Taylor series of $\ln[A^S(L)]$, that of $A^S(L)$ can be used (see App. B):

$$A^S(L_i) \approx 1 - \frac{L_i}{\langle D \rangle} \approx 1 - \frac{S_1}{S_i}[1 - A^S(L_1)], \qquad \text{where } L_i = \frac{S_1}{S_i} L_1, \tag{13}$$

leading to the following equivalent of Eq. (10):

$$A(L_i,S_i) = A^D(L_1,S_1) - \frac{S_1}{S_i} A^D(L_1,S_1)\,[1 - A^S(L_1)], \qquad \text{where } L_i = \frac{S_1}{S_i} L_1. \tag{14}$$

From plots of $A(L_i,S_i)$ *versus* S_1/S_i the strain Fourier coefficients of the profile P_1 are obtained from the intercepts and the size Fourier coefficients can be deduced from the slopes.

In general, Eq. (13) is not inferior to Eq. (9). Which of the two is best depends on the width of the size distribution in the specimen under study. For the infinitely narrow δ-type distribution, Eq. (13) is best; for the very broad exponential distribution [see below Eq. (9)], Eq. (9) is best. For any distribution, both Eq. (13) and Eq. (9) describe at least the initial behaviour of $A^S(L)$. Again, the linear version of the separation method has the advantage of being less sensitive to propagation of random errors (see App. C).

The choice between the logarithmic separation methods and the linear versions should depend on the priorities of the study: for minimal random error choose linear methods; for minimal systematic error choose the logarithmic WA analysis and the logarithmic *or* linear alternative analysis, depending on the expected width of the size distribution. In this paper, only the logarithmic versions of the separation methods are used.

(ii) Recursive analysis

In principle, using Eq. (8), no additional series expansion of $A^S(L)$ is necessary to separate size and strain coefficients. By guessing only one value of either $A^S(L)$ or $A^D(L,S_1)$ for $L \neq 0$, many others can be successively obtained. For example, suppose two sets $A(L,S_1)$ and $A(L,S_2)$ with $S_2 = 2S_1$ are available and the value of $A^S(\Delta L)$ is guessed. Then, from the product relation $A(L,S_i) = A^S(L)A^D(L,S_i)$, one can calculate $A^D(\Delta L,S_1)$ and $A^D(\Delta L,2S_1)$. From Eq. (8), it follows that $A^D(2\Delta L,S_1) = A^D(\Delta L,2S_1)$, so that $A^S(2\Delta L)$ [from $A(2\Delta L,S_1) = A^S(2\Delta L)A^D(2\Delta L,S_1)$] and subsequently $A^D(2\Delta L,2S_1)$ [from $A(2\Delta L,S_2) = A^S(2\Delta L)A^D(2\Delta L,S_2)$] can be calculated. In the same way, size and strain coefficients for $L = 4\Delta L$, $8\Delta L$, *etc.* are obtained. This procedure was first proposed by Eastabrook and Wilson (1952).

The method can be applied several times with different initial guesses for $A^S(\Delta L)$. The possible values of $A^S(\Delta L)$ lie between $A(\Delta L,S_i)$ and 1. In general, the sets of Fourier coefficients obtained with all possible guesses $A^S(\Delta L)$ are not very different and converge with increasing L. An important disadvantage of this method of size-strain separation, compared with the WA analysis and the alternative analysis, is the lack of exactness for $L \downarrow 0$. A determination of $\langle D \rangle$ from the initial slope of $A^S(L)$ or of the stored elastic energy from $\langle e_0^2 \rangle$ (see Sec. II.B) may therefore be problematic. Another disadvantage is that only Fourier coefficients at $L = 2^n\Delta L$ are obtained if $S_2 = 2S_1$, or, in general, at $L = (S_2/S_1)^n\Delta L$, where $n \in \mathbb{Z}$.

From L equal to a few times ΔL onwards, the results obtained by this recursive analysis must resemble those obtained by the alternative analysis. For small L, the alternative analysis is independent of an arbitrary initial guess and therefore more accurate. For larger L, the results using the alternative analysis may become less accurate if the assumption regarding $A^S(L)$ [see Eq. (9)] becomes invalid. In this range, the recursive analysis, which does not use an assumption regarding $A^S(L)$ apart from the value of $A^S(\Delta L)$, can be used to specify a band of possible results [by variation of the initial guess of $A^S(\Delta L)$] for the alternative analysis or any other separation method relying on the neglect of strain gradients. Thus, if strain gradients are known to be small and the detailed results of the alternative analysis lie within the band of the recursive analysis, the application of the alternative analysis is justified.

(iii) Interpolation of Fourier coefficients

A remarkable difference between the WA analysis and the alternative analysis is that the former uses Fourier coefficients of different profiles at the *same* L value, whereas the latter uses Fourier coefficients of different profiles at *different* L values. Specifically, for a first and second order of reflection, the alternative analysis uses $A(L_1,S_1)$ and $A(L_1/2,2S_1)$. In practice, Fourier coefficients of a line profile are obtained only at specific L values, where the step size ΔL is inversely proportional to the length of the measurement range in reciprocal space. The WA analysis is performed most easily with identical measurement ranges for first and second orders of reflection, so that $\Delta L_2 = \Delta L_1$. For the alternative analysis, it would be easiest to measure the second order over a range twice as long, so that $\Delta L_2 = \Delta L_1/2$. In practice, however, the length of the measurement range is usually adapted to the width of the line profiles and limited by neighbouring reflections. Then, both methods require interpolation of Fourier coefficients for the analysis to be performed.

III. APPLICATION TO SIMULATED PROFILES

In the first presentation of the alternative analysis, simulated Fourier coefficients of line profiles were used to determine the ranges of applicability of the WA analysis and the alternative analysis (Berkum, Vermeulen, Delhez, Keijser & Mittemeijer, 1993). The relative amounts of size and strain broadening, the shape of the strain distributions $p(e_L)$ and the degree of strain variation within the columns were the three parameters varied in that investigation. The WA and the alternative analyses were applied to the simulated Fourier coefficients and the quality of the separation was evaluated on the basis of the deviations of the extracted size and strain Fourier coefficients from the true values. The combinations of parameter values for which the results of the WA and the alternative analyses were acceptable are indicated schematically in Fig. 1.

In the investigation mentioned above, the size and strain distributions used were considered as realistic, without correspondence to an actual specimen. In this paper, the merits of both methods are again discussed using simulated Fourier coefficients, but this time the simulations represent a specific specimen in a detailed way. Complete expressions for the elastic strain fields associated with certain microstructural defects are taken as a starting point.

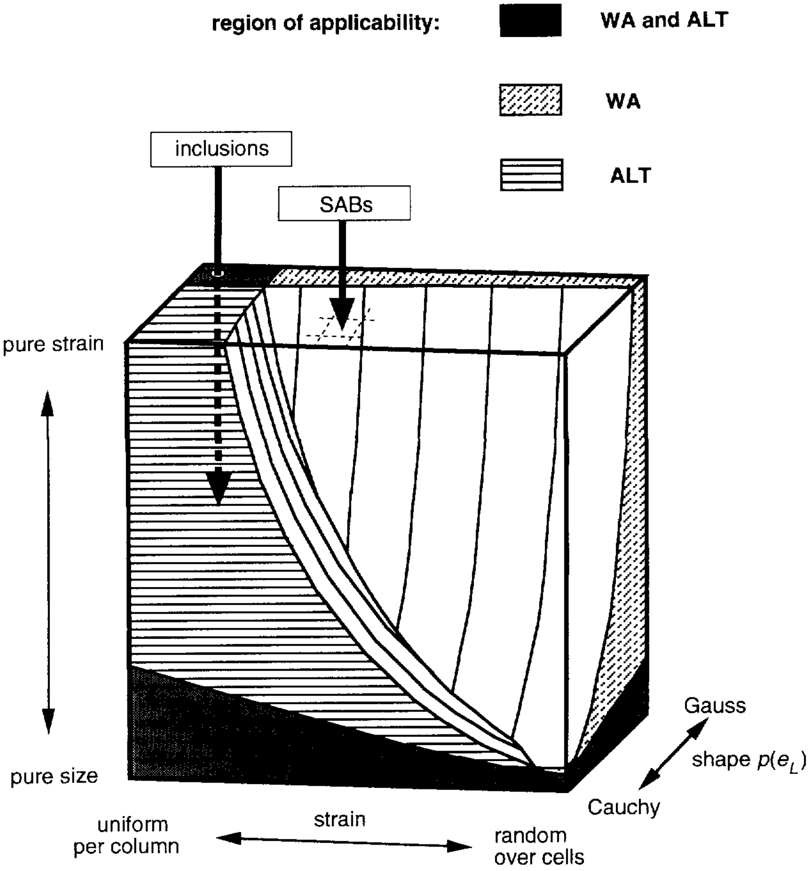

Fig. 1: Regions of applicability of the WA and the alternative (ALT) analyses. The regions are bounded by surfaces where the values of $A^S(L)$ and $A^D(L,S_1)$ obtained by the separation methods deviate 10 % on average from the true (simulated) values for a specified range in L (Berkum, Vermeulen, Delhez, Keijser & Mittemeijer, 1993). The locations in this cube comparable with the broadening caused by misfitting inclusions (see Sec. III.A) and small-angle boundaries ("SABs", see Sec. III.B) have been indicated.

A. Misfitting inclusions

Suppose a specimen consists of misfitting inclusions in a matrix: the inclusions and the surrounding matrix are in a state of stress. The volume misfit may result, for example, from cooling from fabrication to room temperature if a difference exists between the thermal-expansion coefficients of the inclusions and the matrix. Assuming spherical inclusions and matrix crystallites of uniform size, purely elastic accommodation of the misfit and elastic isotropy and ignoring neighbouring distortion fields, the Fourier coefficients of line profiles of the distorted matrix can be calculated. An additional calculation with zero misfit and all other parameters unchanged yields the size coefficients for the system and then the strain coefficients can be inferred. Using this model, the Fourier coefficients of experimental aluminium line profiles of two-phase AlSi alloys have been described to a good level of accuracy (Berkum, Delhez, Keijser & Mittemeijer, 1992).

As a realistic and representative example, Fourier coefficients of broadened Al{200} and Al{400} reflections were calculated for a composite of 12.5 vol.% Si inclusions in an Al matrix. The radii of the inclusions and the matrix crystallites were 76 and 152 nm, respectively. The linear misfit was 2.3×10^{-3}. The Fourier coefficients were defined with respect to the centroid of the profiles as the origin. The results obtained with the WA and the alternative analyses are shown in Fig. 2a.

From Fig. 2a it is clear that both the WA and the alternative analysis provide a good separation up to a high value of the correlation length L (about 75 nm). For the WA analysis, this is probably due to the small strains ($\langle e_L^2\rangle^{1/2} \approx 5\times10^{-4}$) and the moderate deviation from a Gaussian distribution for $p(e_L)$ (*e.g.* $k_2 \approx 3$ to 6, *cf.* App. A). Then, the higher-order terms in the series expansion of $\ln[A^D(L,S_i)]$ [see Eq. (A.2)] are small. The two assumptions applied in the alternative analysis are apparently justified for correlation lengths up to about 75 nm. Indeed, the weak dependence of the true $\langle e_L^2\rangle$ on L (see Fig. 2b) indicates, amongst other things (see Berkum, Delhez, Keijser & Mittemeijer, 1992), that strain gradients in the columns are small. Further, the true $A^S(L)$ (see Fig. 2a) satisfies Eq. (9) within 10% for $L_1 < 75$ nm.

In Fig. 2b, values of $\langle e_L^2\rangle$ calculated from the $A^D(L,S_1)$ as obtained by the WA analysis using the approximation Eq. (5) are shown. These are compared with (i) true values of $\langle e_L^2\rangle$, directly calculated from the strains in the crystallites, and (ii) values of $\langle e_L^2\rangle$ calculated from the true $A^D(L,S_1)$ using Eq. (5). In general, the distributions $p(e_L)$ are non-Gaussian, Eq. (5) is not exact and the values (ii) deviate from the values (i). Then, the values 'experimentally obtained' obviously deviate from the values (i): even a perfect separation of $A^S(L)$ and $A^D(L,S_1)$ would yield the values (ii), not (i). The differences between (ii) and (i) are small in the present case.

By fitting Eq. (A.3) to the $\langle e_L^2\rangle$ as obtained by the WA analysis, the strain broadening is physically interpreted (see Sec. II.A). Depending on the length of the fitting range (3 to 30 nm) and the number of terms fitted (2 to 5), one obtains $\langle e_0^2\rangle = 2.6$ to 2.8×10^{-7} (true value is 2.8×10^{-7}) and $\langle e_0'^2\rangle = 0.7$ to 4×10^{-9} nm^{-2} (true value is 0.49×10^{-9} nm^{-2}). Higher derivatives become rapidly more inaccurate due to the deviations of the obtained $\langle e_L^2\rangle$ from the true $\langle e_L^2\rangle$.

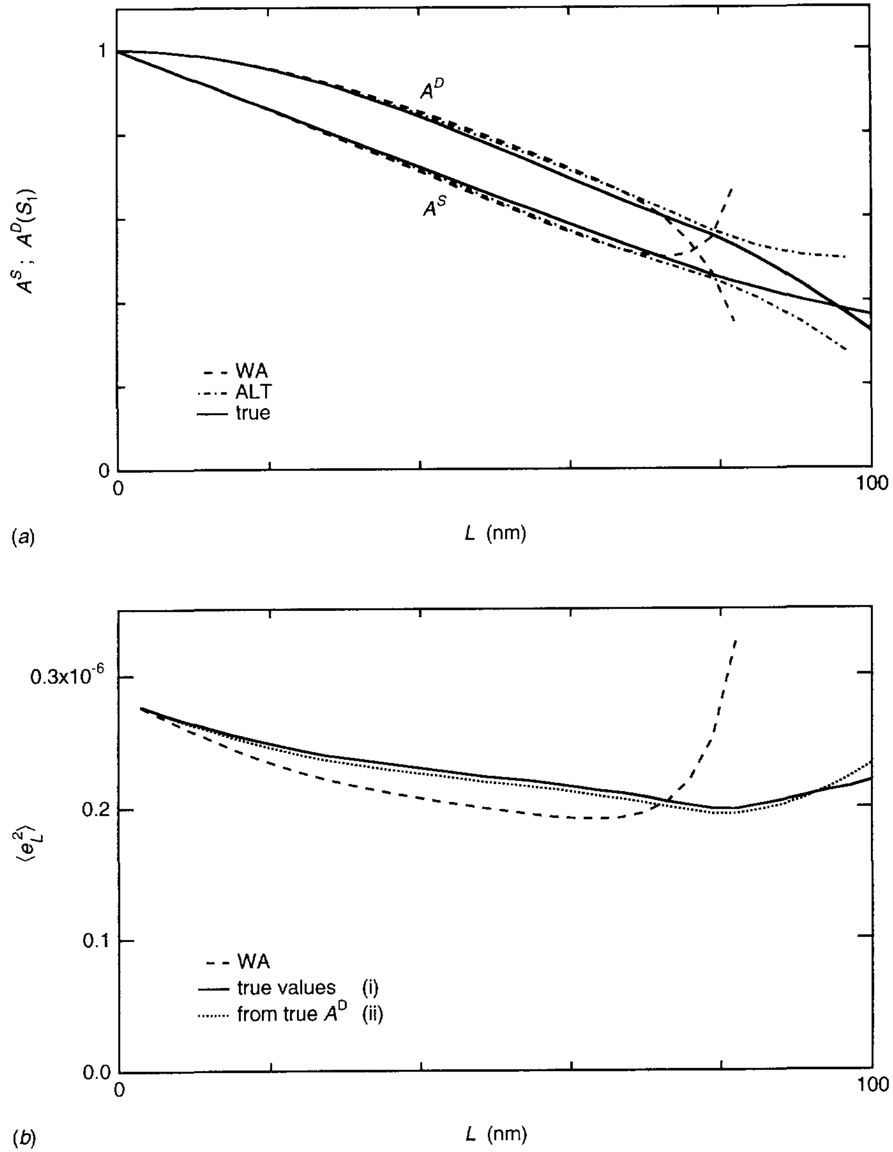

Fig. 2: Results of the WA and the alternative (ALT) analyses applied to simulated {200} and {400} reflections of an Al matrix containing 12.5 vol.% misfitting Si inclusions: (*a*) A^S and $A^D(S_1)$, compared with the true values, (*b*) WA results for $\langle e_L^2 \rangle$, compared with two sets of 'true' values (i) and (ii), which are explained in the text of Sec. III.A. Results of both analyses in terms of the local strain are evaluated in Sec. III.A.

The $A^D(L,S_1)$ as obtained by the alternative analysis can be interpreted by relating the coefficients of a polynomial fit to moments of $p(e_0)$ [first column of Eq. (A.5); see Sec. II.B]. Depending on the length of the fitting range (6 to 60 nm) and the number of terms fitted (1 to 4), the results are $\langle e_0^2 \rangle = 2.3$ to 2.6×10^{-7} (true value is 2.8×10^{-7}) and $\langle e_0^4 \rangle = 2$ to 7×10^{-13} (true value is 5.2×10^{-13}). Because of the errors introduced by the neglect of strain gradients, the inaccuracy of higher moments increases rapidly.

The results obtained using these simulations can also be compared with the applicability regions indicated in Fig. 1. In this example, comparable amounts of size and strain broadening are present, strains are slowly varying with distance and the shapes of $p(e_L)$ are not too far from Gaussian. Therefore, this case should be compared with a location indicated by 'inclusions' in Fig. 1. According to the validity regions indicated both size-strain separation methods should yield reliable results for not too large L, in agreement with the above.

B. Small-angle grain boundaries

As a second example, Wilkens' diffraction model for an array of small-angle grain boundaries is used (Wilkens, 1979). The symmetrical pure tilt boundary, discussed here, is an array of parallel edge dislocations with their Burgers' vectors $\boldsymbol{b}$ perpendicular to the boundary. The model consists of a periodic repetition of such small-angle boundaries with alternating 'sign' (extra half-planes upward/downward). The crystal containing the small-angle boundaries is taken to be infinitely large and hence the line broadening can be considered as pure strain broadening [$A^S(L) = 1$ for all L]. The diffraction vector is taken parallel to $\boldsymbol{b}$. For the calculation of the Fourier coefficients of the line profiles the procedure described by Wilkens is followed.

The results of the WA and the alternative analyses depend significantly on the configuration of the small-angle boundaries, characterized by the ratio Δ/δ, where Δ is the spacing between the small-angle boundaries and δ the spacing between dislocations within a boundary (see Wilkens, 1979). Here, the results for $\Delta/\delta = 2$ are discussed. Poisson's ratio was set to $\frac{1}{3}$ and first and second order of reflection were calculated using $S_1 b = 1$ and $S_2 b = 2$, where $b = |\boldsymbol{b}|$. The results of both separation methods in terms of $A^S(L)$, $A^D(L,S_1)$ and, for the WA analysis, $\langle e_L^2 \rangle$ are shown in Fig. 3.

Both the WA and the alternative analyses yield results that deviate significantly from the true values. Only in the limit $L \downarrow 0$ do both methods function properly. Both methods yield an extensive concave part in $A^S(L)$, corresponding to physically impossible negative values of $p(D)$. In practice, where true values are unknown, this concave part is one of the rare indicators that assumptions in the method applied are incompatible with the specimen analysed. Neither an extrapolation of $\langle e_L^2 \rangle$ to $L = 0$ for the WA analysis, nor a polynomial fit to $A^D(L,S_1)$ for the alternative analysis (see Sec. II.B) yields physically meaningful information.

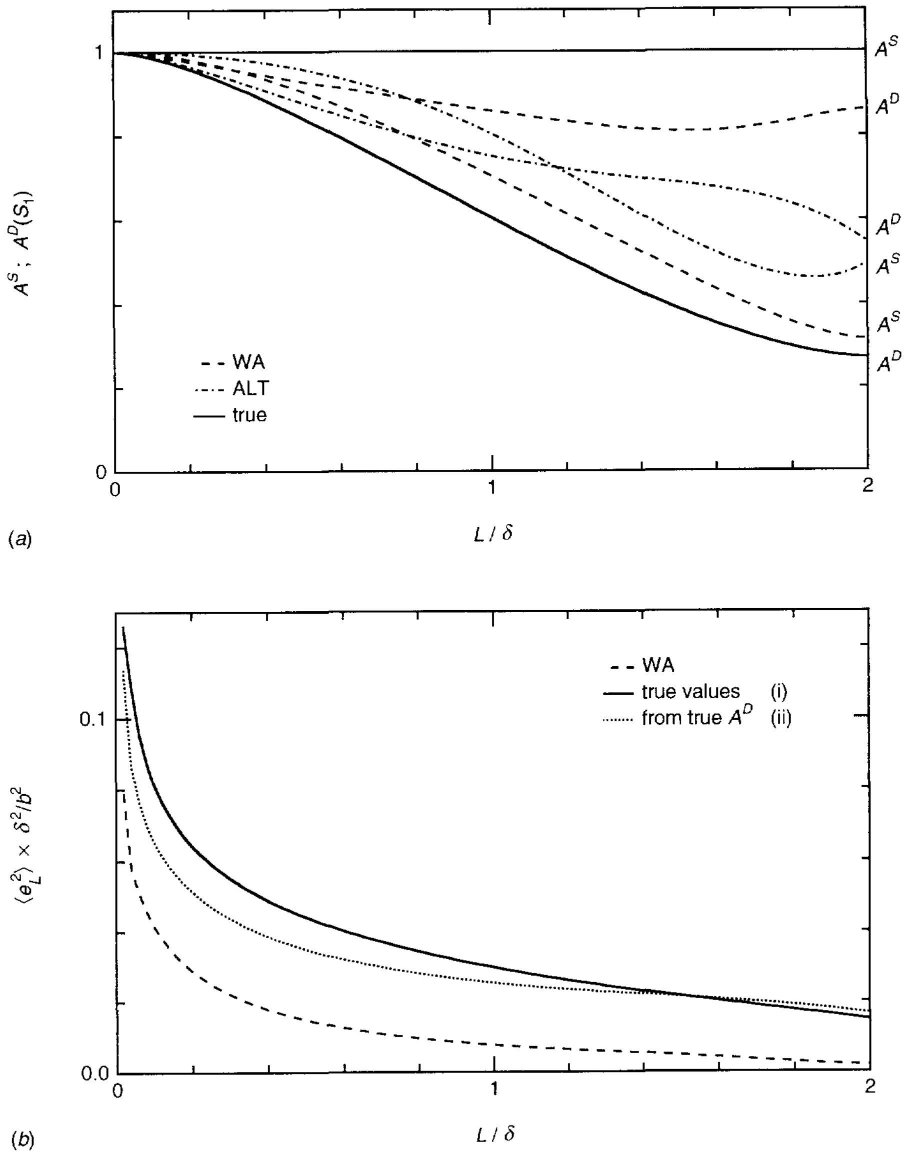

Fig. 3: Results of the WA analysis and the alternative (ALT) analyses applied to first- and second-order line profiles, simulated for a periodic repetition of small-angle boundaries of alternating 'sign' with $\Delta/\delta = 2$: (*a*) A^S and $A^D(S_1)$, compared with the true values, (*b*) WA results for $\langle e_L^2 \rangle$, compared with 'true' values (i) and (ii), which are explained in the text of Sec. III.A. Interpretation of the results of both analyses in terms of the local strain is not meaningful (see Sec. III.B).

The reason for the failure of both methods, already at relatively small L, is violation of the (different) assumptions underlying the methods. The range of L for which the WA analysis is valid depends on the deviation of the actual strain distributions $p(e_L)$ from a Gaussian [see below Eq. (A.2)]. In the present case the distributions are much more 'peaked' than a Gaussian (*e.g.* $k_2 > 100$ for small L, *cf.* App. A). Therefore, the neglect of the term containing $\langle e_L^4 \rangle$ in the expansion of $\ln[A^D(L,S_i)]$ [see Eq. (A.2)] is already problematic for small L [*cf.* deviation of curve (ii) from (i) in the $\langle e_L^2 \rangle$ plot in Fig. 3b]. The range of L for which the alternative analysis is valid depends on the shape of the size distribution and on the magnitude of the strain gradients (see Sec. II.B). Since there is no size broadening simulated in this example (the crystal is taken infinitely large), the failure of the alternative analysis is due to large strain gradients. Indeed, with respect to isolated dislocations, ordering of dislocations in small-angle boundaries decreases the average strains in the specimen, but increases the strain gradients close to the boundary (see Fig. 2b in Wilkens, 1979). The very strong increase in the true $\langle e_L^2 \rangle$ with decreasing L in Fig. 3b confirms this.

In terms of the three broadening dimensions indicated in Fig. 1, the example discussed must be compared with the location marked 'SABs' in this figure: pure strain, strongly non-Gaussian $p(e_L)$ and significant strain gradients. This location pertains to the region where neither of the two size-strain separation methods is applicable, in agreement with the above.

One may question if the example discussed has to be considered as one of pure strain broadening. It might be argued that the small-angle boundaries break up the crystal into domains that diffract incoherently with respect to each other. However, it can be shown that this phenomenon only occurs when lattice defects produce very large local strains concentrated in very small, isolated parts of a specimen (Berkum, Delhez, Keijser & Mittemeijer, 1994). If this would occur in the present case, the $A^S(L)$ values to be obtained using the size-strain separation methods would satisfy $A^S(L) = 1 - |L|/\Delta$ for $|L| \leq \Delta$. Clearly, for $\Delta/\delta = 2$, this result is not obtained either. However, for much larger values of Δ/δ, the small-angle boundaries do tend to act as coherence boundaries. In this case, the WA analysis yields approximately Δ for the average crystallite size, a result that can again be interpreted in a physically meaningful way. The results obtained by the alternative analysis remain ambiguous for large Δ/δ.

IV. APPLICATIONS TO EXPERIMENTAL PROFILES

To test newly developed methods of analysis, it is always desirable to use experimental data in addition to simulated data. Unexpected complications may arise due to the experimental circumstances. Experimental line profiles allow investigation of the (combined) effects of counting statistics, background removal, peak overlap, imperfect standards and deconvolution procedure, which do not occur using simulated data. However, for experimental data no true values are known to check the separation results. A general test on the results is to probe their physical plausibility: values of $A^S(L)$ or $A^D(L,S_1)$ larger than 1 are impossible, a downward curvature of $A^S(L)$ is unrealistic, $A^D(L,S_1)$ rising with increasing L is unlikely, *etc.*

For the present purpose, especially suitable data are those from specimens of which some information on the size or strain is known, either obtained from experiments other than diffraction-line broadening or derived from characteristics of the preparation, deformation or other treatment the specimen has been subjected to. Then, the size and strain parameters obtained using the separation methods can be compared with this information.

A. Microstructural change in thin aluminium layers

Thin aluminium layers were prepared by physical vapour deposition in high vacuum onto Si <100> single-crystal wafers and subsequently annealed at 723 K (for details see Vermeulen, Delhez, Keijser & Mittemeijer, 1994). During cooling to room temperature the Al layers are plastically deformed due to the development of high thermal stresses. At room temperature, considerable relaxation of the residual stresses occurs within a few days. The relaxation process is accompanied by a measurable change in line breadth related to changes in the dislocation density and arrangement (Vermeulen, Delhez & Mittemeijer, 1992). After 12 and 110 h of relaxation at room temperature the Al {111} and {222} reflections were recorded on a Siemens D500 diffractometer, equipped with a scanning position sensitive detector and an incident beam monochromator set to CoKα_1. For all four line profiles the background was subtracted[2], the remainder of the α_2 component of the Kα doublet (about 2% of α_1) was removed and a Fourier transformation was performed. No ideal 'standard' specimen was available for the thin Al layers. Therefore, a direct comparison of the line profiles after 12 and 110 hours of relaxation was made (see Sec. II): the profiles with the larger line breadths (12 h) were deconvoluted with the ones with the smaller line breadths (110 h). Finally, the WA and the alternative analyses were applied. The results, representing the decrease in lattice imperfection evoked by relaxation from 12 to 110 h, are shown in Fig. 4. Due to the relatively small decrease in line broadening during the relaxation, the Fourier coefficients after deconvolution $A(L,S_1)$ [the product of $A^S(L)$ and $A^D(L,S_1)$ in Fig. 4] drop only from 1 to about 0.85 with L increasing from 0 to 100 nm.

---

[2] An additional correction for truncation effects according to Vermeulen, Delhez, Keijser & Mittemeijer (1991, 1992) is possible. It is not incorporated in this paper, because it does not change the conclusions reached.

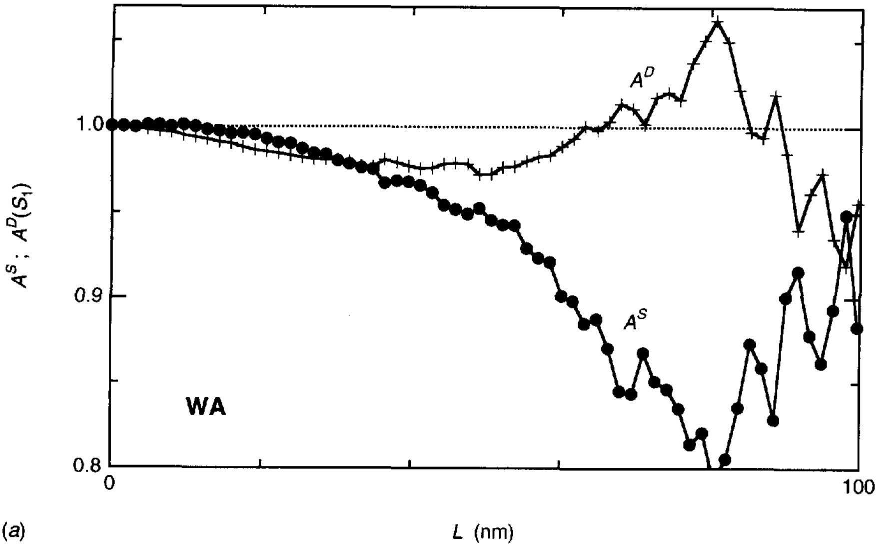

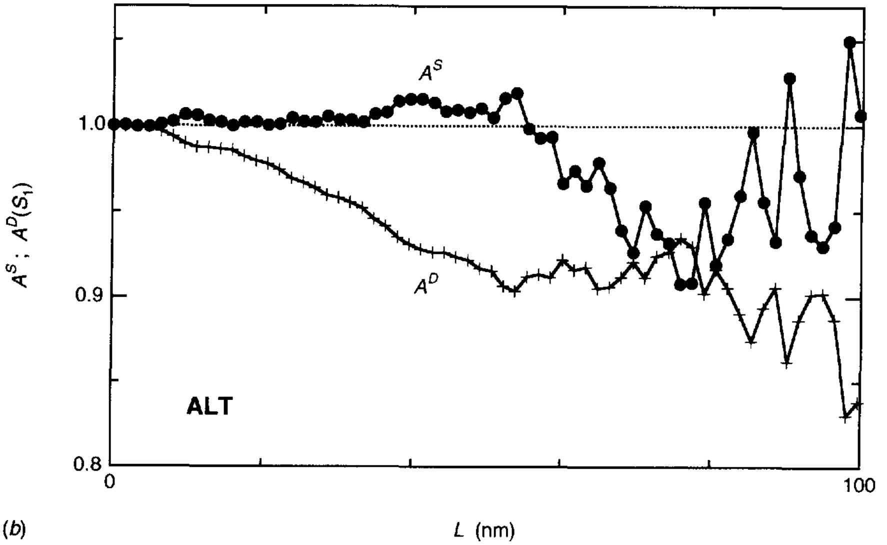

Fig. 4: Results of (*a*) the WA and (*b*) the alternative (ALT) analyses applied to the {111} and {222} reflections of an Al layer after 12 h of relaxation at room temperature using measurements after 110 h as 'standard' profiles. The Fourier coefficients represent only the *change* in the microstructure due to the relaxation between 12 and 110 h. Dashed lines indicate the expected values for $A^S(L)$. Note the vertical scale values.

It is unlikely that the relaxation at room temperature could cause a change in the crystallite sizes. Hence, the values of $A^S(L)$ after 12 and 110 h should be equal. Then, in the above described comparison (12 h data deconvoluted with 110 h data) the size coefficients drop out completely. After size-strain separation the 'size' coefficients, in this case representing the *difference* in size broadening, should be equal to unity.

The WA analysis yields the expected results [$A^S(L) = 1$] up to $L = 10$ nm. For larger values of L, before the results start to scatter due to the effects of counting statistics (at $L = 60$ nm), a significant deviation of $A^S(L)$ from unity is observed. These values are considered to be incorrect, because they indicate an unlikely change in the size distribution during the relaxation. In conclusion, only a small portion of the statistically reliable data can be interpreted by the WA analysis.

The alternative analysis yields the expected results [$A^S(L) = 1$] over a longer range than the WA analysis: up to $L = 35$ nm. Again, for larger L values $A^S(L)$ starts to deviate from unity, indicating that the results become incorrect. In conclusion, a substantial portion of the statistically reliable data can be interpreted by the alternative analysis.

Finally, note that the tangents at $L = 0$ to the $A^S(L)$ curves obtained by both methods are clearly horizontal. Since both methods yield correct $A^S(L)$ for $L \downarrow 0$, this observation supports the assumption, made in advance, of negligible changes in the average crystallite size during relaxation.

A discussion of the line broadening in terms of dislocation density and arrangement will be given in Vermeulen, Delhez, Keijser & Mittemeijer (1994).

B. Ball-milled molybdenum powder

A very different set of experimental line profiles was taken from molybdenum powder plastically deformed by ball milling. The powder was milled for 45 minutes in a horizontally moving cylinder with two balls. From scanning-electron-microscopy the average particle diameter before milling was estimated between 0.5 and 1 μm; after milling it was approximately halved. Lattice-parameter measurements did not indicate any contamination of the Mo powder.

A very thin and flat X-ray diffraction specimen was prepared from the milled powder. The procedure employed was analogous to that used for the standard specimen, which was prepared from annealed Si powder (see Berkum, Sprong, Keijser, Delhez, Sonneveld & Vermeulen, 1994). The Mo {110} and {220} and the Si {220} and {422} reflections were recorded on a Siemens D500 diffractometer using CuKα radiation.

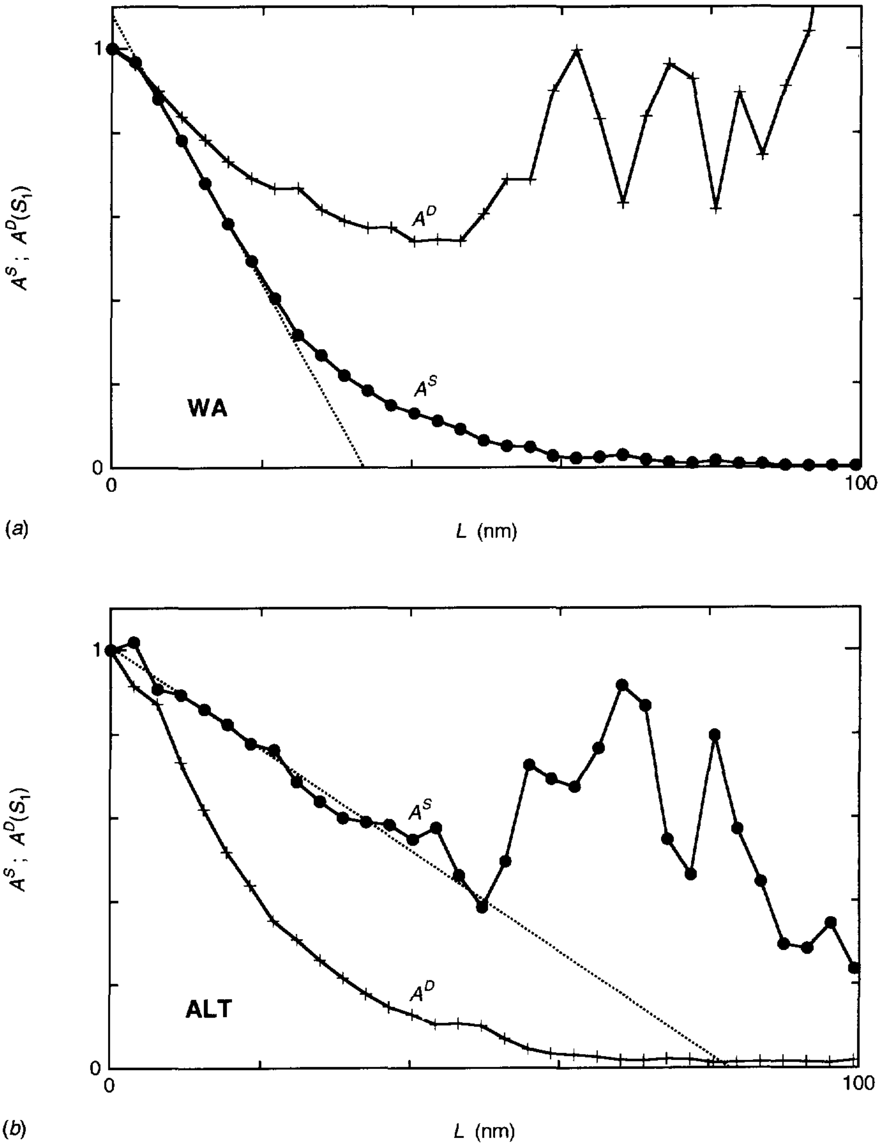

Fig. 5: Results of (*a*) the WA and (*b*) the alternative (ALT) analyses applied to the {110} and {220} reflections of ball-milled Mo in terms of $A^S(L)$ and $A^D(L,S_1)$. Dashed lines are straight line fits to the (approximately) linear parts of $A^S(L)$. The results obtained by the alternative analysis near $L = 0$ are unreliable due to the inaccuracy of interpolation of Fourier coefficients in this range and an unfortunate combination of step sizes ΔL_1 and ΔL_2 [*cf.* Sec. II.C(iii)].

For all line profiles the background was subtracted[3], the α_2 component of the Kα-doublet was removed and a Fourier transformation was performed. The reflection Si {220} was used as standard profile for Mo {110}, Si {422} was used for Mo {220}. The Si {220} and Mo {110} reflections do not correspond very well in 2θ position but their combination is possible because the breadth of the α_2-stripped instrumental line profile for the experimental set-up used here has a flat minimum in this range. Finally, the WA and the alternative analyses were applied. The results are shown in Fig. 5.

The two methods yield opposing results: the WA analysis attributes most of the broadening to size [extrapolation of the linear part of $A^S(L)$ to the abscissa yields $\langle D\rangle = 34$ nm], whereas the alternative analysis detects dominant strain broadening with only a small size contribution ($\langle D\rangle = 83$ nm). For the following reasons the results obtained using the alternative analysis seem to have larger credibility.

Firstly, the value of $\langle D\rangle$ obtained by the WA analysis (34 nm) is very small. The particles of the milled powder are probably still single-crystalline, so that the crystallite diameter is not much smaller than the particle diameter (between 0.25 and 0.5 µm, see above). The area-averaged column length $\langle D\rangle$ for a polyhedral crystallite is about $\frac{1}{2}$ to $\frac{3}{4}$ times its 'diameter' (*cf.* K_k in Langford & Wilson, 1978). Therefore, an average column length of about 100 to 400 nm is to be expected. Hence, the value of $\langle D\rangle$ according to the alternative analysis (83 nm) is closer to the expected value than the value according to the WA analysis.

A second reason for considering the results of the alternative analysis to be more realistic is the behaviour of the obtained $A^D(L,S_1)$. It has been shown for a random distribution of dislocations (Krivoglaz, 1969) and for other distributions (Wilkens, 1970; Krivoglaz, Martynenko & Ryaboshapka, 1983; Groma, Ungár & Wilkens, 1988) that the elastic strains around dislocations give rise to the following behaviour of $A^D(L,S_1)$ for small to moderate L values:

$$-\ln[A^D(L,S_1)] = \frac{\pi}{2} C \rho\, b^2 S_1^2 L^2 \ln\left[\frac{CR_e}{bS_1L}\right], \qquad (15)$$

where ρ is the dislocation density, C and C' are dimensionless constants depending on the angles between the diffraction vector and the Burgers' and line vectors of the dislocations and R_e is a length parameter depending on the configuration of the dislocations. From Eq. (15), it follows that $-L^{-2}\ln[A^D(L,S_1)]$ plotted *versus* $\ln L$ should yield a straight line. In Fig. 6, it can be seen that this behaviour might be present in the $A^D(L,S_1)$ according to the WA analysis for $9 < L < 25$ nm. For the alternative analysis, such behaviour of $A^D(L,S_1)$ is definitely present over

---

[3] See footnote on p. 59.

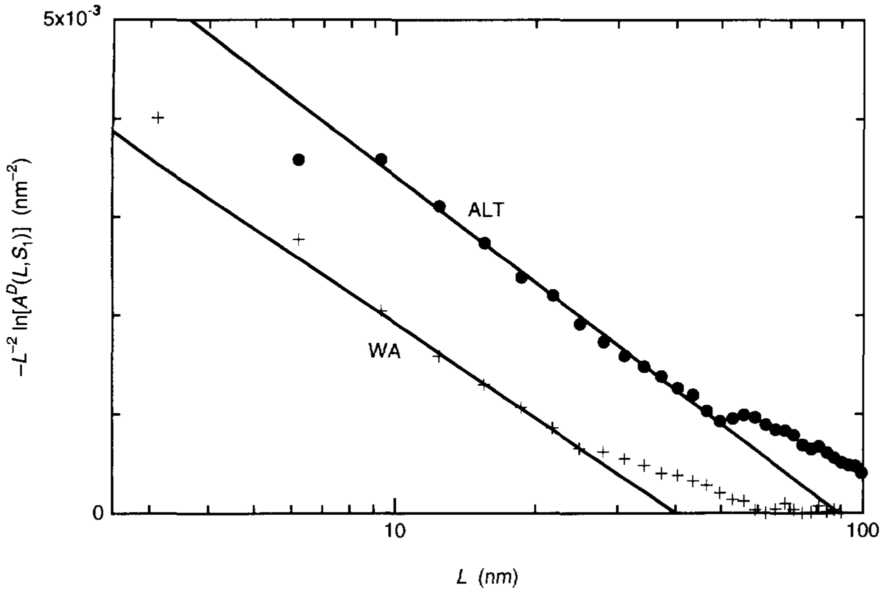

Fig. 6: As Fig. 5, but in terms of $-L^{-2}\ln[A^D(L,S_1)]$ *versus* ln L. The two straight lines indicate hypothetical behaviours according to Eq. (15) for comparison with the experimental results.

a much larger range: $9 < L < 50$ nm [a physical interpretation according to Eq. (15) yields $C\rho = 6.6\times10^{14}$ m^{-2} and $C'R_e = 0.11\times10^3$ nm].

A third indication that the results of the present WA analysis may be less reliable is provided by checking the assumptions underlying the methods. The WA analysis is possible if either $(2\pi LS_i)^2\langle e_L^2\rangle << 1$ or if the $p(e_L)$ are close to Gaussian [see below Eq. (A.2)]. For, say, $L = 10$ nm (approximately the third data point) and $S_i = 9.0$ nm^{-1} (Mo{220}), it follows $\langle e_L^2\rangle = 5\times10^{-6}$ and, therefore, $(2\pi LS_i)^2\langle e_L^2\rangle = 1.6$, so that the first condition is not met. The second condition is also not met, because for strains around dislocations the $p(e_L)$ deviate significantly from being Gaussian: they have tails proportional to $|e_L|^{-3}$ (Wilkens, 1984). The alternative analysis is applicable if both $L << \langle D\rangle$ (see App. B) and $\langle e_0'^2\rangle L^2 << 12\ \langle e_0^2\rangle$ [i.e. Eq. (A.6)]. For the same L value as above (10 nm), the first condition is met by a factor of 8. A check on the second condition is impossible here, because values of $\langle e_0^2\ \rangle$ and $\langle e_0'^2\rangle$ are not available.

A 'hook effect' (physically impossible concave part close to $L = 0$) is obtained in $A^S(L)$ if the WA analysis is applied. Extrapolation to $L = 0$ of the linear part of the corresponding $A^S(L)$ curve gives an ordinate value of 1.08 (see Fig. 5a). The $A^S(L)$ curve obtained by the alternative analysis does not show a systematic "hook effect". The inevitable truncation of the measured line profiles may cause the "hook effect" in the WA analysis; the effects of such truncation on the results of the alternative analysis have not yet been investigated. On the other hand, the "hook effect" in the WA analysis may indicate systematic errors due to violation of the underlying assumption.

WA analyses yielding hook effects and surprisingly small crystallite sizes have been found often in the past for comparable severely deformed metallic specimens (Warren, 1959; Klug & Alexander, 1974 and references therein). Such results may be erroneous because the assumptions inherent to the WA analysis are violated; the alternative analysis may provide more reliable data for such cases.

Also the recursive analysis, described in Sec. II.C(ii), was applied to the line profiles of the ball-milled Mo powder. The results are compared with those obtained using the alternative analysis in Fig. 7. Using the two extreme values for the initial guess of $A^S(\Delta L)$, a range of possible results for the alternative analysis is calculated [*cf.* Sec. II.C(ii)]. The results obtained here by using the alternative analysis fall approximately within this range for L values up to

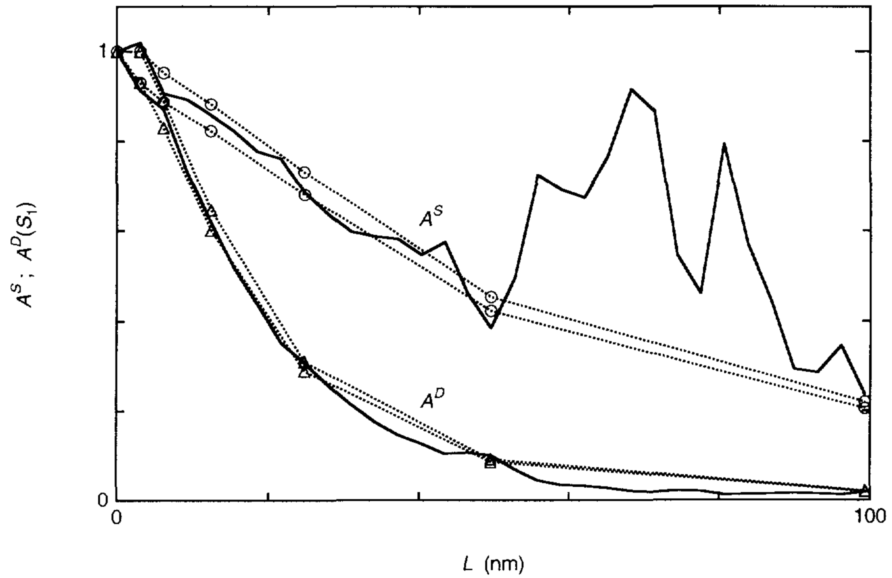

Fig. 7: Results of the recursive (markers and dashed lines) and the alternative (full lines) analyses applied to the {110} and {220} reflections of ball-milled Mo. For the recursive analysis, the two extreme initial guesses $A^S(\Delta L) = 1$ and $A^S(\Delta L) = A(\Delta L, S_1)$, where $\Delta L = 3.1$ nm, were used. Note the increasing step size in L for the recursive analysis.

50 nm. This means that, if the neglect of strain gradients was justified for this specimen (this assumption is inherent in both the recursive and the alternative analyses), the assumption applied to $A^S(L)$ did not introduce significant errors in the size-strain separation.

V. CONCLUSIONS

Using different assumptions on the distributions of crystallite sizes and elastic strains, different methods to interpret diffraction line broadening are possible. The frequently applied Warren-Averbach analysis relies on either small strains or approximately Gaussian strain distributions. The alternative analysis discussed in this paper relies on small strain gradients and large crystallite sizes or a broad size distribution.

For both the Warren-Averbach and the alternative analyses, a logarithmic and a linear version can be derived. The linear versions are less sensitive to propagation of random errors (*e.g.* due to counting statistics); in many cases the logarithmic ones introduce less systematic errors.

Specimens exist for which both methods yield comparable and correct results up to large correlation lengths L, *e.g.* a matrix containing misfitting inclusions. The reverse is also possible: both methods give erroneous results already at small L, *e.g.* crystals containing small-angle grain boundaries. Erroneous results for size and strain are always paired: overestimation of the size broadening goes with underestimation of the strain broadening and *vice versa*. Certainty about the reliability of results obtained in practice is impossible. At least, the results should be in accordance with the assumptions used in the method. In addition, external information available on the specimen concerned can be used to assess the plausibility of the results.

Specimens subjected to severe plastic deformation appear to be analysed more reliably by the alternative analysis. Due to increasing violation of the underlying assumption, with increasing L the Warren-Averbach analysis attributes ever more broadening incorrectly to size, yielding a too small average crystallite size and a too rapid decrease in the mean squared strains $\langle e_L^2 \rangle$. The assumptions used in the alternative analysis appear applicable up to relatively large L for such specimens.

ACKNOWLEDGEMENTS

The authors thank G.J.M. Sprong for preparing the Mo specimens and performing the X-ray measurements and ir. A. Buis for providing scanning-electron-microscopy facilities. These investigations in the programme of the Foundation for Fundamental Research on Matter (FOM) have been supported (in part) by the Netherlands Technology Foundation (STW).

APPENDIX A: SERIES EXPANSION OF $A^D(L,S_i)$

Expansion of the cosine in the general expression Eq. (4) for $A^D(L,S_i)$ in a Taylor series yields:

$$\begin{aligned} A^D(L,S_i) &= 1 - \frac{y^2}{2!}\langle e_L^2\rangle + \frac{y^4}{4!}\langle e_L^4\rangle - \frac{y^6}{6!}\langle e_L^6\rangle + \ldots \\ &= 1 - \frac{1}{2!}y^2\langle e_L^2\rangle + \frac{k_2}{4!}\left[y^2\langle e_L^2\rangle\right]^2 - \frac{k_3}{6!}\left[y^2\langle e_L^2\rangle\right]^3 + \ldots, \end{aligned} \qquad \text{(A.1)}$$

where $y = 2\pi L S_i$ and $k_i = \langle e_L^{2i}\rangle / \langle e_L^2\rangle^i$ $(i \geq 2)$. Substitution of Eq. (A.1) in a Taylor series for $\ln[A^D(L,S_i)]$ in $A^D(L,S_i) = 1$ yields:

$$\ln[A^D(L,S_i)] = -\frac{1}{2!}y^2\langle e_L^2\rangle + \frac{(k_2-3)}{4!}\left[y^2\langle e_L^2\rangle\right]^2 - \frac{(k_3-15k_2+30)}{6!}\left[y^2\langle e_L^2\rangle\right]^3 + \ldots \qquad \text{(A.2)}$$

Restriction of the right-hand side of Eq. (A.2) to the first term leads to Eq. (5). This approximation is reasonable if $y^2\langle e_L^2\rangle << 1$ or if the values of k_i are not too far from those for a Gaussian distribution: $k_2 = 3$, $k_3 = 15$, ... (assuming that $\langle e_L\rangle = 0$, which is always the case if S_i corresponds to the centroid of the structural profile). The two conditions are related: the values of k_i determine the range of y for which the approximation is valid. Fourth, sixth and higher moments of $p(e_L)$ are increasingly influenced by the tails of the distribution. Many distributions have more pronounced tails than a Gaussian and therefore (much) higher values of k_i.

Restriction of the right-hand side of Eq. (A.1) to the first two terms leads to Eq. (11). The conditions for this approximation are $y^2\langle e_L^2\rangle << 1$ or k_i small (as small as possible). The smallest possible value of k_2 for a unimodal distribution is $\frac{9}{5}$ (see App. D). The term containing y^4 (usually the term that limits the applicability of the approximation) is therefore always smaller in Eq. (A.2) than in Eq. (A.1).

To derive the explicit L dependence of $A^D(L,S_i)$, the moments of $p(e_L)$ are expressed in terms of the local strain e_0 and its derivatives. With the assumption that averages of e_0 and its derivatives at the column ends vanish, the following expression has been derived (Turunen, Keijser, Delhez & Pers, 1983):

$$\langle e_L^2\rangle = \langle e_0^2\rangle - \frac{1}{12}\langle e_0'^2\rangle L^2 + \frac{1}{360}\langle e_0''^2\rangle L^4 + \ldots \qquad \text{(A.3)}$$

A comparable expression for the fourth moment of $p(e_L)$ can be analogously derived:

$$\langle e_L^4\rangle = \langle e_0^4\rangle - \frac{1}{2}\langle e_0^2\, e_0'^2\rangle L^2 + \left[\frac{1}{60}\langle e_0''^2\rangle - \frac{1}{240}\langle e_0'^4\rangle\right]L^4 + \ldots \qquad \text{(A.4)}$$

Substitution of such expressions into Eq. (A.1) yields:

$$\begin{array}{rl|l}
A^D(L,S_i) = 1 - \frac{1}{2!}y^2 \Big[& \langle e_0^2\rangle & -\frac{1}{12}\langle e_0'^2\rangle L^2 + \frac{1}{360}\langle e_0''^2\rangle L^4 + \dots \qquad \Big] \\ \cline{2-3}
+\frac{1}{4!}y^4 \Big[& \langle e_0^4\rangle & -\frac{1}{2}\langle e_0^2\, e_0'^2\rangle L^2 + \left(\frac{1}{60}\langle e_0''^2\rangle - \frac{1}{240}\langle e_0'^4\rangle\right)L^4 + \dots \qquad \Big] \\
-\frac{1}{6!}y^6 \Big[& \langle e_0^6\rangle & - \dots \qquad \Big] \\
+\dots & &
\end{array} \qquad \text{(A.5)}$$

If e_0 is slowly varying in space, the derivatives are small on the average and, for small L, the series between square brackets in Eq. (A.5) are dominated by their first terms. In this case, $A^D(L,S_i)$ can be written as a function of y only, which means that Eq. (8) is valid.

With increasing L, the term limiting the applicability of Eq. (8) is in general the second term in the first series in Eq. (A.5). Thus, the range of L for which Eq. (8) is valid is determined by the condition:

$$\langle e_0'^2\rangle L^2 << 12\,\langle e_0^2\rangle \qquad \text{(A.6)}$$

This means that Eq. (8) holds for L up to the order of magnitude of the spatial width of the peaks or humps in e_0.

The difference between the assumptions used in the WA and the alternative analyses [Eqs. (5) and (8), respectively] can be discussed as follows. The terms between square brackets in Eq. (A.5) can be considered to form an infinitely large matrix of terms. The rows of this matrix represent $\langle e_L^2\rangle$, $\langle e_L^4\rangle$, *etc.* [*cf.* Eq. (A.3), Eq. (A.4)]. A similar matrix results on expansion of $\ln[A^D(L,S_i)]$. For either the logarithmic or linear version, in the WA analysis only the first row of the matrix is taken into account, in the alternative analysis only the first column is taken into account. The additional rows are determined by the shape of the frequency distribution $p(e_L)$, the additional columns are determined by the spatial distribution of e_0. For L decreasing to zero, $A^D(L,S_i)$ approaches $1-\frac{1}{2}y^2\langle e_0^2\rangle$ and both approximations used are valid regardless of the nature of the spatial distribution or the frequency distribution of the strain.

APPENDIX B: SERIES EXPANSION OF $A^S(L)$

In the general expression (3) for $A^S(L)$, the distribution $p(D)$ can be expanded in a Taylor series. Integration of the individual terms yields:

$$A^S(L) = 1 - \frac{|L|}{\langle D\rangle} + \frac{|L|^2\, p(0)}{2!\,\langle D\rangle} + \frac{|L|^3\, p'(0)}{3!\,\langle D\rangle} + \dots \tag{B.1}$$

Substitution of Eq. (B.1) in a Taylor series for $\ln[A^S(L)]$ in $A^S(L) = 1$ yields:

$$\ln[A^S(L)] = -\frac{|L|}{\langle D\rangle}\left[1 - |L|\left(\frac{p(0)}{2!} - \frac{1}{2\,\langle D\rangle}\right) - |L|^2\left(\frac{p'(0)}{3!} + \frac{p(0)}{2!\langle D\rangle} - \frac{1}{3\,\langle D\rangle^2}\right) - \dots\right]. \tag{B.2}$$

If the term between square brackets in the right-hand side of Eq. (B.2) is approximated by 1, Eq. (9) is easily derived from Eq. (B.2). This approximation is valid if $|L|/\langle D\rangle << 1$ or if the size distribution $p(D)$ is not too far from the exponential distribution $p(D) = \frac{1}{\langle D\rangle}\exp[-\frac{D}{\langle D\rangle}]$. As for $A^D(L,S_i)$, the two conditions are related: the more $p(D)$ deviates from the exponential distribution, the shorter the range of L for which the approximation is valid. However, for $A^S(L)$, very large values of the coefficients in the expansion, determined by the derivatives $p^{(n)}(0)$, seem physically unrealistic, whereas in the case of $A^D(L,S_i)$ large values of k_i may occur in practice.

Restriction of Eq. (B.1) to two terms on the right-hand side is the basis for Eq. (13). This approximation is justified if $|L|/\langle D\rangle << 1$ or if $p(0)$ and all derivatives $p^{(n)}(0)$ are small. Here, the ideal distribution is $p(D) = \delta(D - \langle D\rangle)$, i.e. the δ-type distribution, representing a monodisperse system, for which the approximation is exact up to $D = \langle D\rangle$.

APPENDIX C: PROPAGATION OF RANDOM ERRORS

I. Warren-Averbach analysis

Suppose Fourier coefficients of a first and a second order of reflection $A(L,S_1)$ and $A(L,S_2)$ with $S_2 = 2S_1$ are used to separate size and strain broadening. For the logarithmic version of the WA analysis Eq. (7), the size Fourier coefficients are calculated from:

$$A^S(L)_{\log} = \sqrt[3]{\frac{A(L,S_1)^4}{A(L,2S_1)}} \tag{C.1}$$

(subscripts log and lin are used to distinguish between values obtained by the logarithmic and the linear versions, respectively). If the random errors in the Fourier coefficients are not too large, the variance of $A^S(L)$, $\sigma^2[A^S(L)]$, can be expressed in the variances of both original coefficients $\sigma^2[A(L,S_1)]$ and $\sigma^2[A(L,2S_1)]$ in the following way (Arley & Buch, 1950):

$$\sigma^2[A^S(L)] \approx \left[\frac{\partial A^S(L)}{\partial A(L,S_1)}\right]^2 \sigma^2[A(L,S_1)] + \left[\frac{\partial A^S(L)}{\partial A(L,2S_1)}\right]^2 \sigma^2[A(L,2S_1)]. \tag{C.2}$$

Substitution of the partial derivatives as calculated from Eq. (C.1) into Eq. (C.2) yields:

$$\sigma_r^2[A^S(L)]_{\log} \approx \frac{16}{9}\,\sigma_r^2[A(L,S_1)] + \frac{1}{9}\,\sigma_r^2[A(L,2S_1)], \tag{C.3}$$

where $\sigma_r^2[x]$ denotes the 'relative variance' $\sigma^2[x]/x^2$.

Using the linear version of the WA analysis Eq. (12), $A^S(L)$ is calculated from:

$$A^S(L)_{\text{lin}} = \frac{1}{3}\,[\,4A(L,S_1) - A(L,2S_1)\,]. \tag{C.4}$$

Substitution of the partial derivatives as calculated from Eq. (C.4) into Eq. (C.2) yields:

$$\sigma_r^2[A^S(L)]_{\text{lin}} \approx \frac{16}{9}\left[\frac{A(L,S_1)}{A^S(L)_{\text{lin}}}\right]^2 \sigma_r^2[A(L,S_1)] + \frac{1}{9}\left[\frac{A(L,2S_1)}{A^S(L)_{\text{lin}}}\right]^2 \sigma_r^2[A(L,2S_1)]. \tag{C.5}$$

The differences between Eqs. (C.3) and (C.5) are the fractions between large square brackets in Eq. (C.5). Since $A(L,S_1) \le A^S(L)$ and $A(L,2S_1) \le A^S(L)$ (otherwise the strain Fourier coefficients exceed unity and the WA analysis is nonsensical), it follows that $\sigma_r^2[A^S(L)]_{\text{lin}} \le \sigma_r^2[A^S(L)]_{\log}$. For not too large errors in the experimental Fourier coefficients, the relative variance $\sigma_r^2[A^D(L,S_1)]$ approximately equals the relative variance $\sigma_r^2[A^S(L)]$ [since $A^S(L)A^D(L,S_1) = A(L,S_1)$] and the conclusion $\sigma_r^2[A^D(L,S_1)]_{\text{lin}} \le \sigma_r^2[A^D(L,S_1)]_{\log}$ is reached. Thus, the linear version of the WA analysis is less sensitive to propagation of random errors in the experimental Fourier coefficients than the logarithmic one.

II. Alternative analysis

In the logarithmic version of the alternative analysis Eq. (10), $A^S(2L)$ is calculated from:

$$A^S(2L)_{\log} = \left[\frac{A(2L,S_1)}{A(L,2S_1)}\right]^2. \tag{C.6}$$

Using Eq. (C.2), the relative variance of $A^S(2L)_{\log}$ equals:

$$\sigma_r^2[A^S(2L)]_{\log} \approx 4\,\left\{\sigma_r^2[A(2L,S_1)] + \sigma_r^2[A(L,2S_1)]\right\}. \tag{C.7}$$

Using the linear version of the alternative analysis Eq. (14), $A^S(2L)$ is calculated from:

$$A^S(2L)_{\text{lin}} = \frac{A(2L,S_1)}{2A(L,2S_1) - A(2L,S_1)} \tag{C.8}$$

and using Eq. (C.2), the relative variance of $A^S(2L)_{\text{lin}}$ equals:

$$\sigma_r^2[A^S(2L)]_{\text{lin}} \approx 4\left[\frac{A(L,2S_1)}{2A(L,2S_1) - A(2L,S_1)}\right]^2 \left\{\sigma_r^2[A(2L,S_1)] + \sigma_r^2[A(L,2S_1)]\right\}. \tag{C.9}$$

The difference between Eqs. (C.7) and (C.9) is the term between large square brackets in Eq. (C.9). Since $A(L,2S_1) \geq A(2L,S_1)$ [otherwise $A^S(2L) > 1$ and the alternative analysis is nonsensical], it follows that $\sigma_r^2[A^S(2L)]_{\rm lin} \leq \sigma_r^2[A^S(2L)]_{\rm log}$. The relative variance of $A^D(2L,S_1)$ approximately equals that of $A^S(2L)$ (*cf.* Sec. C.I), so that $\sigma_r^2[A^D(2L,S_1)]_{\rm lin} \leq \sigma_r^2[A^D(2L,S_1)]_{\rm log}$. Thus, as for the WA analysis, the linear version is less sensitive to propagation of random errors in the experimental Fourier coefficients into the size and strain Fourier coefficients.

APPENDIX D: KURTOSIS OF A UNIMODAL DISTRIBUTION

The central moments $\mu_n(f)$ of a (normalized) probability density function $f(x)$, further denoted as "distribution", are defined as:

$$\mu_n(f) \equiv \int_{-\infty}^{\infty} (x-\mu(f))^n f(x)\, \mathrm{d}x, \tag{D.1}$$

where the mean $\mu(f)$ is given by:

$$\mu(f) \equiv \int_{-\infty}^{\infty} x f(x)\, \mathrm{d}x. \tag{D.2}$$

Moments are always restricted by the inequality $[\mu_n(f)]^{1/n} \geq [\mu_m(f)]^{1/m}$ if $n > m$ (Cramér, 1946). For the kurtosis $k(f)$, here defined as $\mu_4(f)/[\mu_2(f)]^2$, this implies $k(f) \geq 1$. For specific classes of distributions, such inequalities can sometimes be improved, as will be shown below for the kurtosis of a unimodal distribution. For moments with respect to any x other than the mean, $[\mu_n(f)]^{1/n}$ always increases more progressively with increasing n than the central moments. Therefore, an inequality that holds for central moments holds for moments with respect to any reference.

Consider a distribution $f(x)$ that has only one maximum ("unimodal"), that is located exactly at $x = \mu(f)$. For every $f(x)$, there exists exactly one distribution $\varphi(\xi) = f(\xi-\mu(f))$ with mean $\mu(\varphi) = 0$ that has the same central moments as $f(x)$ and, consequently, the same kurtosis. The moments $\mu_n(\varphi)$ are written as the sum of two terms $\mu_n^+(\varphi)$ and $\mu_n^-(\varphi)$:

$$\mu_n^+(\varphi) \equiv \int_0^{\infty} \xi^n\, \varphi(\xi)\, \mathrm{d}\xi \tag{D.3a}$$

$$\mu_n^-(\varphi) \equiv \int_{-\infty}^{0} \xi^n\, \varphi(\xi)\, \mathrm{d}\xi. \tag{D.3b}$$

Further, a "split-uniform" distribution $\upsilon(\xi)$ is introduced: for both $\xi > 0$ and $\xi < 0$, $\upsilon(\xi)$ has a constant value up to a certain $|\xi|$ and equals zero for larger $|\xi|$. There is exactly one split-uniform distribution $\upsilon(\xi)$ that has the same $\mu_0{}^+$, $\mu_2{}^+$, $\mu_0{}^-$ and $\mu_2{}^-$ as $\varphi(\xi)$. Firstly, the attention is concentrated on one side only, say $\xi > 0$.

By equating $\mu_0{}^+$ and $\mu_2{}^+$ of $\upsilon(\xi)$ and $\varphi(\xi)$, the height h and the width b of $\upsilon(\xi)$ (see Fig. D1) are readily obtained in terms of $\mu_0{}^+(\varphi)$ and $\mu_2{}^+(\varphi)$. Then, $\mu_4{}^+(\upsilon)$ can be calculated as:

$$\mu_4{}^+(\upsilon) = \int_0^b \xi^4\, h\, \mathrm{d}\xi = \frac{9}{5}\,\frac{[\mu_2{}^+(\varphi)]^2}{\mu_0{}^+(\varphi)}\,. \qquad \text{(D.4)}$$

For $\xi > 0$, the distributions $\upsilon(\xi)$ and $\varphi(\xi)$ intersect exactly twice: at $\xi = a$ and $\xi = b$ (see Fig. D1). This can be proven by negative demonstration. With zero points of intersection, the areas $\mu_0{}^+$ can never be equal. If $\upsilon(\xi)$ and $\varphi(\xi)$ have equal areas $\mu_0{}^+$ and they intersect only once, then $\mu_2{}^+$ cannot be equal. To prove that, firstly consider the case $\varphi(0) < h$, in which the intersection takes place at $\xi = b$ and the difference in $\mu_2{}^+$ is given by:

$$\mu_2{}^+(\varphi) - \mu_2{}^+(\upsilon) = \int_b^\infty \xi^2\, \varphi(\xi)\, \mathrm{d}\xi - \int_0^b \xi^2\, [\upsilon(\xi) - \varphi(\xi)]\, \mathrm{d}\xi. \qquad \text{(D.5)}$$

Since the areas considered in the two terms on the right-hand side of Eq. (D.5) are equal, *i.e.*

$$\int_b^\infty \varphi(\xi)\, \mathrm{d}\xi = \int_0^b [\upsilon(\xi) - \varphi(\xi)]\, \mathrm{d}\xi, \qquad \text{(D.6)}$$

and every ξ value considered in the first term is larger than in the second term, it follows that $\mu_2{}^+(\varphi) > \mu_2{}^+(\upsilon)$, in contradiction with the definition of $\upsilon(\xi)$. The second possibility to accomplish one point of intersection requires $\varphi(0) > h$, intersection at $\xi = a$ with $a < b$ and $\varphi(\xi) = 0$ for $\xi \geq b$. A reasoning analogous to that for the case $\varphi(0) < h$ yields $\mu_2{}^+(\varphi) < \mu_2{}^+(\upsilon)$, again in contradiction with the definition of $\upsilon(\xi)$. Three or more points of intersection are impossible because $\varphi(\xi)$ would have to be increasing at some interval to accomplish that.

A calculation of the difference in $\mu_4{}^+$ of $\upsilon(\xi)$ and $\varphi(\xi)$ involves three terms corresponding to the regions indicated P, Q and R in Fig. D1:

$$\mu_4{}^+(\varphi) - \mu_4{}^+(\upsilon) = \int_0^a \xi^4\, [\varphi(\xi) - h]\, \mathrm{d}\xi - \int_a^b \xi^4\, [h - \varphi(\xi)]\, \mathrm{d}\xi + \int_b^\infty \xi^4\, \varphi(\xi)\, \mathrm{d}\xi. \qquad \text{(D.7)}$$

From the identity of $\mu_0{}^+$ and $\mu_2{}^+$ of $\upsilon(\xi)$ and $\varphi(\xi)$, it immediately follows that the areas and second moments of the three regions are related by:

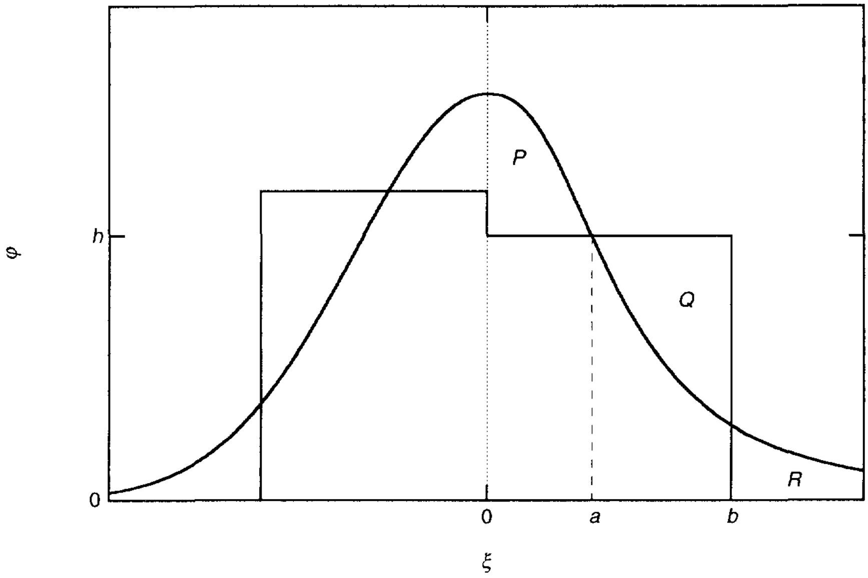

Fig. D1: Arbitrary distribution function (curved line) and the corresponding "split-uniform" distribution (straight lines), with on the right side a height *h* and width *b*. The meaning of the regions *P*, *Q* and *R* is explained in the text.

$$\int_0^a [\varphi(\xi) - h]\,\mathrm{d}\xi + \int_b^\infty \varphi(\xi)\,\mathrm{d}\xi = \int_a^b [h - \varphi(\xi)]\,\mathrm{d}\xi, \tag{D.8}$$

$$\int_0^a \xi^2 [\varphi(\xi) - h]\,\mathrm{d}\xi + \int_b^\infty \xi^2\,\varphi(\xi)\,\mathrm{d}\xi = \int_a^b \xi^2 [h - \varphi(\xi)]\,\mathrm{d}\xi. \tag{D.9}$$

In the following, the region Q is divided in infinitesimal areas Q_i, located at q_i with $a < q_i < b$. Because of Eqs. (D.8) and (D.9), it is possible to find for every Q_i an area P_i at p_i and an area R_i at r_i in region R, such that:

$$P_i + R_i = Q_i, \tag{D.10}$$

$$p_i^2\,P_i + r_i^2\,R_i = q_i^2\,Q_i. \tag{D.11}$$

Using the division of the regions P, Q and R, Eq. (D.7) can be written as:

$$\mu_4^+(\varphi) - \mu_4^+(\upsilon) = \sum_i T_i, \tag{D.12}$$

with

$$T_i = p_i^4 P_i - q_i^4 Q_i + r_i^4 R_i. \tag{D.13}$$

Using Eqs. (D.10) and (D.11), two parameters, say P_i and Q_i, can be eliminated from Eq. (D.13). After some algebraic manipulations, it follows:

$$T_i = (r_i^2 - p_i^2)\,(r_i^2 - q_i^2)\,Q_i. \tag{D.14}$$

Obviously, T_i is always positive, which, using Eq. (D.12), implies $\mu_4^+(\varphi) > \mu_4^+(\upsilon)$.

A completely analogous reasoning for $\xi < 0$ leads to the conclusion $\mu_4^-(\varphi) > \mu_4^-(\upsilon)$. Realizing that $\mu_n = \mu_n^+ + \mu_n^-$ and that $\mu_2(\upsilon) = \mu_2(\varphi)$, it follows immediately that $k(\varphi) > k(\upsilon)$. To calculate $k(\upsilon)$, $\mu_4^+(\upsilon)$ is expressed as in Eq. (D.4) and $\mu_4^-(\upsilon)$ analogously. Then, it follows for $k(\upsilon)$:

$$k(\upsilon) = \frac{9}{5\,[\mu_2(\varphi)]^2}\left\{\frac{[\mu_2^+(\varphi)]^2}{\mu_0^+(\varphi)} + \frac{[\mu_2^-(\varphi)]^2}{\mu_0^-(\varphi)}\right\}. \tag{D.15}$$

This expression can be written exclusively in terms of the ratios $f_0 = \mu_0^+(\varphi)/\mu_0^-(\varphi)$ and $f_2 = \mu_2^+(\varphi)/\mu_2^-(\varphi)$:

$$k(\upsilon) = \frac{9}{5}\,\frac{(f_0+1)(f_2^2+f_0)}{f_0\,(f_2+1)}. \tag{D.16}$$

From Eq. (D.16) it is readily verified that $k(\upsilon) \geq \frac{9}{5}$ and, consequently, $k(\varphi) > \frac{9}{5}$ and $k(f) > \frac{9}{5}$.

REFERENCES

Arley, N. & Buch, K.R. (1950). *Introduction to the Theory of Probability and Statistics* (New York: John Wiley), pp. 79-80.

Berkum, J.G.M. van, Delhez, R., Keijser, Th.H. de & Mittemeijer, E.J. (1992). *Phys. stat. sol. (a)* **134**, 335-350. See Chapter 5 of this thesis.

Berkum, J.G.M. van, Delhez, R., Keijser, Th.H. de & Mittemeijer, E.J. (1994). To be published. See Chapter 7 of this thesis.

Berkum, J.G.M. van, Sprong, G.J.M., Keijser, Th.H. de, Delhez, R., Sonneveld, E.J. & Vermeulen, A.C. (1994). To be published. See Chapter 1 of this thesis.

Berkum, J.G.M. van, Vermeulen, A.C., Delhez, R., Keijser, Th.H. de & Mittemeijer, E.J. (1993). *Mater. Sci. Forum* **133-136**, 77-82. See Chapter 2 of this thesis.

Cramér, H. (1946). *Mathematical methods of statistics* (Princeton: Princeton University Press), p. 176.

Delhez, R. & Mittemeijer, E.J. (1976). *J. Appl. Cryst.* **9**, 233-234.

Eastabrook, J.N. & Wilson, A.J.C. (1952). *Proc. Phys. Soc. London* **B65**, 67-75.

Groma, I., Ungár, T. & Wilkens, M. (1988). *J. Appl. Cryst.* **21**, 47-53.

Hall, W.H. (1949). *Proc. Phys. Soc. London* **62**, 741-743.

Keijser, Th.H. de, Langford, J.I., Mittemeijer, E.J. & Vogels, A.B.P. (1982). *J. Appl. Cryst.* **15**, 308-314.

Keijser, Th.H. de & Mittemeijer, E.J. (1980). *J. Appl. Cryst.* **13**, 74-77.

Klug, H.P. & Alexander, L.E. (1974). *X-ray Diffraction Procedures for Polycrystalline and Amorphous Materials* (New York: John Wiley), pp. 671-708.

Krivoglaz, M.A. (1969). *Theory of X-ray and Thermal Neutron Scattering by Real Crystals* (New York: Plenum), p. 261.

Krivoglaz, M.A., Martynenko, O.V. & Ryaboshapka, K.P. (1983). *Phys. Met. Metall.* **55**, 1-12.

Langford, J.I. (1992). *Accuracy in Powder Diffraction II*, NIST Special Publication 846, eds. Prince, E. & Stalick, J.K. (Washington: US Dpt. of Commerce), pp. 110-126.

Langford, J.I. & Wilson, A.J.C. (1978). *J. Appl. Cryst.* **11**, 102-113.

Mittemeijer, E.J. & Delhez, R. (1978). *J. Appl. Phys.* **49**, 3875-3878.

Stokes, A.R. (1948). *Proc. Phys. Soc. London* **61**, 382-391.

Stokes, A.R. & Wilson, A.J.C. (1944). *Proc. Phys. Soc. London* **56**, 174-181.

Turunen, M.J., Keijser, Th.H. de, Delhez, R., & Pers, N.M. van der (1983). *J. Appl. Cryst.* **16**, 176-182.

Ungár, T., Groma, I. & Wilkens, M. (1989). *J. Appl. Cryst.* **22**, 26-34.

Vermeulen, A.C., Delhez, R., Keijser, Th.H. de & Mittemeijer, E.J. (1991). *Mater. Sci. Forum* **79-82**, 119-124.

Vermeulen, A.C., Delhez, R., Keijser, Th.H. de & Mittemeijer, E.J. (1992). *J. Appl. Phys.* **71**, 5303-5309.

Vermeulen, A.C., Delhez, R., Keijser, Th.H. de & Mittemeijer, E.J. (1994). To be published.

Vermeulen, A.C., Delhez, R. & Mittemeijer, E.J. (1992). *Mater. Res. Soc. Proc.* **230**, 103-108

Warren, B.E. (1959). *Prog. in Metal Phys.* **VIII**, 147-202.

Warren, B.E. & Averbach, B.L. (1950). *J. Appl. Phys.* **21**, 595-599.

Warren, B.E. & Averbach, B.L. (1952). *J. Appl. Phys.* **23**, 497.

Wilkens, M. (1969). *Acta Metall.* **17**, 1155-1159 (in German).

Wilkens, M. (1970). In: *Fundamental Aspects of Dislocation Theory*, NBS Spec. Publ. 317, vol. II, eds. Simmons, J.A., Wit, R. de & Bullough, R. (Washington: US Dpt. of Commerce), pp. 1195-1221.

Wilkens, M. (1979). *J. Appl. Cryst.* **12**, 119-125.

Wilkens, M. (1984). In: *Microstructural Characterization of Materials by Non-Microscopical Techniques*, eds. Hessel Andersen, N., Eldrup, M., Hansen, N., Juul Jensen, D., Leffers, T., Lilholt, H., Pedersen, O.B., Singh, B.N. (Roskilde, Denmark: Risø National Lab.), pp. 153-168.

Williamson, G.K. & Smallman, R.E. (1954). *Acta Cryst.* **7**, 574-581.

Wilson, A.J.C. (1955). *Nuovo Cimento* **1**, 277-283.

CHAPTER 4

DISLOCATION DENSITY AND ARRANGEMENT FROM X-RAY DIFFRACTION-LINE BROADENING

Application of Present Fourier Methods

J.G.M. VAN BERKUM*, A. BORBÉLY**, I. GROMA**, AND T. UNGÁR**
**Laboratory of Materials Science, Delft University of Technology,*
Rotterdamseweg 137, 2628 AL Delft, The Netherlands;
***Institute for General Physics, Eötvös University Budapest,*
P.O. Box 323, H-1445, Budapest, Hungary.

ABSTRACT

The descriptions currently available of the X-ray diffraction-line broadening induced by plastically deformed specimens have been summarized and compared and the meaning of their parameters has been investigated. Procedures have been given for their application in practice, which include preparatory corrections of the measured line profiles and fitting to determine parameter estimates. The procedures have been illustrated by very different sets of experimental data, taken from a tensile-deformed copper single crystal, from a creep-deformed polycrystalline copper specimen and from a ball-milled tungsten powder. Each time, the dislocation density, one or more parameters characterizing the dislocation arrangement and their uncertainties have been determined. The parameters obtained are interpreted in terms of the dislocation structure of the specimen.

I. INTRODUCTION

The dislocation structure of severely plastically deformed materials can be analysed by means of X-ray diffraction-line broadening. Methods have been developed that interpret measured line broadening in terms of "size" and "strain" parameters (*e.g.* Warren & Averbach, 1952). As concerns plastically deformed materials, the assumptions underlying these methods have been criticized (*e.g.* Wilkens, 1979, 1984; Berkum, Vermeulen, Delhez, Keijser & Mittemeijer, 1994) and the meaning of the parameters obtained is ambiguous (Warren, 1959; Berkum, Delhez, Keijser & Mittemeijer, 1994). Other methods, that are directly based on the presence of dislocations as the origin of line broadening, can be more suitable for this class of materials. These methods use the displacement field of a single dislocation in an infinite medium and superimpose these for specific theoretical dislocation arrangements: random (Krivoglaz & Ryaboshapka, 1963), "restrictedly random" (Wilkens, 1970a) and more or less arbitrarily distributed (Krivoglaz, Martynenko & Ryaboshapka, 1983; Groma, Ungár & Wilkens, 1988). Plastically deformed specimens have been analysed using these "dislocation-based" methods in terms of the dislocation density and one or more parameters characterizing the dislocation arrangement (*e.g.* Wilkens, Herz & Mughrabi, 1980; Ungár, Mughrabi, Rönnpagel & Wilkens, 1984; Ungár, Groma & Wilkens, 1989).

Practical questions in the application of the dislocation-based methods concern the number of dislocation-arrangement parameters to be used in fitting line broadening data, the number of data points to be fitted, their weights, and so on. Further, the interpretation of the parameters determined has been insufficiently solved. Finally, usual practical complications are encountered, like corrections for background intensity or instrumental imperfections. The aim of the present paper is to provide unbiased procedures for the problems mentioned and to illustrate their use by means of a variety of experimental data.

II. THEORY

A. Dislocation arrangement

Dislocation-arrangement model currently used for the analysis of line broadening usually assume straight parallel screw dislocations. Sometimes the results are generalized to straight dislocations of edge or mixed character. The dislocation arrangement is characterized by means of one- and more-particle distribution functions, describing the chances of finding one or more intersection points of the dislocation lines somewhere in a plane perpendicular to the dislocation lines. If $w_1(\boldsymbol{r})$ is the one-particle distribution function at position $\boldsymbol{r}$ in the plane (*i.e.* $\boldsymbol{r}$ has only two co-ordinates), then $w_1(\boldsymbol{r})\mathrm{d}\boldsymbol{r}$ is the chance of finding a dislocation intersection within surface element $\mathrm{d}\boldsymbol{r}$ at $\boldsymbol{r}$. If $w_2(\boldsymbol{r},\boldsymbol{r}')$ is the two-particle distribution function, $w_2(\boldsymbol{r},\boldsymbol{r}')\mathrm{d}\boldsymbol{r}\mathrm{d}\boldsymbol{r}'$ is the chance of finding one dislocation in $\mathrm{d}\boldsymbol{r}$ at $\boldsymbol{r}$ *and at the same time* a second one in $\mathrm{d}\boldsymbol{r}'$ at $\boldsymbol{r}'$. Higher-order functions w_3, w_4, and so on can be defined analogously. The dislocation density ρ equals $\langle w_1(\boldsymbol{r})\rangle$, where $\langle ... \rangle$ means averaged over all $\boldsymbol{r}$.

In a real specimen, all dislocation positions are determined, *i.e.* not variable, and the distribution functions merely consist of (sums and products) of δ-functions. It is impossible and undesirable to derive these distribution functions from the measured line broadening. It is more useful to think of (relatively simple) average distribution functions, that, if applied to simulate dislocations positions, could have resulted in the actual set of dislocation positions, but also in an infinite number of other, equivalent sets (*cf.* Wilkens, 1969). Such *average* distribution functions can be taken as smoothly varying in space.

There are two possible Burgers' vectors for straight parallel screw dislocations, which will be denoted as $\boldsymbol{b}$ and $-\boldsymbol{b}$, respectively. Initially, "positive" and "negative" dislocations are not distinguished, which means the distribution of both types are characterized by the same distribution functions. Thus, these functions represent the chance of finding a dislocation, irrespective of its sign.

For a completely random distribution of dislocations $w_1(\boldsymbol{r}) = \langle w_1(\boldsymbol{r})\rangle = \rho$, independent of the position $\boldsymbol{r}$. If, in addition to the random nature of the dislocation distribution, the specimen and, consequently, the number of dislocations are unlimited, the n-particle distribution function $w_n(\boldsymbol{r},\boldsymbol{r}',...,\boldsymbol{r}^{(n)})$ equals $w_1(\boldsymbol{r})\times w_1(\boldsymbol{r}')\times ...\times w_1(\boldsymbol{r}^{(n)}) = \rho^n$, since knowledge on the position of one dislocation does not increase the predictability of the positions of others.

In the restrictedly random dislocation distribution (Wilkens, 1969), $w_1(\boldsymbol{r})$ is again a constant, as in the completely random distribution, but $w_2(\boldsymbol{r},\boldsymbol{r}')$ differs from the random situation in a specific way:

$$w_2(\boldsymbol{r},\boldsymbol{r}') = \rho^2\left(1-\frac{1}{N_p}\right) \qquad \text{for } |\boldsymbol{r}-\boldsymbol{r}'| \le R_p,$$

$$w_2(\boldsymbol{r},\boldsymbol{r}') = \rho^2 \qquad \text{for } |\boldsymbol{r}-\boldsymbol{r}'| > R_p, \tag{1}$$

where $N_p \approx \pi\rho R_p^{\,2}$ and R_p is a length constant. This expression recognizes the occurrence of repulsive forces between dislocations: the chance of finding a neighbouring dislocation within a distance R_p is smaller than beyond R_p. If attractive forces are dominant, the dislocation distribution cannot be described by Eq. (1). In the restrictedly random distribution, the degree and the range of interaction are correlated: the smaller the "interaction distance" R_p, the larger the decrease in the probability of two dislocations within a distance R_p. The two limiting cases are: (i) $N_p \to \infty$ and $R_p \to \infty$, which means no interaction and a completely random dislocation distribution and (ii) $N_p = 1$ and $R_p \sim \sqrt{\rho}$, which means a rather regular distribution (most nearest-neighbour distances between the dislocations are close to $\sqrt{\rho}$ and very few distances are much larger or smaller), that may be due to strong interactions between the dislocations. The functions w_n for $n > 2$ can be derived for this model without additional assumptions (see App. 2 of Wilkens, 1970a), but they are not used in the analysis of line broadening.

A slightly more general dislocation arrangement than the restrictedly random distribution again involves a position-independent $w_1(\boldsymbol{r}) = \rho$, but now the function $w_2(\boldsymbol{r},\boldsymbol{r}')$ depends arbitrarily on $|\boldsymbol{r} - \boldsymbol{r}'|$ (Krivoglaz, Martynenko & Ryaboshapka, 1983). The calculated effects on line broadening are very similar to those of the restrictedly random distribution.

The most general dislocation model applied until now for the analysis of line broadening involves arbitrary one- and two-particle distribution functions for (combinations of) "positive" and "negative" straight parallel screw dislocations (Groma, Ungár & Wilkens, 1988): $w_+(\boldsymbol{r})$ and $w_-(\boldsymbol{r})$ represent the chances of finding a dislocation of the indicated sign at $\boldsymbol{r}$; $w_{++}(\boldsymbol{r},\boldsymbol{r}')$, $w_{--}(\boldsymbol{r},\boldsymbol{r}')$ and $w_{+-}(\boldsymbol{r},\boldsymbol{r}') \equiv w_{-+}(\boldsymbol{r}',\boldsymbol{r})$ represent the chances of finding two dislocations with the indicated signs at $\boldsymbol{r}$ and $\boldsymbol{r}'$, respectively. These new functions are related to $w_1(\boldsymbol{r})$ and $w_2(\boldsymbol{r},\boldsymbol{r}')$ by: $w_1(\boldsymbol{r}) = w_+(\boldsymbol{r}) + w_-(\boldsymbol{r})$ and $w_2(\boldsymbol{r},\boldsymbol{r}') = w_{++}(\boldsymbol{r},\boldsymbol{r}') + w_{--}(\boldsymbol{r},\boldsymbol{r}') + w_{+-}(\boldsymbol{r},\boldsymbol{r}') + w_{-+}(\boldsymbol{r}',\boldsymbol{r})$. In this model, the densities of "positive" and "negative" dislocations are taken equal: $\langle w_+(\boldsymbol{r})\rangle = \langle w_-(\boldsymbol{r})\rangle = \frac{1}{2}\rho$. Since "positive" and "negative" dislocations are distinguished now, the functions define a certain dislocation-dipole polarization. Polarization means that dipole vectors, *i.e.* vectors from a "negative" dislocation to a (neighbouring) "positive" dislocation, have a preferred orientation. It has been shown that dislocation-dipole polarization may account for the asymmetry of broadened line profiles (Gaál, 1984; Groma, Ungár & Wilkens, 1988).

B. Line broadening

The line broadening effects of the elastic distortions around dislocations are most easily expressed in terms of the (complex) Fourier transform F_L of a diffraction-line profile expressed in reciprocal space. The Fourier variable L is a distance in real space, parallel to the diffraction vector. Fourier transforms are normalized to $F_0 = 1$ and the centre of gravity of the line profile in reciprocal space is chosen as the origin of Fourier transformation. In the derivations discussed here elastic isotropy, linear elasticity and kinematical diffraction are assumed.

In the restrictedly random distribution dislocations with $\boldsymbol{b}$ and $-\boldsymbol{b}$ are not distinguished. Therefore, the Fourier transform F_L is real (*i.e.* the broadened line profile is symmetric) and for sufficiently small L it reads (Wilkens, 1970a):

$$F_L = \exp\left\{-\rho^* L^2\left[f^*\left(\frac{L\sin\psi}{2R_p}\right) - K_v\right]\right\}, \tag{2}$$

with

$$K_v \approx \frac{7}{3} - 2\ln 2 + \ln|\boldsymbol{g}.\boldsymbol{b}|, \tag{3}$$

where $\rho^* = \hat{C}\rho$ with $\hat{C} = \frac{1}{2}\pi\, C\, g^2 b^2$, g is the length of the diffraction vector $\boldsymbol{g}$, b is the length of the Burgers' vector $\boldsymbol{b}$, and ψ is the angle between $\boldsymbol{g}$ and the dislocation line vector $\boldsymbol{l}$ (or $-\boldsymbol{l}$). The constant C, which depends on the angles between $\boldsymbol{g}$, $\boldsymbol{b}$ and $\boldsymbol{l}$, has been calculated for dislocations of screw, edge and mixed character (Wilkens, 1970b; see also Wilkens, 1987). The function $f^*(x)$ is given in App. 1 of Wilkens (1970a) for the ranges $x \leq 1$ and $x > 1$ separately. The complicated expression for $x \leq 1$ can be replaced (with very good accuracy) by a truncated Taylor series and a logarithmic function. Thus, $f^*(x)$ reads:

$$f^*(x) \approx -\ln x + \frac{7}{4} - \ln 2 + \frac{x^2}{6} - \frac{32\, x^3}{225\,\pi} \qquad \text{for } x \leq 1, \tag{4a}$$

$$f^*(x) = \frac{512}{90\,\pi\, x} - \left(\frac{11}{24} + \frac{1}{4}\ln 2x\right)\frac{1}{x^2} \qquad \text{for } x > 1. \tag{4b}$$

Instead of R_p, also the "effective outer cut-off radius" R_e is used. For screw dislocations, it follows that $R_e = e^{-1/4} R_p$ (Wilkens, 1970a). Instead of N_p as a dimensionless quantity characterizing the dislocation arrangement, also $M = R_e \sqrt{\rho} \approx e^{-1/4} \sqrt{N_p/\pi}$ is used (Wilkens, 1970b).

The Fourier transform F_L according to Eq. (2) diverges for large L. The following modification of Eq. (2) has been suggested as more realistic for large L (Wilkens, 1970a; also used in Wilkens, 1970b):

$$F_L = \exp\left\{-\rho^* L^2 f^*\left(\frac{L}{R_e'}\right)\right\}, \tag{5}$$

where $R_e' = 2\, R_p \,/\, e^{K_\nu} \sin\psi$. For small L, Eqs. (5) and (2) are identical, whereas for large L, Eq. (5) is strictly decreasing according to $\ln[F_L] \propto -L$, which is the most likely behaviour of any F_L for large L (Eastabrook & Wilson, 1952). In the present paper, the modified expression [Eq. (5)] is used for the restrictedly random distribution, because it appeared to fit experimental F_L values very well.

In case of arbitrary one- and two-particle distribution functions, the Fourier transform is complex (*i.e.* the broadened line profile is asymmetric). Expressions for the modulus $|F_L|$ and argument φ_L [$\tan\varphi_L = \mathrm{Im}(F_L)/\mathrm{Re}(F_L)$] of F_L have been derived for small L (Groma, Ungár & Wilkens, 1988; Ungár, Groma & Wilkens, 1989):

$$|F_L| = \exp\left\{-\rho^* L^2 \ln\frac{R_{\mathrm{eff}}}{L} + \frac{1}{2}\, T \rho^{*2} L^4 \ln\frac{R_2}{L}\, \ln\frac{R_3}{L}\right\}, \tag{6a}$$

$$\varphi_L = -P_0 L^3 \ln\frac{R_1}{L} - \frac{1}{2} P_1 L^5 \ln\frac{R_4}{L}\, \ln\frac{R_5}{L}, \tag{6b}$$

where R_{eff} and $R_{1...5}$ are length parameters, T is a relative measure for the spatial fluctuation of the dislocation density[1] and P_0 and P_1 characterize the dipole polarization and its fluctuation, respectively. Comparing Eqs. (6a) and (5) for small L, it follows that $R_{\text{eff}} = \frac{1}{2}\,\mathrm{e}^{7/4}\,R_e'$ if both expressions are accurate. In App. A, it is shown that an expression very similar to Eq. (6a) (but, obviously, with only two instead of five parameters) is also obtained for the restrictedly random distribution if terms of higher order in L are taken into account. Therefore, the principal advantage of the arbitrary distribution functions over the restrictedly random distribution is the ability to describe the asymmetry of the line broadening.

All parameters in Eq. (6) can be expressed in terms of the distribution functions $w_{\pm}(\boldsymbol{r})$ and $w_{\pm\pm}(\boldsymbol{r},\boldsymbol{r}')$ (Groma, Ungár & Wilkens, 1988; Groma, Ungár & Wilkens, 1989). Except for ρ^*, which equals $\hat{C}\rho = \hat{C}[\langle w_+(\boldsymbol{r})\rangle + \langle w_-(\boldsymbol{r})\rangle]$, these relations are complex and difficult to interpret. By making assumptions on the nature of the distribution functions, the interpretability of the parameters is greatly enhanced. For example, it can be assumed that the specimen has a dislocation-cell structure and that $w_{\pm}(\boldsymbol{r})$ and the internal stress have two different values: one in the case $\boldsymbol{r}$ is in the cell walls and another in the case $\boldsymbol{r}$ is in the cell interiors. Then, the parameters ρ, T, P_0 and P_1 can be interpreted in terms of the two dislocation densities and the two internal stresses (Ungár, Groma & Wilkens, 1989). As a second example of an interpretation of the parameters in Eq. (6), the meaning of the dislocation-density fluctuation parameter T is investigated if it is assumed that all distribution functions are position-independent, *i.e.* that the fluctuation in the dislocation density is completely accounted for by the two-particle distribution functions. The general expression for $T\rho^2 = T\rho^{*2}/\hat{C}^2$ reads (*cf.* Groma, Ungár & Wilkens, 1989):

$$T\rho^2 = \langle w_{++}(\boldsymbol{r},\boldsymbol{r})\rangle + \langle w_{--}(\boldsymbol{r},\boldsymbol{r})\rangle + \langle w_{+-}(\boldsymbol{r},\boldsymbol{r})\rangle + \langle w_{-+}(\boldsymbol{r},\boldsymbol{r})\rangle - [\langle w_+(\boldsymbol{r})\rangle + \langle w_-(\boldsymbol{r})\rangle]^2. \qquad (7)$$

Note that $-\rho^2 \leq T\rho^2 < \infty$ and that $T\rho^2 = 0$ for a completely random dislocation distribution. In the case of position-independent distribution functions, $w_+(\boldsymbol{r})$ and $w_-(\boldsymbol{r})$ are equal to a constant $w_{\pm}$ $(= \frac{1}{2}\rho)$. The functions $w_{++}(\boldsymbol{r},\boldsymbol{r})$, $w_{--}(\boldsymbol{r},\boldsymbol{r})$, $w_{+-}(\boldsymbol{r},\boldsymbol{r})$ and $w_{-+}(\boldsymbol{r},\boldsymbol{r})$ are also constants, further denoted as w_{++}, w_{--} and $w_{+-} = w_{-+}$, respectively, and they represent the chances of finding two dislocations of the indicated signs very close together. Now, T can be expressed as:

$$T = \frac{w_{++} + w_{--} + 2\,w_{+-}}{4\,w_{\pm}^2} - 1. \qquad (8)$$

---

[1] Instead of the product $T \times \rho^{*2}$, a quantity $\Delta\rho^{*2}$ was formerly used (Ungár, Groma & Wilkens, 1989), but since its value can be either positive or negative [cf. Eqs. (7) and (8)] the present notation is preferred.

Thus, in this view T indicates if two (positive or negative) dislocations are relatively more often ($T > 0$) or less often ($T < 0$) near to each other than in case of a completely random distribution ($T = 0$). The restrictedly random distribution is a special case of a distribution in which the dislocations are less often near to each other than in a random distribution; substituting Eq. (1) for $\boldsymbol{r}' = \boldsymbol{r}$ into Eq. (8) indeed yields a negative value $T = -1/N_p$.

III. ANALYSIS IN PRACTICE

A. Preparatory corrections

Experimentally determined line profiles always consist of diffracted intensity superimposed on background intensity, that is usually taken linear in 2θ. For single crystals the background is very low and it is often neglected; for polycrystalline specimens a correct subtraction of the background intensity is crucial for line-broadening analysis. A related problem is the selection of the range in 2θ to be measured and the range to be transformed into F_L. The range is too short if the tails of the diffraction-line profile are truncated significantly; as a result F_L is distorted systematically. On the other hand, if the range is very long, the relatively large counting statistical errors in the tails of the profile may produce spurious oscillations in F_L, especially visible at large L, and merely add "empty" F_L values.

A practical procedure for the selection of the 2θ range and background correction is the following[2]. A 2θ range is measured which is surely long enough or too long. Both tails of the profile are truncated at those 2θ positions beyond which no significant decrease in the measured intensity occurs (a logarithmic scale is useful). A straight line is fitted to, say, 20 to 40 data points on both ends of the range selected and this line is subtracted as background. In case of doubt, the line profile analysis may be performed using two or more different truncations and corresponding backgrounds. The thus corrected intensities are then interpolated to obtain intensities equidistant in reciprocal space, in a number appropriate for Fourier transformation and with the centre of gravity exactly in the middle.

Conventional powder diffractometers give rise to significant instrumental line broadening due to an imperfect diffraction geometry and the wavelength dispersion. The so-called double-crystal diffractometer eliminates this effect almost completely (Wilkens & Eckert, 1964). However, a double-crystal diffractometer is not always available and it is not (routinely) employable for specimens with grains $\lesssim 1$ µm and for reflections at large 2θ. Line profiles

---

[2] A more rigorous solution to the problem of truncation has been given by Vermeulen, Delhez, Keijser & Mittemeijer (1992).

recorded using a powder diffractometer should always be corrected for instrumental broadening, *e.g.* by means of Stokes deconvolution (Stokes, 1949). This correction requires the preparation of a standard specimen (Fawcett *et al.*, 1988; Berkum, Sprong, Keijser, Delhez & Sonneveld, 1994).

B. Parameter estimation

The most likely values of the parameters used in the dislocation models discussed in Sec. II are obtained by fitting the corresponding expressions to the experimentally obtained data. Least-squares fitting of N statistically independent data points involves minimization of

$$\chi^2 = \sum_{i=1}^{N} \frac{(y_i - \eta_i)^2}{\sigma_i^2}, \tag{10}$$

where y_i are the experimental data points, η_i the corresponding values of the fitting function and σ_i^2 the variances of y_i. If the fitting function has m adjustable parameters, the fit is good if $\chi^2 \approx (N{-}m)$ (*e.g.* Press, Flannery, Teukolsky & Vetterling, 1986). In the present case, the Fourier transform F_L is fitted, although the F_L values do not meet the requirement of being statistically independent. In principle, fitting intensities instead of F_L or incorporating covariances of the F_L values in χ^2 are more correct procedures, but both are extremely laborious. Due to the neglect of the covariances, χ^2 according to Eq. (10) may differ significantly from $N{-}m$ for statistically good fits. Nevertheless, it is assumed that χ^2 still has relative meaning, so that it can be used for parameter estimation and for comparing different fits to the same data.

The variances of the real and imaginary parts of F_L due to the counting statistical errors in the measured intensities and the estimated background have been derived by Wilson (1967) for the case that the errors are relatively small. The variances of $|F_L|$ and φ_L have been derived in the same way. If the (usually small) contributions of the uncertainties in the background slope (in case of $|F_L|$) and background level and slope (in case of φ_L) to $\sigma^2(|F_L|)$ and $\sigma^2(\varphi_L)$ are omitted, the variances read:

$$\sigma^2(|F_L|) = \frac{S + 2[S - 2\,S_n + q(S{-}S_n)]\,|F_L|^2 + S_n\,|F_{2L}|\cos(\varphi_{2L}{-}2\varphi_L)}{2\,S_n^2}, \tag{11a}$$

$$\sigma^2(\varphi_L) = \frac{S - S_n\,|F_{2L}|\cos(\varphi_{2L}{-}2\varphi_L)}{2\,S_n^2\,|F_L|^2}, \tag{11b}$$

where S and S_n are the number of counts in the peak before and after background subtraction, respectively, and q is the quotient of the number of intensities used to calculate F_L and the number used to estimate the background.

The expressions given for F_L are all valid only for small L, but the exact range of validity is not known in advance. Therefore, the following (rather laborious) procedure is proposed. Suppose F_L values are obtained with a step size ΔL in L. Then, the function is fitted to F_L repeatedly over different ranges $[\Delta L, L_{\mathrm{up}}]$, where $L_{\mathrm{up}} = m\Delta L$, $(m+1)\Delta L$, ... until L_{up} reaches the point where $|F_L|$ has decreased to about $\sigma(|F_L|)$. The parameter values and $\chi^2/(N-m)$ are saved as a function of L_{up}. From a plot of $\chi^2/(N-m)$ *versus* L_{up} the range of L_{up} in which relatively good fits are obtained is selected. Finally, the specimen is characterized by the average parameter values obtained in the "good" fits. Unfortunately, due to the bias of χ^2 (covariances of the data points ignored) reliable error estimates of the parameters are impossible.

Experimental data can be analysed using different dislocation models and corresponding fitting functions. The selection of the most suitable model depends on the accuracy of the experimental data and the nature of the specimen. Equation (6) require more accurate data than Eqs. (2) or (5), because of the larger number of adjustable parameters. On the other hand, specimens with uncommon dislocation arrangements may need the larger flexibility of Eq. (6) for a sufficient description of the measured data. For almost symmetrical line profiles, Eq. (6b) yields relatively large uncertainties of the parameters; restricting Eq. (6b) to the first term may provide more accurate estimates of P_0 and R_1. On fitting Eqs. (6a) and (6b) to the experimental data discussed in Sec. IV, it was experienced that R_2 and R_3 took similar values and that taking R_3 equal to R_2 did not give significantly worse fits. The same held for R_4 and R_5. Therefore, Eq. (6a) is used only with $R_3 = R_2$ and Eq. (6b) only with $R_5 = R_4$.

Additional remarks:

(i) The variance of $|F_L|$ is often fairly constant for all L, so that unweighted fitting yields about the same results.

(ii) If the measured line profile with Fourier transform F_L^H is deconvoluted with an instrumental profile with Fourier transform F_L^G to a profile with Fourier transform F_L^F, then $\sigma^2(F_L^F) \approx \sigma^2(F_L^H)/(F_L^G)^2$ (*cf.* Delhez, Keijser & Mittemeijer, 1980).

(iii) Fitting $\ln|F_L|$ instead of $|F_L|$ accelerates the procedure, because the exponential is avoided. In that case it is essential to use the correct standard deviations: $\sigma(\ln|F_L|) = \sigma(|F_L|)/|F_L|$.

(iv) All expressions for F_L in Sec. II.B are non-linear in L and can only be fitted using iterative fitting routines. For the smallest L values, Eqs. (2) and (5) can be linearized, since $f^*(x) \approx -\ln x + \frac{7}{4} - \ln 2$ and, consequently, $\ln|F_L|/L^2$ is linear in $\ln L$. In that case, (weighted) linear least-squares routines are applicable. The standard deviations can be calculated from Eq. (11a) using $\sigma(\ln|F_L|/L^2) = \sigma(|F_L|)/(|F_L|L^2)$.

IV. EXPERIMENTAL EXAMPLES

The procedures outlined in the previous section will be illustrated using three widely different sets of experimental data. The specimens considered are a tensile-deformed copper single crystal, a fatigued polycrystalline copper specimen and a ball-milled tungsten powder. The first two specimens were measured using a double-crystal diffractometer, the third one using a conventional powder diffractometer. The examples are in order of increasing structural ambiguity, *i.e.* the dislocation structures become less well-defined. Also, the accuracies of the measurements (counting statistics, peak-to-background ratios and instrumental broadening) decrease for the specimens in the order given.

A. Tensile-deformed copper single crystal

A copper single crystal was tensile deformed in the [001] direction up to the resolved shear stress $\hat{\tau} = 75.6$ MPa. From the bulk of the deformed crystal, a specimen was prepared with a plane surface perpendicular to the tensile axis ("axial case"). From this specimen, the (002) reflection was recorded using a double-crystal diffractometer with CuKα_1 radiation. The same specimen (not the same measurement) was used as an illustration previously (Ungár, Groma & Wilkens, 1989) and, together with other related specimens, discussed extensively in earlier papers (Ungár, Mughrabi, Rönnpagel & Wilkens, 1984; Ungár, Mughrabi & Wilkens, 1984).

The background intensity was removed according to the procedure described in Sec. III.A. Within the range of measurement, the tails of the line profile do not become completely horizontal. However, the measured intensity in the tails is more than 1000 times less than the top intensity, so the truncation error is very small. Due to the large asymmetry of the line profile, F_L in a plot of $\mathrm{Im}(F_L)$ *versus* $\mathrm{Re}(F_L)$ spins round the origin a number of times before it becomes indetermined. Therefore, φ_L calculated as $\arctan[\mathrm{Im}(F_L)/\mathrm{Re}(F_L)]$) is incorrect by a multiple of π above certain L values. Before fitting Eq. (6b), this effect has been eliminated.

The results of fitting Eq. (6a) to $|F_L|$ obtained for this measurement are shown in Fig. 1. The best fits are obtained for $80 < L_{\mathrm{up}} < 150$ nm. For $L > 150$ nm, $|F_L|$ becomes noisy (see Fig. 1a) and no better fits can be expected. The average parameter values obtained in the best fits are: $\rho^* = 0.51 \times 10^{15}$ m^{-2}, $R_{\mathrm{eff}} = 0.22$ µm, $T = 0.43$ and $R_2 = 0.12$ µm. The parameters change approximately 10 to 20% over the selected range of L_{up}. For a translation of ρ^* to ρ, see Ungár, Groma & Wilkens (1989). The positive value of T indicates that dislocations are relatively often near to each other, *i.e.* some clustering of the dislocations [see Eq. (8)]. This agrees with the dislocation-cell structure observed by transmission-electron-microscopy (TEM) for this specimen (Ungár, Mughrabi, Rönnpagel & Wilkens, 1984).

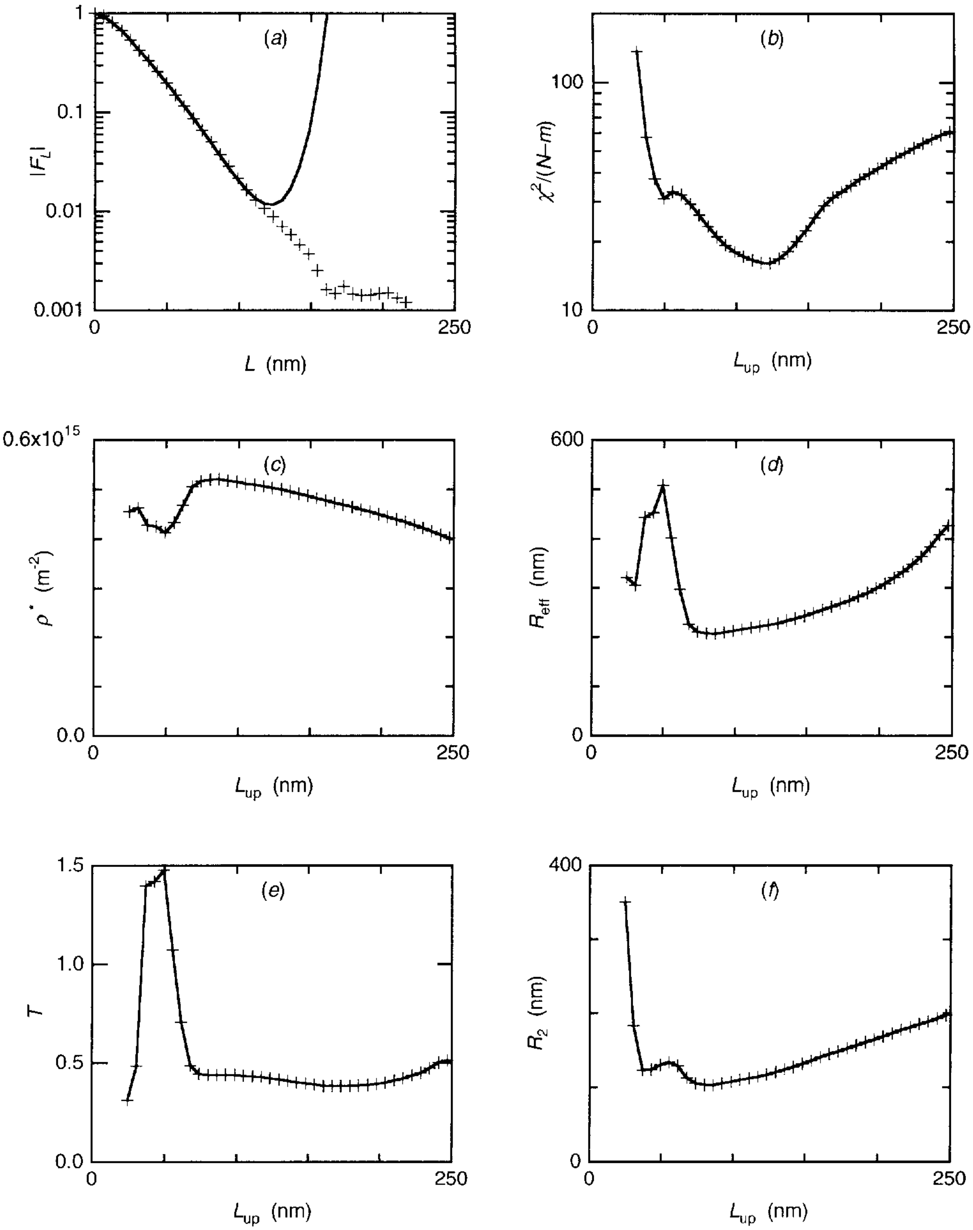

Fig. 1: Fitting Eq. (6a) to $|F_L|$ of the (002) reflection of a tensile-deformed [001] copper single crystal over different ranges $[\Delta L, L_{up}]$ in L (ΔL = 6.2 nm is the step size of the F_L values): (*a*) one of the fits (L_{up} = 117 nm) and (*b*) goodness-of-fit $\chi^2/(N-m)$, (*c*) dislocation density ρ^*, (*d*) first length parameter R_{eff}, (*e*) relative dislocation-density fluctuation T and (*f*) second length parameter R_2 ($R_3 = R_2$) as a function of L_{up}.

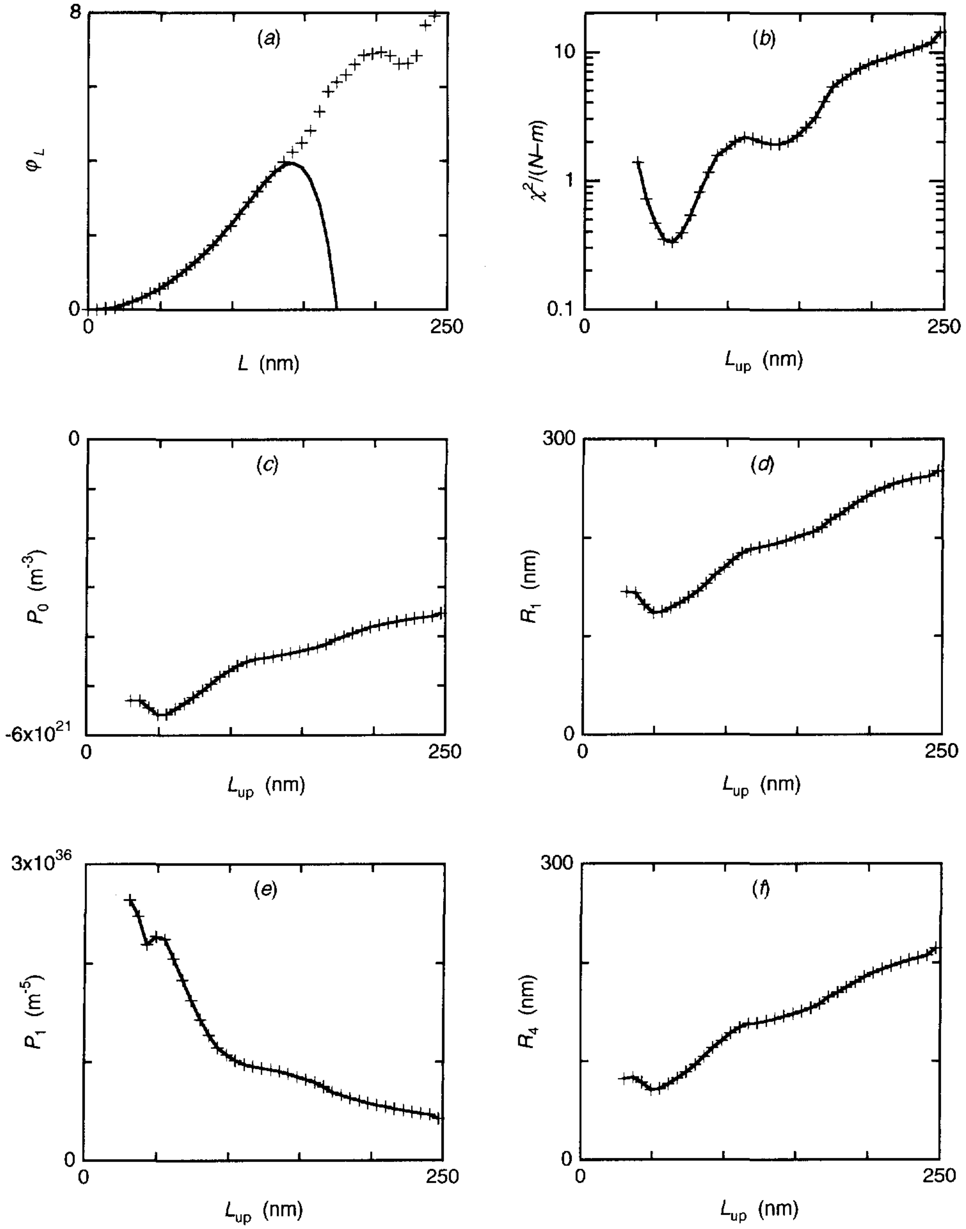

Fig. 2: Fitting Eq. (6b) to φ_L of the (002) reflection of a tensile-deformed [001] copper single crystal over different ranges $[\Delta L, L_{up}]$ in L (ΔL = 6.2 nm is the step size of the F_L values): (*a*) one of the fits (L_{up} = 136 nm) and (*b*) goodness-of-fit $\chi^2/(N-m)$, (*c*) dipole polarization P_0, (*d*) first length parameter R_1, (*e*) dipole-polarization fluctuation P_1 and (*f*) second length parameter R_4 ($R_5 = R_4$) as a function of L_{up}.

The dislocation structure of the specimen cannot be a perfect restrictedly random distribution, because the line broadening is asymmetric. Nevertheless, $\chi^2/(N-m)$ values obtained from fitting Eq. (5) to $|F_L|$ are not much larger than those in Fig. 1b. The corresponding parameters are $\rho^* = 0.61\times10^{15}$ m^{-2} and $R_e' = 0.045$ μm [the value $\frac{1}{2}$ $e^{7/4}$ $R_e' = 0.13$ μm can be compared with R_{eff}, see below Eq. (6)]. The difference between these results and those obtained from fitting Eq. (6a) is probably larger than the experimental error. Since $\chi^2/(N-m)$ is somewhat worse and the asymmetrical line broadening indicates a complex dislocation arrangement, the results obtained from fitting Eq. (5) are judged less reliable.

The argument φ_L has been fitted using Eq. (6b), see Fig. 2. The fits up to $L_{\mathrm{up}} = 150$ nm are selected as good fits (the fits for $L_{\mathrm{up}} \approx 60$ nm are judged as accidentally, not significantly better). The parameters obtained in these fits are $P_0 = -4.3$ to -5.6×10^{21} m^{-3}, $R_1 = 0.13$ to 0.20 μm, $P_1 = 0.9$ to 2.6×10^{36} m^{-5} and $R_4 = 0.07$ to 0.15 μm. A positive value for P_0 is in accordance with the sign of the internal stresses expected in the axial direction in a tensile-deformed specimen (see Ungár, Groma & Wilkens, 1989). The ratio $|P_0|/\rho^{*3/2} \approx 0.43$ is relatively high (*cf.* Sec. IV.B), indicating a significant dislocation-dipole polarization. This is not surprising for a uni-axially deformed single crystal.

In principle, the parameters ρ, T, P_0 and P_1 used here to characterize the dislocation structure can be translated to the parameters used in the composite model for dislocation-cell structures (see Ungár, Groma & Wilkens, 1989). Since dislocation cells have been observed in this specimen, this translation would be useful here. However, due to the uncertainties in the parameter estimates and the sensitivity of the translation to the relatively uncertain coefficients T and P_1, such a procedure is unreliable in the present case. The method of subdividing the measured profile into two symmetrical subprofiles (Ungár, Mughrabi, Rönnpagel & Wilkens, 1984), in spite of its additional assumption (cell walls and cell interiors diffracting incoherently), is probably more suitable to determine dislocation densities and internal stresses in cell walls and cell interiors. Of course, a characterization by means of ρ, T, P_0 and P_1 is more generally applicable.

B. Creep-deformed polycrystalline copper

The measurements discussed below are part of a series of measurements undertaken for the investigation of the internal stresses in subgrain structures formed after plastic deformation. The specimens concerned were short cylindrical rods of pure copper with average grain sizes of 68 μm, deformed by a constant uni-axial compressive stress without lubrication. Two specimens are considered here: (i) a specimen deformed at room temperature (298 K) and (ii) a specimen deformed in three steps at 298, 473 and 573 K. For more details on the specimen and its deformation procedure, see Borbély, Maier, Renner, Straub, Ungár & Blum (1993).

Copper {220} diffraction-line profiles were recorded using a double-crystal diffractometer. By means of movable slits placed in front of the specimen, reflections of individual grains were selected and measured. Here, reflections from lattice planes perpendicular to the direction of compression ("axial case") are considered. The selection of the 2θ range to be transformed and the background correction were performed according to the procedure described in Sec. III.A. The range of measurement was sufficient to avoid (perceptible) truncation errors. Due to the smaller grain sizes of these specimens, smaller peak intensities and larger background intensities ("peak-to-background ratio" $\approx$ 500) were obtained than in the case of the copper single crystal in Sec. IV.A. Consequently, $|F_L|$ becomes noisy at somewhat smaller values of L (*i.e.* larger values of $|F_L|$).

Fitting Eq. (6a) to $|F_L|$ yields $\rho^* = 0.53\times10^{15}$ m^{-2}, $R_{\text{eff}} = 0.15$ μm, $T \approx 0.9$ and $R_2 \approx 0.07$ μm after deformation at room temperature and $\rho^* = 0.56\times10^{15}$ m^{-2}, $R_{\text{eff}} = 0.18$ μm, $T \approx 1.1$ and $R_2 \approx 0.08$ μm after deformation at 573 K ($30 < L_{\text{up}} < 80$ nm). The uncertainties in the parameter values are again 10 to 20 %. The positive T value, implying significant clustering of dislocations, is consistent with the distinct dislocation-cell structures observed by means of TEM (see Borbély, Maier, Renner, Straub, Ungár & Blum, 1993). The TEM observations indicate dislocation cells with narrower cell walls than in the case of the copper single crystal (Ungár, Mughrabi, Rönnpagel & Wilkens, 1984), which agrees with the larger T value found here. The slight increase of T after deformation at 573 K with respect to deformation at room temperature is of the order of the experimental error. If it is a true increase, it indicates an increased clustering of the dislocations, which agrees with the sharpening of the dislocation-cell walls observed by TEM (Borbély, Maier, Renner, Straub, Ungár & Blum, 1993).

As expected, the asymmetry of line profiles of specimens deformed in compression is reversed with respect to the tensile-deformed specimen in Sec. IV.A: a reflection with a diffraction vector parallel to the deformation axis ("axial case") now yields a positive P_0, whereas reflections with diffraction vectors perpendicular to the deformation axis ("side case") yield negative P_0. For two "axial" measurements of two different grains in the specimen deformed at room temperature, an analysis of φ_L using only the first term of Eq. (6b) yields $P_0 = 3.7\times10^{21}$ m^{-3} and $R_1 = 130$ nm, and $P_0 = 1.7\times10^{21}$ m^{-3} and $R_1 = 210$ nm, respectively. The uncertainties of the parameter values are about 10 %, so that it can be concluded that the dislocation-dipole polarizations in different grains in the same specimen are significantly different. Including the second term of Eq. (6b) in the fitting does not improve the fits significantly. The asymmetries of the measurements after deformation at 573 K are too small to do a meaningful analysis using Eq. (6b). Apparently, the sharpening of the dislocation-cell walls after deformation at elevated temperatures is accompanied by a decrease in the dipole polarization.

The ratio $|P_0|/\rho^{*3/2}$ (0.30 and 0.14 for the two measurements after deformation at room temperature and even smaller after deformation at 573 K) indicates a smaller dislocation-dipole polarization than that obtained in the case of the tensile-deformed single crystal (0.43, see Sec. IV.A), although the macroscopic stress applied was uni-axial in both cases. A possible explanation is the fact that the local stresses in the present polycrystalline specimens are not completely uni-axial due to the forces the (elastically anisotropic) grains exert onto each other. This may also explain the observed differences in dipole polarization between grains in a single specimen.

In spite of the strong clustering of the dislocations, the restrictedly random distribution has also been used to interpret the measured line broadening. The results of fitting Eq. (5) are $\rho^* = 0.62\times10^{15}$ m^{-2} and $R_e' = 0.032$ μm ($\frac{1}{2}\,e^{7/4}\,R_e' = 0.092$ μm) after deformation at room temperature, and $\rho^* = 0.62\times10^{15}$ m^{-2} and $R_e' = 0.044$ μm ($\frac{1}{2}\,e^{7/4}\,R_e' = 0.13$ μm) after deformation at 573 K. Comparing results obtained by fitting Eq. (6a) and Eq. (5), here and in Sec. IV.A, it can be concluded that systematic differences exist, but that they decrease as the asymmetries of the line profiles decrease.

C. Ball-milled tungsten powder

A pure tungsten powder (> 99.5 mass%, Fluka Chemika) was severely plastically deformed by means of ball milling for 1 h using two balls in a horizontally moving vessel. The milling produced some smaller particle fragments. To reduce additional line broadening due to the finite sizes of these fragments, the milled powder was "washed" three times (washing was performed by suspending the powder in 2-propanol and removing the suspension from the sediment after 30 minutes). From scanning-electron-microscope observations, it was concluded that after this treatment nearly all particles are larger than 1 μm. Since the line broadening from the dislocations is large, the line broadening contribution of the finite size of the particles of the "washed" powder is very small. A diffractometer specimen was prepared by suspending a small amount of the "washed" powder once more in 2-propanol and now sedimenting it onto a flat single crystal substrate. A standard specimen of exactly the same geometry was prepared from an annealed Si powder to measure the instrumental broadening (Berkum, Sprong, Keijser, Delhez & Sonneveld, 1994). Both the silicon and the tungsten layer are almost fully transparent due to their open "coral-like" structure and their thinness ($\lesssim 20$ μm).

X-ray diffraction-line profiles were recorded on a Siemens D500 powder diffractometer using CuKα radiation. In addition to the procedures described in Sec. III.A., the α_2 component of the CuKα spectrum was removed from the line profiles according to Delhez & Mittemeijer (1975). To obtain Fourier coefficients of the instrumental line profile at the reciprocal space positions of the tungsten reflections, Fourier coefficients of the two nearest silicon reflections were interpolated. The measured tungsten profiles are broader than the measured instrumental profiles by a factor of 5 to 10 (widths at half height), so the applied correction for instrumental broadening is not very critical.

The elastic isotropy of tungsten, in combination with the all-sided deformations during ball milling, permits a direct comparison of the broadening of all reflections of tungsten. Thus, the derived dependence of the fitting functions on the length g of the diffraction vector can be checked: the same results should be obtained for all reflections if the fitting parameters are corrected for their g dependence. On fitting Eq. (5), a constant value of ρ^*/g^2 is to be expected, since $\hat{C} \propto g^2$ [see below Eq. (3)]. Secondly, since $R_e' \propto e^{K_v}$ [see below Eq. (5)] and $e^{K_v} \propto g$ [*cf.* Eq. (3)], a constant $R_e'g$ is to be expected.

Using CuKα radiation, eight reflections are available in principle, but the last three reflections are unsuitable for this check, because of their very low intensities ({222} and {400}), peak overlap ({321} and {400}) and truncation ({400}). This leaves five reflections to be used in the comparison. Unweighted fitting of Eq. (5) to $|F_L|$ was performed. This is justified as long as $F_L^G \approx 1$ [see (i) and (ii) at the end of Sec. III.B], which holds reasonably for the L ranges considered. The parameter estimates converge properly for increasing L_{up} (see Fig. 3). The average results for the five reflections (see Table I) are $\rho^*/g^2 = 0.46\times10^{-3}$ and $R_e'g = 25$ and the standard deviations are 16 and 20 %, respectively. The results agree sufficiently well to conclude that the g dependence of the fitting function is acceptable. Nevertheless, there is a small decreasing trend in ρ^*/g^2 and an increasing trend in $R_e'g$. The trend in ρ^*/g^2 may be due to truncation and background overestimation, since these effects

Table I: Dislocation density ρ^* and length parameter R_e', both corrected for their g dependence, for five different reflections $\{hkl\}$ of a ball-milled tungsten powder, obtained by repeatedly fitting Eq. (5) to $|F_L|$ according to the procedure described in Sec. III.B.

$\{hkl\}$	g (nm^{-1})	$\rho^*/g^2\times10^3$	$R_e'\,g$
110	4.47	0.58	21
200	6.32	0.47	23
211	7.74	0.52	21
220	8.94	0.36	29
310	9.99	0.38	28

usually increase with increasing g and they cause an underestimation of the broadening and, consequently, of ρ^*. The trend may also be due to a little finite-grain-size broadening to the measured line broadening (in spite of the precautions taken, see above), since then the broadening and therefore ρ^* is overestimated by an amount that decreases with increasing g. Thus, the small trends observed do not necessarily indicate a deficiency of the g dependence of the fitting function.

The ball milling has produced a very high dislocation density ($\rho \approx 10^{16}$ m^{-2}). Further, the value of $M' = R_e' \sqrt{\rho^*}$ is an indication of the true value of the dislocation-arrangement parameter M (Wilkens, 1970b). The present value $M' = 0.5$ is very small, indicating strong interactions

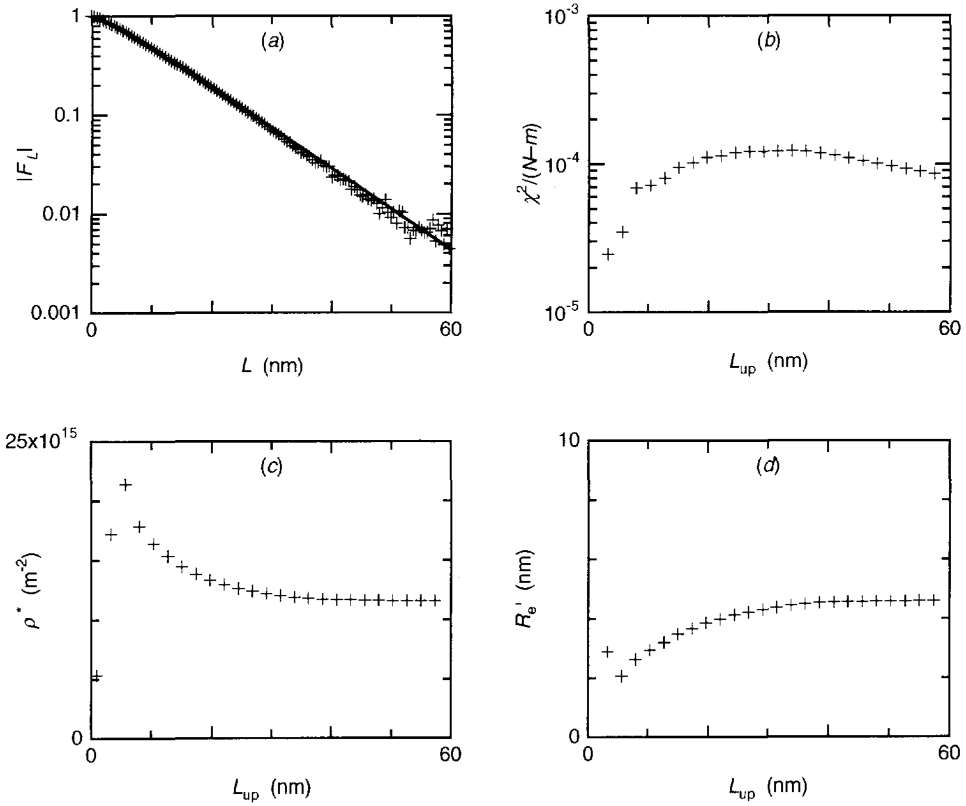

Fig. 3: Fitting Eq. (5) to $|F_L|$ of the {110} reflection of a ball-milled tungsten powder over different ranges $[\Delta L, L_{up}]$ in L ($\Delta L = 0.47$ nm is the step size of the F_L values): (*a*) fit for $L_{up} = 60$ nm and (*b*) goodness-of-fit $\chi^2/(N-m)$, (*c*) dislocation density ρ^* and (*d*) length parameter R_e' as a function of L_{up} (not all possible L_{up} have been included).

between the dislocations [see below Eq. (1)]. This is not surprising with such a high dislocation density: on distances of the order of 10 nm ($\approx 1/\sqrt{\rho}$) the forces between dislocations are very strong. The combination of a high dislocation density ($\rho \approx 10^{15}$ m^{-2}) and a strong interaction ($M \approx 0.5$ to 1) has also been observed for dislocation-cell walls (Ungár, Mughrabi, Rönnpagel & Wilkens, 1984). Therefore, the dislocation structure of the ball-milled tungsten powder may resemble the dislocation structure of dislocation-cell walls.

The asymmetries of the line profiles of the ball-milled tungsten powder after correction for instrumental broadening were negligible. Therefore, no attempt was made to interpret φ_L. No dislocation-dipole polarization is to be expected for these specimens, since in the deformation process all particles have been hit from several sides. Besides, each line profile originates from a large number of particles, so any polarization within the particles would probably be cancelled in the measurement. The small asymmetry is consistent with the restrictedly random distribution assumed in the interpretation.

V. CONCLUSIONS

A detailed interpretation of X-ray diffraction-line broadening induced by plastic deformation is possible using several methods currently available. A careful preparation of the experimental data and weighted fitting with special attention to the fitting range are essential for their application in practice. For high-resolution measurements with good counting statistics and peak-to-background ratios (*e.g.* taken from single crystals), the dislocation density, the dislocation-dipole polarization, and parameters characterizing their spatial fluctuations can be determined with uncertainties of the order of 10 to 20%. If the measurements do not meet these requirements or if the dislocation structure of the specimen can be described with fewer parameters (*e.g.* if the line broadening is symmetrical, *i.e.* the dipole polarization is negligible), the restrictedly random distribution can provide an adequate description of the experimental data. It includes the dislocation density and one parameter to characterize the dislocation arrangement. If the dipole polarization is small, analysis by means of the restrictedly random distribution or by means of a more general model yields comparable results.

The dislocation arrangements of a tensile-deformed copper single crystal and of a creep-deformed polycrystalline copper specimen are both characterized by clustering of dislocations and a more or less pronounced dipole polarization. They cannot be described by means of a restrictedly random distribution. The dislocation arrangement in a ball-milled tungsten powder is characterized by an extremely high dislocation density, strong repulsive dislocation interactions and no dipole polarization and can be described by a restrictedly random distribution.

ACKNOWLEDGEMENTS

The authors wish to thank Dr. J.I. Langford for providing the tungsten powder and Ir. A. Buis for providing scanning-electron-microscope facilities. Prof. E.J. Mittemeijer is thanked for critically reading the manuscript.

APPENDIX A: HIGHER-ORDER TERMS IN THE RESTRICTEDLY RANDOM DISTRIBUTION

In the derivation of F_L for the restrictedly random distribution [see Eq. (2)], terms of a higher order than L^2 have been neglected (Wilkens, 1970a). Below, it is shown that a small extension of the derivation adds a higher-order term that is very similar to the one obtained for arbitrary one- and two-particle distribution functions [see Eq. (6a)].

In Eq. (2.12) of Wilkens (1970a), ln F_L has been expressed as:

$$\ln F_L = \sum_{k=1}^{\infty} T_k. \tag{A.1}$$

The first term T_1 is given by Eq. (4.9) of Wilkens (1970a)[3]. From each term T_k for $k \geq 2$, the leading term $T^*_{k(1)}$ proves to be proportional to L^2. The sum $\sum T^*_{k(1)}$ for $k \geq 2$ is given by Eq. (5.9) of Wilkens (1970a). The derivation of Eq. (2) is based exclusively on the terms T_1 and $\sum T^*_{k(1)}$ for $k \geq 2$ in Eq. (A.1). The remainders $T_k - T^*_{k(1)}$ for $k \geq 2$ are proportional to L^4 or higher powers of L and they have been neglected in Eq. (2).

According to p. 1205 and Eq. (2.13b) of Wilkens (1970a), the remainder for $k \geq 2$ can be written as:

$$T_2 - T^*_{2(1)} = \frac{(2\pi g L)^4}{4!}\left[\langle e_L^4\rangle_{(2)} + \langle e_L^4\rangle_{(3)} - 3\langle e_L^2\rangle^2\right], \tag{A.2}$$

where $\langle e_L^2\rangle$ is given by Eq. (4.7) of Wilkens (1970a). It is argued that for sufficiently small L, $\langle e_L^4\rangle_{(2)}$ and $\langle e_L^4\rangle_{(3)}$ can be written as:

$$\langle e_L^4\rangle_{(2)} \approx 3\left(\frac{b}{2\pi}\right)^4 \pi^2 \rho^2 C^2 \left[f^{*2}(L') - f^*(L') + \frac{15}{16}\right], \tag{A.3}$$

$$\langle e_L^4\rangle_{(3)} \approx \frac{\langle e_L^4\rangle_{(2)}}{N_p} + \frac{3}{2N_p}\left(\frac{b}{2\pi}\right)^4 \pi^2 \rho^2 C^2 \left[f^*(L') - 2\ln 2 - \frac{\pi^2}{6} + \frac{1}{12}\right], \tag{A.4}$$

---

[3] Eq. (4.9) of Wilkens (1970a) contains an error: the right-hand side is the expression for $-T_1$ instead of T_1.

where $L' = \frac{1}{2} L \sin\psi / R_p$. Substitution of Eqs. (A.3) and (A.4) into Eq. (A.2) yields:

$$T_2 - T^*_{2(1)} = \tfrac{1}{2}\rho^{*2} L^4 \left[-f^*(L') + \tfrac{15}{16} + \tfrac{1}{N_p}\left(f^{*2}(L') - \tfrac{1}{2}f^*(L') + \tfrac{47}{48} - \tfrac{\pi^2}{12} - \ln 2\right)\right]. \tag{A.5}$$

where $\rho^* = \hat{C}\rho$ with $\hat{C} = \frac{1}{2}\pi\, C\, g^2 b^2$. Using Eq. (4a) for $f^*(x)$ in Eqs. (2) and (A.5), adding the two results for $\ln F_L$ [*cf.* Eq. (A.1)] and neglecting terms of higher order than L^4, yields the following expression for small L:

$$\ln F_L = -\rho^* L^2 \ln\frac{R_e''}{L} + \frac{1}{2N_p}\rho^{*2} L^4 \ln\frac{R_2'}{L}\ln\frac{R_3'}{L}, \tag{A.6}$$

where

$$R_e'' = \frac{e^{7/4} R_p}{e^{K_v} L \sin\psi}, \tag{A.7}$$

$$R_2' = \frac{R_p}{\sin\psi}\exp\left(\frac{N_p + 3 + N'}{2}\right), \tag{A.8}$$

$$R_3' = \frac{R_p}{\sin\psi}\exp\left(\frac{N_p + 3 - N'}{2}\right), \tag{A.9}$$

with

$$N'^2 = (N_p - \tfrac{1}{2})^2 - \frac{47}{12} + \frac{\pi^2}{3} + 4\ln 2 + \frac{\pi\sin^2\psi}{3\hat{C}}. \tag{A.10}$$

In the last term in the right-hand side of Eq. (A.10), that originates from T_1 and the term proportional to x^2 in $f^*(x)$, $N_p \approx \pi\rho R_p^2$ [see below Eq. (1)] has been substituted.

The remainders $T_k - T^*_{k(1)}$ for $k \geq 3$ are still neglected in Eq. (A.6). If they also contribute to the L^4 term of $\ln F_L$, they will alter the proportionality constant of this term and the constants R_2' and R_3', but the structure of this term (L and ρ^* dependences) is expected to remain unchanged.

Comparison of Eqs. (A.6) and (6a) shows that the structures of the terms up to the order of L^4 remains unchanged if a general dislocation arrangement is restricted to the restrictedly random distribution: only the constants R_{eff}, T, R_2 and R_3 are replaced by R_e'', N_p^{-1}, R_2' and R_3', respectively. All parameters in Eq. (A.6) can be related to two adjustable parameters ρ^* and R_p (note that $N_p \approx \pi\rho R_p^2$). In Sec. II.B it was argued that $T = -N_p^{-1}$ in case of a restrictedly random distribution, so that the coefficient of the L^4 term in Eq. (A.6) cannot be correct. This deviation is probably due to the approximations inherent in the Eqs. (A.3) and (A.4) and the neglect of the remainders $T_k - T^*_{k(1)}$ for $k \geq 3$. Nevertheless, the correspondence between the Eqs. (A.6) and (6a) (*e.g.* the two logarithmic factors, the ρ^* dependence) proves that a relatively simple dislocation-arrangement model already provides a reasonably detailed description of line broadening.

REFERENCES

Berkum, J.G.M. van, Delhez, R., Keijser, Th.H. de & Mittemeijer, E.J. (1994). To be published. See Chapter 8 of this thesis.

Berkum, J.G.M. van, Sprong, G.J.M., Keijser, Th.H. de, Delhez, R. & Sonneveld, E.J. (1994). To be published. See Chapter 1 of this thesis.

Berkum, J.G.M. van, Vermeulen, A.C., Delhez, R., Keijser, Th.H. de & Mittemeijer, E.J. (1994). *J. Appl. Cryst.* In the press. See Chapter 3 of this thesis.

Borbély, A., Maier, H.J., Renner, H., Straub, S., Ungár, T. & Blum, W. (1993). *Scripta Metall. Mater.* **29**, 7-12.

Delhez, R., Keijser, Th.H. de & Mittemeijer, E.J. (1980). In: *Accuracy in Powder Diffraction*, NBS Spec. Publ. 567, eds. Block, S. & Hubbard, C.R. (Washington: Dpt. of Commerce), pp. 213-253.

Delhez, R. & Mittemeijer, E.J. (1975). *J. Appl. Cryst.* **8**, 609-611.

Eastabrook, J.N. & Wilson, A.J.C. (1952). *Proc. Phys. Soc. London* **B65**, 67-75.

Fawcett, T.G., Crowder, C.E., Brownell, S.J., Zhang, Y., Hubbard, C., Schreiner, W., Hamill, G.P., Huang, T.C., Sabino, E., Langford, J.I., Hamilton, R. & Louër, D. (1988). *Powder Diffr.* **3**, 209-218.

Gaál, I. (1984). In: *Microstructural Characterization of Materials by Non-Microscopical Techniques*, eds. Hessel Andersen, N., Eldrup, M., Hansen, N., Juul Jensen, D., Leffers, T., Lilholt, H., Pedersen, O.B., Singh, B.N. (Roskilde, Denmark: Risø National Lab.), pp. 249-254.

Groma, I., Ungár, T. & Wilkens, M. (1988). *J. Appl. Cryst.* **21**, 47-53.

Groma, I., Ungár, T. & Wilkens, M. (1989). Unpublished paper.

Krivoglaz, M.A. & Ryaboshapka, K.P. (1963). *Phys. Met. Metall.* **15**, 14-26.

Krivoglaz, M.A., Martynenko, O.V. & Ryaboshapka, K.P. (1983). *Phys. Met. Metall.* **55**, 1-12.

Press, W.H., Flannery, B.P., Teukolsky, S.A. & Vetterling, W.T. (1986). *Numerical Recipes. The Art of Scientific Computing* (Cambridge: Cambridge University Press), Chap. 14.

Stokes, A.R. (1948). *Proc. Phys. Soc. London* **61**, 382-391.

Ungár, T., Groma, I. & Wilkens, M. (1989). *J. Appl. Cryst.* **22**, 26-34.

Ungár, T., Mughrabi, H., Rönnpagel, D. & Wilkens, M. (1984). *Acta Metall.* **32**, 333-342.

Ungár, T., Mughrabi, H. & Wilkens, M. (1984). In: *Microstructural Characterization of Materials by Non-Microscopical Techniques*, eds. Hessel Andersen, N., Eldrup, M., Hansen, N., Juul Jensen, D., Leffers, T., Lilholt, H., Pedersen, O.B., Singh, B.N. (Roskilde, Denmark: Risø National Lab.), pp. 539-544.

Vermeulen, A.C., Delhez, R., Keijser, Th.H. de & Mittemeijer, E.J. (1992). *J. Appl. Phys.* **71**, 5303-5309.

Warren, B.E. (1959). *Prog. in Metal Phys.* **VIII**, 147-202.

Warren, B.E. & Averbach, B.L. (1952). *J. Appl. Phys.* **23**, 497.

Wilkens, M. (1969). *Acta Metall.* **17**, 1155-1159 (in German).

Wilkens, M. (1970). In: *Fundamental Aspects of Dislocation Theory*, NBS Spec. Publ. 317, vol. II, eds. Simmons, J.A., Wit, R. de & Bullough, R. (Washington: US Dpt. of Commerce), pp. 1195-1221.

Wilkens, M. (1970b). *Phys. stat. sol. (a)* **2**, 359-370.

Wilkens, M. (1979). *J. Appl. Cryst.* **12**, 119-125.

Wilkens, M. (1984). In: *Microstructural Characterization of Materials by Non-Microscopical Techniques*, eds. Hessel Andersen, N., Eldrup, M., Hansen, N., Juul Jensen, D., Leffers, T., Lilholt, H., Pedersen, O.B., Singh, B.N. (Roskilde, Denmark: Risø National Lab.), pp. 153-168.

Wilkens, M. (1987). *Phys. stat. sol. (a)* **104**, K1-K6.

Wilkens, M. & Eckert, K. (1964) *Z. Naturforschg.* **19a**, 459-470.

Wilkens, M., Herz, K. & Mughrabi, H. (1980). *Z. Metallkde.* **71**, 376-384.

CHAPTER 5

CHARACTERIZATION OF DEFORMATION FIELDS AROUND MISFITTING INCLUSIONS IN SOLIDS BY MEANS OF DIFFRACTION-LINE BROADENING

J.G.M. VAN BERKUM, R. DELHEZ, TH.H. DE KEIJSER, AND E.J. MITTEMEIJER
Laboratory of Materials Science, Delft University of Technology,
Rotterdamseweg 137, 2628 AL Delft, The Netherlands

ABSTRACT

Variations in the local elastic distortions in crystalline solids, induced by finely dispersed misfitting inclusions, cause (X-ray) diffraction-line broadening. They can be analysed by modelling the specimen under study and matching the accordingly simulated diffraction profiles to measured ones. The non-uniform strains in the matrix are described by a theory due to Eshelby. As an example, specimens composed of silicon precipitates in an aluminium matrix are used. The simulations using the model offer the possibility for a quantitative analysis of the misfit and the stored elastic energy and predict characteristics of line profiles which are also observed experimentally: asymmetry of the profile increasing with the volume fraction of inclusions and an unusual behaviour of the mean squared strain $\langle e_L^2 \rangle$ as a function of the correlation distance L.

I. INTRODUCTION

Two-phase materials consisting of a dispersion of fine particles in a matrix are commonly applied in practice. Examples of practical and scientific interest are precipitation-hardened aluminium alloys and particle-reinforced metal-matrix composites. The difference in the thermal-expansion coefficients of the matrix and the particles results in a difference in shrinkage on cooling to room temperature. The associated volume misfit and the accompanying elastic distortion of (at least) the matrix may play a crucial role in the properties of the two-phase material.

The equivalent inclusion method, developed by Eshelby, provides a detailed description of the deformation field in a two-phase assembly (Eshelby, 1956; Withers, Stobbs & Pedersen, 1989). The average stress or strain predicted by this method can be tested experimentally. Measurement of the average lattice parameter by X-ray or neutron diffraction suits this purpose and has been applied to precipitating alloys (*e.g.* Mittemeijer, Mourik & Keijser, 1981) as well as to metal-matrix composites (*e.g.* Withers, Juul Jensen, Lilholt & Stobbs, 1987; Ledbetter & Austin, 1987). Alternative techniques include measurement of yield stress (Arsenault & Taya, 1987), Young's modulus, thermal expansion coefficient or Bauschinger effect (Withers, Stobbs & Pedersen, 1989).

Diffraction-line broadening is a phenomenon that is sensitive to variations in the local elastic strain within the matrix and the inclusion and therefore it is of great value as an additional, independent source of information. It has already been used for a comparative investigation of the integral breadths of aluminium-silicon alloys of different compositions (Mourik, Keijser, Pers & Mittemeijer, 1988; Berkum, Delhez, Keijser, Mittemeijer & Mourik, 1991). In the present paper, experimentally observed line broadening is interpreted on an absolute scale. In this first attempt, a necessarily simple model of the specimens is used for line-profile simulations: spherical inclusions in spherical crystallites, elastic isotropy, no plastic accommodation of the misfit and no interaction of stress fields of neighbouring inclusions.

II. DIFFRACTION-LINE BROADENING

Broadening of (X-ray) diffraction-line profiles is caused by non-ideal optics of the instrument, wavelength dispersion and structural imperfections of the specimen. The non-instrumental, structural line broadening from polycrystalline samples is often divided in size broadening and strain broadening. Size broadening is caused by a finite size of the crystallites (or coherently scattering domains). Strain broadening is due to varying displacements of the atoms with respect to their reference lattice positions.

Structurally broadened line profiles can be characterized by breadth measures, which can be interpreted in terms of size and strain (Keijser, Langford, Mittemeijer & Vogels, 1982). In the more rigorous methods of analysis, the intensity distribution is expressed as a Fourier series:

$$P(h_3) = K \sum_{n=-\infty}^{+\infty} A(n,l) \cos 2\pi n h_3 + B(n,l) \sin 2\pi n h_3, \qquad (1)$$

where K is (approximately) constant over h_3, n is the harmonic number, l is the order of reflection, A and B are the cosine and sine Fourier coefficients, and h_3 is the length of the diffraction vector in reciprocal space in units $1/|\boldsymbol{a}_3|$, where $|\boldsymbol{a}_3|$ is the length of a unit cell in the direction of the diffraction vector. The relation between h_3 and the diffraction angle 2θ is:

$$h_3 = \frac{2\,|\boldsymbol{a}_3|\sin\theta}{\lambda}, \tag{2}$$

where λ is the wavelength.

According to a well-known concept in the kinematical diffraction theory, crystallites can be taken to consist of independently diffracting columns of unit cells, perpendicular to the diffracting lattice planes (Bertaut, 1949). In practice, the influence of the position of the columns with respect to each other on the intensity distribution is not significant and is ignored. Then, if both size and strain broadening occur, the Fourier coefficients A and B are given by (Warren, 1969):

$$A(n,l) = \frac{N_n}{N}\,\langle\cos 2\pi l Z_n\rangle, \tag{3}$$

$$B(n,l) = -\,\frac{N_n}{N}\,\langle\sin 2\pi l Z_n\rangle, \tag{4}$$

where N_n is the number of n-pairs in the sample (an n-pair denotes two unit cells in the same column, n cells apart), N is the total number of unit cells in the sample, and Z_n is the difference of the displacements in the direction of the diffraction vector of the two unit cells of the n-pair considered: $Z_n = n \times e_n$, where e_n is the average value of the strain between the two cells of the n-pair (in what follows, beside e_n also e_L is used for the strain over the distance L, where $L = n \times |\boldsymbol{a}_3|$). The brackets $\langle\ \rangle$ mean averaging over all n-pairs in the sample.

For the interpretation of measured line broadening, Eqs. (3) and (4) cannot be used directly. Many suggestions for approximations exist (for a review see Delhez, Keijser & Mittemeijer, 1982). In the Warren-Averbach analysis (Warren & Averbach, 1950, 1952), the logarithm of the cosine term in Eq. (3) is approximated (truncation of Taylor expansion) and the structure parameters obtained by this analysis are the average column length $\langle N_3\rangle$ and mean squared strains $\langle e_n^2\rangle$. These parameters are not compatible with parameters used in the common models of the imperfect solid state, like dislocation density, misfit, concentration gradients, *etc.*

Criticism on the Warren-Averbach analysis (*e.g.* Wilkens & Hartmann, 1963; Wilkens, 1979; Ryaboshapka, 1981) has concerned the justification of the truncation of the series expansion of the logarithm of the cosine term and the physical significance of the parameter $\langle N_3\rangle$. As an alternative, if it is assumed that size broadening is negligible, N_n/N can be replaced by 1 in Eqs. (3) and (4). The then resulting averaged cosine and sine terms can be further elaborated for the case of broadening by specific configurations of dislocations in cold-worked single crystals (for a brief survey see Wilkens, 1988). In the cases where it applies, this approach provides directly interpretable structure parameters.

In this paper, a method is suggested that avoids approximate elaborations of Eqs. (3) and (4). Here, complete line profiles are simulated, using Eqs. (1) to (4), for comparison with measured ones. To calculate N_n and Z_n in Eqs. (3) and (4), a model is designed that represents the microstructure of the specimen under investigation as closely as possible. In this way, the relation between characteristics of the line profiles and the physical input parameters can be studied in a straightforward manner. Examples of such characteristics are integral breadth and asymmetry of the profile. Moreover, the behaviour of the frequently published $\langle e_L^2 \rangle$ curve can now be analysed on the basis of the model calculations.

III. MODEL

The method of simulating line profiles is applied to matrix reflections of specimens containing finely dispersed misfitting particles in elastically distorted matrix crystallites. In this paper, it is

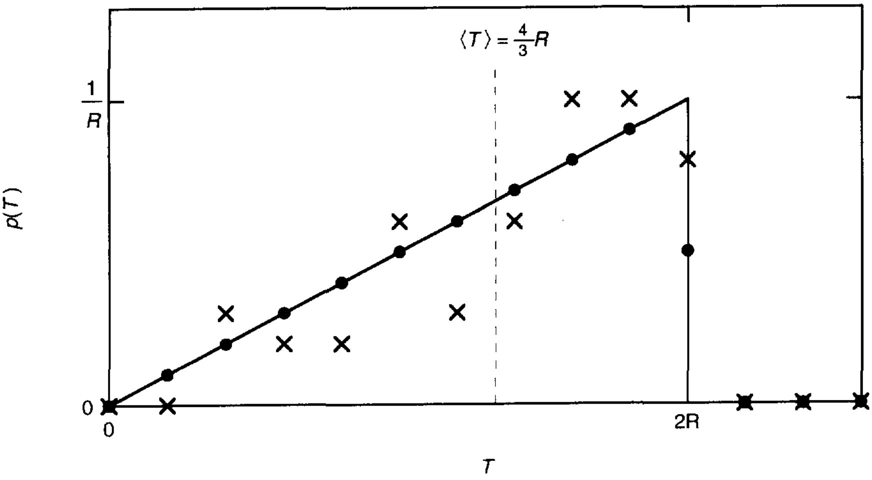

Fig. 1: Column-length distribution $p(T)$ for a sphere of radius R divided in infinitesimally narrow columns (full line, see App. A); one particular division in real columns of specific lateral dimensions (x) and the average of all possible divisions in real columns of the same lateral dimensions (●).

assumed that all crystallites are spherical and of the same size. According to the kinematical diffraction theory, size broadening is solely determined by the column-length distribution $p(N_3)$, giving the fraction of columns with length $T = N_3|\boldsymbol{a}_3|$. The column-length distribution of a sphere divided into columns of infinitesimally small cross section is shown by the full line in Fig. 1 (see App. A). A collection of columns of *finite* cross section can only approximate a spherical crystallite (as long as each column is composed of a whole number of unit cells). There is an infinite number of distributions of columns of identical cross section all approximating the same smooth sphere. One example of such a (necessarily discrete) distribution is shown by the crosses in Fig. 1. The *average* shape obtained from all nearly spherical crystallites corresponding to these column-length distributions is a smooth sphere and the *average* column-length distribution is represented by the collection of data points on the full line given in Fig. 1 (dots). In the simulations, the last distribution will be used. The values of N_n [see below Eq. (4)] are obtained from the column-length distribution by using:

$$N_n = \sum_{N_3 = |n|}^{\infty} (N_3 - |n|)\, p(N_3). \tag{5}$$

Now, a misfitting particle is introduced in the centre of a crystallite in two steps (see Fig. 2). Firstly, a cavity of radius ρ_0^A is created by removing some material from the centre of the crystallite. Thus, the central and therefore longest columns of the crystallite miss one or more unit cells. The influence of these missing cells on the size broadening can be accounted for by omitting those n-pairs from N_n of which the upper or lower cell is located in the cavity.

In the second step, the particle of radius ρ_0^B is inserted into the cavity and glued to the matrix. The linear-misfit parameter is defined as $\varepsilon = (\rho_0^B - \rho_0^A)/\rho_0^A$. The assembly thus formed is

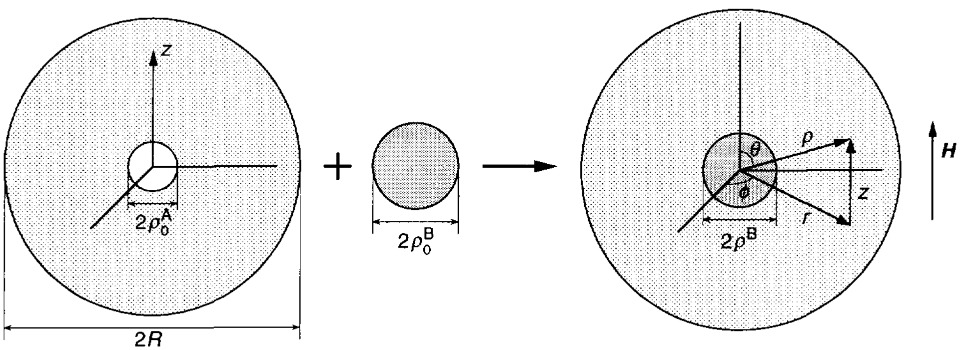

Fig. 2: Matrix and inclusion are assembled and allowed to relax. The cylindrical and the polar coordinate systems are defined with respect to the direction of the diffraction vector ***H***.

allowed to relax in order to minimize its mechanical strain energy and an equilibrium state of stress is developed. Interaction of stress fields of neighbouring crystallites is neglected. It is assumed that deformations and the interaction of the particle and the matrix are purely elastic. Then, application of elasticity theory shows that in an *infinite*, continuous and isotropic matrix the radial and tangential elastic strain components fall off with respect to the centre of the crystallite as ρ^{-3}, ρ being the distance to the centre (see Fig. 2). Eshelby (1956) has developed a theory to describe the elastic distortions brought about by point defects in a *finite* matrix. For the case considered here, the finiteness of the matrix induces a uniform dilatation of the spherical matrix, superimposed on the non-uniform strains corresponding to the infinitely large specimen. Eshelby's theory for a point defect is adopted here for the case of a misfitting inclusion, composed of a number of atoms. The theory is probably even more suited to the latter case, since then ignoring electronic interaction is justified.

In App. B, it is derived that atoms in a unit cell at a height z' above the equatorial plane ($z = 0$, see Fig. B1) in a column of length T are subjected to an average displacement $\langle f \rangle_{T,z'}$ with respect to the equatorial plane in the direction of the diffraction vector. The average strain e_n between two unit cells, a distance of n unit-cell dimensions apart, in a column of length T is given by:

$$e_n = \frac{1}{n}\{\langle f \rangle_{T,z'} - \langle f \rangle_{T,z'-n|a_3|}\}. \tag{6}$$

Using Eqs. (5), (6), (A.4) and (B.8), N_n and e_n can be calculated and substituted into Eqs. (3) and (4).

IV. EXPERIMENTS AND SIMULATION

A. Experiments

The model described in the previous section has been applied to the case of two-phase aluminium-silicon alloys. In the past, ribbons of AlSi alloys with five different compositions (2.0, 3.6, 5.1, 10.4 and 16.1 wt.% of Si, corresponding to 2.3, 4.2, 5.9, 11.9 and 18.2 vol.% of Si after precipitation) were prepared by the melt-spinning technique (Delhez, Keijser, Mittemeijer, Mourik, Pers, Katgerman & Zalm, 1982). The specimens were then annealed at 447 K for 1841 h to obtain complete precipitation of silicon. Subsequent cooling to room temperature induces strains due to the large difference between the thermal-expansion coefficients of the aluminium matrix and the silicon precipitates. The specimens were stored (*i.e.* aged) for 0.5 to 12 days at room temperature between annealing and measurement. Meltspun ribbons of pure aluminium, that were subjected to an identical heat treatment as the specimens under investigation, were used for a standard specimen. The aluminium matrix {400} reflections were recorded on a Siemens D500 diffractometer using CuKα-radiation. The {400} reflection was selected, because it does not suffer from serious overlap with silicon precipitate reflections.

The diffractometer specimens are composed of ribbons having varying thicknesses, causing small, unpredictable specimen displacements in the diffractometer. Due to these specimen displacements, the positions of the centroids of the experimental profiles do not yield accurate values for the average matrix lattice parameter a. Therefore, the dilatation of the matrix predicted by Eq. (B.4) [causing a lattice-parameter change $\Delta a/a = e_U$, see Eq. (B4)] cannot be investigated accurately using these specimens[1].

B. Simulations

The values of the input parameters for the aluminium {400} line-profile simulations, pertaining to the specimens discussed above, were taken as follows.

Unfortunately, the dimension of the unit cell in the direction of the diffraction vector cannot be equal to the interplanar spacing, since then the computation time is too large due to the enormous number of unit cells. Hence, a larger unit-cell dimension is adopted. It is realized that the inaccuracy caused by approximating the "true" displacement field by its average value over the unit-cell volume (see App. B) increases as the cell is enlarged (especially in the neighbourhood of the inclusion). Here, a suitable value for the unit-cell dimension appears to be 15 times the interplanar spacing: $|a_3| = 15\times0.1012 = 1.518$ nm.

The average radius of the silicon precipitates (ρ^B) was determined from X-ray diffraction line-breadth measurements. The sizes determined from different reflections and from specimens of different compositions, simply using the Scherrer equation, are remarkably constant (Mittemeijer, Mourik & Keijser, 1981). This suggests that the precipitates are approximately spheres of the same average size for all compositions[2] (the size mentioned is an underestimation of the true size, because a possible broadening by non-uniform strains in the precipitate was ignored). In a subsequent series of measurements, size and strain broadening were separated according to the single-line Voigt analysis (Keijser, Langford, Mittemeijer & Vogels, 1982) and the precipitate size was obtained as a function of annealing time at 445 K (Fig. 8 in Mourik, Mittemeijer & Keijser, 1983). Extrapolation to the annealing time of 1841 h

---

[1] For this reason, in order to determine precise lattice-parameter values for such specimens, a Debye-Scherrer camera technique was used and a Nelson-Riley extrapolation applied (Mittemeijer, Mourik & Keijser, 1981).

[2] TEM investigations support this (Rooyen & Mittemeijer, 1989; Agarwal, Koczak & Herman, 1973).

yields an average size parameter of 60 to 70 nm for the specimens under study. Since this is a volume-averaged column length (Delhez, Keijser & Mittemeijer, 1982) and the precipitate is taken spherical (see above), the radius is $\frac{2}{3}$ times the estimated size parameter. Thus, in all simulations the silicon precipitate radius is kept at 45.5 nm (which equals 30 unit cells).

The radius R of the aluminium matrix crystallites in the model follows directly from the precipitate radius and the volume fraction of silicon precipitates y_B, since $y_B = (\rho^B)^3/R^3$. Hence, the average matrix radius in the simulations ranges from 80 nm for specimens containing 18.2 vol.% of Si to 160 nm for specimens containing 2.3 vol.% of Si. From X-ray diffraction experiments on these alloys, it followed that the matrix-crystallite size parameter ($= \frac{3}{2} R$ for spheres) is of the order of 200 nm or more (Delhez, Keijser, Mittemeijer, Mourik, Pers, Katgerman & Zalm, 1982), which complies with the above values.

The values of the elastic constants of aluminium and silicon are obtained from the literature (Smithells, 1976) using the relations for isotropic crystals $\mu = s_{44}{}^{-1}$ and $K = (3s_{11} + 6s_{12})^{-1}$ with s_{ij} as the elastic compliance, yielding $C = 0.73$ and $C' = 0.34$ [see Eqs. (B.2) and (B.4)]. In principle, anisotropy of the matrix or the inclusion modifies the displacement field and has to be taken into account. For aluminium, however, the value of μ in any particular direction does not deviate more than 5 % from the average value, corresponding with a deviation of only 2 % in C at the most. Therefore, it is assumed that the effect of anisotropy can be ignored.

All model parameters are available now, except for the misfit parameter ε. For the misfit, an arbitrary starting value is chosen, which is adjusted until satisfactory agreement is obtained between measured and simulated line profiles. Using Eqs. (5), (6), (A.4), and (B.8), with the values for C, C', R and ρ^B [taking ρ^B for ρ_0^A in Eq. (B.8)] indicated above and the starting value for ε, the parameters N_n and e_n can be calculated. Then, by substitution into Eqs. (3) and (4), the Fourier coefficients of the structural profile can be obtained and by an inverse Fourier transformation the structural profile itself.

A measured profile (h profile) can be conceived as the convolution of a structural profile (f profile) with an instrumental profile (g profile, depending on diffractometer setting, wavelength distribution and specimen characteristics like absorption, flatness, displacement, *etc.*). A measured profile of the standard specimen is taken as the instrumental profile. A simulated h profile is obtained by convolution of the simulated f profile with the measured g profile. This convolution is carried out by multiplication of the Fourier coefficients. In general, the 2θ position of the centroid of a simulated profile does not correspond exactly with that of a measured profile due to specimen displacement (see Sec. IV.A). For easier comparison, the simulated profiles have been shifted such that their centroids coincide with those of the measured profiles.

V. RESULTS AND DISCUSSION

A. Misfit Parameter

Since the thermal history of the specimens studied is (very closely) the same, a single value of the misfit parameter ε is expected to hold for all specimens, notwithstanding their different amounts of inclusions (see Sec. IV.A). This proved to be the case: a satisfactory agreement between measured and simulated *h* profiles for all alloys was obtained with $\varepsilon = 2.3\times10^{-3}$. As an illustration, in Fig. 3 the experimental and, using $\varepsilon = 2.3\times10^{-3}$, simulated Al {400} *h* profiles for the Al 4.2 vol.% Si and the Al 11.9 vol.% Si alloys are shown, together with the measured instrumental *g* profile.

It follows from Fig. 3b that the simulation for the Al 4.2 vol.% Si alloy is nearly perfect: only at the high-angle side the sloping is somewhat too gentle. The small ripples in the tails are due to the ripples in the tails of the experimentally determined *g* profile (this was convoluted with the simulated *f* profile to obtain the *h* profile). The simulation for the Al 11.9 vol.% Si alloy (Fig. 3c) deviates somewhat more from the experiment: although the centroids are forced to coincide (see end of Sec. IV.B), the peak positions of the simulated α_1 and α_2 components do not correspond exactly with the experimental ones. The overall impression is that the simulated profile, as compared to the experimental one, is pushed to the low-angle side near the top and to the high-angle side near the bottom. The simulated profile is more asymmetric than the experimental one (for discussion, see Sec. V.B).

For the present experimental *h* profiles, the instrumental broadening is of the order of the structural broadening. Hence, a more critical test for the validity of the strain model proposed involves comparison of simulated and experimental *structural* broadening. Then, deconvolution of the measured *h* profile with the *g* profile is required. Deconvolution is established by dividing the (complex) Fourier coefficients of the measured *h* profile by the corresponding ones of the *g* profile. The Fourier coefficients of the experimental *f* profile, obtained by division, are only accurate up to a certain harmonic number (Delhez, Keijser & Mittemeijer, 1980). Unfortunately, a sufficiently accurate reconstruction of the (deconvoluted) experimental *f* profile by subsequent inverse transformation is not possible due to the noise in the signals and the relatively limited amount of structural broadening (see above). Therefore, in Fig. 4, Fourier coefficients of the simulated and measured *f* profiles are compared. As indicated, the higher harmonics exhibit pronounced scatter due to the noise in the measured signals and, moreover, humps and jumps occur that do not represent structural broadening but are very probably due to differences in ribbon thickness, transparency, flatness, *etc.* between the specimens to be investigated (containing Si) and the standard specimen (without Si). Also, in correspondence

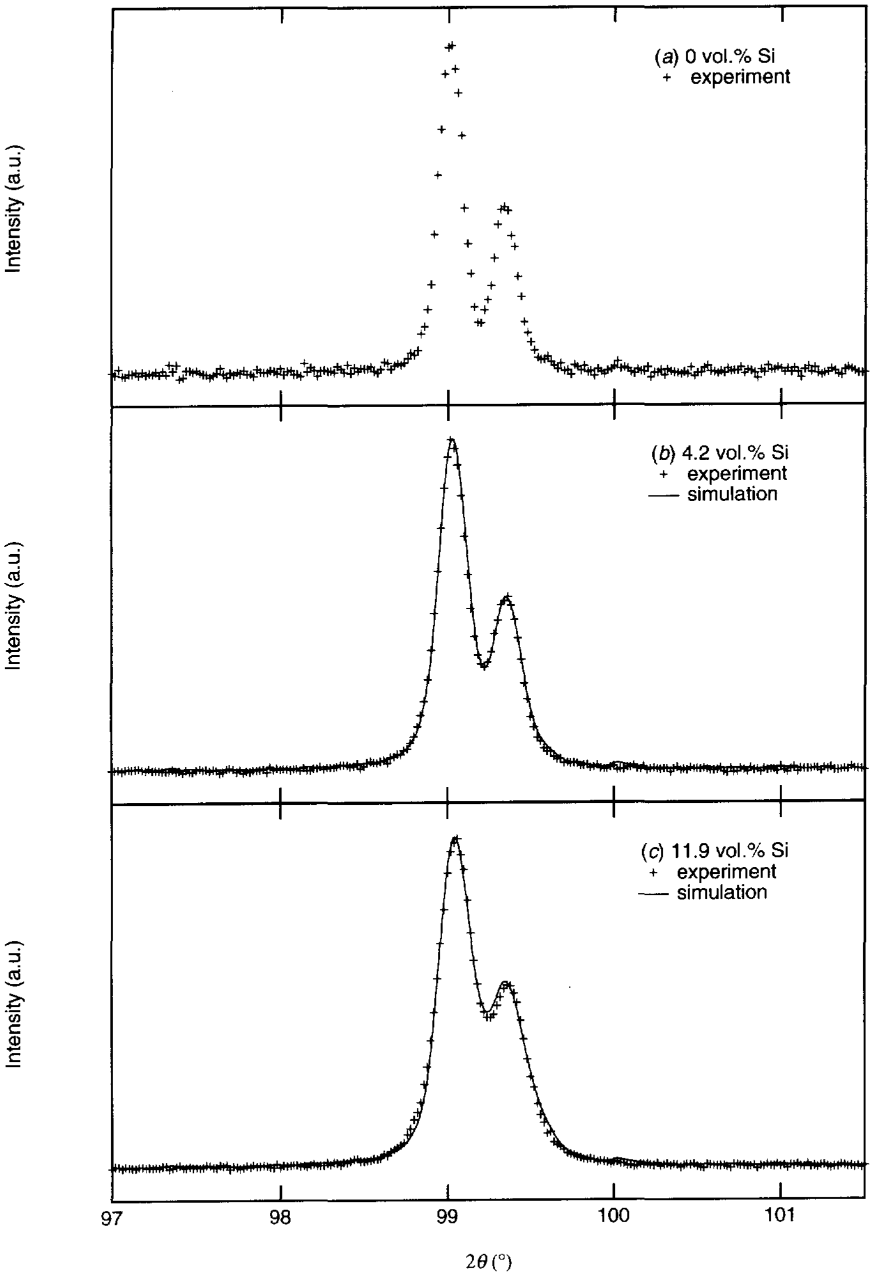

Fig. 3: Experimental CuKα Al {400} *h* profiles for (*a*) the standard specimen, (*b*) the Al 4.2 vol.% Si alloy and (*c*) the Al 11.9 vol.% Si alloy, together with two simulated *h* profiles, using $\varepsilon = 2.3 \times 10^{-3}$.

with the above discussion of Fig. 3c, the simulated sine coefficients, representing the line-profile asymmetry, show a systematic difference with the experimental ones for the Al 11.9 vol.% Si alloy (Fig. 4b; see further Sec. V.B). Despite these effects, it is concluded that on the whole there is agreement between simulation and experiment.

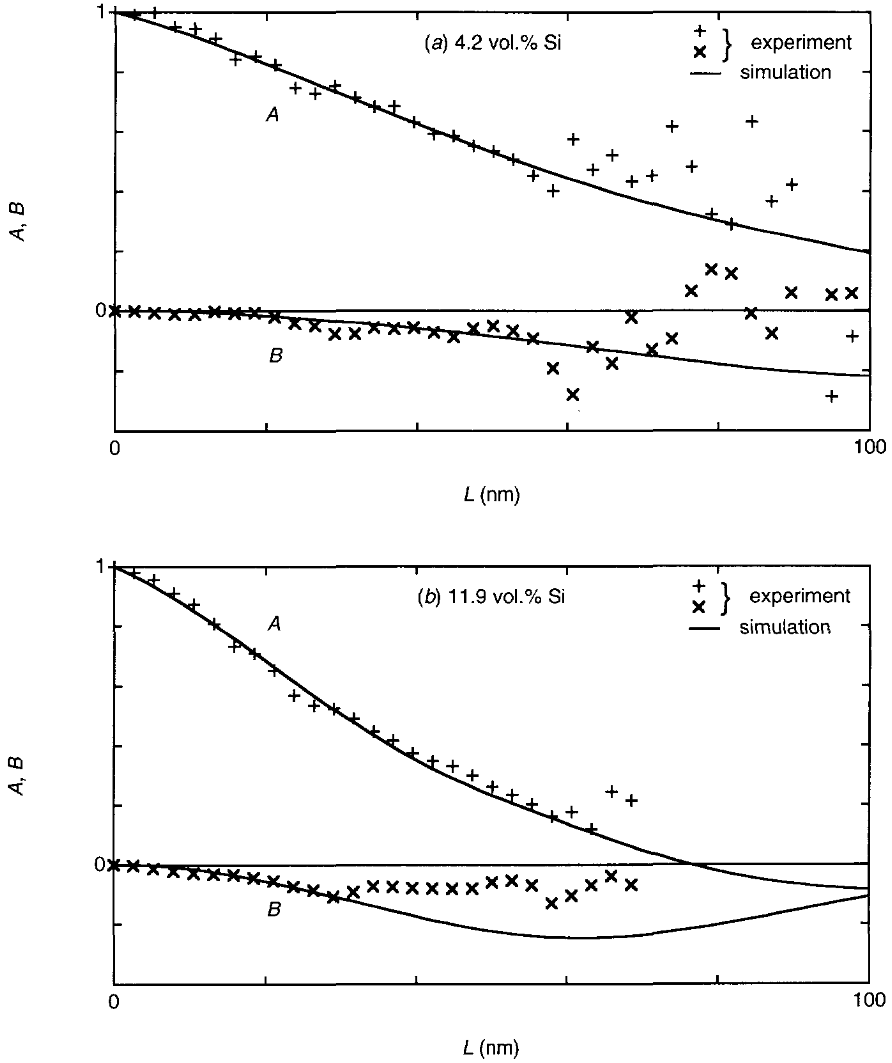

Fig. 4: Fourier coefficients A and B of experimental and simulated (ε = 2.3×10^{-3}) *structural f* profiles for (*a*) the Al 4.2 vol.% Si and (*b*) the Al 11.9 vol.% Si alloys as a function of the correlation distance L.

The fact that a single value of ε can be used to obtain a reasonable fit of simulated profiles to experimental profiles for all alloys indicates that the model used is in principle correct. The value obtained for the misfit, $\varepsilon = 2.3\times10^{-3}$, is smaller than the value of the thermally-induced misfit $\varepsilon_{\text{th}} = 3.1\times10^{-3}$ (Mourik, Keijser, Pers & Mittemeijer, 1988), *i.e.* the misfit introduced during the cooling from the annealing temperature (447 K) to room temperature as a consequence of the difference in thermal expansion between the silicon particles and the aluminium matrix. Consequently, appreciable stress relaxation has taken place during the storage (*i.e.* ageing) at room temperature (see Sec. IV.A). This relaxation and a further relaxation over a period of 4 years at room temperature is discussed in a separate paper (Berkum, Delhez, Keijser, Mittemeijer & Mourik, 1991).

B. Line-Profile Asymmetry

In a real specimen, the shape and size of the inclusions or precipitates, the shape and size of the matrix crystallites and the misfit parameter all vary. Simulations show that this leads to an asymmetry of the total profile which is smaller than that of the profile of an individual matrix crystallite/inclusion combination. The asymmetry of the simulated profiles can be larger than the asymmetry of the experimental profiles (see Figs. 3c and 4b and their discussion), because in the simulations all matrix crystallites as well as all inclusions are taken identical.

In spite of the above, the asymmetries of the simulated and the experimental {400} *h* profiles show an important qualitative correspondence. For the low silicon-content alloys, the *h* profiles are broader on the low-angle side of the peak maximum (as the instrumental *g* profile). The asymmetry for the aluminium-silicon alloys decreases with increasing silicon content and for the highest silicon contents the asymmetry is even reversed. The asymmetry of the simulated profiles shows the same trend, although the total change in asymmetry from 0 to 18.2 vol.% is significantly larger. In the light of the present simple model this is a promising result: the shape of the distribution of the local elastic strains is in qualitative agreement with the theoretically predicted one.

C. Dependence on Second-Phase Content

In the past (Mourik, Keijser, Pers & Mittemeijer, 1988; Berkum, Delhez, Keijser, Mittemeijer & Mourik, 1991), the dependence of line broadening on silicon content was studied by comparing integral breadths instead of complete line profiles or Fourier coefficients. The integral breadth β, *i.e.* the integrated intensity divided by the maximum intensity, is often interpreted in terms of the microstructure of the specimen. For an exclusively strain-broadened profile, β ($= \beta^{\text{D}}$) can be related, in an approximate way, to the mean squared strain $\langle e_n^2 \rangle$ for $n = 0$ (Stokes & Wilson, 1944):

$$\beta^{\mathrm{D}} = k \langle e_0^2 \rangle^{1/2} \tan\theta, \tag{7}$$

where k is a constant depending on the strain distribution in the specimen and β^{D} is in radians 2θ. In practice, rather arbitrarily, often $k = 4$ is taken. In principle, for the present strain distribution k can be evaluated from simulations if the contribution of size broadening is negligible or corrected for.

For an exclusively size-broadened profile ($\beta = \beta^{\mathrm{S}}$), it holds (*e.g.* Bertaut, 1962):

$$\beta^{\mathrm{S}} = \frac{\lambda}{\langle T \rangle \cos\theta}, \tag{8}$$

where $\langle T \rangle$ is the volume-averaged column length and β^{S} is in radians 2θ.

For the aluminium-silicon alloys considered here, it follows from experiment (Mourik, Keijser, Pers & Mittemeijer, 1988) and also from the present simulations that the total integral breadth of the f profile is proportional to $y_{\mathrm{Si}}^{1/2}$. It is tempting to explain this by assuming predominant strain broadening[3] and combining Eq. (7) and the expression derived for $\langle e_0^2 \rangle$ in specimens containing misfitting particles (Mourik, Keijser, Pers & Mittemeijer, 1988):

$$\langle e_0^2 \rangle = \tfrac{4}{5} C^2 \frac{\varepsilon^2}{(1+\varepsilon)^6} y_{\mathrm{B}}, \tag{9}$$

where C is a constant (see App. B). This explanation is incorrect since the simulations indicate that the contribution of size broadening cannot be ignored. However, for the present model (see Sec. III) it was found that also the size broadening is practically proportional to $y_{\mathrm{Si}}^{1/2}$ [size broadening is inversely proportional to the average column length $\langle T \rangle$, which not only depends on the radius of the aluminium matrix crystallite (proportional to $y_{\mathrm{Si}}^{-1/3}$), but also on the missing cells in the matrix due to the presence of the inclusion (of constant size)]. Thus, the y_{Si}

---

[3] In practice, this approach can be used in a phenomenological way to estimate $\langle e_0^2 \rangle$ from experimental data if one is able to calibrate the (effective) value of k, which depends on the relative contributions of size and strain broadening to the total β. These relative contributions change with the reflection, the size of the matrix-precipitate assembly, and the misfit, but they were found to be almost independent of y_{Si}. To give an example: k=4.5 for the Al {400} f profile when simulated with misfit $\varepsilon = 2.3\times10^{-3}$ and precipitate radius 45.5 nm and k=5.5 for the same reflection if the h profile is simulated and Voigt profiles are assumed to eliminate instrumental broadening (Langford, 1978). This kind of elimination is often applied in practice; here it leads to a small overestimation of β^{f}.

dependence of the total β (combined effect of size and strain broadening) is also very close to ${y_{Si}}^{1/2}$ (as observed).

D. Elastic Strains and Stored Energy

From a materials-science perspective the mean squared strain for $n = 0$, $\langle e_0^2 \rangle$, is an important quantity, since it is directly proportional to E, the stored elastic energy per unit volume of the aluminium matrix. According to Faulkner (1960), their relationship is given by:

$$E = \frac{15}{2} \mu_A \langle e_0^2 \rangle \tag{10}$$

Combining Eqs. (9) and (10) and substituting $\varepsilon = 2.3 \times 10^{-3}$ (see Sec. V.A), results in a stored-energy density of $450 y_B$ kJ/m^3 [for comparison: a dislocation density of 10^{14} m^{-2} in aluminium corresponds to approximately 100 kJ/m^3 (Hirth & Lothe, 1982)].

Application of the Warren-Averbach method yields values of the mean squared strain $\langle e_L^2 \rangle$ as a function of the correlation distance L ($= n \times |\boldsymbol{a}_3|$) (Warren, 1969). For the present strain model, values of $\langle e_L^2 \rangle$ have been calculated directly from the model and are shown in Fig. 5. The

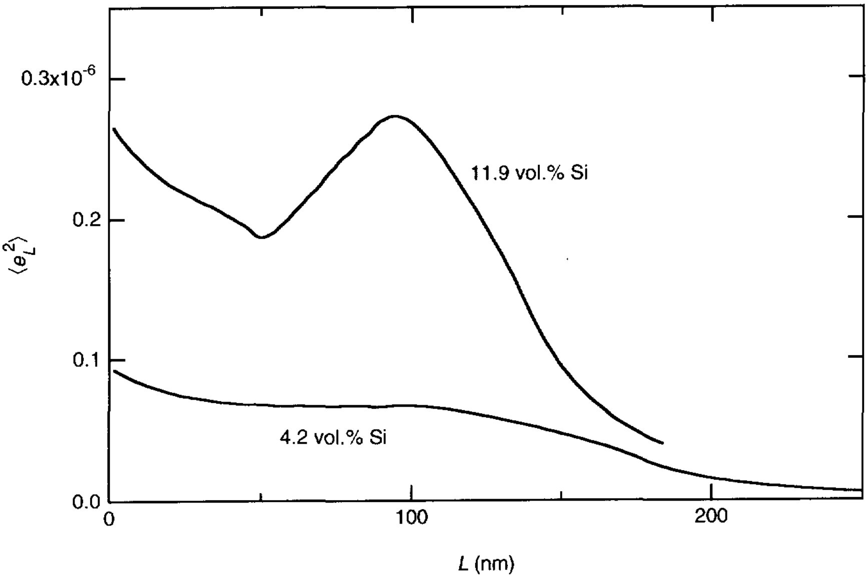

Fig. 5: Mean squared strain $\langle e_L^2 \rangle$ *versus* the correlation distance L ($0 < L < 2R$) as obtained from the model calculations for the Al 4.2 vol.% Si and Al 11.9 vol.% Si alloys ($\varepsilon = 2.3 \times 10^{-3}$).

appearance of these $\langle e_L^2 \rangle$ curves is unusual: for the Al 4.2 vol.% Si alloy, $\langle e_L^2 \rangle$ is approximately constant for $50 \leq L \leq 100$ nm; for the Al 11.9 vol.% Si alloy, $\langle e_L^2 \rangle$ shows a minimum at $L \approx 50$ nm and a maximum at $L \approx 100$ nm.

The typical shape of an $\langle e_L^2 \rangle$ curve shows a continuous decrease for increasing L. Such a behaviour can be understood qualitatively. In the neighbourhood of a lattice imperfection (*i.e.* a dislocation, a misfitting solute atom or precipitate, *etc.*), atoms exhibit relatively large displacements. Values of $|e_L|$ for *small* correlation distances increase steeply on approaching the imperfection and reach a high maximum value at the imperfection. For a *larger* correlation distance, the influence of the imperfection is earlier felt, but the value of $|e_L|$ rises more smoothly and reaches a lower maximum value, all due to the larger averaging distance L [or n, *cf.* Eq. (6)]. Since the mean *squared* strain $\langle e_L^2 \rangle$ is dependent on the variance in the individual e_L values, it is largest for small L and decreases as L increases.

The unusual behaviour in Fig. 5 can be explained as a consequence of the missing contribution of the volume occupied by the inclusion to the diffraction by the matrix. In the present case the diameter $2\rho^{\mathrm{B}}$ of the silicon particles is almost 100 nm (note that for $L > 100$ nm the usual $\langle e_L^2 \rangle$ behaviour results; see Fig. 5). The unit cells nearest to the inclusion experience relatively large radial displacements. However, in Fig. 2 only unit cells above or under the inclusion, not aside of it, have an appreciable portion of their displacement in the direction of the diffraction vector $\boldsymbol{H}$. A pair of two unit cells in the same column, composed of one above and one under the inclusion (having displacements in opposite directions), gives a relatively large contribution to the specific average $\langle e_L^2 \rangle$, where L is the distance between the two cells. For the smallest L values ($L \ll 2\rho^{\mathrm{B}}$), there are not many contributions to $\langle e_L^2 \rangle$ of pairs encompassing the inclusion. As L increases, $\langle e_L^2 \rangle$ contains more and more (large) contributions of such pairs until L reaches the diameter of the inclusion. The usual behaviour of $\langle e_L^2 \rangle$ involves a decrease for all L (see above). Together with the effect discussed here, the net resulting curves will show a decrease followed by a plateau or even an increase for $\langle e_L^2 \rangle$ up to an L value equal to the diameter of the inclusion and the usual decrease for L values larger than that (see Fig. 5).

For the specimens considered here an *experimental* determination of $\langle e_L^2 \rangle$ was not possible, because in the experimental line profiles some additional size broadening occurs and no two orders of reflection could be measured well enough to separate size and strain broadening. Recently Scardi, Lutterotti & Di Maggio (1991) reported experimental $\langle e_L^2 \rangle$ values that show a behaviour similar to that shown in Fig. 5. Their specimens consisted of large tetragonal zirconia crystallites in which small monoclinic zirconia crystallites were formed, accompanied by a partly elastic accommodation of the specific volume difference. Hence, the present strain model may provide an explanation for these results.

VI. CONCLUSIONS

Variations in the local elastic strain in the crystalline solid state can be studied in detail by diffraction-line profile analysis. A first evaluation of the distortion field in a matrix around misfitting particles from diffraction-line profiles has been presented. The relatively simple model proposed has been tested for two-phase aluminium-silicon alloys in which non-uniform strains are generated by the difference in thermal shrinkage between the silicon precipitates and the aluminium matrix. Comparison of simulated and experimental diffraction profiles gave the following results:

- A single value for the linear-misfit parameter provided satisfactory agreement between simulated and experimental line profiles for five AlSi alloys differing in Si content.
- The value of the misfit (2.3×10^{-3}) confirmed the earlier deduction of stress relaxation on ageing at room temperature.
- The simulations confirmed the experimentally observed linear dependence of integral breadth on the square root of the volume fraction of precipitates.
- The asymmetry of the simulated and the experimental profiles indicated the necessity for a more complex model, but nevertheless proved that the theoretical strain distribution is qualitatively correct.
- The stored energy per m^3 of the aluminium matrix was found to be 4.5 kJ per vol.% Si.
- The unusual behaviour of the mean squared strain as a function of the correlation distance found by the model calculations was explained and evidence exists that such a behaviour occurs in practice.

ACKNOWLEDGEMENT

The authors wish to thank Dr. P. van Mourik for providing the aluminium-silicon specimens and the experimental data.

APPENDIX A: COLUMN-LENGTH DISTRIBUTION OF A SPHERE

When a sphere of radius R is cut into parallel columns of equal but infinitesimally small cross section, the length T of these columns can be represented by a column-length distribution $p(T)$. The function $p(T)$ is defined such that $p(T)\mathrm{d}T$ is the fraction of columns having a length between T and $T+\mathrm{d}T$. Columns of length T are located at a ring of radius r around the central axis, parallel to the cutting direction, where:

$$r = \sqrt{R^2 - \tfrac{1}{4}T^2} \qquad \text{for } 0 \le T \le 2R. \qquad (A.1)$$

From Eq. (A.1), it follows:

$$\frac{\mathrm{d}r}{\mathrm{d}T} = -\frac{T}{4r} \qquad \text{for } 0 \le T < 2R. \qquad (A.2)$$

The total number of columns is determined by the largest cross section of the sphere: πR^2. The fraction of the total number occupied by the columns of length T to T–dT is equal to $2\pi r\mathrm{d}r/\pi R^2$. Thus, using Eq. (A.2), it follows:

$$-p(T)\mathrm{d}T = \frac{2\pi r\mathrm{d}r}{\pi R^2} = -\frac{T\mathrm{d}T}{2R^2} \qquad \text{for } 0 \le T < 2R, \qquad (A.3)$$

and the column-length distribution equals:

$$p(T) = \frac{T}{2R^2} \qquad \text{for } 0 \le T < 2R,$$

$$p(T) = 0 \qquad \text{for } T \ge 2R. \qquad (A.4)$$

Equation (A.4) is presented by the full line drawn in Fig. 1.

APPENDIX B: AVERAGE DISPLACEMENT IN A UNIT CELL AROUND A MISFITTING INCLUSION

The elastic strain caused by a misfitting particle B in the centre of a continuous, isotropic and infinite matrix A at a distance ρ from the centre of the inclusion is given by Christian (1965):

$$e_{\rho\rho} = -2\,C\,\varepsilon\frac{(\rho_0^{\mathrm{A}})^3}{\rho^3} \qquad \text{for } \rho \ge \rho_0^{\mathrm{A}}, \qquad (B.1)$$

$$e_{\varphi\varphi} = e_{\theta\theta} = C\,\varepsilon\frac{(\rho_0^{\mathrm{A}})^3}{\rho^3} \qquad \text{for } \rho \ge \rho_0^{\mathrm{A}}, \qquad (B.2)$$

where $e_{\rho\rho}$, $e_{\varphi\varphi}$ and $e_{\theta\theta}$ are the normal components of the local strain, $C = 3K_{\mathrm{B}}/(3K_{\mathrm{B}}+4\mu_{\mathrm{A}})$, with K and μ being the bulk and shear moduli and the linear misfit ε equals $(\rho_0^{\mathrm{B}}-\rho_0^{\mathrm{A}})/\rho_0^{\mathrm{A}}$ where ρ_0^{A} and ρ_0^{B} are the radii of the undeformed cavity and particle, respectively.

When considering displacements in a particular direction, *e.g.* the z direction, Eqs. (B.1) and (B.2) are rewritten into cylindrical co-ordinates (r,z,φ) (see also Fig. 2) and the strain component in the z direction is obtained as:

$$e_{zz}(r,z) = e_{\rho\rho}\cos^2\theta + e_{\theta\theta}\sin^2\theta = C\,\varepsilon\,(\rho_0^{\mathrm{A}})^3\,\frac{r^2-2z^2}{(r^2+z^2)^{5/2}}\,. \tag{B.3}$$

Note that e_{zz} is independent of φ, *i.e.* it shows cylindrical symmetry.

The additional effect of the finiteness of the matrix was first solved by Eshelby (1956) and is here a uniform dilatation e_{U} of the matrix, which reads (Christian, 1965):

$$e_{\mathrm{U}} = \frac{\Delta V^{\mathrm{A}}}{3V^{\mathrm{A}}} = C'\,\varepsilon\,\frac{(\rho_0^{\mathrm{A}})^3}{R^3}\,, \tag{B.4}$$

where R is the radius and V^{A} the volume of the spherical matrix and $C' = 4C\mu_{\mathrm{A}}/3K_{\mathrm{A}}$.

According to the linear theory of elasticity, the displacement component f in the z direction is obtained by integration of the strain over the distance concerned in the column. The lower limit of integration is set to zero so that displacements are defined with respect to the plane $z = 0$ (see Fig. B1):

$$f(r,z) = \int_0^z e_{zz}(r,z')\mathrm{d}z' = \varepsilon\,(\rho_0^{\mathrm{A}})^3\left[\frac{C\,z}{(r^2+z^2)^{3/2}} + \frac{C'\,z}{R^3}\right]. \tag{B.5}$$

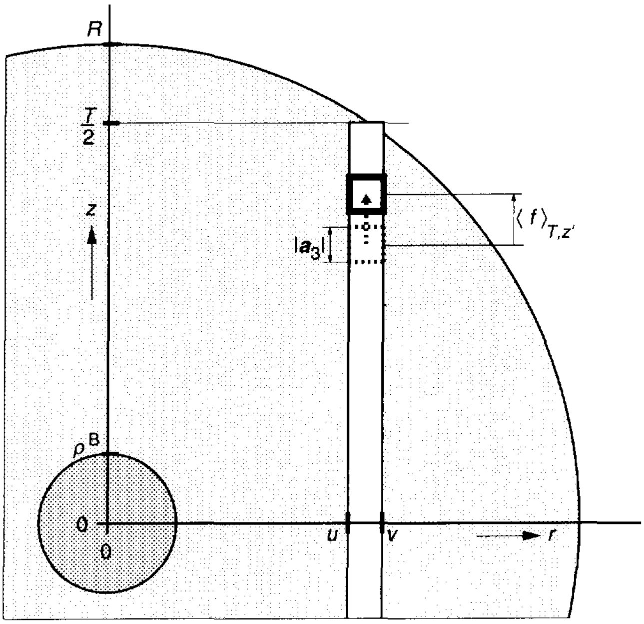

Fig. B1: Illustration of the various parameters used in the derivation of the average displacement $\langle f\rangle_{T,z'}$.

In principle $f(r,z)$ is a continuous function. In the description of diffraction used here, a certain displacement has to be assigned to each unit cell of the crystallite. In fact, this discreteness and the assumption of continuity in the elasticity theory are incompatible. Here this incompatibility is relieved by assigning to a unit cell at height z' in a column of length T an average displacement $\langle f \rangle_{T,z'}$. Averaging in the vertical direction extends from $z' - \frac{1}{2}|\boldsymbol{a}_3|$ to $z' + \frac{1}{2}|\boldsymbol{a}_3|$ and in the horizontal (radial) direction from u to v, where u and v are given by:

$$u = 0 \qquad \text{for } T = 2R$$

$$u = \sqrt{R^2 - \tfrac{1}{4}\left(T + \tfrac{1}{2}|\boldsymbol{a}_3|\right)^2} \qquad \text{for } T < 2R, \tag{B.6}$$

$$v = \sqrt{R^2 - \tfrac{1}{4}\left(T - \tfrac{1}{2}|\boldsymbol{a}_3|\right)^2} \qquad \text{for } T \leq 2R. \tag{B.7}$$

The volume over which $f(r,z)$ is averaged equals $\pi|\boldsymbol{a}_3|(v^2-u^2)$. Thus the average value of the displacement for the unit cell (T,z') is found by integration as follows:

$$\langle f \rangle_{T,z'} = \frac{2\pi}{\pi\,|\boldsymbol{a}_3|\,(v^2-u^2)} \int\limits_{z'-\frac{1}{2}|\boldsymbol{a}_3|}^{z'+\frac{1}{2}|\boldsymbol{a}_3|} \int\limits_{u}^{v} f(r,z)\, r\, \mathrm{d}r\mathrm{d}z = \frac{C'\,\varepsilon\,(\rho_0^{\mathrm{A}})^3\, z'}{R^3} + \frac{2\,C\,\varepsilon\,(\rho_0^{\mathrm{A}})^3}{|\boldsymbol{a}_3|\,(v^2-u^2)} \times$$

$$\left(\sqrt{u^2+(z'+\tfrac{1}{2}|\boldsymbol{a}_3|)^2} - \sqrt{u^2+(z'-\tfrac{1}{2}|\boldsymbol{a}_3|)^2} - \sqrt{v^2+(z'+\tfrac{1}{2}|\boldsymbol{a}_3|)^2} + \sqrt{v^2+(z'-\tfrac{1}{2}|\boldsymbol{a}_3|)^2} \right) \tag{B.8}$$

REFERENCES

Agarwal, S.C., Koczak, M.J. & Herman, H. (1973). *Scripta Metall.* **7**, 365-370.

Arsenault, R.J. & Taya, M. (1987). *Acta Metall.* **35**, 651-659.

Berkum, J.G.M. van, Delhez, R., Keijser, Th.H. de, Mittemeijer, E.J. & Mourik, P. van (1991). *Scripta Metall. Mater.* **25**, 2255-2258. See Chapter 6 of this thesis.

Bertaut, F. (1949). *C. R. Acad. Sci. Paris* **228**, 187-189, 492-494.

Bertaut, E. (1962). In: *International Tables for X-ray Crystallography*, vol. III, eds. MacGillavry, C.H., Rieck, G.D. & Lonsdale, K. (Birmingham: Kynoch), p. 318.

Christian, J.W. (1965). *The Theory of Transformations in Metals and Alloys* (Oxford: Pergamon), pp. 188-198.

Delhez, R., Keijser, Th.H. de & Mittemeijer, E.J. (1980). In: *Accuracy in Powder Diffraction*, NBS Spec. Publ. 567, eds. Block, S. & Hubbard, C.R. (Washington: Dpt. of Commerce), pp. 213-253.

Delhez, R., Keijser, Th.H. de & Mittemeijer, E.J. (1982). *Fresenius Z. anal. Chem.* **312**, 1-16.

Delhez, R., Keijser, Th.H. de, Mittemeijer, E.J., Mourik, P. van, Pers, N.M. van der, Katgerman, L. & Zalm, W.E. (1982). *J. Mater. Sci.* **17**, 2887-2894.

Eshelby, J.D. (1956). *Solid State Phys.* **3**, 79-144.

Faulkner, E.A. (1960). *Phil. Mag.* **5**, 519-521.

Hirth, J.P. & Lothe, J. (1982). *Theory of Dislocations*, 2nd ed. (New York: McGraw-Hill), pp. 63-64.

Keijser, Th.H. de, Langford, J.I., Mittemeijer, E.J. & Vogels, A.B.P. (1982). *J. Appl. Cryst.* **15**, 308-314.

Langford, J.I. (1978). *J. Appl. Cryst.* **11**, 10-14.

Ledbetter, H.M. & Austin, H.W. (1987). *Mater. Sci. Eng.* **89**, 53-61.

Mittemeijer, E.J., Mourik, P. van & Keijser, Th.H. de (1981). *Phil. Mag.* **A43**, 1157-1164.

Mourik, P. van, Keijser, Th.H. de, Pers, N.M. van der & Mittemeijer, E.J. (1988). *Scripta Metall.* **22**, 1547-1551.

Mourik, P. van, Mittemeijer, E.J. & Keijser, Th.H. de (1983). *J. Mater. Sci.* **18**, 2706-2720.

Rooyen, M. van & Mittemeijer, E.J. (1989). *Metall. Trans.* **20A**, 1207-1214 .

Ryaboshapka, K.P. (1981). *Zavodskaya Laboratoriya* **47**, 26-33.

Scardi, P., Lutterotti, L. & Di Maggio, R. (1991). *Powder Diffr.* **6**, 20-25.

Smithells, C.J. (1976). *Metals Reference Book* (London: Buttersworths), p. 975.

Stokes, A.R. & Wilson, A.J.C. (1944). *Proc. Phys. Soc. London* **56**, 174-181.

Warren, B.E. (1969). *X-ray Diffraction* (Reading, Massachusetts: Addison-Wesley), pp. 264-268.

Warren, B.E. & Averbach, B.L. (1950). *J. Appl. Phys.* **21**, 595-599.

Warren, B.E. & Averbach, B.L. (1952). *J. Appl. Phys.* **23**, 497.

Wilkens, M. (1979). *J. Appl. Cryst.* **12**, 119-125.

Wilkens, M. (1988). In: *Proc. 8th Int. Conf. on the Strength of Metals and Alloys (ICSMA 8)*, eds. Kettunen, P.O., Lepistö, T.K. & Lehtonen, M.E. (Oxford: Pergamon), pp. 1-6.

Wilkens, M. & Hartmann, R.J. (1963). *Z. Metallkde.* **54**, 676-682.

Withers, P.J., Juul Jensen, D., Lilholt, H. & Stobbs, W.M. (1987). In: *Proc. 6th Int. Conf. on Composite Materials (ICCM VI)*, Vol. 2, eds. Matthews, F.L., Buskell, N.C.R., Hodgkinson, J.M. & Morton, J. (London: Elsevier Applied Science), pp. 255-264.

Withers, P.J., Stobbs, W.M. & Pedersen, O.B. (1989). *Acta Metall.* **37**, 3061-3084.

CHAPTER 6

NOTE ON RELAXATION OF COOLING-INDUCED STRAINS IN TWO-PHASE AlSi ALLOYS AT ROOM TEMPERATURE

J.G.M. VAN BERKUM, R. DELHEZ, TH.H. DE KEIJSER, E.J. MITTEMEIJER, AND
P. VAN MOURIK
Laboratory of Materials Science, Delft University of Technology,
Rotterdamseweg 137, 2628 AL Delft, The Netherlands

I. INTRODUCTION

Supersaturated aluminium-silicon alloys, made by rapid quenching from the melt, have been aged at elevated temperatures. After precipitation of all silicon, cooling to room temperature leads to an average lattice parameter of the aluminium matrix larger than the equilibrium value (Mittemeijer, Mourik & Keijser, 1981) and to lattice-parameter variations around the average value (Mourik, Keijser, Pers & Mittemeijer, 1988). These findings have been based on observations of shift and broadening of X-ray diffraction lines and have been explained successfully from the large difference in the thermal expansion coefficient, and thus in shrinkage on cooling, of the aluminium matrix and the silicon precipitates. It has been shown that Eshelby's theory, originally developed for point imperfections, provides reasonable estimates of the magnitudes of the deviation of the average lattice parameter as well as of the lattice-parameter variation, both as a function of silicon content. In view of the relatively small values of thermal misfit in the specimens concerned, fully elastic accommodation of the misfit has been assumed. In particular if large misfit values occur, plastic accommodation of (part of) the thermal misfit can be realized during cooling already (Taya, Lulay & Lloyd, 1991).

Stress relaxation in aluminium films is a well-known phenomenon in integrated circuits technology (*e.g.* Hershkovitz, Blech & Komem, 1985; Korhonen, Paszkiet, Black & Li, 1990; Cohen, 1990) as well as in metal-matrix composites (*e.g.* Withers, Juul Jensen, Lilholt & Sobbs, 1987). It has been shown that stresses induced by thermal expansion mismatch can relax considerably within a few hours at room temperature.

In view of these observations, the measurements have been repeated on the specimens used in the original line-shift and line-broadening analyses, after twelve and four years of ageing at room temperature respectively, to assess a possible relaxation of the residual stress. Moreover, the original line broadening data have been reanalysed with the time interval between cooling and measurement as an extra variable.

Stress relaxation at room temperature is also of technical importance, since AlSi alloys are extensively used as commercial casting alloys.

II. THEORY

The following equation has been derived for the deviation of the average lattice parameter of a matrix A with respect to its equilibrium (strain-free) value, caused by spherical misfitting particles B in this matrix (Mittemeijer, Mourik & Keijser, 1981):

$$\Delta a_{\mathrm{A}} = 4\, a_{\mathrm{A}} \frac{\mu_{\mathrm{A}}}{3\, K_{\mathrm{A}}}\, C \frac{\varepsilon}{(1+\varepsilon)^3}\, y_{\mathrm{B}}, \tag{1}$$

where a_{A} is the lattice parameter of the matrix, $C = 3K_{\mathrm{B}}/(3K_{\mathrm{B}}+4\mu_{\mathrm{A}})$ with μ and K denoting the shear and bulk moduli, y_{B} is the volume fraction of the particles and ε is the linear misfit parameter. For the case considered, $\varepsilon = \Delta\alpha\Delta T$, the product of the differences in thermal expansion coefficient and in temperature. Using Bragg's law, Δa_{A} can be straightforwardly related to a shift of diffraction-line position.

Using the same model, an equation can be obtained for the mean square of the relative lattice-parameter variation (mean squared strain $\langle e^2 \rangle$) (Mourik, Keijser, Pers & Mittemeijer, 1988):

$$\langle e^2 \rangle^{1/2} = \frac{2}{5}\sqrt{5}\, C \frac{\varepsilon}{(1+\varepsilon)^3} \sqrt{y_{\mathrm{B}}}. \tag{2}$$

The root mean squared strain $\langle e^2 \rangle^{1/2}$ is related to the integral line breadth β as (Delhez, Keijser & Mittemeijer, 1982):

$$\beta = k \langle e^2 \rangle^{1/2} \tan\theta, \tag{3}$$

where k is a constant, depending on the strain distribution in the specimen. In practice, rather arbitrarily, often $k = 4$ is taken. Also Mourik, Keijser, Pers & Mittemeijer (1988) adopted this value. From line-profile simulations based on the model of misfitting particles in a matrix (see Berkum, Delhez, Keijser & Mittemeijer, 1992), it followed that the integral breadth and the root mean squared strain are related by Eq. (3) with $k = 5.5$. In the following, this improved k value is used.

Stress relaxation will manifest itself by a decrease in line shift and line broadening. Probably the stored elastic energy, which is proportional to $\langle e^2 \rangle$, has to be considered as the driving force for stress relaxation. This means that the relative decrease of $|\Delta a|$ and β will increase with the misfit parameter as well as with the volume fraction of B particles [see Eq. (2)]. In the literature, various behaviours of stress or strain in time are proposed (*e.g.* Hershkovitz, Blech & Komem, 1985; Korhonen, Paszkiet, Black & Li, 1990; Solberg, 1985). Here, the time dependence will not be investigated in detail, since per specimen only two (incidentally three) measurements in time were available.

III. EXPERIMENTAL

Ribbons of aluminium-silicon alloys of different compositions have been prepared by the melt-spinning technique and annealed at elevated temperatures (397 to 448 K) until all silicon was expected to be precipitated. Part of the specimens, utilized by Mittemeijer, Mourik & Keijser (1981), were in a sufficiently good shape to determine their lattice parameter again in the same way as 12 years ago: from Debye-Scherrer photographs using the Nelson-Riley extrapolation (see Mittemeijer, Mourik & Keijser, 1981). Concerning the line broadening, all specimens (annealed at 447 K) and data files used by Mourik, Keijser, Pers & Mittemeijer (1988) were still available (including the reference for removal of instrumental broadening). X-ray diffraction measurements have been performed in the same way as 4 years ago (see Mourik, Keijser, Pers & Mittemeijer, 1988). The correction for instrumental broadening was also identical, *i.e.* by using Voigt functions (Delhez, Keijser & Mittemeijer, 1982). Only the problem of the Al {331} and Al {420} reflections being overlapped by the tails of the Si {531} reflection, in the past solved by an educated guess (Mourik, Keijser, Pers & Mittemeijer, 1988), has been handled in an improved way for the old as well as for the new data files. Now, three split-pseudo-Voigt profiles have been fitted to the corresponding intensity data using the program PROFIT (Langford, Louër, Sonneveld & Visser, 1986). The actually recorded number of counts at a certain 2θ position have been distributed over the three profiles according to the ratio of their relative intensities at that 2θ position as established by the pseudo-Voigt fits. In this way, no assumption on the peak shape has been applied directly to the actual profiles. Line breadths have been determined of the separate profiles thus obtained.

IV. RESULTS

The results of the present and of the former lattice-parameter measurements are shown in Table I. For the specimens with 12.5 vol.% Si ("AlSi 12.5"), it is clear that Δa_{Al}, the difference between the actual value of the lattice parameter and the equilibrium value, has been reduced significantly on ageing at room temperature for 12 years. The increase for AlSi 2.8 cannot be considered as statistically significant. Since the specimens containing 25.1 and 38.2 vol.% Si are not in our possession anymore, the dependence of Δa_{Al} *versus* y_{Si} cannot be investigated.

The results of the old line-broadening measurements have been plotted in Fig. 1a [note that values for Al {331} and {420} differ slightly from those in Mourik, Keijser, Pers & Mittemeijer (1988) due to the present improved data evaluation]; Fig. 1b shows the results of the new measurements after four years of ageing at room temperature.

The theoretical, "unrelaxed" misfit value $\Delta\alpha\Delta T$ for the specimens concerned in Fig. 1 equals 3.1×10^{-3}. All data points in Fig. 1a indicate a smaller misfit value than the theoretical one, implying that in the first few days after cooling to room temperature appreciable stress relaxation by some form of plastic accommodation has already occurred. In the time period covered by Fig. 1a, the specimen AlSi 18.2 has been measured twice: after 3 and after 12 days of ageing at room temperature. The clear decrease in line breadth between the two sets of measurements confirms that a rapid stress relaxation was taking place. Such a decrease, for a single specimen, is meaningful, since only the small random errors due to counting statistics (1 to 3 %) have to be considered. Comparisons between data points from different specimens, however, are more difficult, since then the inaccuracies due to silicon-content determination,

Table I: Lattice-parameter deviation* Δa_{Al} for the aluminium matrix of fully precipitated aluminium-silicon alloys after two different ageing times at room temperature

Si content (vol.%)	precipitation temperature (K)	Δa_{Al} (10^{-5} nm) at 293 K after	
		a few days	12 years
2.8	397	0.3	1.1
12.5	397	6	2
12.5	425	7	4
12.5	448	7	2

* Equilibrium value of the lattice parameter of pure aluminium at 293 K: 0.40496 nm (see Mittemeijer, Mourik & Keijser, 1981). Accuracy of lattice-parameter values is approximately 1×10^{-5} nm; for the specimen with 2.8 vol.% Si somewhat better because of sharper lines.

sample inhomogeneity, insufficient flatness of the sample, *etc.* have to be taken into account. For this reason, fitting of relaxation models to the deviations from the theoretical line in Fig. 1a did not give reliable results. Nevertheless, the "scatter" of the data points in Fig. 1a seems to give a clear indication of stress relaxation. The specimen yielding the relatively largest breadth (AlSi 5.9) was the first to be measured (after 10 hours), whereas specimens yielding relatively narrow lines were measured later (*e.g.* AlSi 11.9 after $5^1/_2$ days).

The data for the three specimens richest in Si, shown in Fig. 1b, confirm that continued stress relaxation can take place on ageing at room temperature again. The specimen AlSi 18.2, for example, showing on average 80 % of its theoretically predicted breadth after 3 days and 70 % after 12 days (see Fig. 1a), has decreased to about 55 % after 4 years (see Fig. 1b).

The clear downward curvature of β *versus* $\sqrt{y_{\mathrm{Si}}}$ after 4 years of ageing at room temperature may be understood if the total stored elastic energy in the specimen is the driving force for stress relaxation [see below Eq. (3)]. The relative decrease in β is largest for the specimens richest in silicon.

Surprisingly, the specimens containing 2.3 and 4.2 vol.% Si show a somewhat larger line breadth after 4 years of ageing at room temperature (see Fig. 1b), as compared to a few days (see Fig. 1a). It has to be realized that errors due to correction for instrumental broadening are relatively large for these data points (the net, structural, broadening is smaller than the instrumental broadening). If the increase is a real structural effect, it may be caused by a continuation of precipitation at room temperature. From Fig. 5 in Mourik, Keijser & Mittemeijer (1985), one would expect no increase in lattice parameter (and, thus, in line breadth) after 1841 h at 448 K for a liquid-quenched specimen containing 2.3 at.% Si (= 2.8 vol.% Si). The precipitation in Mourik, Keijser & Mittemeijer (1985), however, may have been accelerated by the manifold cooling and heating, necessary for the lattice-parameter measurements: every cooling is followed by stress relaxation at room temperature, causing less resistance against further precipitation at the annealing temperature. This is especially important in the low silicon-content specimens, where the diffusion distances in the final stage of precipitation are largest, realizing that the precipitate sizes are approximately independent of the overall silicon content (Mittemeijer, Mourik & Keijser, 1981). Then, the small increase of the aluminium matrix lattice parameter of the specimen containing 2.8 vol.% Si on ageing at room temperature (see Table I), after the precipitation treatment of 512 h at 397 K, can also be understood as the result of continued precipitation.

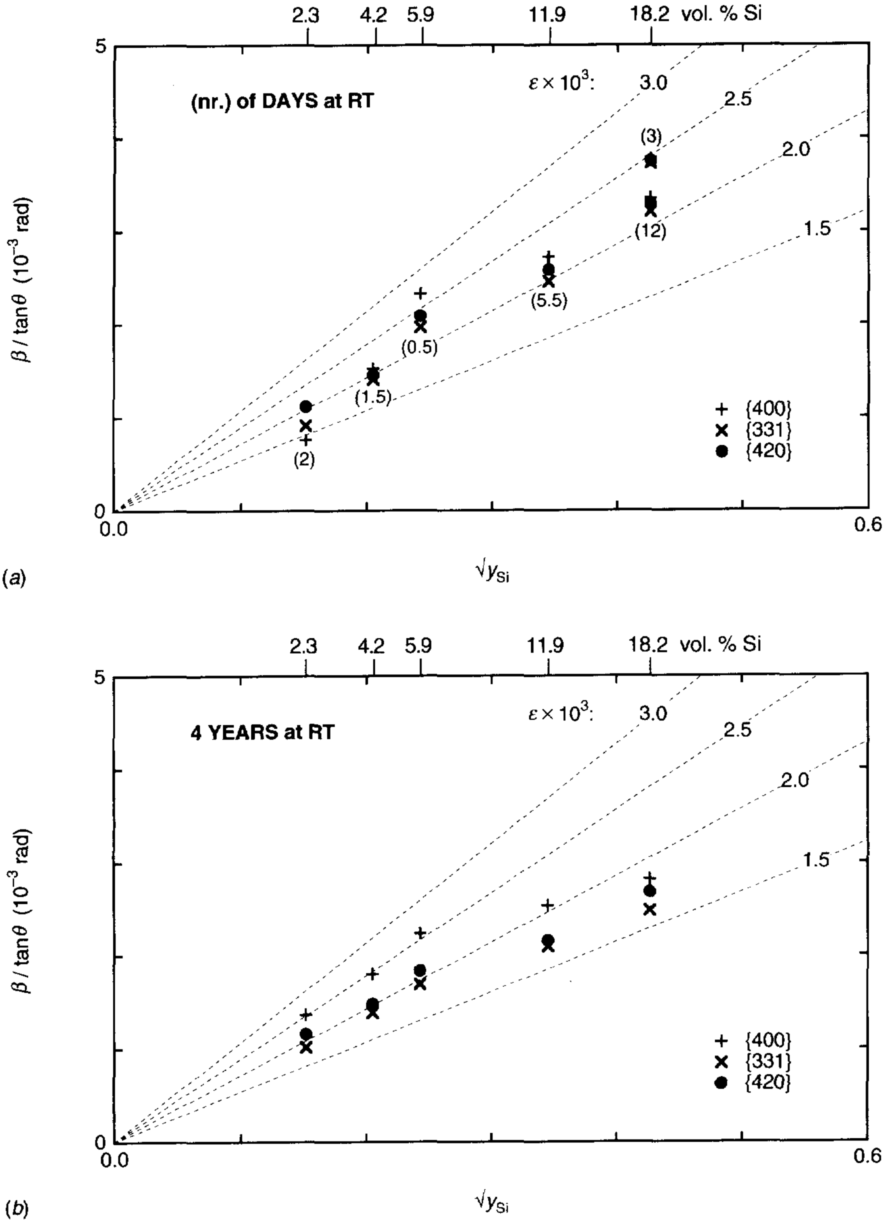

Fig. 1: Normalized integral breadth, $\beta/\tan\theta$, corrected for instrumental broadening, of three aluminium matrix reflections *versus* the square root of the volume fraction of silicon precipitates, $\sqrt{y_{\text{Si}}}$, after ageing at room temperature (RT) for (*a*) 0.5 to 12 days (number of days indicated in brackets) and (*b*) 4 years. Dashed lines are theoretical behaviours on the basis of Eqs. (2) and (3) using $k = 5.5$ and the indicated value of the misfit ε.

The {400} reflection is clearly more broadened than the {420}, which in turn is more broadened than the {331} (see Fig. 1)[1]. This order of the normalized breadths [$\beta/\tan\theta$, see Eq. (3)] of the three reflections is not equal to their order in 2θ position. Therefore, it is not likely that the differences are due to instrumental effects. It is suggested that the elastic anisotropy of the aluminium matrix explains the observations. As for most cubic materials, the Young's modulus in a given crystallographic direction increases with the sum $h^2k^2 + k^2l^2 + h^2l^2$, where h, k and l are the indices of the unit vector in that direction (Nye, 1972). This sum takes the values 0, 0.16 and 0.27 for the unit vectors perpendicular to the {400}, {420} and {331} lattice planes, respectively. As Young's modulus increases, the elastic compliance of the lattice, and thus the strain, will decrease, as observed in Figs. 1a and 1b.

V. CONCLUSION

The difference in thermal expansion coefficients of precipitate and matrix in two-phase aluminium-silicon alloys causes non-uniform strains, which result in an increase of the average lattice parameter and of the lattice-parameter variation around the mean value. An appreciable relaxation of these strains on ageing at room temperature is observed. This results in decreased X-ray diffraction-line shift and line broadening after 12 and 4 years respectively. A large fraction of the misfit strains is already accommodated in the first few days after cooling to room temperature. Stress relaxation is more pronounced as the overall silicon content increases, which is to be expected if the stored elastic energy is considered as the driving force for relaxation.

REFERENCES

Berkum, J.G.M. van, Delhez, R., Keijser, Th.H. de & Mittemeijer, E.J. (1992). *Phys. stat. sol. (a)* **134**, 335-350. See Chapter 5 of this thesis.

Cohen, J.B. (1990). *Adv. X-ray Anal.* **33**, 25-32.

Delhez, R., Keijser, Th.H. de & Mittemeijer, E.J. (1982). *Fresenius Z. anal. Chem.* **312**, 1-16.

Hershkovitz, M., Blech, I.A. & Komem, Y. (1985). *Thin Solid Films* **130**, 87-93.

Korhonen, M.A., Paszkiet, C.A., Black, R.D. & Li, Che-Yu (1990). *Scripta Metall. Mater.* **24**, 2297-2302.

Langford, J.I., Louër, D., Sonneveld, E.J. & Visser, J.W. (1986). *Powder Diffr.* **1**, 211-221.

Mittemeijer, E.J., Mourik, P. van & Keijser, Th.H. de (1981). *Phil. Mag.* **A42**, 1157-1164.

---

[1] The {400} reflection of AlSi 2.3 in Fig. 1a is the only exception. This may be caused by inaccuracy of the measurement or the correction for instrumental broadening (the net, structural broadening is the least of all).

Mourik, P. van, Keijser, Th.H. de & Mittemeijer, E.J. (1985). In: *Rapidly Solidified Materials*, eds. Lee, P.W. & Carbonara, R.S. (Metals Park, Ohio: American Society for Metals), pp. 341-350.

Mourik, P. van, Keijser, Th.H. de, Pers, N.M. van der & Mittemeijer, E.J. (1988). *Scripta Metall.* **22**, 1547-1551.

Nye, J.F. (1972). *Physical Properties of Crystals* (Oxford: Clarendon Press), p. 145.

Solberg, J.K. & Thon, H. (1985). *Scripta Metall.* **19**, 431-434.

Taya, M., Lulay, K.E. & Lloyd, D.J. (1991). *Acta Metall. Mater.* **39**, 73-87.

Withers, P.J., Juul Jensen, D., Lilholt, H. & Stobbs, W.M. (1987). In: *Proc. 6th Int. Conf. Composite Materials (ICCM VI)*, Vol. 2, eds. Matthews, F.L., Buskell, N.C.R., Hodgkinson, J.M. & Morton, J. (London: Elsevier Applied Science), pp. 255-264.

CHAPTER 7

DIFFRACTION-LINE BROADENING DUE TO LATTICE DISTORTIONS

I. Order-Dependence of Line Shape and Line Width and Coherency of Diffraction

J.G.M. van Berkum
Laboratory of Materials Science, Delft University of Technology,
Rotterdamseweg 137, 2628 AL Delft, The Netherlands.

ABSTRACT

Broadening of (X-ray) diffraction lines is often due to the distortion fields associated with lattice defects as dislocations. A general, flexible model for distributions of lattice defects and their distortion fields is presented. Parameters of the model are the mean and variance of the distances between the defects, and the extent and the variance of the amplitudes of the distortion fields. The order-dependence of the shape and width of line profiles is studied as a function of these model parameters. In contrast with the generally adopted point of view that line broadening can be subdivided into order-independent ("size") and order-dependent ("strain") broadenings, it is shown that the order-dependence is complex in general. Only if the strain fields around the defects are confined to regions small compared to the distances between the defects and the strains are sufficiently large, the line broadening (in reciprocal space) becomes order-independent. In that extreme case, it is allowed to subdivide the specimen into domains scattering incoherently with respect to each other and, thus, to speak of "size" broadening.

I. INTRODUCTION

A structurally imperfect specimen gives rise to broadening of (X-ray) diffraction-line profiles. In the generally adopted theories (*e.g.* Warren, 1969; Wilson, 1970), two kinds of structural line broadening are distinguished, that can occur simultaneously: (i) size broadening, caused by a finite size of "domains" in the specimen diffracting incoherently with respect to each other and (ii) strain broadening, due to varying displacements of the atoms with respect to their reference positions. Size broadening is independent of the order of reflection and strain broadening is order-dependent. In this paper, instrumental line broadening is not dealt with.

An important class of specimens studied using diffraction-line broadening concern deformed crystalline solids, as cold worked metals. The structural line broadening is due to the produced lattice defects (usually predominantly dislocations) with their associated distortion fields. The grains in such specimens are usually so large that the broadening due to their finite sizes is negligible. Although strains are the main source of line broadening, it has been suggested that (arrangements of) lattice defects can act as "coherency boundaries" and thereby break up the grains into incoherently diffracting domains which are small enough to produce significant "size" broadening (Warren, 1959).

Incoherency of diffraction, as it is discussed here[1], is a statistical phenomenon: domains can be considered to scatter incoherently if the phase difference (reduced *modulo* 2π) between a wave scattered in one domain and a wave scattered in another domain takes any value between 0 and 2π with equal probability. The intensity scattered by the assembly of domains then equals the sum of the intensities scattered by the domains separately (*e.g.* Sommerfeld, 1964; Fowles, 1968). Phase differences are proportional to the scalar product of the diffraction vector and the position (difference) vector from one scatterer to the other. Therefore, incoherency of diffraction depends on the length of the diffraction vector, *i.e.* the order of reflection, and on the predictability of the distances between the scatterers, *i.e.* the correlation in the positions of the scatterers.

In this paper, line profiles are calculated on the basis of a general flexible model for the strain field in a deformed specimen. The model consists of a spatial distribution of lattice defects, which distort the surrounding material (Sec. II). The occurrence of size broadening is not presupposed, *i.e.* the interference (phase differences) of all scattered waves is taken into account. From the order-dependence of the calculated line-profile characteristics, the incoherency of the diffraction process and the concept of "size" broadening is investigated

---

[1] The limited coherency of the incident radiation in the directions parallel and perpendicular to the direction of wave propagation [usually ~1 μm and a few tens of nm's respectively for X-rays (Cowley, 1981)] is ignored in this paper.

(Sec. IV). The results have severe implications for those methods of analysis that use the order-dependence of measured line broadening for an interpretation in terms of size and strain. This is demonstrated in the following paper (Berkum, Delhez, Keijser & Mittemeijer, 1994) using both calculated and experimental line profiles. The following paper also shows that the microstructural model developed here provides an alternative, applicable in practice, for the interpretation of measured line broadening of deformed solids.

II. MODEL

A line profile $I(2\theta)$, measured as a function of the diffraction angle 2θ, corresponds to a profile $I'(s,d^*)$ in reciprocal space with $s = [2\sin\theta / \lambda] - d^*$, where λ is the wavelength of the radiation used and, here, for d^* the average length of the diffraction vector $\boldsymbol{H}$ is taken, *i.e.* the value of $2\sin\theta / \lambda$ at the centroid of $I'(s,d^*)$. The profile $I'(s,d^*)$ can be expressed as a Fourier series:

$$I'(s,d^*) = K \sum_{L=-\infty}^{+\infty} \{A(L,d^*)\cos(2\pi Ls) + B(L,d^*)\sin(2\pi Ls)\}, \qquad (1)^2$$

where K is (approximately) a constant, A and B are the cosine and sine Fourier coefficients and L is called the "correlation length", a distance in real space parallel to $\boldsymbol{H}$ (*i.e.* perpendicular to the diffracting planes). Theoretically, L takes only discrete values, but in practice L can be considered as a continuous variable. Within the kinematical diffraction theory, the Fourier coefficients of a line profile broadened by lattice distortions can be written as (Warren, 1959, 1969):

$$A(L,d^*) = \langle\cos(2\pi d^* Z_L)\rangle = \int_{-\infty}^{\infty} p_{Z_L}(Z_L)\cos(2\pi d^* Z_L)\,\mathrm{d}Z_L \qquad (2)$$

$$B(L,d^*) = \langle\sin(2\pi d^* Z_L)\rangle = \int_{-\infty}^{\infty} p_{Z_L}(Z_L)\sin(2\pi d^* Z_L)\,\mathrm{d}Z_L, \qquad (3)$$

where Z_L is the elongation which a length L parallel to $\boldsymbol{H}$ experiences due to the presence of lattice distortions and $p_{Z_L}(Z_L)$ is the probability density function of Z_L in the diffacting volume of the specimen (in the rest of this paper, probability density functions are called distributions and they have unit area). In the following, only $L \geq 0$ is considered [Fourier coefficients for $L < 0$ follow from $A(-L,d^*) = A(L,d^*)$ and $B(-L,d^*) = -B(L,d^*)$]. Size broadening is not accounted for explicitly in Eqs. (2) and (3), since the occurrence of incoherently diffracting

---

[2] In textbooks (*e.g.* Warren, 1969), often a (fictitious) unit-cell dimension a_3 in the direction of the diffraction vector is chosen and the dimensionless quantities $n = L/a_3$, $l = d^*a_3$ and $h_3 = (d^*+s)a_3$ are used.

domains within the grains is *not* presupposed. In what follows, Fourier coefficients of broadened line profiles are calculated for an infinitely large specimen containing (point, line or planar) lattice defects (see Fig. 1). The spatial distribution of these defects is varied (Sec. II.C), as well as the amplitude (Sec. II.B) and spatial extent (Sec. II.D) of the distortion fields associated with the defects. The method of calculating the distribution $p_{Z_L}(Z_L)$ for (overlapping) distortion fields is outlined in Sec. II.A. By substitution of $p_{Z_L}(Z_L)$ in Eqs. (2) and (3), the Fourier coefficients and thereby the line profile itself are obtained.

A. Defects and distortions

A specimen usually contains many diffracting crystals, each containing many lattice defects with associated distortion fields. Therefore, the strain field in such a specimen can only be described meaningfully in a statistical way. Here, statistical formulations that are considered reasonable for specimens in practice are used to describe the strain along an infinitely long axis $\boldsymbol{x}$ parallel to $\boldsymbol{H}$ (see Fig. 1) and to calculate the corresponding distribution $p_{Z_L}(Z_L)$. A single column along $\boldsymbol{x}$ is considered representative for all columns making up a complete, three-dimensional specimen. The co-ordinate x along $\boldsymbol{x}$ is considered as a continuous variable. The elongation $Z_L(x)$ of the correlation length L can be calculated from the strain component e_{xx} parallel to $\boldsymbol{x}$ (in the following, e_{xx} is denoted as e):

$$Z_L(x) = \int_{x-\frac{1}{2}L}^{x+\frac{1}{2}L} e(x')\,\mathrm{d}x'. \tag{4}$$

On the axis $\boldsymbol{x}$, a number of positions x_i (i is an integer) are selected at which significant contributions to the strain field $e(x)$ along $\boldsymbol{x}$ are centred. These positions can be considered as the projections of crystal defects close to the axis $\boldsymbol{x}$ (see Fig. 1). The distances between two successive projected defects $D_i = x_i - x_{i-1}$ are considered independent stochastic variables. For all variables D_i, the probability density of $D_i = D$ is given by the function $p_D(D)$ with mean $\langle D\rangle$.

The meaning of the average projected-defect distance $\langle D\rangle$ for a given three-dimensional spatial distribution of lattice defects depends on the character of the defect. In case of planar defects, the axis $\boldsymbol{x}$ intersects the defects and the meaning of $\langle D\rangle$ is straightforward. In case of linear defects (ρ defects per unit area) or point defects (c defects per unit volume), the defects that are relatively far from $\boldsymbol{x}$ (say, at distances larger than $\rho^{-1/2}$ or $c^{-1/3}$) do not affect $e(x)$ significantly, because their strain fields are shielded off by others closer to $\boldsymbol{x}$. In a section containing $\boldsymbol{x}$ bounded by lines parallel to $\boldsymbol{x}$ at distances $\rho^{-1/2}$ from $\boldsymbol{x}$, there are about $2\rho^{1/2}$ linear defects per unit length along $\boldsymbol{x}$, so that $\langle D\rangle \approx \frac{1}{2}\rho^{-1/2}$ for linear defects. In a cylinder round $\boldsymbol{x}$ with

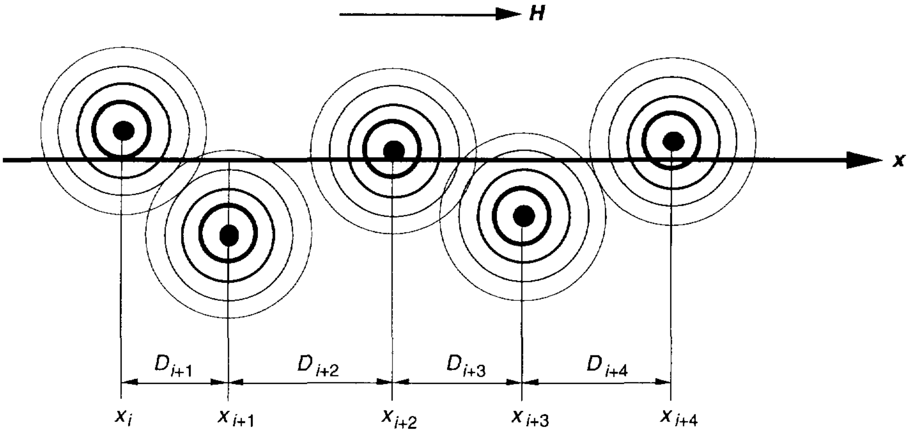

Fig. 1: Crystal defects with associated distortion fields projected onto an axis ***x*** parallel to the diffraction vector ***H***. The projected-defect distances $D_i = x_i - x_{i-1}$ have been indicated.

a radius $c^{-1/3}$, there are about $\pi c^{1/3}$ point defects per unit length along ***x***, so that $\langle D \rangle \approx \frac{1}{\pi} c^{-1/3}$ for point defects. Thus, the average projected-defect distance $\langle D \rangle$ is, according to these examples, two to three times smaller than the average defect distance in space (here, $\rho^{-1/2}$ or $c^{-1/3}$). If the spatial distribution of the defects is not isotropic, *i.e.* different in the directions parallel and perpendicular to ***H***, this interpretation should be adapted accordingly.

The total strain field $e(x)$ is written as the sum of "component" strain fields $e_i(x)$, *i.e.* the strain along ***x*** induced in the column by the individual lattice defects:

$$e(x) = \sum_{i=-\infty}^{\infty} e_i(x). \tag{5}$$

Each component $e_i(x)$ is written as the product of a dimensionless amplitude a_i, different for each projected defect, and a dimensionless normalized "spreading" function $f(x-x_i)$, which is, apart from the location x_i, taken equal for all projected defects:

$$e_i(x) = a_i\, f(x-x_i). \tag{6}$$

In reality, the shape and width of the component strain field may be different for each projected defect (*e.g.* depending on the distance from the defect to the axis ***x*** and/or on the orientation with respect to ***x***), but, in practice, Eq. (6) already provides a satisfactory description of line broadening (see Berkum, Delhez, Keijser & Mittemeijer, 1994). Here, $f(x)$ represents the "average" shape and width of the component strain fields. The amplitudes a_i are considered independent stochastic variables. For all a_i, the probability density of $a_i = a$ is given by the function $p_a(a)$. Since the centroid of the line profile is taken as its origin, the average strain $\langle e \rangle$ is nil (Wagner, 1966), which implies $\langle a \rangle = 0$.

According to Eqs. (4), (5) and (6), the elongation Z_L at the position x depends on the two sets of variables $\{x_i\}$ and $\{a_i\}$:

$$Z_L(x,\{x_i\},\{a_i\}) = \sum_{i=-\infty}^{\infty} a_i F_L(x-x_i), \tag{7}$$

where

$$F_L(x-x_i) = \int_{x-\frac{1}{2}L}^{x+\frac{1}{2}L} f(x'-x_i)\,\mathrm{d}x' \tag{8}$$

(the order of summation and integration has been reversed). To find the distribution $p_{Z_L}(Z_L)$ for specific distributions $p_D(D)$ and $p_a(a)$ and for a specific $f(x)$, two equivalent procedures are possible. In the first procedure, the projected defect positions x_i and amplitudes a_i are given for a single infinitely long axis $\boldsymbol{x}$. Then, Z_L is considered as a function of x along $\boldsymbol{x}$, and the corresponding $p_{Z_L}(Z_L)$ is calculated from this $Z_L(x)$. In the second procedure, Z_L at a single arbitrary position x along $\boldsymbol{x}$ is considered for variable values of x_i and a_i for defects in the neighbourhood (see below) of x. From this $Z_L(\{x_i\},\{a_i\})$ at the position x, which in fact is independent of x, $p_{Z_L}(Z_L)$ is calculated. In the following, the second procedure is used in a slightly modified way.

A general expression for the distribution of stochastic variables which are themselves functions of stochastic variables is given in textbooks on statistics (*e.g.* Arley & Buch, 1950; Martin, 1971). As a special case, the distribution $p_z(z)$ of one stochastic variable z, which is a function of the stochastic variables $y_1, y_2, y_3, \ldots$, which have a joint probability distribution $p_y(y_1, y_2, y_3, \ldots)$, can be derived:

$$p_z(z) = \int \ldots \int \left| \frac{\partial y_1}{\partial z} \right| p_y(y_1(z, y_2, y_3, \ldots), y_2, y_3, \ldots)\,\mathrm{d}y_2\,\mathrm{d}y_3 \ldots, \tag{9}$$

where y_1 is any of the variables y_i and the integrations over $y_2, y_3, \ldots$ include all their possible values. The partial derivative $\partial y_1/\partial z$ should be either positive for all z or negative for all z.

The distribution of $Z_L(\{x_i\},\{a_i\})$ at the arbitrary position x is now written in accordance with Eq. (9) by substituting $Z_L = z$ and $p_{\{x_i\},\{a_i\}}(\{x_i\},\{a_i\}) = p_y(y_1, y_2, y_3, \ldots)$, where $p_{\{x_i\},\{a_i\}}(\{x_i\},\{a_i\})$ is the joint probability distribution of $\{x_i\}$ and $\{a_i\}$. Arbitrarily, a_j is assigned the role of y_1. According to Eq. (7), a_j and its partial derivative to Z_L equal:

where $[A(L,d^*)]_{x,\{x_i\}\backslash\{x_0\}}$ and $[B(L,d^*)]_{x,\{x_i\}\backslash\{x_0\}}$ are Fourier coefficients for fixed x and fixed $\{x_i\}\backslash\{x_0\}$. These can be expressed in terms of the moments $\langle Z_L{}^n\rangle_{x,\{x_i\}\backslash\{x_0\}}$ of $[p_{Z_L}(Z_L)]_{x,\{x_i\}\backslash\{x_0\}}$ by a series expansion of the cosine and sine, respectively:

$$\begin{aligned}[A(L,d^*)]_{x,\{x_i\}\backslash\{x_0\}} &= \int_{-\infty}^{\infty} [p_{Z_L}(Z_L)]_{x,\{x_i\}\backslash\{x_0\}} \cos(2\pi d^* Z_L)\, dZ_L \\ &= 1 - \frac{(2\pi d^*)^2}{2!} \langle Z_L{}^2\rangle_{x,\{x_i\}\backslash\{x_0\}} + \frac{(2\pi d^*)^4}{4!} \langle Z_L{}^4\rangle_{x,\{x_i\}\backslash\{x_0\}} - \cdots \end{aligned} \tag{22}$$

$$\begin{aligned}[B(L,d^*)]_{x,\{x_i\}\backslash\{x_0\}} &= \int_{-\infty}^{\infty} [p_{Z_L}(Z_L)]_{x,\{x_i\}\backslash\{x_0\}} \sin(2\pi d^* Z_L)\, dZ_L \\ &= -\frac{(2\pi d^*)^3}{3!} \langle Z_L{}^3\rangle_{x,\{x_i\}\backslash\{x_0\}} + \ldots. \end{aligned} \tag{23}$$

A term proportional to $\langle Z_L\rangle_{x,\{x_i\}\backslash\{x_0\}}$ has been omitted in Eq. (23), because it is nil if $\langle a\rangle = 0$ [see below Eq. (6)]. Using Eq. (7) and the independence of a_i and a_j for $i \neq j$, so that $\langle a_i{}^m a_j{}^n\rangle = \langle a_i{}^n\rangle\langle a_j{}^n\rangle$, the moments $\langle Z_L{}^n\rangle_{x,\{x_i\}\backslash\{x_0\}}$ can be expressed in terms of the moments $\langle a^n\rangle$ of $p_a(a)$. Some examples are:

$$\langle Z_L{}^2\rangle_{x,\{x_i\}\backslash\{x_0\}} = \langle a^2\rangle \sum_{i=-\infty}^{\infty} F_L^2(x-x_i) \tag{24}$$

$$\langle Z_L{}^3\rangle_{x,\{x_i\}\backslash\{x_0\}} = \langle a^3\rangle \sum_{i=-\infty}^{\infty} F_L^3(x-x_i) \tag{25}$$

$$\langle Z_L{}^4\rangle_{x,\{x_i\}\backslash\{x_0\}} = \langle a^4\rangle \sum_{i=-\infty}^{\infty} F_L^4(x-x_i) + 3\,\langle a^2\rangle^2 \sum_{i=-\infty}^{\infty} \sum_{j\neq i} F_L^2(x-x_i)\, F_L^2(x-x_j). \tag{26}$$

Now, $A(L,d^*)$ and $B(L,d^*)$ can be calculated by numerical integration of $[A(L,d^*)]_{x,\{x_i\}\backslash\{x_0\}}$ and $[B(L,d^*)]_{x,\{x_i\}\backslash\{x_0\}}$ over x and $\{x_i\}\backslash\{x_0\}$ (only small $|i|$ are important), according to Eq. (17), where for each set of x and $\{x_i\}\backslash\{x_0\}$ values, $[A(L,d^*)]_{x,\{x_i\}\backslash\{x_0\}}$ and $[B(L,d^*)]_{x,\{x_i\}\backslash\{x_0\}}$ are given by Eqs. (22) and (23). The moments occurring in Eqs. (22) and (23) are given by expressions like Eqs. (24)-(26) (again, only small $|i|$ are important). Note that, by using the moments $\langle Z_L{}^n\rangle_{x,\{x_i\}\backslash\{x_0\}}$, the multiple convolution for $[p_{Z_L}(Z_L)]_{x,\{x_i\}\backslash\{x_0\}}$ [*cf.* Eq. (19)] is avoided.

Next, specific functions $p_a(a)$, $p_D(D)$ and $f(x)$ will be considered.

B. Distribution of strain amplitudes

The behaviour of the Fourier coefficients $A(L,d^*)$ and $B(L,d^*)$ at large L values proves to be influenced appreciably by the shape of $p_a(a)$. For moderate L, the effect of the shape of $p_a(a)$ is less and, for the investigation of the order-dependence of line broadening, the shape of $p_a(a)$ is of minor importance and the attention can be restricted to some relatively simple shapes.

If $p_a(a)$ is taken symmetrical with respect to $a = 0$, then $\langle a^{2n+1}\rangle = 0$, $\langle Z_L^{2n+1}\rangle_{x,\{x_i\}\backslash\{x_0\}} = 0$, $[B(L,d^*)]_{x,\{x_i\}\backslash\{x_0\}} = 0$ [see Eq. (23)] and consequently $B(L,d^*) = 0$, so that the structurally broadened line profile is symmetrical. It has been shown that some lattice defects produce asymmetrical line profiles [*e.g.* misfitting inclusions (Berkum, Delhez, Keijser & Mittemeijer, 1992) or polarized dislocation dipoles (Gaál, 1984; Groma, Ungár & Wilkens, 1988)]. However, many line profiles recorded in practice are approximately symmetrical after correction for instrumental broadening, so a symmetrical $p_a(a)$ provides a realistic simulation.

If $p_a(a)$ is taken Gaussian, also the expression for $[A(L,d^*)]_{x,\{x_i\}\backslash\{x_0\}}$ is simplified significantly. In that case, $[p_{Z_L}(Z_L)]_{x,\{x_i\}\backslash\{x_0\}}$ is a convolution of Gaussians [see Eq. (19)] and thus it is a Gaussian itself with a variance given by Eq. (24). Then, Eq. (22) reduces to (*cf.* Warren, 1959, p.152):

$$[A(L,d^*)]_{x,\{x_i\}\backslash\{x_0\}} = \exp\left(-2\pi^2 d^{*2}\langle Z_L{}^2\rangle_{x,\{x_i\}\backslash\{x_0\}}\right). \qquad (27)$$

Note that, although a Gaussian $p_a(a)$ implies a Gaussian $[p_{Z_L}(Z_L)]_{x,\{x_i\}\backslash\{x_0\}}$ (*i.e.* the distribution of Z_L *for fixed x and* $\{x_i\}\backslash\{x_0\}$), $p_{Z_L}(Z_L)$ or the strain distribution need not be Gaussian. The operator Ξ ,which includes the integrations over x and $\{x_i\}\backslash\{x_0\}$, can make the shape of $p_{Z_L}(Z_L)$ drastically different from that of $[p_{Z_L}(Z_L)]_{x,\{x_i\}\backslash\{x_0\}}$. The shape of the full $p_{Z_L}(Z_L)$ depends on L and the functions $f(x)$, $p_D(D)$ and, of course, $p_a(a)$.

C. Distribution of defect distances

According to Eq. (17), the operator Ξ depends on the distribution $p_D(D)$, which gives the probability density of a projected defect distance $D_i = D$. A flexible and comprehensive type of distribution is the (continuous) Poisson distribution (see Fig. 2), which has "many practical applications" (Arley & Buch, 1950):

$$p_D(D) = \frac{\mu}{\Gamma(\mu)\langle D\rangle}\left(\frac{\mu D}{\langle D\rangle}\right)^{\mu-1}\exp\left(-\frac{\mu D}{\langle D\rangle}\right) \qquad (\mu \geq 1), \qquad (28)$$

where μ is a constant that, for a given $\langle D\rangle$, governs the variance $\sigma^2(D)$ of $p_D(D)$:

$$\sigma^2(D) = \langle D^2\rangle - \langle D\rangle^2 = \frac{\langle D\rangle^2}{\mu}. \qquad (29)$$

The distribution for $\mu = 1$ is obtained if for each small interval Δx on the axis x there is a chance $\Delta x/\langle D\rangle$ of finding a defect, independent of the positions of other defects ("randomly" distributed defects). For $\mu = \infty$, the distribution is infinitely narrow $[\sigma^2(D) = 0]$ and the defects are distributed perfectly regular: $x_i = i\langle D\rangle$ ("periodically" distributed defects). In that case, the operator Ξ reduces to:

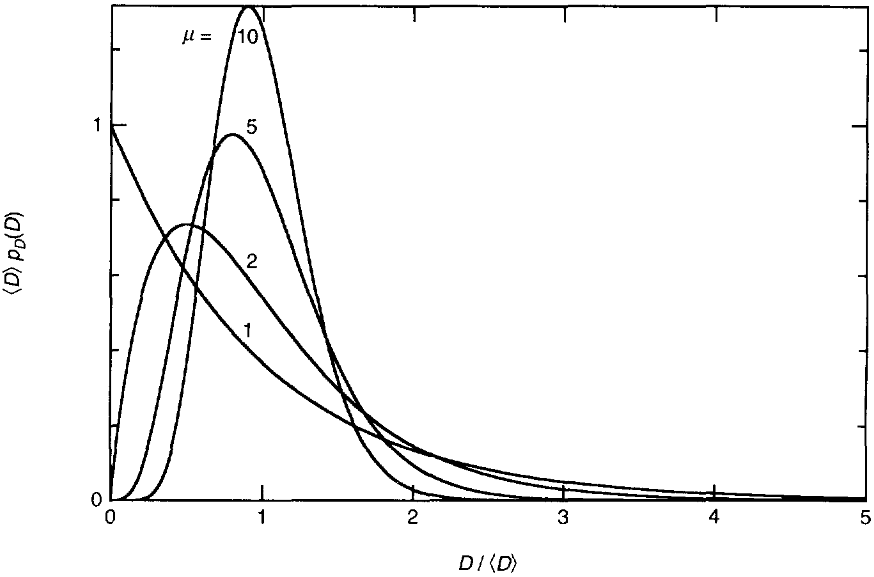

Fig. 2: Examples of the (normalized) distribution functions $p_D(D)$ according to Eq. (28), giving the probability density of a projected-defect distance $D_i = D$.

$$\Xi(F(x,\{x_i\})) = \frac{1}{\langle D\rangle} \int_{-\frac{1}{2}\langle D\rangle}^{\frac{1}{2}\langle D\rangle} F(x,i\langle D\rangle)\,\mathrm{d}x. \tag{30}$$

In the following, predominantly periodically distributed lattice defects are considered. This may not be the most realistic case, but for the line broadening phenomena discussed the type of projected-defect distance distribution proves to be relatively unimportant.

Note that with periodically distributed defects the strain field $e(x)$ is never periodic, because the amplitudes a_i are independent variables (*cf.* Fig. 3). Therefore, the range of meaningful Fourier coefficients in the present model is not necessarily limited to small L, as is the case with models employing periodic boundary conditions (*e.g.* Wilkens, 1979).

D. Shape of the component strain fields

The shape and width of the strain fields of the individual lattice defects is represented by the function $f(x)$. The following normalization of $f(x)$ is used here:

$$\int_{-\infty}^{\infty} f^2(x)\,\mathrm{d}x = C, \tag{31}$$

where C is a length constant [since $f(x)$ is dimensionless]. With such a normalization the "strain content" $\int e^2(x)\mathrm{d}x$ and, consequently, the stored elastic energy associated with a single defect in an infinitely long column is independent of the shape or width of $f(x)$. Next, it will be shown that, for the present model, a similar statement holds for a distribution of defects.

The mean squared strain $\langle e^2\rangle$ for a distribution of defects in a column is calculated as follows. Using Eqs. (5) and (6) and the additivity of variances of independent variables, it follows for arbitrary $p_a(a)$:

$$\langle e^2\rangle_{x,\{x_i\}} = \langle a^2\rangle \sum_{i=-\infty}^{\infty} f^2(x-x_i), \tag{32}$$

where $\langle e^2\rangle_{x,\{x_i\}}$ is the variance of e for fixed x and $\{x_i\}$ resulting from varying all a_i. To obtain $\langle e^2\rangle$, $\{x_i\}$ is kept fixed to an arbitrary set of values and x is varied from $-\infty$ to ∞ [*cf.* the "first" procedure below Eq. (8)]:

$$\langle e^2\rangle = \lim_{A\to\infty} \frac{1}{A} \int_{-\frac{1}{2}A}^{\frac{1}{2}A} \langle e^2\rangle_{x,\{x_i\}}\,\mathrm{d}x, \tag{33}$$

where A is the averaging range in x. After substitution of Eq. (32) into Eq. (33) and reversal of the order of integration and summation, the terms $f^2(x-x_i)$ can be integrated separately. For $A \to \infty$, these integrations yield C [see Eq. (31)] for all defects. The number of such terms (= the number of defects in A) approaches $A/\langle D\rangle$ if $A \to \infty$ (law of large numbers). Thus, $\langle e^2\rangle$ is obtained as:

$$\langle e^2\rangle = \frac{C\langle a^2\rangle}{\langle D\rangle}. \tag{34}$$

Hence, in the present model, the mean squared strain and, consequently, the stored energy in the columns with arbitrary defect distributions are independent of the shape or width of the component strain fields. This is a consequence of the independence of the amplitudes of the component strain fields of adjacent projected defects and the chosen normalization of $f(x)$.

If the lattice defects are screw dislocations, $f(x)$ is a Lorentzian (see App. A):

$$f(x) = \sqrt{\frac{2\,C}{\pi\,w}}\;\frac{1}{1+(x/w)^2}, \tag{35}$$

where w is the half width at half height of $f(x)$. For edge dislocations, $f(x)$ shows a similar behaviour in a certain direction (see App. A). From a comparison of $A(L,d^*)$ behaviours calculated using Eq. (35) and using other shapes for $f(x)$ [*e.g.* $f(x) \propto e^{-|x|}$, which occurs on crossing a pure tilt boundary at right angles (Hirth & Lothe, 1982)], it was concluded that the shape of $f(x)$ is not critical. An example of the behaviour of the strain $e(x)$ using Eq. (35), $\mu = \infty$ (*i.e.* periodically distributed defects) and a Gaussian $p_a(a)$ is given in Fig. 3.

With $f(x)$ according to Eq. (35), the integration according to Eq. (8) can be performed analytically and Eq. (24) can be written as:

$$\langle Z_L^{2}\rangle_{x,\{x_i\}\backslash\{x_0\}} = \frac{2w\langle D\rangle\langle e^2\rangle}{\pi}\sum_{i=-\infty}^{\infty}\left[\arctan\left(\frac{x-x_i+\frac{1}{2}L}{w}\right)-\arctan\left(\frac{x-x_i-\frac{1}{2}L}{w}\right)\right]^2 . \qquad (36)$$

Considerations for calculations:

Only in the limits $w \downarrow 0$ and $w \to \infty$, the Fourier coefficients $A(L,d^*)$ can be calculated analytically (see Apps. B and C). Otherwise, numerical calculations are required. For Gaussian $p_a(a)$ and arbitrary μ, Eq. (36) is substituted into Eq. (27), Eq. (27) into Eq. (20), and Eq. (17) is used for the operator Ξ with Eq. (28) for $p_D(D)$. Laguerre integration can be used for the integrations over x_i in Eq. (17) (Abramowitz & Stegun, 1965). The integrations over x_i for $i \geq 2$ and $i \leq -2$ can be programmed as recursive functions. If $w/\langle D\rangle$ is not too large, the series in

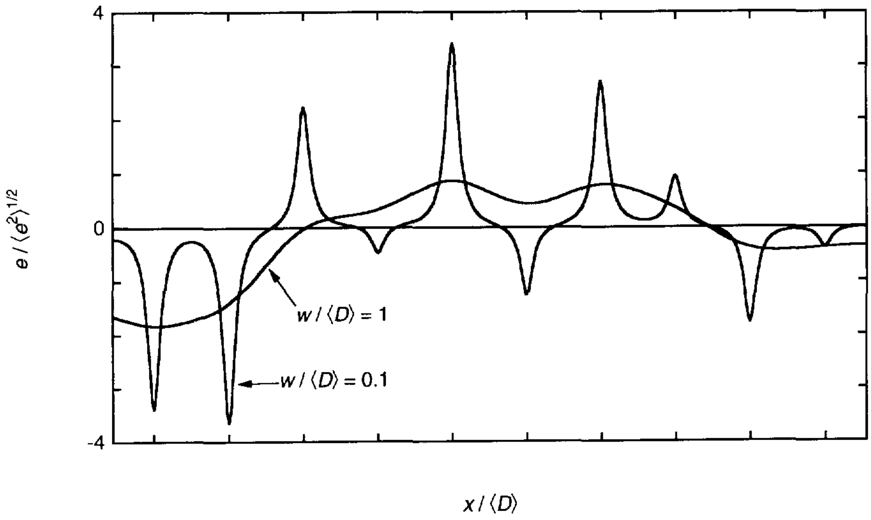

Fig. 3: Examples of the behaviour of the strain field $e(x)$ for two different values of the relative width $w/\langle D\rangle$ of the component strain fields, using periodically distributed defects ($\mu = \infty$), a Gaussian $p_a(a)$ and a Lorentzian $f(x)$.

Eq. (36) converge rapidly for increasing $|i|$. Evidently, calculations for $\mu = \infty$, using Eq. (36) with $x_i = i\langle D\rangle$ substituted into Eq. (27) and using Eq. (30) for the operator Ξ, are less laborious.

III. SCALING OF LINE BROADENING

In this section, it will be shown that line broadening can usefully be investigated on a relative scale using the concept of "isomorphous strain fields". Two infinitely large distorted crystals, numbered 1 and 2, have isomorphous strain fields if their strain fields $e_1(x_1,y_1,z_1)$ and $e_2(x_2,y_2,z_2)$ are related by:

$$\frac{e_1(x_1,y_1,z_1)}{\langle e_1^2\rangle^{1/2}} = \frac{e_2(x_2,y_2,z_2)}{\langle e_2^2\rangle^{1/2}} \qquad \text{if } x_2 = qx_1,\ y_2 = qy_1 \text{ and } z_2 = qz_1, \qquad (37)$$

where q is a constant (in fact, q is a factor that scales the extent of the strain field in crystal 2 to that of the strain field in crystal 1). Using Eqs. (4) and (37) it follows that:

$$\frac{Z_{L_1}(x_1,y_1,z_1)}{\langle e_1^2\rangle^{1/2}} = q^{-1}\,\frac{Z_{L_2}(x_2,y_2,z_2)}{\langle e_2^2\rangle^{1/2}} \qquad \text{if } x_2 = qx_1,\ y_2 = qy_1,\ z_2 = qz_1 \text{ and } L_2 = qL_1. \qquad (38)$$

Using Eq. (38) and Eqs. (2) and (3) it follows for two such crystals:

$$A_1(L_1,d_1^*) = A_2(L_2,d_2^*) \qquad \text{if } L_2 = qL_1 \text{ and } d_2^*\langle e_2^2\rangle^{1/2} = q^{-1}d_1^*\langle e_1^2\rangle^{1/2} \qquad (39)$$

$$B_1(L_1,d_1^*) = B_2(L_2,d_2^*) \qquad [\textit{idem}], \qquad (40)$$

and, subsequently, using Eq. (1):

$$I'_1(s_1,d_1^*) = I'_2(s_2,d_2^*) \qquad \text{if } s_2 = q^{-1}s_1 \text{ and } d_2^*\langle e_2^2\rangle^{1/2} = q^{-1}d_1^*\langle e_1^2\rangle^{1/2}. \qquad (41)$$

Thus, for crystals with isomorphous strain fields, the line profile widths are proportional to $d^*\langle e^2\rangle^{1/2}$ and the line profiles do not change if plotted on an $s/(d^*\langle e^2\rangle^{1/2})$ scale. In addition, if the two crystals are finite, it can be shown that this remains valid if the external surfaces are also "scaled", *i.e.* if the surface of one crystal is given by $F(x_1,y_1,z_1) = 0$ and that of the other one by $F(q^{-1}x_2,q^{-1}y_2,q^{-1}z_2) = 0$.

Two crystals with dislocations as the only type of lattice imperfection have isomorphous strain fields if they have "morphologically identical" dislocation configurations, *i.e.* for every dislocation with Burgers' vector $\boldsymbol{b}$ at (x_1,y_1,z_1) in crystal 1, there is a dislocation with the same $\boldsymbol{b}$ at $(x_2 = qx_1, y_2 = qy_1, z_2 = qz_1)$. To compare the mean squared strains of crystal 1 and crystal 2, equivalent averagings should be performed, *i.e.* the averaging in crystal 2 should occur over a q times larger (linearly) region than in crystal 1. Then, since all stress and strain components around a dislocation in an infinite medium are proportional to r^{-1}, where r is the distance to the dislocation core (Hirth & Lothe, 1982), it immediately follows that $\langle e_2{}^2\rangle^{1/2} = q^{-1}\langle e_1{}^2\rangle^{1/2}$ and the conditions for Eq. (41) become $s_2 = q^{-1}s_1$ and $d_2^* = d_1^*$. Hence, for crystals with morphologically identical dislocation configurations, the occurrence of isomorphous line profiles according to Eq. (41) is only guaranteed if the same order of reflection is considered. Then, the widths of these line profiles are proportional to $\langle e^2\rangle^{1/2}$. Comparing crystals with various values of q, the dislocation density ρ in the crystal, *i.e.* the total line length divided by the volume, is proportional to $q/q^3 = q^{-2}$. Therefore, for a given dislocation configuration the width of a line profile is proportional to $\sqrt{\rho}$.

For the strain model in Sec. II (for given sets $\{x_i\}$ and $\{a_i\}$), strain fields are isomorphous if μ [*cf.* Eq. (28)] and $w/\langle D\rangle$ are constant. Then, the scaling factor q is $\langle D\rangle$ (*cf.* Fig. 3). The following 'relative' quantities are introduced: $L_\mathrm{r} = L/\langle D\rangle$, $w_\mathrm{r} = w/\langle D\rangle$, $d_\mathrm{r}^* = d^*\langle D\rangle$, $s_\mathrm{r} = s\langle D\rangle$ and the relative integral breadth $\beta_\mathrm{r}(d_\mathrm{r}^*) = \int I'(s_\mathrm{r},d_\mathrm{r}^*)\mathrm{d}s_\mathrm{r} \,/\, I'(0,d_\mathrm{r}^*)$ instead of $\beta(d^*) = \int I'(s,d^*)\mathrm{d}s \,/\, I'(0,d^*)$. Then, from Eqs. (39) to (41) it follows that for constant μ, w_r and $d_\mathrm{r}^*\langle e^2\rangle^{1/2}$, the Fourier coefficients $A(L_\mathrm{r},d_\mathrm{r}^*)$ and $B(L_\mathrm{r},d_\mathrm{r}^*)$, the line profile $I'(s_\mathrm{r},d_\mathrm{r}^*)$ and its integral breadth $\beta_\mathrm{r}(d_\mathrm{r}^*)$ can be calculated independent of $\langle D\rangle$. It is readily verified that all expressions for $A(L,d^*)$ and $B(L,d^*)$ in Sec. II can be written exclusively in terms of relative quantities.

IV. ORDER-DEPENDENCE OF LINE BROADENING

Diffraction-line broadening on the basis of the microstrain model of Sec. II will be discussed on a relative scale, *i.e.* independent of the average defect distance $\langle D\rangle$ (see Sec. III). Periodically distributed defects ($\mu = \infty$), a Gaussian amplitude distribution $p_a(a)$ and $f(x)$ as given by Eq. (35) are used, unless stated otherwise. The discussion concentrates on the behaviour of the cosine Fourier coefficients $A(L_\mathrm{r},d_\mathrm{r}^*)$ and the relative integral breadth β_r as a function of the relative length of the diffraction vector d_r^* (*i.e.* order of reflection). If the profile $I'(s_\mathrm{r},d_\mathrm{r}^*)$) is symmetrical, its integral breadth $\beta_\mathrm{r}(d_\mathrm{r}^*)$ (in the same units as s_r) can be calculated from the cosine Fourier coefficients:

$$\beta_\mathrm{r}(d_\mathrm{r}^*) = \left[\int_{-\infty}^{\infty} A(L_\mathrm{r},d_\mathrm{r}^*)\,\mathrm{d}L_\mathrm{r}\right]^{-1}. \qquad (42)$$

The behaviour of $\beta_\mathrm{r}(d_\mathrm{r}^*)$ as a function of $d_\mathrm{r}^*\langle e^2\rangle^{1/2}$ and w_r is shown in Fig. 4a. As expected, $\beta_\mathrm{r}(d_\mathrm{r}^*)$ increases with increasing $d_\mathrm{r}^*\langle e^2\rangle^{1/2}$. The magnitude and rate of increase strongly depend on the relative width w_r of the strain fields of the individual defects. In the following, firstly two extreme cases (infinitely broad and infinitely narrow component strain fields; see Secs. IV.A and IV.B, respectively) are discussed; then, intermediate cases are considered (see Sec. IV.C).

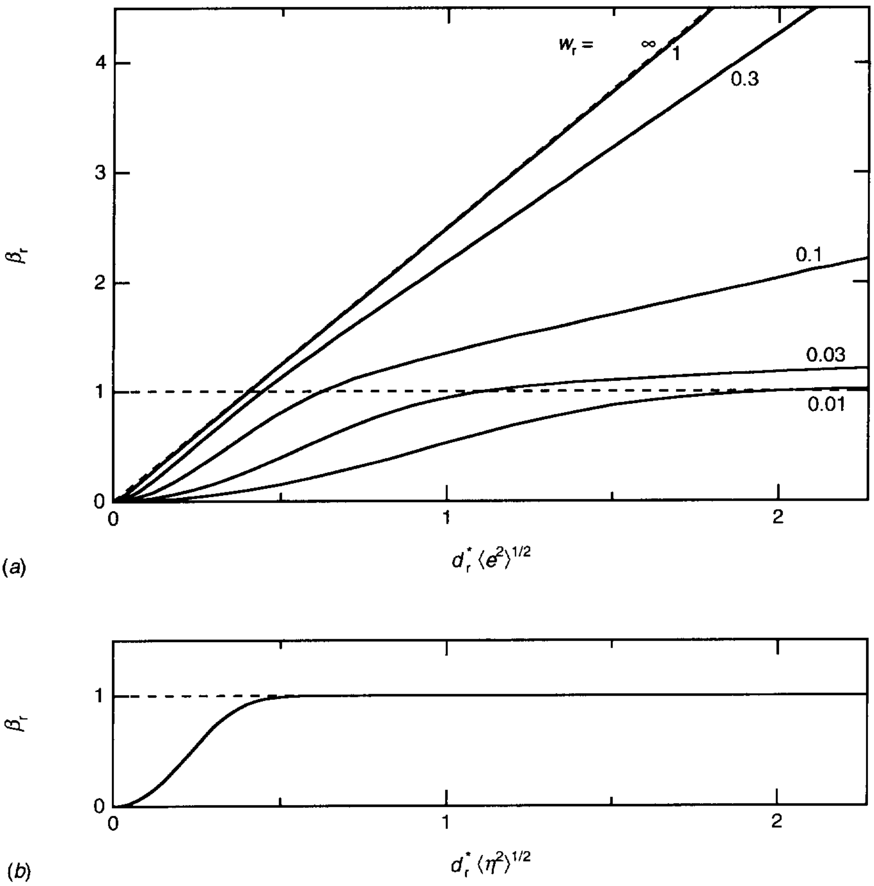

Fig. 4: Relative integral breadth β_r of line profiles in reciprocal space (*a*) as a function of $d_r^*\langle e^2\rangle^{1/2}$ for different relative widths w_r of the component strain fields and (*b*) as a function $d_r^*\langle \eta^2\rangle^{1/2}$ for infinitely narrow component strain fields ($w_r \downarrow 0$).

A. Infinitely broad component strain fields

For $w_r \rightarrow \infty$, the breadth increases linearly with $d_r^*\langle e^2\rangle^{1/2}$ (see App. B and Fig. 4a):

$$\beta_r(d_r^*) = \sqrt{2\pi}\, d_r^*\langle e^2\rangle^{1/2}. \tag{43}$$

This behaviour is well-known for the strain broadening from specimens with a uniform lattice spacing d within each grain and a Gaussian spacing distribution over the grains, where $\langle e^2\rangle^{1/2} = (\langle d^2\rangle - \langle d\rangle^2)/\langle d\rangle^2$ (Stokes & Wilson, 1944). This is understandable, since for increasing w_r the strain gradients along x decrease and the strain becomes uniform over a small length scale while remaining Gaussian on a very large scale (*cf.* Fig. 3). In the past, Eq. (43) or its equivalent on a 2θ scale ($\beta = 2\sqrt{2\pi}\,\langle e^2\rangle^{1/2}\tan\theta$) has often been used for strain broadening *in general.*

The Fourier coefficients for $w_\mathrm{r} \to \infty$ are given by Eq. (B.1). They are perfectly Gaussian and strongly order-dependent: $\ln[A(L_\mathrm{r},d_\mathrm{r}^*)] \propto d_\mathrm{r}^{*2}$. The line shape of $I'(s_\mathrm{r})$ is also Gaussian. The shape, width and order-dependence of $I'(s_\mathrm{r})$ are independent of the shape of $p_D(D)$, $p_a(a)$ and $f(x)$ (see App. B).

B. Infinitely narrow component strain fields

In the limit $w_\mathrm{r} \downarrow 0$, the relative integral breadth $\beta_\mathrm{r}(d_\mathrm{r}^*)$ reads [see Eq. (C.5) and Fig. 4b]:

$$\beta_\mathrm{r}(d_\mathrm{r}^*) = \frac{1-\exp(-2\pi^2 d_\mathrm{r}^{*2}\langle\eta^2\rangle)}{1+\exp(-2\pi^2 d_\mathrm{r}^{*2}\langle\eta^2\rangle)}, \tag{44}$$

where the dimensionless parameter $\langle\eta^2\rangle = \pi w_\mathrm{r}\langle e^2\rangle$ is used to characterize the strain content of "infinitely narrow component strain fields" (see App. C). For small w_r, the mean squared strain $\langle e^2\rangle$ is an inconvenient parameter, because it has to take very large values to produce non-zero line broadening (*cf.* Fig. 4a).

For small $d_\mathrm{r}^*\langle\eta^2\rangle^{1/2}$, Eq. (44) reduces to $\beta_\mathrm{r}(d_\mathrm{r}^*) \approx \pi^2 d_\mathrm{r}^{*2}\langle\eta^2\rangle$. For this case, the Fourier coefficients show an approximately exponential behaviour: $A(L_\mathrm{r},d_\mathrm{r}^*) \approx \exp(-2\pi^2 d_\mathrm{r}^{*2}\langle\eta^2\rangle L_\mathrm{r})$ [*cf.* Eq. (C.4)], so that the corresponding line profile is approximately Lorentzian. This case leads to appreciable line broadening only if $\langle D\rangle$ is relatively small, as for example pertains to paracrystalline materials (see App. C).

For larger $d_\mathrm{r}^*\langle\eta^2\rangle^{1/2}$, $\beta_\mathrm{r}(d_\mathrm{r}^*)$ approaches asymptotically to 1 [see Eq. (44) and Fig. 4b]. For $d_\mathrm{r}^*\langle\eta^2\rangle^{1/2} \gtrsim \frac{1}{2}$, an increase of $\langle\eta^2\rangle$ (strain content) or d_r^* (order of reflection) does not lead to an increase of the line breadth. The Fourier coefficients and the corresponding line profile for large $d_\mathrm{r}^*\langle\eta^2\rangle^{1/2}$ approach [*cf.* Eq. (C.4) with $E = 0$]:

$$A(L_\mathrm{r},d_\mathrm{r}^*) = 1 - L_\mathrm{r} \qquad \text{for } L_\mathrm{r} \le 1 \text{ ; zero otherwise} \tag{45}$$

$$I'(s_\mathrm{r}) \propto \frac{\sin^2(\pi s_\mathrm{r})}{s_\mathrm{r}^2}. \tag{46}$$

Thus, the line broadening becomes completely independent of $\langle\eta^2\rangle^{1/2}$ and d_r^*. Apparently, the line broadening from defects with large strains confined to distances very much smaller than the average defect distance is order-independent. This type of strain broadening can be conceived as pure "size broadening": small but perfect crystals induce exactly the same $I'(s_\mathrm{r})$, $A(L_\mathrm{r},d_\mathrm{r}^*)$ and

$\beta_r(d_r^*)$ as the strained, infinitely large crystal considered (*e.g.* Delhez, Keijser & Mittemeijer, 1982).

The structure producing this type of broadening consists of blocks of undistorted material ("domains") shifted with respect to each other over distances $\langle D\rangle\eta_i$ [see Eq. (C.1)]. The phase differences corresponding with these shifts are $2\pi d_r^*\eta_i$ (*modulo* 2π). For $d_r^*\langle\eta^2\rangle^{1/2} \gtrsim \frac{1}{2}$, these phase differences are almost uniformly distributed between $-\pi$ and π, or 0 and 2π. Thus, incoherency of diffraction can be understood for such $d_r^*\langle\eta^2\rangle^{1/2}$ values (see Sec. I). A practical example of such a structure is a specimen with small-angle boundaries with relatively high dislocation densities in the boundaries, in which the lattice distortion due to the dislocations in the boundaries is large but limited to narrow regions adjacent to the boundaries [see results for large D/d of Wilkens (1979)].

Order-independent line broadening ("size broadening") for $w_r \downarrow 0$ also occurs if the defects are not periodically distributed. For an arbitrary $p_D(D)$, $\beta_r(d_r^*)$ approaches asymptotically to $\mu/(\mu+1)$ for $d_r^*\langle\eta^2\rangle^{1/2} \gtrsim \frac{1}{2}$ [*cf.* Eq. (C.25); for μ, see Eq. (28)]. The theory of "true" size broadening states that in the case of a distribution of crystal sizes T, the size broadening β^S equals T_v^{-1}, where $T_v = \langle T^2\rangle/\langle T\rangle$ is a volume-weighted average (*e.g.* Delhez, Keijser & Mittemeijer, 1982). Using Eq. (28) for the distribution of T, it follows $T_v = \langle T\rangle(\mu+1)/\mu$ and indeed, $\beta^S\langle T\rangle = \mu/(\mu+1)$ is obtained. Also the size Fourier coefficients calculated using Eq. (28) for the size distribution are exactly equal to the Fourier coefficients obtained for the strained, infinitely large crystal with large $d_r^*\langle\eta^2\rangle^{1/2}$ [*i.e.* Eq. (C.23) with $E = 0$].

C. Component strain fields with intermediate widths

For intermediate w_r, the dependence of $\beta_r(d_r^*)$ on $d_r^*\langle e^2\rangle^{1/2}$ is complex (see Fig. 4a). For small $d_r^*\langle e^2\rangle^{1/2}$, the relation is always quadratic: $\beta_r(d_r^*) \propto d_r^{*2}\langle e^2\rangle$. For large $d_r^*\langle e^2\rangle^{1/2}$, $\beta_r(d_r^*)$ can be described by a straight line with, if extrapolated, a positive intercept of the ordinate. With increasing w_r, the slope increases from 0 to $\sqrt{2\pi}$, whereas the intercept decreases from 1 to 0. For $w_r \geq 1$, the behaviour is almost as for $w_r \to \infty$. For $w_r \leq 0.01$, $\beta_r(d_r^*)$ behaves almost as in the limit $w_r \downarrow 0$.

The behaviour of the Fourier coefficients for three intermediate w_r values is shown in Fig. 5. The shapes of the curves change from more or less straight lines for small w_r to a Gaussian for large w_r. The tails of the corresponding line profiles become less pronounced with increasing w_r. It has been shown theoretically that the tangent to $A(L,d^*)$ in $L = 0$ is always inversely proportional to the crystal size and that the curvature d^2A/dL^2 in $L = 0$ is proportional to $d^{*2}\langle e^2\rangle$ (Eastabrook & Wilson, 1952). Since here the Fourier coefficients are calculated for an infinitely long column, always a horizontal tangent in $L_r = 0$ is observed (see Fig. 5d).

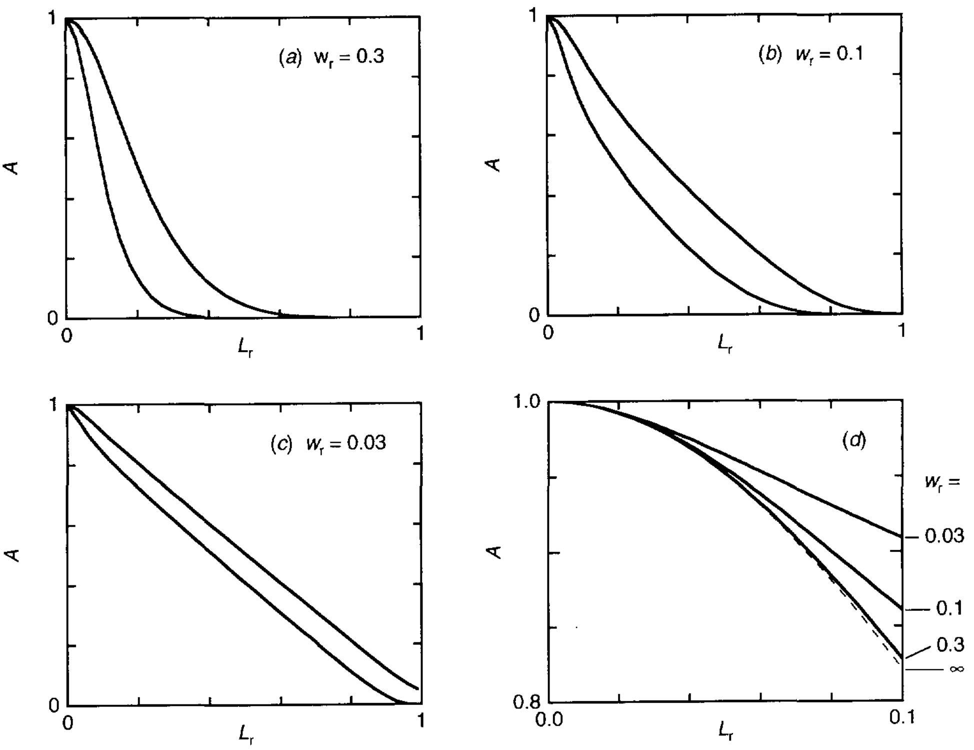

Fig. 5: Fourier coefficients of broadened line profiles calculated for three intermediate values (indicated) of the relative width w_r of the component strain fields: (*a*)-(*c*) using $d_r^*\langle e^2\rangle^{1/2} = 1$ (first order; upper line) and $d_r^*\langle e^2\rangle^{1/2} = 2$ (second order; lower line), (*d*) using $d_r^*\langle e^2\rangle^{1/2} = 1$, behaviour at small L_r.

Further, since $d_r^{*2}\langle e^2\rangle$ is the same for all sets of Fourier coefficients shown in Fig. 5d, the initial curvature is independent of w_r. The next term in the expansion of $A(L_r,d_r^*)$ is proportional to L^4, $\langle e^4\rangle$ and the mean squared strain derivative $\langle e'^2\rangle$ (Berkum, Vermeulen, Delhez, Keijser & Mittemeijer, 1994). Since $e(x)$ has more extreme values and steeper peaks for smaller w_r (see Fig. 3), both $\langle e^4\rangle$ and $\langle e'^2\rangle$ increase with decreasing w_r. Consequently, the smaller w_r, the smaller the L_r value at which the downward parabolic behaviour of $A(L_r,d_r^*)$ disappears and upward curvature starts.

The shape of a first and a second order of reflection are markedly different: in general, the tails of $A(L_r,d_r^*)$ for the higher order of reflection are more pronounced in a relative sense [*e.g.* relative to the width at $A(L_r,d_r^*) = 0.5$] (see Figs. 5a-c). The tails of the corresponding line profiles are also more pronounced for the higher order of reflection. The differences in line width between a first and a second order of reflection are influenced strongly by w_r. In general, the difference diminishes with decreasing w_r (see Fig. 5a-c). Since order-dependence of line broadening can be related to incoherency of diffraction, this observation can be interpreted as a gradual loss of coherency of the diffraction with decreasing w_r. In the limit $w_r \downarrow 0$, incoherent diffraction by the blocks of undistorted material between the defects ("domains") is obtained, as discussed in Sec. IV.B.

The influence of the distribution of the projected-defect positions on $A(L_r,d_r^*)$ for intermediate w_r is shown in Fig. 6. The Fourier coefficients are most sensitive to μ [for μ, see Eq. (28)] at larger L_r values: the larger μ, the faster $A(L_r,d_r^*)$ decreases to zero ($\mu = \infty$ corresponds to periodically distributed defects). At small L_r the Fourier coefficients are usually slightly larger for larger μ. For large w_r the Fourier coefficients become less dependent of μ (*cf.* Sec. IV.A).

Experimental observations suggest that the distortion fields in plastically deformed specimens are best described by w_r values of the order of 0.1 (Berkum, Delhez, Keijser & Mittemeijer, 1994). Therefore, the conclusions reached for intermediate w_r values are most relevant for practice.

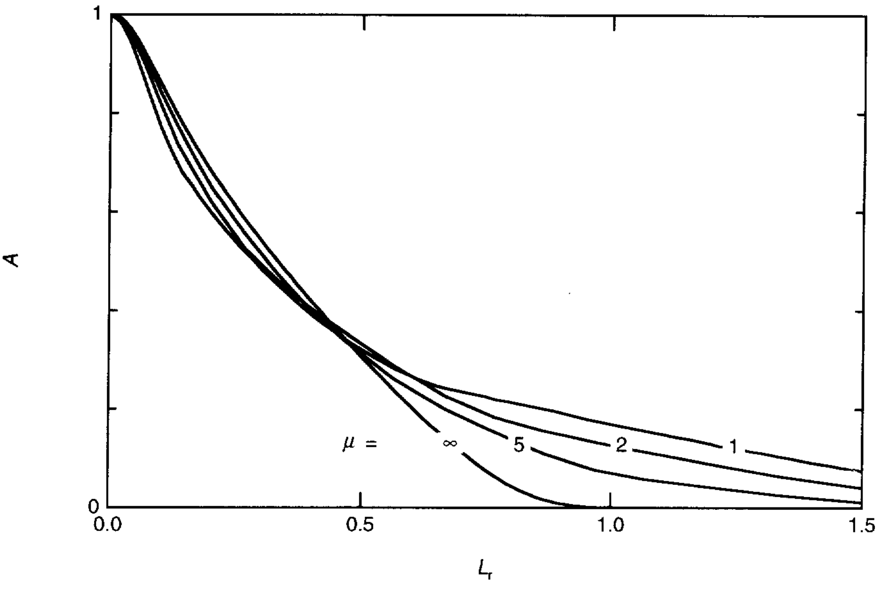

Fig. 6: Fourier coefficients of broadened line profiles calculated for different defect-distance distributions characterized by μ [see Eq. (28)], using $w_r = 0.1$ and $d_r^{*2}\langle e^2\rangle = 1$. The step size in L_r used was relatively large, which produced the kinks in the curves.

V. CONCLUSIONS

The diffraction-line broadening due to lattice distortions associated with crystal defects can be described by means of a general statistical model for the strain field in a column parallel to the diffraction vector. The strain-field model consists of a superposition of component strain fields, each of which associated with a crystal defect close to the column, with statistically determined amplitudes and distances between the projections of the defects onto a line parallel to the diffraction vector. For constant widths of the component strain fields relative to the average projected-defect distance (constant w_r), the line breadth is proportional to the average projected-defect distance and the line shape is independent of this distance.

The order-dependence of the line shape and the line width (integral breadth) is influenced strongly by the width of the component strain fields relative to the average projected-defect distance, which determines the "peakedness" of the overall strain field. For a large relative width of the component strain fields, *i.e.* a smooth overall strain field, the line shape is close to Gaussian and the line width is proportional to the order of reflection. For a very small relative width of the component strain fields, *i.e.* a sharply peaked overall strain field, the line has much more pronounced tails than a Gaussian and the line width is increasing with the squared order of reflection for small diffraction vectors (*i.e.* small 2θ) and small mean squared strains and becomes constant for larger diffraction vectors (*i.e.* larger 2θ) and larger mean squared strains. In the latter case, the regions between the projected defects can be considered as independently diffracting domains, *i.e.* the line broadening might as well be described as size broadening with the regions between the projected defects acting as separate crystals.

If the relative width of the component strain fields is intermediate, which pertains to practical specimens, the order-dependence of the line width cannot be seized in a simple relationship. The line shape changes with the order of reflection: the tails become more pronounced with increasing order. The consequences for methods that use the order-dependence to interpret measured line broadening in terms of size and strain are treated in the next paper (Berkum, Delhez, Keijser & Mittemeijer, 1994).

ACKNOWLEDGEMENTS

The author is very much indebted to Prof. E.J. Mittemeijer, Dr. Th.H. de Keijser, and Dr. R. Delhez for stimulating discussions and critical comments on the manuscript.

APPENDIX A: STRAIN FIELDS ROUND DISLOCATIONS

Consider a straight screw dislocation in the z direction and through the origin of a rectangular co-ordinate system (x,y,z) in an infinite, elastically isotropic medium. The only non-vanishing displacement component is u_z in the z direction (Hirth & Lothe, 1982):

$$u_z(x,y,z) = \frac{b}{2\pi} \arctan\left(\frac{y}{x}\right), \tag{A.1}$$

where b is the length of the Burgers' vector. Consider an arbitrary line making an angle φ with the z direction and having its closest distance Δ to the z axis at the position (x_0,y_0,z_0), where $\Delta = \sqrt{x_0^2+y_0^2}$. Introduce a second rectangular co-ordinate system (x',y',z') with its origin at $(x,y,z) = (0,0,z_0)$, the z' direction parallel to the line and the x' axis through $(x,y,z) = (x_0,y_0,z_0)$ (see Fig. A1). Then, the position $(x,y,z) = (x_0,y_0,z_0)$ becomes $(x',y',z') = (\Delta,0,0)$. The line is defined by $(x',y',z') = (\Delta,0,p)$, where p is a variable. The co-ordinates (x,y,z) are related to (x',y',z') by:

$$\begin{aligned} x &= x'\cos\theta - y'\sin\theta\cos\varphi - z'\sin\theta\sin\varphi \\ y &= x'\sin\theta + y'\cos\theta\cos\varphi + z'\cos\theta\sin\varphi \\ z &= z_0 \qquad\quad - y'\sin\varphi \qquad\quad + z'\cos\varphi, \end{aligned} \tag{A.2}$$

where $\theta = \arctan(x_0/y_0)$. In the z' direction the displacement $u_{z'}$ equals $u_z \cos\varphi$. The strain in the z' direction $e_{z'z'}$ is identical to $\partial u_{z'}/\partial z'$. Expressing u_z according to Eq. (A.1) in terms of x', y' and z' using Eq. (A.2), $e_{z'z'}$ can now be calculated along the line (use $x' = \Delta$ and $y' = 0$):

$$e_{z'z'} = \frac{b}{2\pi\Delta} \frac{\cos\varphi\sin\varphi}{1 + (\frac{z'\sin\varphi}{\Delta})^2}. \tag{A.3}$$

Thus, the strain along any line passing a screw dislocation behaves as a Lorentzian, with an amplitude and a width depending on the distance and the orientation of the line with respect to the dislocation line. For edge dislocations, the same procedure leads to the conclusion that only the tails of the strain profile along a line parallel to the Burgers' vector behaves Lorentzian.

APPENDIX B: INFINITELY BROAD COMPONENT STRAIN FIELDS

If the strain fields of the individual defects are much broader than the average defect distance ($w >> \langle D \rangle$), the strain $e(x)$ consists of very many statistically independent contributions $e_i(x)$ [see Eqs. (5) and (6)]. Therefore, the distribution $[p_e(e)]_{x,\{x_i\}\backslash\{x_0\}}$ of e for fixed x and $\{x_i\}\backslash\{x_0\}$ is Gaussian (central limit theorem), independent of the shape of $p_a(a)$. The variance $\langle e^2 \rangle_{x,\{x_i\}\backslash\{x_0\}}$

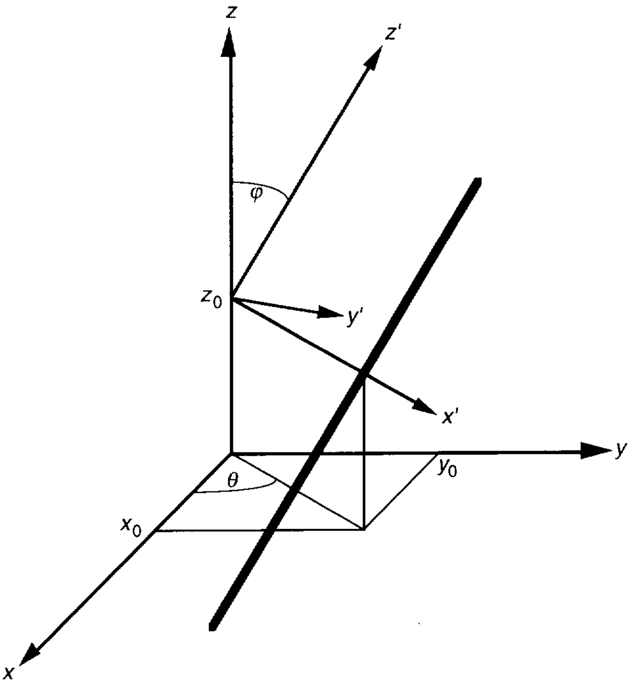

Fig. A1: The relation between two rectangular co-ordinate systems (x,y,z) and (x',y',z') and an arbitrary line (thick line) with its closest distance to the z axis at $(x,y,z) = (x_0,y_0,z_0)$.

is independent of x or $\{x_i\}\backslash\{x_0\}$, since the large and small strains are not confined to regions round and between the positions x_i, respectively, if $w >> \langle D\rangle$. Therefore, $\langle e^2\rangle_{x,\{x_i\}\backslash\{x_0\}} \approx \langle e^2\rangle$, independent of $p_D(D)$. Further, $e(x)$ is approximately constant over distances much smaller than w (*cf.* Fig. 3), so that $Z_L(x) \approx Le(x)$ [see Eq. (4)] for $L << w$. In that case, $[p_{Z_L}(Z_L)]_{x,\{x_i\}\backslash\{x_0\}}$ has the same shape as $[p_e(e)]_{x,\{x_i\}\backslash\{x_0\}}$, which is Gaussian, and Eq. (27) is applicable, even if $p_a(a)$ is not Gaussian. The variance $\langle Z_L{}^2\rangle_{x,\{x_i\}\backslash\{x_0\}} \approx L^2\langle e^2\rangle_{x,\{x_i\}\backslash\{x_0\}} \approx L^2\langle e^2\rangle$ is independent of x or $\{x_i\}$. Thus, in the limit $w/\langle D\rangle \rightarrow \infty$, Eq. (27) reduces to:

$$A(L,d^*) = \exp\left(-2\pi^2 d^{*2} L^2 \langle e^2\rangle\right) \qquad \text{for } L << w. \tag{B.1}$$

If $w/\langle D\rangle = \infty$ and $\langle D\rangle$ is non-zero, $w = \infty$, so that the condition $L << w$ can be neglected. Then, the Fourier transform and, consequently, the corresponding line profile are Gaussian and the integral breadth can be calculated from Eq. (B.1) using Eq. (42):

$$\beta = \sqrt{2\pi}\, d^*\langle e^2\rangle^{1/2}. \tag{B.2}$$

The above expressions hold for any shape $f(x)$ of the strain fields of the individual defects.

If $w/\langle D\rangle$ is large but finite, Eq. (B.1) holds approximately. If $d^*\langle e^2\rangle^{1/2} \gtrsim 1/w$, $A(L,d^*)$ decreases virtually to zero for $L << w$ and the restriction $L >> w$ can again be neglected. For smaller $d^*\langle e^2\rangle^{1/2}$, Eq. (B.1) is not an acceptable approximation for large L and β deviates from Eq. (B.2) (*cf.* Fig. 4 for $w/\langle D\rangle = 1$).

APPENDIX C: INFINITELY NARROW COMPONENT STRAIN FIELDS[3]

In the limit $w/\langle D\rangle \downarrow 0$, the strain field of an individual defect is a delta function. Therefore, it is enclosed by the correlation length L completely or not at all. If L encloses defect i, then L is elongated by an amount $\langle D\rangle\eta_i$, where $\eta_i = Fa_i/\langle D\rangle$ with F being the full area under $f(x)$ [using Eq. (35) for $f(x)$, $F = \sqrt{\pi w C}$]. In general, if m projected defects, numbered 1 to m, are enclosed in the interval $[x - \frac{1}{2}L\ , x + \frac{1}{2}L]$, then $Z_L(x)$ can be written as:

$$Z_L(x) = \langle D\rangle \sum_{i=1}^{m} \eta_i. \tag{C.1}$$

In the following, only the case of a Gaussian $p_a(a)$ with a variance $\langle a^2\rangle$ is considered. Sine coefficients are nil in this case. Since all a_i are statistically independent, the distribution of Z_L for fixed x and fixed $\{x_i\}$ is also Gaussian and it has a variance $m\langle D\rangle^2\langle\eta^2\rangle$, where $\langle\eta^2\rangle = F^2\langle a^2\rangle/\langle D\rangle^2$ [$= \pi w\langle e^2\rangle/\langle D\rangle$ if Eq. (35) is used for $f(x)$]. For fixed $\{x_i\}$, the interval $[x - \frac{1}{2}L$, $x + \frac{1}{2}L]$ encloses different numbers m of defects for different positions x. If the chance that L encloses m defects is denoted as $p_m(m)$, then $p_{Z_L}(Z_L)$ can be written as the sum of partial distributions $[p_{Z_L}(Z_L)]_m$ (one for each m):

$$p_{Z_L}(Z_L) = \sum_{m=0}^{\infty} p_m(m)\, [p_{Z_L}(Z_L)]_m, \tag{C.2}$$

where $[p_{Z_L}(Z_L)]_m$ is Gaussian with a variance $m\langle D\rangle^2\langle\eta^2\rangle$. Substituting Eq. (C.2) in Eq. (2) and solving the integral [*cf.* Eq. (27)] for each m separately yields:

$$A(L,d^*) = \sum_{m=0}^{\infty} p_m(m) \exp(-2\pi^2 d^{*2} m\langle D\rangle^2\langle\eta^2\rangle) = \sum_{m=0}^{\infty} p_m(m)\, E^m, \tag{C.3}$$

---

[3] For very narrow distortion fields, *i.e.* w of the order of the lattice spacing d, the use of a continuum model becomes questionable. However, is was found that Fourier coefficients calculated from discrete lattice planes displaced according to the present strain-field model and from the continuum model itself are identical for L values equal to a multiple of d.

where $E = \exp(-2\pi^2 d^{*2}\langle D\rangle^2\langle\eta^2\rangle)$. In the following, Eq. (C.3) is elaborated by calculating, for given L, $p_m(m)$ from $p_D(D)$ according to Eq. (28).

I. Periodically distributed defects

If projected defects are always separated by a distance $\langle D\rangle$, then $p_m(m)$ is easily calculated. A correlation length $L < \langle D\rangle$ encloses no projected defects with a probability $(\langle D\rangle - L)/\langle D\rangle$ or one defect with a probability $L/\langle D\rangle$, *i.e.* $p_m(0) = (\langle D\rangle - L)/\langle D\rangle = 1 - L_r$ ($L_r \equiv L/\langle D\rangle$), $p_m(1) = L/\langle D\rangle = L_r$ and $p_m(m) = 0$ for $m > 1$. Correspondingly, an arbitrary length L encloses M defects with a probability $M+1-L_r$ or $M+1$ defects with a probability $L_r - M$, where M is the integer part of L_r. Thus: $p_m(M) = M+1-L_r$, $p_m(M+1) = L_r - M$ and all other $p_m(m)$ are nil. Calculating $A(L,d^*)$ using Eq. (C.3) and these $p_m(m)$ values yields:

$$A(L,d^*) = (M + 1 - L_r)\, E^M + (L_r - M)\, E^{M+1}. \tag{C.4}$$

The relative integral breadth $\beta_r(d^*) \equiv \beta(d^*)\langle D\rangle$ of a line profile can be calculated from Eq. (C.4) using Eq. (42) by collecting the terms containing equal powers of E, yielding:

$$\beta_r(d^*) = \frac{1}{2(1 + E + E^2 + \ldots) - 1} = \frac{1 - E}{1 + E}. \tag{C.5}$$

II. Non-periodically distributed defects: integer μ

Using the projected-defect distance distribution $p_D(D)$ according to Eq. (28), the distribution $p_m(m)$ has been calculated for integer μ. Firstly, consider $p_m(0)$, *i.e.* the chance that L encloses no defects. The chance that an arbitrary position in the column is within an undistorted region with a length between D and $D + \mathrm{d}D$ is proportional to $D\, p_D(D)\, \mathrm{d}D$. Since $\int D\, p_D(D)\, \mathrm{d}D = \langle D\rangle$, this chance, if normalized correctly, equals $D\, p_D(D)\, \mathrm{d}D / \langle D\rangle$. The chance that a length L round this arbitrary position fits in the undistorted region is nil if $D < L$ and $(D-L)\, p_D(D)\, \mathrm{d}D / \langle D\rangle$ if $D \geq L$. To calculate $p_m(0)$, all $D \geq L$ have to be taken into account:

$$p_m(0) = \frac{1}{\langle D\rangle} \int_L^{\infty} (D - L)\, p_D(D)\, \mathrm{d}D. \tag{C.6}$$

Substituting Eq. (28) in Eq. (C.6), dividing the integrand in Eq. (C.6) in two terms and using Eq. (3.351.2) of Gradshteyn & Ryzhik (1980) for both terms yields:

$$p_m(0) = \mathrm{e}^{-\mu L_\mathrm{r}}\left[\sum_{k=0}^{\mu}\frac{(\mu L_\mathrm{r})^k}{k!} - L_\mathrm{r}\sum_{k=0}^{\mu-1}\frac{(\mu L_\mathrm{r})^k}{k!}\right]$$

$$= \mathrm{e}^{-\mu L_\mathrm{r}}\left[(1-L_\mathrm{r})\sum_{k=0}^{\mu}\frac{(\mu L_\mathrm{r})^k}{k!} - \frac{(\mu L_\mathrm{r})^\mu}{\mu!}\right]. \qquad \text{(C.7)}$$

To calculate $p_m(1)$, suppose the defect enclosed by L is situated at a distance D_1 from one end of the correlation length L and, consequently, at a distance $L–D_1$ from the other end. To accomplish that, the lengths of the two undistorted regions bounding the defect have to be larger than D_1 and $L–D_1$, respectively. The joint probability P_1 of such an event equals:

$$P_1 = \left[\int_{D_1}^{\infty} p_D(D)\,\mathrm{d}D\right]\left[\int_{L-D_1}^{\infty} p_D(D)\,\mathrm{d}D\right]. \qquad \text{(C.8)}$$

The probability $p_m(1)$ follows from P_1 by accounting for the fact that D_1 can take all values between 0 and L and for the chance $\mathrm{d}D_1/\langle D\rangle$ that there is a defect between D_1 and $D_1+\mathrm{d}D_1$ from one end of L:

$$p_m(1) = \frac{1}{\langle D\rangle}\int_0^L P_1\,\mathrm{d}D_1. \qquad \text{(C.9)}$$

Analogously, the more general expression for $p_m(m)$ for $m \geq 1$ can be derived. For $m \geq 1$, the correlation length L encompasses $m–1$ undistorted regions completely and two parts of undistorted regions at both ends (*cf.* Fig. C1). The distance from one end of L to the first defect enclosed by L is denoted as D_1, from the first defect to the second one as D_2, and so on, leaving $L_m \equiv L–D_1–D_2–...D_m$ for the distance from the last defect enclosed by L to the other end of L. The joint probability density P_m of exactly the distances $D_1, D_2, ... D_m$ and L_m equals:

$$P_m = \left[\int_{D_1}^{\infty} p_D(D)\,\mathrm{d}D\right] p_D(D_2)\,p_D(D_3)\,...\,p_D(D_m)\left[\int_{L_m}^{\infty} p_D(D)\,\mathrm{d}D\right]. \qquad \text{(C.10)}$$

Substituting Eq. (28) in Eq. (C.10) and solving the two integrals using Eq. (3.351.2) of Gradshteyn & Ryzhik (1980), P_m can be written as:

$$P_m = \mathrm{e}^{-\mu L_\mathrm{r}}\left[\frac{\mu^\mu}{(\mu-1)!\,\langle D\rangle^\mu}\right]^{m-1}\sum_{k=0}^{\mu-1}\sum_{k'=0}^{\mu-1}\frac{1}{k!\,k'!}\left(\frac{\mu}{\langle D\rangle}\right)^{k+k'} D_1^k\,(D_2\,D_3\,...\,D_m)^{\mu-1}\,L_m^{k'}.$$

$$\text{(C.11)}$$

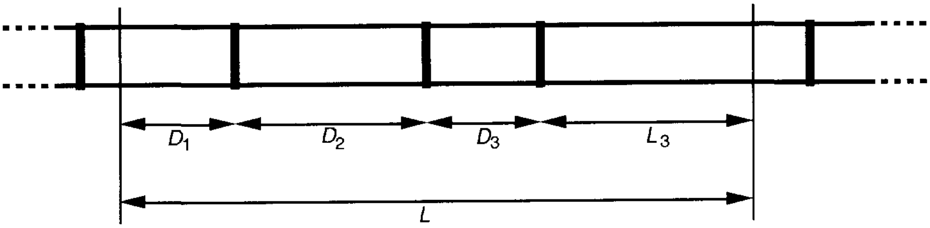

Fig. C1: Example of a correlation length L enclosing three defects (solid vertical bars). Consequently, L consists of two complete undistorted regions (D_2 and D_3) and two parts (D_1 and $L_3 \equiv L - D_1 - D_2 - D_3$) of undistorted regions at both ends.

The calculation of $p_m(m)$ from P_m involves m integrations: D_m can take all values between 0 and $L_{m-1} = L - D_1 - D_2 - \ldots D_{m-1}$, D_{m-1} can take all values between 0 and L_{m-2}, ... D_2 can take all values between 0 and $L_1 = L - D_1$, and, finally, D_1 can take all values between 0 and L. The probability of a defect between D_1 and $D_1 + \mathrm{d}D_1$ equals $\mathrm{d}D_1 / \langle D \rangle$. Thus, $p_m(m)$ reads:

$$p_m(m) = \frac{1}{\langle D \rangle} \int_{D_1=0}^{L} \int_{D_2=0}^{L_1} \cdots \int_{D_m=0}^{L_m} P_m \;\mathrm{d}D_m \ldots \mathrm{d}D_2 \, \mathrm{d}D_1 . \qquad \text{(C.12)}$$

For the integration that is performed firstly, that over D_m, only the last two factors on the right-hand side of Eq. (C.11) (*i.e.* the powers of D_m and $L_m^{k'}$) have to be considered. Using the binomial theorem, $L_m^{k'}$ can be expressed as:

$$L_m^{k'} = (L_{m-1} - D_m)^{k'} = \sum_{j=0}^{k'} \binom{k'}{j} L_{m-1}^{k'-j} (-D_m)^j \qquad \text{(C.13)}$$

and the integration over D_m yields:

$$\int_0^{L_{m-1}} D_m^{\mu-1} \, L_m^{k'} \, \mathrm{d}D_m = f_0 \, L_{m-1}^{k'+\mu} \qquad \text{(C.14)}$$

with

$$f_0 = \sum_{j=0}^{k'} \binom{k'}{j} \frac{(-1)^j}{\mu + j} . \qquad \text{(C.15)}$$

One by one, the integrations over D_{m-1} to D_2 can be performed analogously, with the integration over D_i yielding a power of L_{i-1} and a factor f_{m-i} [*cf.* Eq. (C.14)]:

$$f_i = \sum_{j=0}^{k'+i\mu} \binom{k'+i\mu}{j} \frac{(-1)^j}{\mu + j} . \qquad \text{(C.16)}$$

In the case of the last integration (over D_1), a power of L remains and the factor is denoted as F:

$$F = \sum_{j=0}^{k'+(m-1)\mu} \binom{k'+(m-1)\mu}{j} \frac{(-1)^j}{\mu+j}. \tag{C.17}$$

Thus, $p_m(m)$ for $m \geq 1$ reduces to [*cf.* Eqs. (C.11) and (C.12)]:

$$\begin{aligned} p_m(m) &= \frac{1}{\langle D \rangle} \mathrm{e}^{-\mu L_\mathrm{r}} \left[\frac{\mu^\mu}{(\mu-1)!\,\langle D \rangle^\mu} \right]^{m-1} \\ &\times \sum_{k=0}^{\mu-1} \sum_{k'=0}^{\mu-1} \frac{1}{k!\,k'!} \left(\frac{\mu}{\langle D \rangle} \right)^{k+k'} f_0 f_1 \cdots f_{m-2}\, F\, D^{k+k'+(m-1)\mu+1}. \end{aligned} \tag{C.18}$$

By using the relation, obtained by conjecture and verified for many n and p values:

$$\sum_{j=0}^{n} \binom{n}{j} \frac{(-1)^j}{p+j} = \frac{n!\,(p-1)!}{(n+p)!}, \tag{C.19}$$

where n is a non-negative integer and p is a positive integer, it can be shown that:

$$f_0 f_1 \cdots f_{m-2}\, F = [((\mu-1)!]^{m-1} \frac{k!\,k'!}{(k+k'+(m-1)\mu+1)!}. \tag{C.20}$$

Substituting Eq. (C.20) in Eq. (C.18) yields:

$$p_m(m) = \frac{1}{\mu} \mathrm{e}^{-\mu L_\mathrm{r}} \sum_{k=0}^{\mu-1} \sum_{k'=0}^{\mu-1} \frac{(\mu L_\mathrm{r})^{k+k'+(m-1)\mu+1}}{(k+k'+(m-1)\mu+1)!}. \tag{C.21}$$

The double sum can be written as a single sum by introducing $\kappa = k + k'$ and counting how often κ occurs in Eq. (C.21):

$$p_m(m) = \mathrm{e}^{-\mu L_\mathrm{r}} \sum_{\kappa=0}^{2\mu-2} \frac{\mu - |\kappa-\mu+1|}{\mu} \frac{(\mu L_\mathrm{r})^{\kappa+(m-1)\mu+1}}{(\kappa+(m-1)\mu+1)!}. \tag{C.22}$$

Finally, substituting Eqs. (C.22) and (C.7) in Eq. (C.3), the Fourier coefficients of the structurally broadened line profile are obtained:

$$\begin{aligned} A(L,d^*) = \mathrm{e}^{-\mu L_\mathrm{r}} \Bigg[& (1-L_\mathrm{r}) \sum_{k=0}^{\mu-1} \frac{(\mu L_\mathrm{r})^k}{k!} + \frac{(\mu L_\mathrm{r})^\mu}{\mu!} \\ & + \sum_{\kappa=0}^{2\mu-2} \frac{\mu-|\kappa-\mu+1|}{\mu} \sum_{m=1}^{\infty} \frac{(\mu L_\mathrm{r})^{\kappa+(m-1)\mu+1}}{(\kappa+(m-1)\mu+1)!} E^m \Bigg]. \end{aligned} \tag{C.23}$$

For $\mu = 1$, Eq. (C.23) reduces to a simple exponential behaviour:

$$A(L,d^*) = e^{-L_r} \sum_{m=0}^{\infty} \frac{L_r^{\,m}}{m!} E^m = e^{-L_r(1-E)}. \tag{C.24}$$

Note that Fourier coefficients $A(L,d^*)$ for infinitely narrow component strain fields [see Eqs. (C.4), (C.23) and (C.24)] have a negative slope in $L = 0$, which is usually interpreted as an indication of size broadening. The initial slope equals $-(1-E)/\langle D\rangle$, conventionally interpreted as a "domain size" equal to $\langle D\rangle/(1-E)$ (*e.g.* Warren, 1969), and it is independent of μ. For all component strain fields with a finite width, $A(L,d^*)$ is horizontal and curved downward in $L = 0$ (see Fig. 5 and its discussion in Sec. IV.C)

The relative integral breadth $\beta_r(d^*)$ has been calculated from $A(L,d^*)$ according to Eq. (C.23) using Eq. (42), Eq. (3.351.2) of Gradshteyn & Ryzhik (1980) and the well-known expressions for the sums of arithmetic and geometric series, yielding:

$$\beta_r(d^*) = \frac{\mu\,(1-E)}{\mu\,(1+E) + 1-E}\,. \tag{C.25}$$

For very small $d^*\langle D\rangle\langle\eta^2\rangle^{1/2}$, it follows from Eq. (C.25) [for E, see below Eq. (C.3)] that $\beta_r(d^*) \approx \pi^2 d^{*2}\langle D\rangle^2\langle\eta^2\rangle$. The proportionality $\beta \propto d^{*2}$ has been derived theoretically and observed experimentally for the class of "paracrystalline" materials (Kulshreshtha, Dweltz & Radhakrishnan, 1971). The ideal paracrystal can indeed be considered as a special case of the model presented in this paper: infinitely narrow component strain fields ($w/\langle D\rangle \downarrow 0$) with the average defect distance $\langle D\rangle$ equal to the average lattice spacing d. Since the root mean squared spacing deviation $d\langle\eta^2\rangle^{1/2}$ in such a structure is much smaller than the spacing d itself and d^{*-1} is usually a small multiple of d, the quantity $d^*\langle D\rangle\langle\eta^2\rangle^{1/2}$ is small (as required for the discussed quadratic behaviour of β). The other limiting case occurs for $d^*\langle D\rangle\langle\eta^2\rangle^{1/2} \to \infty$ (*i.e.* $E \downarrow 0$): $\beta_r(d^*) = \mu/(\mu+1)$, which is discussed in Sec. III.B.

REFERENCES

Abramowitz, M. & Stegun, I.A. (1965). *Handbook of Mathematical Functions* (New York: Dover), pp. 890, 923.

Arley, N. & Buch, K.R. (1950). *Introduction to the Theory of Probability and Statistics* (New York: John Wiley), pp. 39, 47-48.

Berkum, J.G.M. van, Delhez, R., Keijser, Th.H. de & Mittemeijer, E.J. (1992). *Phys. stat. sol. (a)* **134**, 335-350. See Chapter 5 of this thesis.

Berkum, J.G.M. van, Delhez, R., Keijser, Th.H. de & Mittemeijer, E.J. (1994). To be published. See Chapter 8 of this thesis.

Berkum, J.G.M. van, Vermeulen, A.C., Delhez, R., Keijser, Th.H. de & Mittemeijer, E.J. (1994). *J. Appl. Cryst.* In the press. See Chapter 3 of this thesis.

Cowley, J.M. (1981). *Diffraction Physics* (Amsterdam: Elsevier Science), pp. 73, 141.

Delhez, R., Keijser, Th.H. de & Mittemeijer, E.J. (1982). *Fresenius Z. anal. Chem.* **312**, 1-16.

Eastabrook, J.N. & Wilson, A.J.C. (1952). *Proc. Phys. Soc. London* **B65**, 67-75.

Fowles, G.R. (1968). *Introduction to Modern Optics* (New York: Holt, Rinehart and Winston), pp. 61-83.

Gaál, I. (1984). In: *Microstructural Characterization of Materials by Non-Microscopical Techniques*, eds. Hessel Andersen, N., Eldrup, M., Hansen, N., Juul Jensen, D., Leffers, T., Lilholt, H., Pedersen, O.B., Singh, B.N. (Roskilde, Denmark: Risø National Lab.), pp. 249-254.

Gradshteyn, I.S. & Ryzhik, I.M. (1980). *Table of Integrals, Series, and Products* (New York: Academic), p. 310.

Groma, I., Ungár, T. & Wilkens, M. (1988). *J. Appl. Cryst.* **21**, 47-53.

Hirth, J.P. & Lothe, J. (1982). *Theory of Dislocations*, 2nd ed. (New York: John Wiley), pp. 60, 78, 733.

Kulshreshtha, A.K., Dweltz, N.E. & Radhakrishnan, T. (1971). *J. Appl. Cryst.* **4**, 116-125.

Martin, B.R. (1971). *Statistics for Physicists* (London: Academic), pp. 22-24.

Sommerfeld, A. (1964). *Optics. Lectures on Theoretical Physics*, vol. IV (New York: Academic), pp. 191-193.

Stokes, A.R. & Wilson, A.J.C. (1944). *Proc. Phys. Soc. London* **56**, 174-181.

Wagner, C.N.J. (1966). In: *Local Atomic Arrangements*, eds. Cohen, J.B. & Hilliard, J.E. (New York: Gordon and Breach), pp. 219-269

Warren, B.E. (1959). *Prog. in Metal Phys.* **VIII**, 147-202.

Warren, B.E. (1969). *X-ray Diffraction* (Reading, Massachusetts: Addison-Wesley), pp. 264-275.

Wilkens, M. (1979). *J. Appl. Cryst.* **12**, 119-125.

Wilson, A.J.C. (1970). *Elements of X-ray Crystallography* (Reading, Massachusetts: Addison-Wesley), pp. 191-222.

CHAPTER 8

DIFFRACTION-LINE BROADENING DUE TO LATTICE DISTORTIONS

II. Methods of Analysis: Line-Profile Decomposition Using Size and Strain Parameters *versus* Line-Profile Simulation Using a Generally Applicable Strain-Field Model

J.G.M. VAN BERKUM, R. DELHEZ, TH.H. DE KEIJSER, AND E.J. MITTEMEIJER
Laboratory of Materials Science, Delft University of Technology,
Rotterdamseweg 137, 2628 AL Delft, The Netherlands.

ABSTRACT

The adequacy of two methods frequently applied to analyse X-ray diffraction-line broadening (the Warren-Averbach analysis and the Williamson-Hall analysis) is investigated by applying them to simulated line profiles. These line profiles are calculated using a realistic and flexible model for the spatial distribution of lattice defects and their associated strain fields. The "size" and "strain" parameters deduced by the methods mentioned are discussed with reference to the strain-field model. It is concluded that only in limiting cases the results can be related directly to the microstructure. Experimental line profiles taken from a ball-milled tungsten powder are used to show that the line-profile simulations on the basis of the present model pertain to realistic situations. It is shown that, in principle, an interpretation of measured line broadening is possible directly in terms of strain-field parameters.

I. INTRODUCTION

Broadening of (X-ray) diffraction-line profiles is caused by non-ideal optics of the instrument, wavelength dispersion and structural imperfectness of the specimen. Usually, the structurally broadened line profile is considered as a convolution of (i) a size-broadened profile, due to a finite size of domains in the specimen diffracting incoherently with respect to each other, and (ii) a strain-broadened profile, due to varying displacements of the atoms with respect to their reference positions (*e.g.* Warren, 1969). Size broadening is independent of the order of reflection; strain broadening is order-dependent. A number of methods of analysis use measured line profiles of two or more orders of reflection and try to separate "size" and "strain" contributions on the basis of the order-dependence of the measured line broadening.

An important class of materials studied using diffraction-line broadening are cold-worked metals. The grains or crystals in such specimens are usually too large to cause appreciable size broadening effects. Therefore, the line broadening observed must be entirely due to the distortion fields associated with the large number of lattice defects present after deformation (predominantly dislocations in this case). Nevertheless, size-strain separation methods like the Warren-Averbach analysis (Warren & Averbach, 1950, 1952) and the Williamson-Hall analysis (Hall, 1949; Williamson & Hall, 1953) usually attribute a significant part of the broadening to "size". As an explanation, it has been suggested that the lattice defects or combinations of them act as "coherence boundaries", that break up the crystals into domains diffracting essentially incoherently with respect to each other (Warren, 1959). However, it has been shown that parts of a crystal can be considered to diffract incoherently only in case of exceptional strain fields: large distortions concentrated in small isolated regions of a crystal (Berkum, 1994; hereafter called paper I).

The size-strain separation methods mentioned, based on decomposition of measured line profiles, involve specifications of the order-dependences of the size and the strain broadenings, that affect the results obtained to an unknown extent. A completely different approach of line-broadening analysis is matching line profiles simulated on the basis of a microstrain model to measured line profiles (see *e.g.* Berkum, Delhez, Keijser & Mittemeijer, 1992). The line-profile calculation itself involves no assumptions, apart from those inherent to the kinematical diffraction theory. Therefore, if adequate strain models can be developed, this approach can be more valuable than the existing size-strain separation methods.

The aim of this paper is twofold: (i) assessing the meaning of the "size" and "strain" obtained by line-profile decomposition according to the Williamson-Hall analysis and the Warren-Averbach analysis and (ii) investigating the possibility of an interpretation of line broadening directly in terms of strain-field parameters by line-profile simulation. For the first part, line profiles that are calculated on the basis of a realistic and flexible model for the strain field in a distorted specimen (see paper I) and line profiles measured from a cold-worked specimen are used; for the second part, the experimental line profiles are used again.

II. MODEL

To describe a line profile, the crystal is divided in columns parallel to the (average) diffraction vector ***H***. Then, the broadening is exclusively determined by the behaviour of the strain component e parallel to ***H*** as a function of the position x in each column (the axis $\boldsymbol{x}$ is parallel to ***H***). The behaviours of $e(x)$ occurring in practice are so complicated that they can be described meaningfully only in a statistical way. In paper I, a realistic statistical description of $e(x)$ for an infinitely long column is proposed, where the column is considered representative for all columns together in a three-dimensional specimen. (Effects due to the finite size of the crystals are neglected, since these effects are often very small in practice. If this is not the case, they can easily be included.) It is assumed that the column passes a number of lattice defects (*e.g.* dislocations) close enough to "feel" their strain fields. The average distance between the projections onto the column of these defects is denoted $\langle D\rangle$. Usually, the average projected-defect distance $\langle D\rangle$ is two to three times smaller than the average distance between the defects in three dimensions (see paper I). The total strain field $e(x)$ is the sum of "component strain fields" induced in the column by the individual defects i (i is an integer). The component strain fields in the column are characterized by a certain shape function with a width w, taken equal for all projected defects, and with a maximum value a_i, that varies from one projected defect to the other, *e.g.* because of varying orientations and distances of the defects with respect to $\boldsymbol{x}$. For each projected defect, the probability density of a value $a_i = a$ is given by the distribution function $p_a(a)$ with a mean $\langle a\rangle = 0$ and a variance $\langle a^2\rangle$. The variance of the total local strain, the mean squared strain $\langle e^2\rangle$, is proportional to $\langle a^2\rangle/\langle D\rangle$ and independent of w [see Eq. (34) of paper I].

The nature of the total strain field is strongly influenced by the ratio $w/\langle D\rangle$, the *relative* width of the component strain fields. For large $w/\langle D\rangle$ ($\gtrsim 1$), the component strain fields of the individual defects overlap strongly and the strain is smoothly varying with position in the column. Strain gradients in the column are small. For small $w/\langle D\rangle$ ($\lesssim 0.01$), the component strain fields produce isolated sharp peaks in the total strain field, leaving relatively little distorted regions in between the projected defects.

For the purpose of evaluating the Williamson-Hall analysis and the Warren-Averbach analysis, the average projected-defect distance $\langle D\rangle$, the individual strain field width w and the mean squared strain $\langle e^2\rangle$ are expected to be the most relevant parameters (see Conclusions of paper I). Other model parameters are kept constant: the projected defects are taken periodically distributed (*i.e.* all projected defects have a distance $\langle D\rangle$ to their nearest neighbours), the distribution $p_a(a)$ is taken Gaussian and the shape of the individual strain fields is taken Lorentzian, with w as its half width at half maximum. These choices are based on relevance for practice and reasons of convenience (see paper I). To avoid misunderstandings, the following remarks are made. Firstly, although the distribution of projected defects is periodic, the total strain field is never periodic (see *e.g.* Fig. 3 of paper I), because the maximum strain values a_i are independent variables. Secondly, the shape of the distribution $p_e(e)$ depends on the shape of $p_a(a)$ and the shape of the individual strain fields, but, in spite of the shapes adopted, it is neither Gaussian, nor Lorentzian, because it also depends strongly on the ratio $w/\langle D\rangle$ (see App. A).

On the basis of the strain field $e(x)$ diffraction-line profiles $I'(s,d^*)$ can be calculated as a function of $s = 2\sin\theta/\lambda - d^*$ in reciprocal space, where λ is the wavelength of the radiation used, 2θ is the diffraction angle and d^* is the average length of the diffraction vector $\boldsymbol{H}$, which is taken here as the value of $2\sin\theta/\lambda$ at the centroid of I'. The profile $I'(s,d^*)$ can be expressed as a Fourier series (*e.g.* Warren, 1969):

$$I'(s,d^*) = K \sum_{L=-\infty}^{+\infty} \{A(L,d^*)\cos(2\pi Ls) + B(L,d^*)\sin(2\pi Ls)\}, \tag{1}$$

where K is (approximately) a constant, A and B are the cosine and sine Fourier coefficients and the harmonic parameter L is a distance in real space perpendicular to the reflecting planes, sometimes called the "correlation length", which in practice can be considered as a continuous variable. For the present strain-field model, Fourier coefficients can be expressed in terms of quantities relative to the average projected-defect distance $\langle D\rangle$: $L_r \equiv L/\langle D\rangle$, $w_r \equiv w/\langle D\rangle$ and $d_r^* \equiv d^*\langle D\rangle$ (see Sec. III of paper I). For a Gaussian $p_a(a)$, the cosine Fourier coefficients for a certain L_r and d_r^* are completely determined by $\langle e^2\rangle$ and w_r [substitute $x_r \equiv x/\langle D\rangle$, L_r, w_r and d_r^* into Eqs. (20), (30) and (36) of paper I]:

$$A(L_r,d_r^*) = \int_{-\frac{1}{2}}^{\frac{1}{2}} \exp(-2\pi^2 d_r^{*2}\langle Z_{L_r}^2\rangle_{x_r})\,\mathrm{d}x_r, \tag{2}$$

where, in case of periodically distributed projected defects and Lorentzian component strain fields:

$$\langle Z_{L_r}^2\rangle_{x_r} = \frac{2\,w_r\langle e^2\rangle}{\pi} \sum_{i=-\infty}^{\infty} \left[\arctan\left(\frac{x_r - i + L_r/2}{w_r}\right) - \arctan\left(\frac{x_r - i - L_r/2}{w_r}\right)\right]^2. \tag{3}$$

The sine coefficients $B(L_r,d_r^*)$ are nil in case of symmetrical $p_a(a_i)$. In general, $A(L_r,d_r^*)$ has to be evaluated numerically. Note that d_r^* and $\langle e^2\rangle$ occur only in the combination $d_r^*\langle e^2\rangle^{1/2}$ [see Eqs. (2) and (3)]; therefore, using $d_r^*\langle e^2\rangle^{1/2}$ as a variable, the influence of both parameters is investigated at the same time.

III. LINE-PROFILE DECOMPOSITION OF SIMULATED LINE PROFILES

Methods of analysis based on line-profile decomposition conceive the line profile $I'(s,d^*)$ as the convolution of an order-independent size-broadened profile $I'^S(s)$ and an order-dependent strain-broadened profile $I'^D(s,d^*)$. Usually, the characteristics of two or more line profiles $I'(s,d^*)$ with different values for the length d^* of the diffraction vector are used to estimate characteristics of $I'^S(s)$ and $I'^D(s,d^*)$. The size and strain broadenings are then translated to size and strain parameters that are intended to characterize the microstructure of the specimen.

In the following, broadened line profiles are calculated on the basis of the strain-field model presented in the previous section. Subsequently, these line profiles, as if they were real measurements, are analysed by means of the Williamson-Hall analysis and the Warren-Averbach analysis in terms of size and strain parameters.

A. Williamson-Hall analysis

Procedure

A number of methods use the integral breadths $\beta(d^*)$ (*i.e.* areas divided by heights) of line profiles $I'(s,d^*)$ to estimate the integral breadths β^S of $I'^S(s)$ and $\beta^D(d^*)$ of $I'^D(s,d^*)$ (for an overview, see Klug & Alexander, 1974). All these methods assume that $\beta^D(d^*) \propto d^*$ [*e.g.* $\beta^D(d^*) = \sqrt{2\pi}\, e\, d^*$, where e is a strain parameter] and that $I'^S(s)$ and $I'^D(s,d^*)$ have specific shapes. These assumptions make them liable to systematic errors. Nevertheless, the methods are applied frequently and therefore one of them, the classical, linear version of the Williamson-Hall plot, is investigated here.

In the linear version of the Williamson-Hall analysis (Williamson & Hall, 1953)[1], it is assumed that β^S and $\beta^D(d^*)$ are linearly additive. Further, β^S is identified with $(D_{WH})^{-1}$ and $\beta^D(d^*)$ is identified with $\sqrt{2\pi}\, e_{WH}\, d^*$ (for discussion of the numerical factor, see Stokes & Wilson, 1944), where D_{WH} and e_{WH} are a size and a strain parameter, respectively. Therefore, a straight line is drawn through the data points in a plot of $\beta(d^*)$ *versus* d^* and the intercept of the ordinate is interpreted as $(D_{WH})^{-1}$ and the slope is interpreted as $\sqrt{2\pi}\, e_{WH}$. If more than two orders of reflection are available and they do not lie on a straight line, the analysis should not be applied.

---

[1] On 2θ scale, instead of on s scale, the Williamson-Hall analyis involves a plot of $\beta \cos\theta$ *versus* $\sin\theta$. Then, the intercept of the ordinate is interpreted as λ/D_{WH} and the slope is interpreted as $2\sqrt{2\pi}\, e_{WH}$.

For the general strain-field model, $A(L_r,d_r^*)$ is given by Eqs. (2) and (3). Since the line profiles are symmetrical [*i.e.* all $B(L_r,d_r^*)$ are nil; see below Eq. (3)], the relative integral breadth $\beta_r(d_r^*) \equiv \beta(d_r^*)\langle D\rangle$ can be calculated according to:

$$\beta_r(d_r^*) = \left[\int_{-\infty}^{\infty} A(L_r,d_r^*)\, \mathrm{d}L_r \right]^{-1} . \tag{4}$$

The behaviour of $\beta_r(d_r^*)$ as a function of $d_r^* \langle e^2\rangle^{1/2}$ is always more or less S-shaped (see Fig. 4a of paper I). Consequently, the Williamson-Hall analysis should in fact not be applied. If the Williamson-Hall analysis is applied nevertheless, the slope and the intercept can take many different values (even negative intercepts are possible).

Only for relatively large $d_r^* \langle e^2\rangle^{1/2}$, say $d_r^* \langle e^2\rangle^{1/2} \geq 1/\sqrt{10\, w_r}$, $\beta_r(d_r^*)$ follows a straight line (see Fig. 4a of paper I) and a Williamson-Hall analysis may be meaningful. To investigate the meaning of the parameters D_{WH} and e_{WH} in this case, $\beta_r(d_r^*)$ of a first and a second order of reflection have been calculated using $d_r^* \langle e^2\rangle^{1/2} = 1/\sqrt{10\, w_r}$ for the first order (*e.g.* $d^* = 5\ \mathrm{nm}^{-1}$, $\langle D\rangle = 40$ nm, $w = 4$ nm and $\langle e^2\rangle = 25\times10^{-6}$, which are reasonable values for cold-worked metals). From these $\beta_r(d_r^*)$ values, the size and strain parameters D_{WH} and e_{WH} have been deduced by means of the Williamson-Hall analysis. Since D_{WH} and e_{WH} refer to the size of and the strain within independently diffracting "domains" in the specimen and the line broadening is calculated from the strain field in an infinitely long coherently diffracting column, it is not self-evident what values of D_{WH} and e_{WH} should be expected. Rather arbitrarily, D_{WH} is compared with the average projected-defect distance $\langle D\rangle$ and e_{WH} with the root mean squared strain $\langle e^2\rangle^{1/2}$.

Results and discussion

The results obtained by means of the Williamson-Hall analysis as a function of w_r are shown in Fig. 1a. For very large w_r, all broadening is attributed to strain (*i.e.* $\beta^S = 0$ and $D_{WH} = \infty$), because $\beta_r(d_r^*) \propto d_r^*$ [see Eq. (43) of paper I]. The strain parameter e_{WH} equals $\langle e^2\rangle^{1/2}$. Thus, according to the Williamson-Hall analysis, a smoothly varying strain field induces pure strain broadening.

For $w_r \downarrow 0$, the Williamson-Hall analysis attributes all broadening to size (*i.e.* $\beta^D = 0$ and $e_{WH} = 0$) and D_{WH} equals $\langle D\rangle$. This is understandable too, since $d_r^* \langle e^2\rangle^{1/2} = 1/\sqrt{10\, w_r}$ becomes very large for $w_r \downarrow 0$, in which case β_r approaches 1 and becomes independent of the order of reflection (see Fig. 4b of paper I for large $\langle \eta^2\rangle^{1/2}$). Therefore, the line through the two calculated data points has zero slope and an intercept of the ordinate $\beta_r = 1$. Thus, in the Williamson-Hall analysis the broadening due to a sharply peaked strain field is interpreted as pure size broadening, with a size parameter D_{WH} equal to the average projected-defect distance.

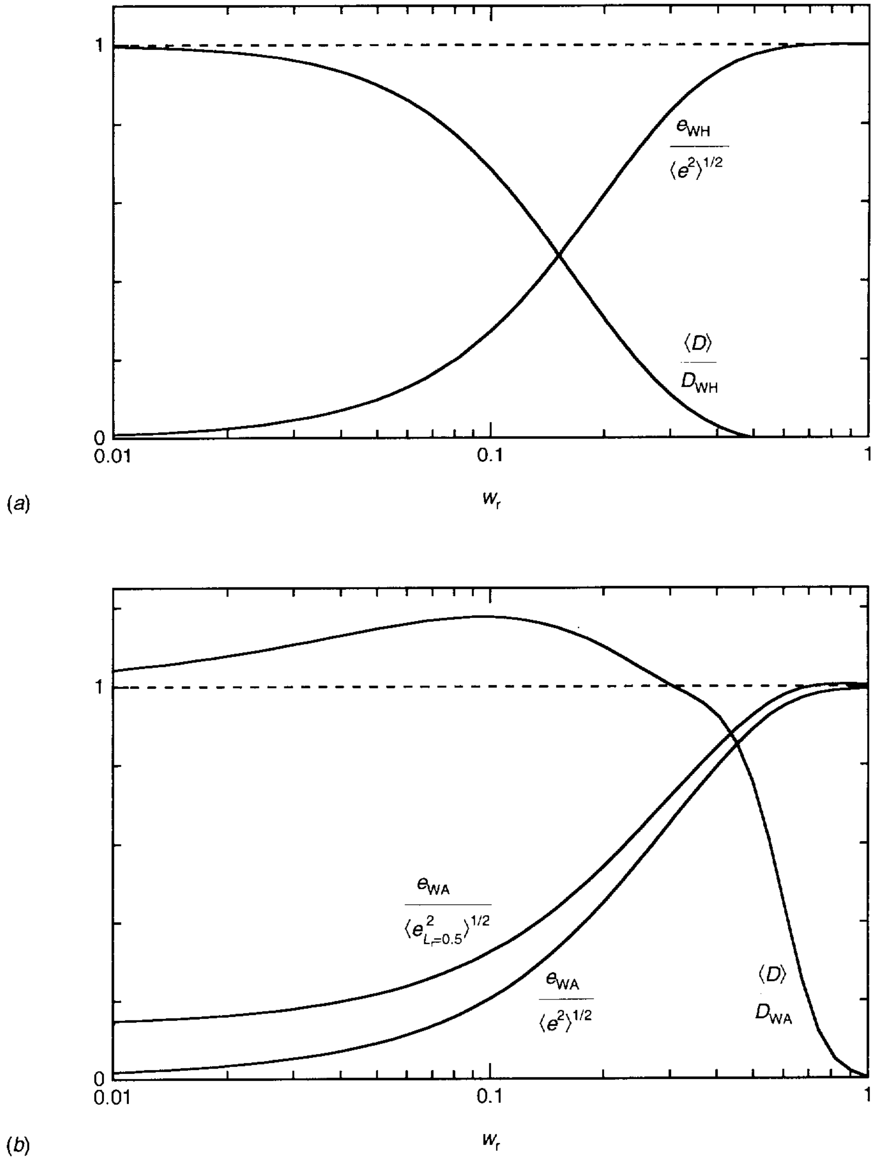

Fig. 1: Results of (*a*) the Williamson-Hall analysis and (*b*) the Warren-Averbach analysis applied to a first and second order line profile, calculated using $d_r^* \langle e^2\rangle^{1/2} = 1/\sqrt{10}\, w_r$ for the first order, as a function of the relative width w_r of the component strain fields. The size parameters D_{WH} and D_{WA} are compared with the average projected-defect distance $\langle D\rangle$. The strain parameters e_{WH} and e_{WA} are compared with the root mean squared strain $\langle e^2\rangle^{1/2}$ and, in the case of e_{WA}, also with the true $\langle e^2_{L_r}\rangle^{1/2}$ at a relative correlation length $L_r = \frac{1}{2}$ (for the definitions of the size and strain parameters, see text).

For intermediate w_r, the Williamson-Hall analysis attributes the calculated line broadening partly to size and partly to strain (see Fig. 1a). The size parameter D_{WH} is always larger than $\langle D\rangle$; the strain parameter e_{WH} is always smaller than $\langle e^2\rangle^{1/2}$. The deviations appear to be correlated: with increasing w_r the decrease of $\langle D\rangle/D_{WH}$ approximately equals the increase of $e_{WH}/\langle e^2\rangle^{1/2}$. However, the relation between the resulting values for D_{WH} and e_{WH} and the simulated strain field is unclear. In practice, without additional information on the nature of the strain field in the specimen, D_{WH} can be anywhere between $\langle D\rangle$ and ∞ and e_{WH} between 0 and $\langle e^2\rangle^{1/2}$. The cause of this is that the Williamson-Hall analysis is based on assumptions regarding the integral breadths and shapes of the size- and strain-broadened profiles that do not hold.

B. Warren-Averbach analysis

Procedure

Several methods for line-profile decomposition use the Fourier coefficients $A(L,d^*)$ of two or more line profiles $I'(s,d^*)$ to estimate the Fourier coefficients $A^S(L)$ of $I'^S(s)$ and $A^D(L,d^*)$ of $I'^D(s,d^*)$ [note that $A^S(L)A^D(L,d^*) = A(L,d^*)$]. Since a set of Fourier coefficients represents a line profile in all its details, such Fourier methods can yield more detailed information on the microstructure than methods based on breadth parameters. A frequently applied Fourier method is the so-called Warren-Averbach analysis (Warren & Averbach, 1950, 1952).

In the Warren-Averbach analysis, it is assumed that $\ln[A^D(L,d^*)] = -2\pi^2L^2d^{*2}\langle e_L^2\rangle$ and, consequently, that $\ln[A(L,d^*)] = \ln[A^S(L)] - 2\pi^2L^2d^{*2}\langle e_L^2\rangle$, where $\langle e_L^2\rangle$ is the variance of e_L, the strain e averaged over a length L (see also App. A)[2]. Therefore, a straight line is drawn through the data points in a plot of $\ln[A(L,d^*)]$ *versus* d^{*2} and the intercept of the ordinate is interpreted as $\ln[A^S(L)]$ and the slope is interpreted as $-2\pi^2L^2\langle e_L^2\rangle_{WA}$ (the subscript WA is added to $\langle e_L^2\rangle$ to distinguish the values obtained by means of the Warren-Averbach analysis from the true values). When $A^S(L)$ and $\langle e_L^2\rangle_{WA}$ are obtained for many L values, a size parameter $D_{WA} = \lim_{L\downarrow 0}[\mathrm{d}A^S/\mathrm{d}L]^{-1}$ and a strain parameter $e_{WA} = \lim_{L\downarrow 0}\langle e_L^2\rangle_{WA}^{1/2}$ can be calculated in principle. In practice, both limits for $L \downarrow 0$ cannot be determined reliably and one proceeds otherwise. To obtain D_{WA}, usually a straight line is fitted to $A^S(L)$ in the L region where it has a reasonably straight portion and D_{WA} is taken as the L value at the intersection of the fitted line and the L axis. For e_{WA}, the value of $\langle e_L^2\rangle_{WA}^{1/2}$ at $L = \frac{1}{2}D_{WA}$ can be chosen (Klug & Alexander, 1974).

---

[2] The Warren-Averbach analysis can also be performed without taking the logarithm (Delhez & Mittemeijer, 1976). Advantages and drawbacks of both versions have been discussed by Berkum, Vermeulen, Delhez, Keijser & Mittemeijer (1994).

If L, d^* and the strains $e(x)$ are sufficiently small, the assumption used in the Warren-Averbach analysis is correct and the relation $\ln[A(L,d^*)]$ *versus* d^{*2} is linear. To determine if practical L, d^* and $e(x)$ values are small enough, the linearity of the relation is investigated for Fourier coefficients $A(L_r,d_r^*)$ calculated from the general strain-field model. Regardless of the linearity, the Warren-Averbach analysis is applied to Fourier coefficients of a first and a second order line profile, calculated using the same w_r and $d_r^* \langle e^2\rangle^{1/2}$ as in Sec. III.A, to investigate the meaning of the parameters D_{WA} and e_{WA}. The results of different practical procedures to calculate D_{WA} and e_{WA} (see above) deviate, in particular for D_{WA}, but it was found that the trend and limiting cases discussed below are always the same. Here, for D_{WA}, a straight line is fitted to $A^S(L_r)$ for $\frac{1}{3} < L_r < \frac{2}{3}$ [this is the straightest part of $A^S(L_r)$ for all w_r]; for e_{WA}, the value of $\langle e_{L_r}^2\rangle_{WA}^{1/2}$ at $L_r = \frac{1}{2}$ is taken (note that $L_r = L/\langle D\rangle$). For the same reason as for D_{WH} and e_{WH} (see Sec. III.A), it is not self-evident what values of D_{WA} and e_{WA} should be expected. As in Sec. III.A, D_{WA} is compared with $\langle D\rangle$. For e_{WA}, both the true $\langle e^2\rangle^{1/2}$ and $\langle e_{L_r}^2\rangle^{1/2}$ at $L_r = \frac{1}{2}$ are used as references.

Results and discussion

For practical values of L_r, d_r^*, and $\langle e^2\rangle^{1/2}$, the linearity of the relation $\ln[A(L_r,d_r^*)]$ *versus* d_r^{*2} strongly depends on the relative width w_r of the component strain fields (see Fig. 2). Nevertheless, the true lines always start in $A(L_r,d_r^*) = 1$ for $d_r^{*2}\langle e^2\rangle = 0$. Hence, for all values of L_r, a Warren-Averbach analysis for infinitely small $d_r^{*2}\langle e^2\rangle$ yields $A^S(L_r) = 1$ and $D_{WA} = \infty$, corresponding with the infinite column length considered. For all L_r, the initial slope also yields exactly the true $\langle e_{L_r}^2\rangle$. However, due to the curvature of the true lines (explained briefly in App. A), straight lines through data points for practical $d_r^{*2}\langle e^2\rangle$ can yield intercepts deviating from zero and slopes deviating from $\langle e_{L_r}^2\rangle$ (see Figs. 2b and c).

For very large w_r ($\gtrsim 1$), the true line remains straight up to large $d_r^{*2}\langle e^2\rangle$ and the straight line fitted in the Warren-Averbach analysis coincides with the true line (see Fig. 2a). Therefore, the "true" values are obtained (see Fig. 1b): $D_{WA} = \infty$ and $e_{WA} = \langle e_{L_r}^2\rangle^{1/2}$ at $L_r = \frac{1}{2}$, which is almost equal to $\langle e^2\rangle^{1/2}$ in this case (*cf.* Fig. A1a). Apparently, a smoothly varying strain $e(x)$ does not break up the column in "domains". The line broadening is interpreted as pure strain broadening.

For very small w_r ($\lesssim 0.01$), the true line is strongly curved at very small $d_r^{*2}\langle e^2\rangle$ and almost straight in the range where experimental data points are usually situated (see Fig. 2c). Since a straight line through the two data points coincides with a large portion of the true line, it appears a meaningful description of the behaviour of the Fourier coefficients, in spite of the deviation at very small $d_r^{*2}\langle e^2\rangle$. In paper I, it was found that, for the case $w_r \downarrow 0$, the relatively

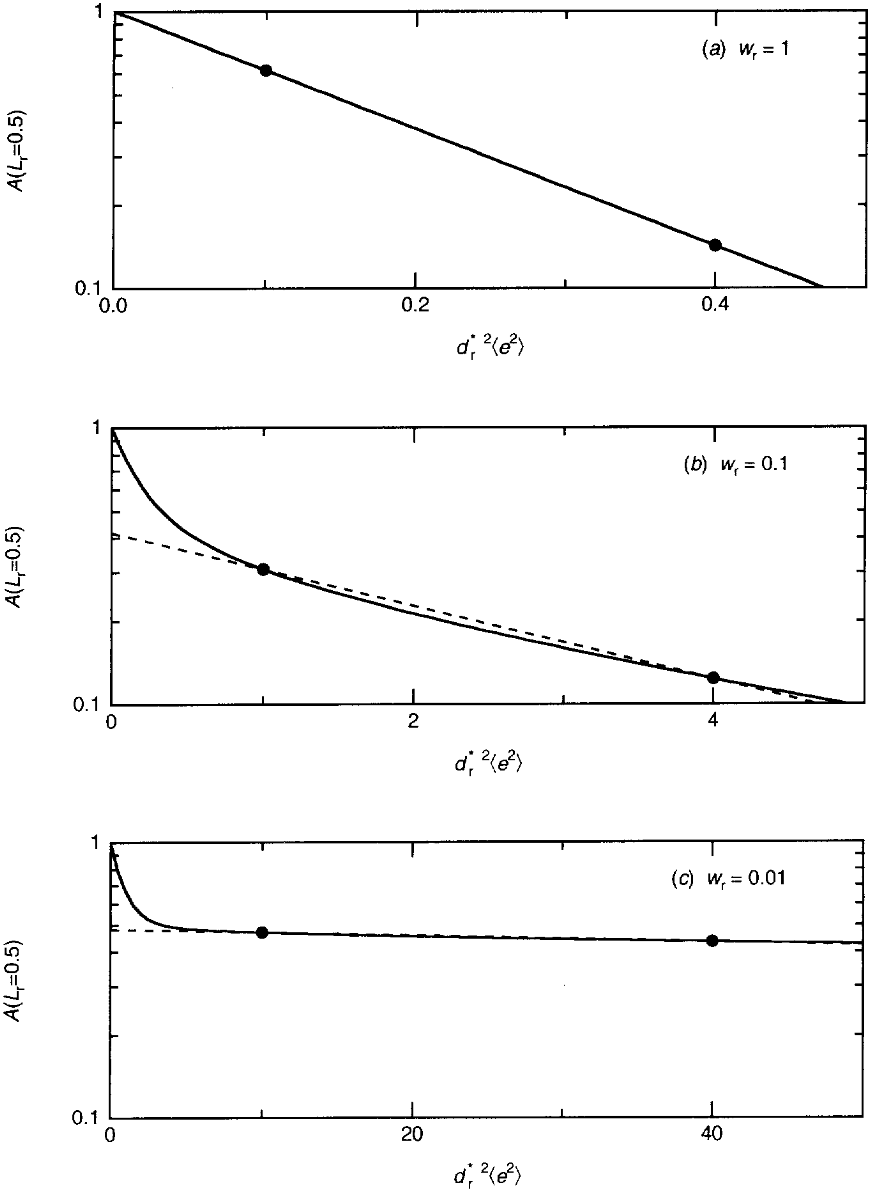

Fig. 2: Behaviour of ln[$A(L_r,d_r^*)$] as a function of $d_r^{*2}\langle e^2\rangle$ for a relative correlation length $L_r = 0.5$ and three relative widths w_r of the component strain fields: (a) $w_r = 1$, (b) $w_r = 0.1$, and (c) $w_r = 0.01$. The dots represent Fourier coefficients of a first and second order of reflection with $d_r^*\langle e^2\rangle^{1/2} = 1/\sqrt{10}\ w_r$ for the first order. In the Warren-Averbach analysis, the intercept of the ordinate and the slope of the dashed line are used to calculate size and strain parameters (for $w_r = 1$, the dashed line coincides with the full line).

little distorted regions between the "walls of distortion" near the projected defects can be considered to scatter incoherently with respect to each other. This complies with the almost horizontal true line (see Fig. 2c): nearly pure size and little strain broadening. For $w_r \downarrow 0$, the size parameter D_{WA} tends to $\langle D \rangle$ and the strain parameter vanishes (see Fig. 1b).

For intermediate w_r values (~0.1), the true line does not have straight parts (see Fig. 2b). The straight line through the data points deviates from the true line in an arbitrary way. Different results would be obtained from different pairs of reflections (*cf.* also Wilkens, 1979). Knowing the true line, one would not apply the Warren-Averbach analysis in such a case. If, however, as usual in practice, only two data points are available and the curvature of the true line is unknown, the results of the Warren-Averbach analysis deviate from the "true" values in an unknown way.

An example of the results of the Warren-Averbach analysis for intermediate w_r in terms of $A^S(L_r)$ and $\langle e^2_{L_r} \rangle_{WA}$ is shown in Fig. 3. The mean squared strains $\langle e^2_{L_r} \rangle_{WA}$ are much smaller than the true $\langle e^2_{L_r} \rangle$, except in the impracticable limit $L_r \downarrow 0$. The resulting behaviour of $A^S(L_r)$ is a problem on itself. It is curved downward for small L_r, which is in contradiction with the theoretical basis of the Warren-Averbach analysis. Truncation of the line profiles can cause such a "hook effect" (Young, Gerdes & Wilson, 1967), but this effect is absent in the present calculations. Here, the hook effect is exclusively due to the violation of the assumption underlying the Warren-Averbach analysis. Calculating a size parameter D_{WA}, the theoretically correct method (using $\lim\limits_{L \downarrow 0} [\mathrm{d}A^S/\mathrm{d}L]$) yields $D_{WA} = \infty$, which complies with the infinitely long column used in the calculations. In practice, however, a straight line fit to some part of $A^S(L_r)$ is used, which yields $D_{WA}/\langle D \rangle$ values ranging from 0.6 to 1.2. Further, it follows from Fig. 1b that D_{WA} and e_{WA} depend strongly on w_r. As in the case of the Williamson-Hall analysis, it is concluded that, for intermediate w_r, the relation between the Warren-Averbach parameters (D_{WA} and e_{WA}) and the strain-field parameters is unclear. The cause of this is that the Warren-Averbach analysis is based on assumptions regarding the Fourier coefficients of the strain-broadened line profile that do not hold for practical values of L, d^*, and $\langle e^2 \rangle^{1/2}$.

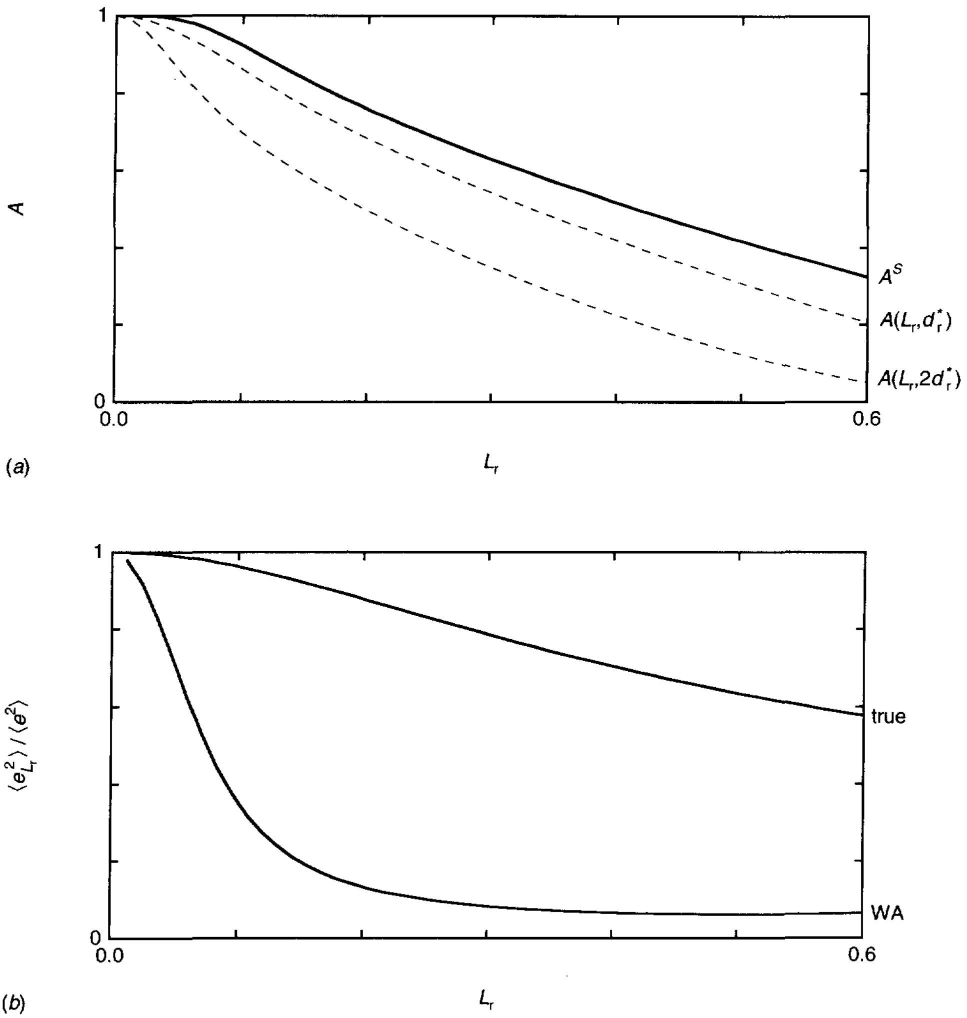

Fig. 3: Results of the Warren-Averbach analysis applied to Fourier coefficients $A(L_r,d_r^*)$ and $A(L_r,2d_r^*)$ of a first and second order line profile, respectively, calculated using $w_r = 0.1$ and $d_r^* \langle e^2 \rangle^{1/2} = 1$ ($= 1/\sqrt{10}\, w_r$) for the first order, in terms of (*a*) size coefficients $A^S(L_r)$ [$A(L_r,d_r^*)$ and $A(L_r,2d_r^*)$ have been included for comparison] and (*b*) relative mean squared strains $\langle e_{L_r}^2 \rangle_{WA} / \langle e^2 \rangle$ [the true $\langle e_{L_r}^2 \rangle / \langle e^2 \rangle$ have been included for comparison].

IV. LINE-PROFILE SIMULATION USING THE STRAIN-FIELD MODEL

The observed deficiencies of classical size-strain separation methods urge for an alternative method for the analysis of line broadening from distorted specimens. Simulation (and matching) of line profiles on the basis of a strain-field model constitutes such a method. The model parameters can be adapted and refined until certain characteristics of the simulated line profile fit certain characteristics of the measured one. The effect of instrumental line broadening, always present in measured line profiles, should either be removed from the measured line profile, or added to the simulated line profile (see *e.g.* Berkum, Delhez, Keijser & Mittemeijer, 1992). If the fit succeeds, the model and the model parameters can provide a reasonable description of the strain field in the specimen and a physically meaningful characterization of the specimen is thus obtained.

The strain-field model presented in Sec. II, can be used in a line-profile simulation method. For this model, a single line-profile parameter, like the integral breadth $\beta(d^*)$, is usually not sufficient to determine the three model parameters. Fitting the full experimental line profile $I'(s)$ on the basis of Eqs. (1) to (3) is laborious, because each step in an iterative procedure involves a Fourier transformation. Therefore, fitting the Fourier coefficients $A(L,d^*)$ is advantageous. Equations (2) and (3) assume, among other things, periodically distributed projected defects. For small and moderate L_r, the Fourier coefficients are not much affected by the distribution of projected defects along the column, but for large L_r they are (see Fig. 6 of paper I). Therefore, the fitting should be restricted to, say, $L_r \lesssim 1$, or a more general strain-field model (see paper I) should be used.

The reliability of the results is very much enhanced if more than one line profile can be fitted simultaneously. In general, only orders of the same reflection can be used, because the strain field may be systematically different in different crystallographic directions in the diffracting crystals. In the case of isotropic lattice distortion, all reflections of a deformed specimen can be used to determine a single set of model parameters (see *e.g.* Sec. V).

In the next section, the merits of line-profile simulation as a method of analysis (fitting Fourier coefficients calculated from a strain-field model to experimental ones) are investigated by applying the method to experimental line profiles.

V. LINE-PROFILE DECOMPOSITION AND LINE-PROFILE SIMULATION OF EXPERIMENTAL LINE PROFILES

A. Experimental

To obtain a sample representative of a cold-worked metal, a tungsten powder (>99.5 weight %, Fluka Chemika) was ball milled for 1 h using two balls in a horizontally moving vessel. Tungsten was chosen because of its elastic isotropy. Ball milling was used, because it is a many-sided ("isotropic") deformation procedure, that is expected to produce dislocations with all possible combinations of Burgers' and line vectors. For these two reasons, the strain field in the specimen can be considered equivalent in all crystallographic directions and a simultaneous analysis of all measurable reflections is possible. Thus, the dependence of the integral breadth and the Fourier coefficients on the length of the diffraction vector can be studied with much more detail than in the case of an anisotropic material or an "anisotropic" deformation procedure (using CuKα radiation, eight reflections can be analysed for tungsten).

If the broadening effect of dislocations is to be investigated separately, other origins of line broadening should preferably be absent. The ball milling of tungsten produced some small particle fragments (see Fig. 4a), which would give rise to additional line broadening due to their finite sizes. These fragments were removed by suspending the milled powder in 2-propanol and removing the suspension from the sediment after 30 minutes and repeating this procedure two times using the sediment. The average particle size after this treatment is definitely larger than 1 μm (see Fig. 4b). The line broadening due to such an average particle size is a negligible fraction of the total broadening.

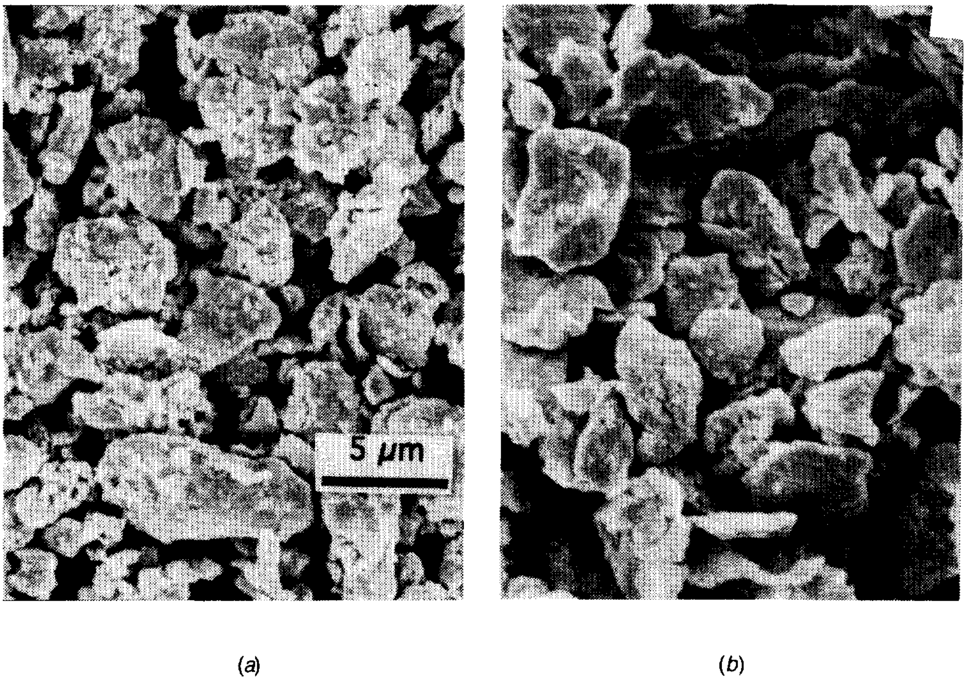

(*a*) (*b*)

Fig. 4: Scanning-electron-microscope observations of a ball-milled tungsten powder (*a*) before and (*b*) after removal of the smallest particles by means of sedimentation.

A diffractometer specimen was prepared by suspending a small amount of the fractionated powder once more in 2-propanol and now sedimenting it onto a flat Si (510) single-crystal substrate. From a silicon powder a standard specimen of exactly the same geometry was prepared to measure the instrumental broadening (Berkum, Sprong, Keijser, Delhez & Sonneveld, 1994). The difference in the absorption coefficients of tungsten and silicon is of no importance, because both the silicon and the tungsten layer are almost fully transparent due to their open "coral-like" structure and their thinness (~ 10 to 20 μm).

The X-ray diffraction-line profiles were recorded on a Siemens D500 diffractometer using CuKα radiation and a graphite diffracted-beam monochromator. The divergence of the incident beam was 1° and the receiving-slit width was 0.05 °2θ. The specimens were rotated around the normal to their surfaces during the measurements. For the tungsten specimen, the complete 2θ range (27° to 167°) was measured; for the silicon standard specimen, a sufficiently long range around each peak. For all profiles linear backgrounds were subtracted and the CuKα_2 components were removed according to Delhez & Mittemeijer (1975). The profiles were then translated to intensity distributions $I'(s,d^*)$ in reciprocal space (with d^* corresponding to the centroid of I') and Fourier transformed. To obtain Fourier coefficients of the instrumental line profile for the d^* of the tungsten reflections, Fourier coefficients of the two nearest silicon reflections were interpolated linearly. Finally, the Fourier coefficients of the tungsten profiles were divided by those of the instrumental profiles to obtain the Fourier coefficients of the structurally-broadened line profiles (Stokes, 1948).

The resulting sine coefficients were small for all reflections [~ $0.07\times A(L=0,d^*)$ at most], indicating almost symmetrical line profiles. Therefore, the integral breadths β can be calculated from the Fourier coefficients using Eq. (4), but with a finite range of integration in L. Here, the range of integration (summation) was gradually increased and β was taken as the plateau reached in a plot of the integral *versus* the range of integration. In this way, β of the structurally-broadened line profiles was obtained without imposing any assumptions on the shape of the measured profiles.

B. Line-profile decomposition using size and strain parameters

The integral breadths of the eight reflections of the ball-milled tungsten powder lie reasonably on a straight line having a positive intercept with the ordinate (see Fig. 5a). The last two reflections show minor deviations from this line, which may be due to truncation effects (the {321} and {400} reflections probably have a little overlap and the {400} reflection is cut at $2\theta = 167°$). Exclusion of the last or last two reflections from the analysis does not alter the conclusions reached. Earlier measurements of integral breadths from tungsten *filings* yielded

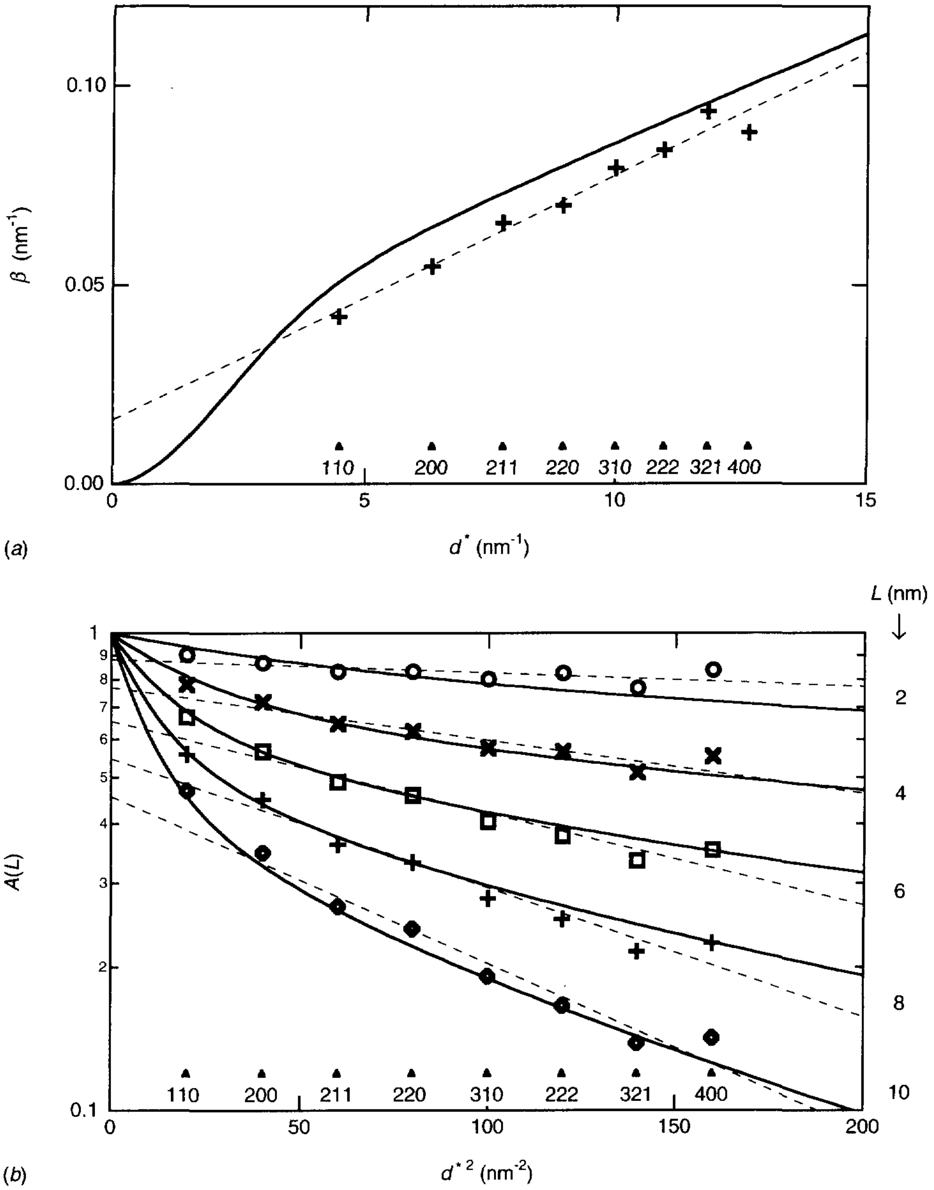

Fig. 5: (*a*) Integral breadth β and (*b*) Fourier coefficients $A(L)$ as a function of the length d^* of the diffraction vector for the structurally broadened line profiles ({*hkl*} indicated at the bottom) of a ball-milled and fractionated tungsten powder. Dashed lines (straight-line fits to all eight data points) have been used in the Williamson-Hall analysis (*a*) and the Warren-Averbach analysis (*b*). *Full lines have been calculated from the present strain-field model* using $\langle D \rangle = 21$ nm, $w_r = 0.115$ and $\langle e^2 \rangle^{1/2} = 6.8 \times 10^{-3}$.

results very similar to Fig. 5a (Williamson & Hall, 1953; Langford, 1992). The size and strain parameters determined from Fig. 5a by means of the linear version of the Williamson-Hall analysis (see Sec. III.A) are D_{WH} = 62 nm and $e_{WH} = 2.5\times10^{-3}$, *i.e.* the broadening is interpreted as partly due to size, partly due to strain, corresponding to an intermediate w_r value. Hence, according to Sec. III.A, the Williamson-Hall size and strain parameters cannot be linked easily with the microstructure of the ball-milled powder.

The cosine Fourier coefficients of the experimental structurally-broadened line profiles plotted logarithmically as a function of d^{*2} do *not* lie on a straight line (see Fig. 5b). A similar curvature can be observed in other, recently published data obtained from ball-milled tungsten (Wagner, Yang & Boldrick, 1992). On the other hand, such curvature was not found by McKeehan & Warren (1953) and Aqua & Wagner (1964). The absence of such a curvature may be due to insufficient annealing of the standard specimen they used (see Williamson & Smallman, 1956). According to Sec. III.B, the Warren-Averbach analysis in this case (curved lines in Fig. 5b) yields parameters that cannot be linked easily with the microstructure of the ball-milled powder. If it is performed nevertheless, the results depend on the reflections incorporated in the analysis. Using straight line fits to all eight reflections (see Fig. 5b) and the practical procedures described in Sec. III.B to calculate D_{WA} and e_{WA}, the results are D_{WA} = 17 nm and $e_{WA} = 1.3\times10^{-3}$; using *e.g.* only {110} and {220}, the results are D_{WA} = 23 nm and $e_{WA} = 2.2\times10^{-3}$. A (precarious) extrapolation of the $\langle e_L^2\rangle^{1/2}$ to $L = 0$ yields ~ 3×10^{-3} for all 8 reflections and ~ 5×10^{-3} for {110} and {220}. The $A^S(L)$ results always show a small "hook effect".

C. Line-profile simulation using the strain-field model

Fourier coefficients calculated according to Eqs. (2) and (3) have been fitted to the experimental Fourier coefficients of all eight reflections simultaneously (*cf.* Sec. IV). It was found that the parameter values $\langle D\rangle$ = 21 nm, w_r = 0.115 and $\langle e^2\rangle^{1/2} = 6.8\times10^{-3}$ yield the best fit (see the curved lines in Fig. 5b). The curved lines and the data points agree fairly well (the data points for L = 2 nm are probably the least accurate due to the unavoidable truncation of the measured profiles). This is remarkable, considering the simplicity of the strain-field model used at present. With the strain field defined by the parameter values determined, the results of the Williamson-Hall analysis and the Warren-Averbach analysis can be predicted: for w_r = 0.115, Fig. 1a yields $D_{WH} \approx 1.6\ \langle D\rangle$ and $e_{WH} \approx 0.33\ \langle e^2\rangle^{1/2}$ and Fig. 1b yields $D_{WA} \approx 0.85\ \langle D\rangle$ and $e_{WA} \approx 0.24\ \langle e^2\rangle^{1/2}$. Thus, the results obtained in Sec. V.B are close to these predicted values.

The behaviour of the integral breadth corresponding to the strain-field parameters estimated from the behaviour of the Fourier coefficients is indicated by the full line in Fig. 5a.

The discrepancy between the lines calculated using the model and the experimental data points is ascribed to the periodic distribution of projected defects adopted in the model: it can be shown that non-periodic distributions yield Fourier coefficients that are comparable to the ones calculated here at small L, but that vanish more gradually at larger L (see Fig. 6 in paper I). Consequently, such distributions yield smaller β values [*cf.* Eq. (4)], with a better correspondence to the present experimental data.

Since, in the present analysis based on line-profile simulations, the mean squared strain is included as a parameter, the stored-elastic-energy density E is readily calculated using $E = \frac{15}{2}\mu \langle e^2 \rangle$ (Faulkner, 1960), where $\mu = 160.6$ GPa (Smithells, 1976) is the shear modulus. For the ball-milled tungsten powder, one obtains $E = 1.1\times10^6$ J/m^3. This value is close to the results of Fecht *et al.* (1990), who obtained $E \geq 1.3\times10^6$ J/m^3 from calorimetric measurements on also severely ball-milled tungsten. The strain values obtained by means of line-profile decomposition (1 to 5×10^{-3}) are significantly smaller than the root mean squared strain value obtained by means of line-profile simulation (6.8×10^{-3}). In the past, it has been observed that stored energies calculated from Warren-Averbach strains are smaller than those calculated from calorimetric measurements (Michell & Haig, 1957). The present results suggest that such discrepancies can be due to underestimation of the mean squared strain by the Warren-Averbach analysis and that line-profile simulation using the present model provides more accurate root mean squared strain and stored-energy values.

V. CONCLUSIONS

In general, the results obtained in practice by application of the classical Williamson-Hall analysis and the Warren-Averbach analysis to broadened line profiles from coarse-grained distorted specimens cannot be related directly to the microstructure of the specimen. The cause is that the assumptions underlying the methods, on which the division into a "size" and a "strain" broadening is based, are not justified for most practical cases. Only in two limiting cases, the Williamson-Hall and the Warren-Averbach results can be interpreted in a physically meaningful way: (i) if the methods indicate dominant strain broadening, it can be concluded that the strain gradients in the specimen, in the direction of the diffraction vector, are small and that the values obtained for the usual strain parameters equal the true root mean squared strain, and (ii) if the methods indicate dominant size broadening, it can be concluded that the strain in the specimen, in the direction of the diffraction vector, is confined to very narrow bands with relatively little-distorted regions in between and that the values obtained for the usual size parameters equal the average distance between these bands.

On the other hand, by simulation and matching of line profiles on the basis of a strain-field model, line broadening from distorted specimens can be analysed without additional assumptions imposed upon the kinematical diffraction theory, in contrast with the classical methods. The present strain-field model (see Berkum, 1994), involving only three adjustable parameters, is able to describe the broadening of all eight reflections of a ball-milled tungsten powder with reasonable accuracy. The strain-field parameters obtained are readily physically interpretable, *e.g.* in terms of stored elastic energy.

ACKNOWLEDGEMENTS

The authors are grateful to Dr. J.I. Langford for providing the tungsten powder and Ir. A. Buis for providing scanning-electron-microscope facilities.

APPENDIX A: STRAIN DISTRIBUTIONS

The results of the Warren-Averbach analysis, as discussed in Sec. III.B, can also largely be understood from an investigation of the frequency distributions $p_L(e_L)$ of $e_L(x)$, the average of $e(x)$ in the interval $[x-\frac{1}{2}L, x+\frac{1}{2}L]$. The function $e_L(x)$ can be considered as $e(x)$ smoothed by a rectangular window of width L. Thus, the variance $\langle e_L^2\rangle$ decreases continuously[3] with increasing "smoothing", *i.e.* increasing L. Because in the shape function of the strain fields of the individual defects, x and w occur only in the combination x/w [see Eq. (35) of paper I] and the contributions of the individual defects to e_L are uncorrelated, the behaviours of $\langle e_L^2\rangle$ *versus* L for different w coincide if they are displayed as a function of L/w. In relative quantities, this statement holds for $\langle e_{L_\mathrm{r}}^2\rangle$ *versus* $L_\mathrm{r}/w_\mathrm{r}$ (see Fig. A1a). Thus, $\langle e_{L_\mathrm{r}}^2\rangle$ *versus* L_r decreases faster for small w_r than for large w_r. This can be understood from the sharply peaked behaviour of $e(x_\mathrm{r})$ for small w_r, which is flattened by the smoothing much faster than the smooth $e(x_\mathrm{r})$ for large w_r.

The shape of $p_{L_\mathrm{r}}(e_{L_\mathrm{r}})$ can be characterized by the kurtosis k_{L_r}, here defined as $\langle e_{L_\mathrm{r}}^4\rangle/\langle e_{L_\mathrm{r}}^2\rangle^2$ (see Fig. A1b). For $L_\mathrm{r} >> 1$, the strain $e_{L_\mathrm{r}}(x)$ consists of many contributions of different defects of comparable magnitude. The contributions are statistically independent, because the values a_i are drawn independently. Then, according to the central limit theorem (the distribution of the sum of many independent variables becomes Gaussian), the shape of $p_{L_\mathrm{r}}(e_{L_\mathrm{r}})$ has to become Gaussian for large L_r. For a Gaussian distribution $k_{L_\mathrm{r}} = 3$. Indeed, k_{L_r} decreases with increasing L_r to approximately 3 for $L_\mathrm{r} \geq 1$ (see Fig. A1b). Further, k_{L_r} increases with decreasing w_r, in

---

[3] This does not necessarily hold if the grains are small and enclose misfitting second-phase particles (*cf.* Berkum, Delhez, Keijser & Mittemeijer, 1992).

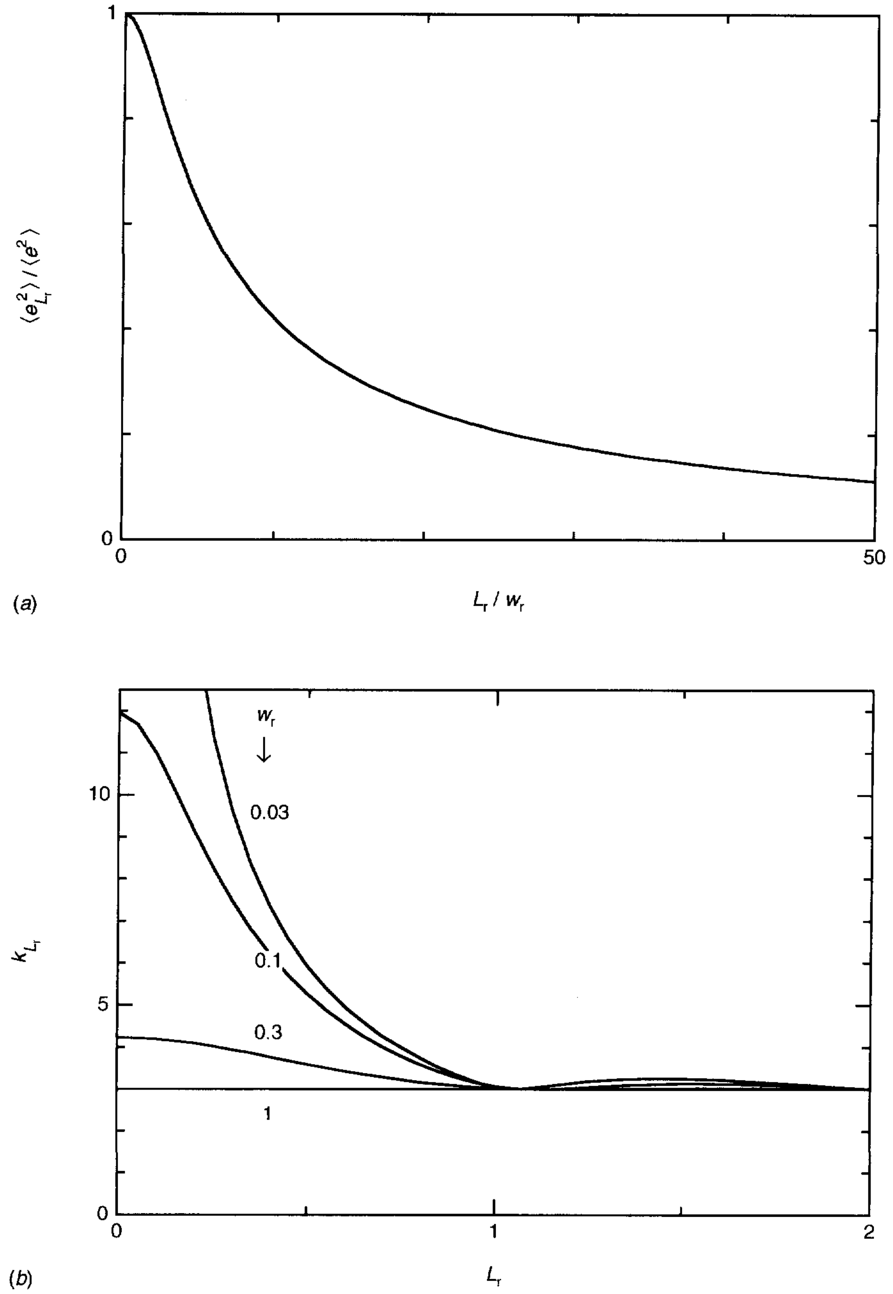

Fig. A1: Characteristics of the frequency distributions $p_{L_r}(e_{L_r})$ of e_{L_r}: (*a*) relative variance $\langle e_{L_r}^2 \rangle / \langle e^2 \rangle$ *versus* L_r/w_r and (*b*) kurtosis $k_{L_r} \equiv \langle e_{L_r}^4 \rangle / \langle e_{L_r}^2 \rangle^2$ *versus* L_r for different values of the relative width w_r of the individual strain fields [if $p_{L_r}(e_{L_r})$ is Gaussian, then $k_{L_r} = 3$].

particular for small L_r, because the maximum values of $e_{L_r}(x)$ become increasingly extreme with decreasing w_r, which affects $\langle e^4_{L_r}\rangle$ more than $\langle e^2_{L_r}\rangle^2$. The oscillations in Fig. A1b ($k_{L_r} = 3$ for integer values of L_r and slightly larger in between) originate from the adopted periodicity for the distribution of the projected-defect distances. For non-periodic defect-distance distributions, k_{L_r} decreases more smoothly to 3.

If, for a specific L, the distribution $p_L(e_L)$ is Gaussian, the assumption used in the Warren-Averbach analysis (see Sec. III.B) is correct for this L value (Warren, 1959) and the line in the Warren-Averbach plot is straight. For large w_r, $p_L(e_L)$ is always nearly Gaussian and straight lines should be obtained, which agrees with Fig. 2a. If $p_L(e_L)$ is non-Gaussian, the assumption in the Warren-Averbach analysis can still be justified if L and $\langle e^2\rangle$ are sufficiently small (Warren, 1959). Apparently, for $w_r = 0.1$ and $w_r = 0.01$, the values of L and $\langle e^2\rangle$ pertaining to Figs. 2b and 2c are not small enough in this sense, which results in curved lines.

Since the behaviour of $\langle e^2_L\rangle$ has been discussed extensively in the past, the $\langle e^2_L\rangle$ calculated here are confronted with some expressions in the literature. The horizontal tangent to $\langle e^2_L\rangle$ in $L = 0$ and the parabolic decay for small L, derived for infinitely large grains by Turunen, Keijser, Delhez & Pers (1983), are both present in Fig. A1a. For $2.5 < L/w < 15$, the $\langle e^2_L\rangle$ values in Fig. A1a (note that $L/w = L_r/w_r$) are approximately proportional to $\ln(C/L)$, the behaviour derived for strains around dislocations for small but not too small L (Wilkens, 1970). For larger L, the behaviour of $\langle e^2_L\rangle$ depends strongly on the details of the spatial ordering of the defects. Since only one projected-defect distance distribution is considered here (the periodic one), the present $\langle e^2_L\rangle$ behaviour for larger L is quite unique. Finally, for very large L, $\langle e^2_L\rangle$ is proportional to L^{-1} [the $\langle e^2_L\rangle$ according to Eq. (4.7) and the equation below Eq. (A.8) of Wilkens (1970) also show this behaviour]. This relation always holds for very large L, because then the local strain $e_L(x)$ consists of *many* statistically independent contributions; a direct consequence is that $\ln[A(L,d^*)] \propto -L$ for very large L (Eastabrook & Wilson, 1952).

REFERENCES

Aqua, E.N. & Wagner, C.N.J. (1964). *Phil. Mag.* **9**, 565-589.

Berkum, J.G.M. van, Delhez, R., Keijser, Th.H. de & Mittemeijer, E.J. (1992). *Phys. stat. sol. (a)* **134**, 335-350. See Chapter 5 of this thesis.

Berkum, J.G.M. van (1994). To be published. See Chapter 7 of this thesis.

Berkum, J.G.M. van, Sprong, G.J.M., Keijser, Th.H. de, Delhez, R. & Sonneveld, E.J. (1994). To be published. See Chapter 1 of this thesis.

Berkum, J.G.M. van, Vermeulen, A.C., Delhez, R., Keijser, Th.H. de & Mittemeijer, E.J. (1994). *J. Appl. Cryst.* In the press. See Chapter 3 of this thesis.

Delhez, R. & Mittemeijer, E.J. (1975). *J. Appl. Cryst.* **8**, 609-611.

Delhez, R. & Mittemeijer, E.J. (1976). *J. Appl. Cryst.* **9**, 233-234.

Eastabrook, J.N. & Wilson, A.J.C. (1952). *Proc. Phys. Soc. London* **B65**, 67-75.

Faulkner, E.A. (1960). *Phil. Mag.* **5**, 519-521.

Fecht, H.J., Hellstern, E., Fu, Z. & Johnson, W.L. (1990). *Metall. Trans.* **21A**, 2333-2337.

Hall, W.H. (1949). *Proc. Phys. Soc.* **62**, 741-743.

Klug, H.P. & Alexander, L.E. (1974). *X-ray Diffraction Procedures for Polycrystalline and Amorphous Materials* (New York: John Wiley), pp. 661-665.

Langford, J.I. (1992). In: *Accuracy in Powder Diffraction II*, NIST Special Publication 846, eds. Prince, E. & Stalick, J.K. (Washington: US Dpt. of Commerce), pp. 110-126.

McKeehan, M. & Warren, B.E. (1953). *J. Appl. Phys.* **24**, 52-56.

Michell, D. & Haig, F.D. (1957). *Phil. Mag.* **2**, 15-32.

Smithells, C.J. (1976). *Metals Reference Book* (London: Buttersworths), p. 976.

Stokes, A.R. (1948). *Proc. Phys. Soc. London* **61**, 382-391.

Stokes, A.R. & Wilson, A.J.C. (1944). *Proc. Phys. Soc. London* **56**, 174-181.

Turunen, M.J., Keijser, Th.H. de, Delhez, R., & Pers, N.M. van der (1983). *J. Appl. Cryst.* **16**, 176-182.

Wagner, C.N.J., Yang, E. & Boldrick, M.S. (1992). *Adv. X-ray Anal.* **35**, 585-592.

Warren, B.E. (1959). *Prog. in Metal Phys.* **VIII**, 147-202.

Warren, B.E. (1969). *X-ray Diffraction* (Reading, Massachusetts: Addison-Wesley), pp. 264-268.

Warren, B.E. & Averbach, B.L. (1950). *J. Appl. Phys.* **21**, 595-599.

Warren, B.E. & Averbach, B.L. (1952). *J. Appl. Phys.* **23**, 497.

Wilkens, M. (1970). In: *Fundamental Aspects of Dislocation Theory*, NBS Spec. Publ. 317, vol. II, eds. Simmons, J.A., Wit, R. de & Bullough, R. (Washington: US Dpt. of Commerce), pp. 1195-1221.

Wilkens, M. (1979). *J. Appl. Cryst.* **12**, 119-125.

Williamson, G.K. & Hall, W.H. (1953). *Acta Metall.* **1**, 22-31.

Williamson, G.K. & Smallman, R.E. (1956). *Phil. Mag.* **1**, 34-46.

Young, R.A., Gerdes, R.J. & Wilson, A.J.C. (1967). *Acta Cryst.* **22**, 155-162.

SUMMARY

The analysis of line broadening in X-ray powder diffraction is in principle a powerful tool in microstructural research. It requires accurate line-broadening measurements and a physically meaningful interpretation of the experimental data.

One of the experimental requirements, discussed in detail in this thesis, is the preparation of a standard specimen, *i.e.* a specimen that contains no structural defects that contribute to the measured line broadening. A standard specimen allows an experimental determination of the instrumental line broadening. In Chapter 1, the requirements for a standard specimen (there are a lot of requirements besides the absence of structural defects) have been discussed and it has been concluded that they are partly contradictory. Two of these contradictions are: (i) counting and crystal statistics urge for a thicker specimen, but thick specimens yield additional line broadening and (ii) to avoid structural broadening larger particles are wanted, but that deteriorates the crystal statistics. Because of these contradictions, a perfect standard specimen is impossible and an optimum standard specimen has been developed. The resulting recipe for its preparation is easily applicable and it yields reproducible results. The optimum standard specimen allows very accurate measurements of instrumental line profiles with random and systematic errors of the order of 0.001 °2θ.

The interpretation of structural line broadening is considered the most difficult part of line-broadening analysis. In the General Introduction, most of the existing methods of interpretation have been qualified as *analytical* methods, because they are based on approximate analytical formulae, derived from the general diffraction theory. These methods translate experimental data directly to parameter values. They do not assume the presence of specific types of crystal imperfections and therefore they have been considered generally applicable. However, because the parameters used are not specified in terms of imperfections, their meaning is often unclear. In Chapter 8, it has been found that, in general, the "size" and "strain" obtained by application of the Warren-Averbach and the Williamson-Hall analysis to coarse-grained distorted specimens cannot be related directly to the microstructure of the specimens. There are two exceptions: (i) if the methods attribute all measured broadening to "size", the strain in the grains is completely concentrated in relatively narrow regions and the size parameter equals the average distance between these regions and (ii) if the methods attribute all measured broadening to "strain", the specimen is distorted by a rather smooth strain field and the strain parameter equals the root mean squared strain.

The Warren-Averbach analysis fails to yield a meaningful interpretation if the approximate description of strain broadening used is invalid for the microstructure of the specimen (see Chapters 2 and 3). Using other approximate descriptions of size and strain broadening, alternative methods can be developed that are applicable to part of the specimens for which the Warren-Averbach analysis is inapplicable. One such alternative has been applied to line-broadening measured from two plastically deformed specimens and it yielded results that were more believable than those of the Warren-Averbach analysis (Chapter 3).

A completely different approach to line-broadening analysis is used in *model-based* methods. In these methods, line broadening calculated from a microstructural model is fitted to the measured line broadening and thus the optimum model-parameter values are obtained. The main advantage of model-based methods is that the meaning of the parameters is clear and undisputed; the disadvantage is that they are only applicable to specimens with a microstructure that can be described by the model.

A number of existing methods based on models for dislocation configurations have been discussed in Chapter 4. It has been concluded that the models and the formulae used are related closely. A recipe has been developed for the selection of the most suitable method and for its execution in practice. If the measurements performed have a very high precision and accuracy, which may be the case *e.g.* with single crystals measured in a double-crystal diffractometer, significant information on the dislocation arrangement can be obtained in addition to the dislocation density.

Based on a model for misfitting inclusions in a matrix, a new method for the interpretation of line broadening has been developed (Chapter 5). Its application has been illustrated by means of line-broadening measurements of five different aluminium-silicon alloys, consisting of very fine silicon precipitates in a pure aluminium matrix. The integral breadths as well as the Fourier coefficients of the broadened line profiles have been described by the model with sufficient accuracy. The misfit value determined (2.3×10^{-3}) is smaller than expected on the basis of the difference in shrinkage on cooling from the precipitation to room temperature (3.1×10^{-3}). Apparently, a considerable plastic accommodation of the misfit takes place during cooling or immediately afterwards. Surprisingly, between a few days and four years of ageing at room temperature, the misfit value decreases further in the case of aluminium-silicon alloys with a high silicon content, *i.e.* a relatively large stored-energy density (Chapter 6).

In Chapter 7, the strain field that is produced in a column of a specimen distorted by lattice defects has been modelled statistically. In the strain-field model, the total strain field in the column is described as the superposition of "component strain fields" of projected defects. The projected-defect distances and the amplitudes of the component strain fields are considered stochastic variables. In a relatively simple version, the average projected-defect distance and the root mean squared amplitude and the width of the component strain fields are adjustable parameters. Using this model, frequently observed behaviours of the integral breadths of Fourier coefficients of broadened line profiles have been simulated and are thereby better understood (Chapter 7). In particular, it has been found that if two relatively little distorted regions are separated by a very small region with a high strain, the two regions can be considered to diffract incoherently. The strain-field model has also been used to interpret the line-broadening measured from a ball-milled tungsten powder (Chapter 8). A reasonable fit between calculated and experimental Fourier coefficients of all eight reflections has been obtained with three model parameters: an average projected-defect distance of 21 nm, a halfwidth of the component strain fields of 2.4 nm, and a total root mean squared strain of 6.8×10^{-3}. The experimentally obtained Fourier coefficients deviated systematically from the description of strain broadening assumed in the Warren-Averbach method.

The dislocation-configuration models and the strain-field model assume that the grains are so large that their sizes do not contribute to the line broadening. This assumption is certainly justified if the average grain size is larger than 1 μm, *i.e.* for most technologically relevant materials. If the grains size is smaller, the size broadening is readily included in the models, if desired with the average grains size as an adjustable parameter. If a significant influence of the grain boundaries on the strains within the grains is expected, a more rigorous adaptation of the model is necessary.

In this thesis, a considerable number of methods for line-broadening analysis have been presented. In practice, the method most suitable for the specimen under study has to be selected. In general, model-based methods should be preferred over analytical methods if it is reasonable to assume that the model used contains the essential characteristics of the microstructure of the specimen and is sufficiently flexible. Advance knowledge on the specimen, *e.g.* from its mechanical or thermal history of from transmission-electron-microscopy, is indispensable in this decision. The choice between the specific models and the more general model should depend on the information desired (*e.g.* dislocation density or stored energy) and the availability of a suitable model.

An aspect that has largely been ignored is that the strain field in a specimen may be systematically different in different crystallographic directions. In this thesis, only the behaviour of the strain in a single direction has been considered or the strain in all directions has been considered equivalent. However, if the same (or equivalent) grains contribute to reflections with different orientations of the diffraction vector, the experimental information is available to reconstruct the (possibly anisotropic) strain field around the lattice defects in three dimensions. In principle, the approach of line-broadening analysis used in the model-based methods discussed in this thesis can be extended to make possible such a reconstruction.

SAMENVATTING

De meeste materialen zijn kristallijn, dat wil zeggen dat ze bestaan uit een regelmatige rangschikking van atomen. Die rangschikking is echter nooit perfect: de richting van de stapeling kan veranderen (kristalgrenzen), er kunnen stapelfouten (dislocaties) optreden of er zitten vreemde atomen of clusters van vreemde atomen (precipitaten of insluitsels) in het materiaal die niet precies in de rangschikking passen. De mechanische eigenschappen van een materiaal zijn vaak sterk afhankelijk van zulke kristalfouten (meestal vervormt het materiaal minder gemakkelijk door kristalfouten en wordt het daardoor sterker) en daarom is het belangrijk te weten welke en hoeveel kristalfouten het materiaal bevat. In dit proefschrift is vooral naar dislocaties en precipitaten gekeken.

Bij röntgendiffractie wordt röntgenstraling op een preparaat van een bepaald materiaal gericht en vervolgens gemeten onder welke hoeken het preparaat die straling verstrooit. Als er kristalfouten in het materiaal zitten, dan blijkt de verstrooide straling niet meer geconcentreerd te zijn op precies te berekenen hoeken, maar min of meer verspreid rond deze hoeken. Dat verschijnsel wordt röntgendiffractie-lijnverbreding genoemd. Als de posities en de aard van alle kristalfouten in een preparaat bekend zijn, dan is de lijnverbreding in principe exact uit te rekenen. In de praktijk moet echter de omgekeerde weg gevolgd worden: lijnverbreding gemeten aan een preparaat moet vertaald worden naar informatie over kristalfouten in het materiaal. Er zijn daarvoor in het verleden vele methodes ontwikkeld, waarvan een aantal in dit proefschrift besproken en geëvalueerd zijn. Daarnaast zijn er een aantal nieuwe methodes ontwikkeld die voor bepaalde soorten preparaten betere informatie over de kristalfouten opleveren dan de bestaande methodes.

Voordat er over analysemethodes gepraat wordt, moet de lijnverbreding wel goed gemeten worden. Een van de problemen die zich daarbij voordoen, is dat het instrument, een diffractometer, zelf ook wat lijnverbreding veroorzaakt. Deze "instrumentele lijnverbreding" kan gemeten worden aan een zogenaamd "standaardpreparaat", een preparaat dat vrijwel geen kristalfouten bevat. In hoofdstuk 1 zijn de eisen ten aanzien van zo'n standaardpreparaat geformuleerd en is gebleken dat die eisen deels tegenstrijdig zijn. Er is daardoor geen perfecte standaard mogelijk; een optimale standaard is het hoogst haalbare. Met behulp van de optimale standaard, ontwikkeld in hoofdstuk 1, kan de instrumentele lijnverbreding tot op 0.001° nauwkeurig gemeten worden.

In de hoofdstukken 2 en 3 is een veel toegepaste methode voor de interpretatie van lijnverbreding, de Warren-Averbach-analyse, geëvalueerd. Er is daarbij gebruik gemaakt van gemeten lijnverbreding, maar ook van computersimulaties. Bij computersimulaties wordt een (realistisch) preparaat met kristalfouten bedacht en met behulp van een computer de lijnverbreding uitgerekend die gemeten zou worden als het preparaat echt was. Vervolgens wordt de berekende lijnverbreding geïnterpreteerd met behulp van een analysemethode alsof het echte metingen betreft. Uiteindelijk worden de interpretatie en de oorspronkelijke kristalfouten vergeleken: als ze goed overeenkomen dan is de methode geschikt voor de analyse van het gesimuleerde preparaat. Ten aanzien van de Warren-Averbach-analyse is gebleken dat de lijnverbreding van bijvoorbeeld preparaten met veel dislocaties waarschijnlijk niet goed geïnterpreteerd wordt. Daarom is er een methode ontwikkeld die veel lijkt op de Warren-Averbach-analyse en die de lijnverbreding van een deel van de preparaten waarvoor de Warren-Averbach analyse niet geschikt is wel goed interpreteert. De beide methodes vullen elkaar dus gedeeltelijk aan.

Een nadeel van beide voorgaande methodes is dat het niet direct duidelijk is wat hun interpretatie betekent; eigenlijk moeten hun interpretaties nog een keer geïnterpreteerd worden in termen van kristalfouten. In alle andere methodes die besproken zijn in dit proefschrift is de interpretatie veel duidelijker, doordat ze direct gebaseerd zijn op de aanwezigheid van een of meer typen kristalfouten. Dat betekent natuurlijk wel dat deze methodes alleen preparaten met uitsluitend "hun" type(n) kristalfouten kunnen analyseren. In de praktijk is er overigens vaak één type kristalfout dominant aanwezig en is het bekend welk type dat is. De vraag is dan alleen nog hoeveel ervan zijn en soms hoe ze verdeeld zijn over het materiaal.

In hoofdstuk 4 zijn een aantal bestaande methodes voor de analyse van preparaten met dislocaties besproken. Het is gebleken dat de verschillende methodes zeer nauw verwant zijn en dat hun interpretaties, als ze op de juiste manier bekeken worden, goed overeenstemmen. De besproken methodes verschillen in de hoeveelheid informatie die ze uit de gemeten lijnverbreding proberen te halen: alleen het aantal dislocaties of ook hun verdeling over het materiaal in meer of minder detail. De conclusie over hun toepasbaarheid is niet verrassend: hoe nauwkeuriger de meting, hoe meer betrouwbare informatie over de dislocaties verkregen kan worden.

Precipitaten of insluitsels passen meestal niet precies in het omliggende materiaal. Voor de aluminium-silicium legeringen besproken in de hoofdstukken 5 en 6 is de oorsprong van deze mispassing een verschil in uitzettingscoëfficient: bij afkoeling van 170 °C naar kamertemperatuur krimpen de silicium-precipitaten veel minder dan het aluminium eromheen. Door middel van analyse van de lijnverbreding van deze preparaten is gebleken dat de mispassing na afkoelen kleiner is dan op grond van het verschil in uitzettingscoëfficient verwacht wordt. Dat betekent dat tijdens of direct na het afkoelen het materiaal blijvend moet zijn vervormd. Een opvallend resultaat is dat gedurende lange tijd (jaren!) de mispassing bij kamertemperatuur blijft afnemen en het aluminium dus blijft bewegen.

Voor alle kristalfouten behalve kristalgrenzen wordt de lijnverbreding niet door de fouten zelf veroorzaakt, maar door de atomen eromheen die door zo'n fout een klein beetje verplaatst zijn. Zulke verplaatsingen zijn groot dichtbij de fout en worden kleiner naarmate de afstand tot de fout toeneemt. In de hoofdstukken 7 en 8 is een methode voor de interpretatie van lijnverbreding ontwikkeld die niet gebaseerd is op specifieke kristalfouten, maar op het karakter van de atoomverplaatsingen eromheen. Daardoor is deze methode algemener toepasbaar dan bijvoorbeeld de methodes voor dislocaties of precipitaten. De methode is gebruikt om de lijnverbreding van kogelgemalen wolfraampoeder te interpreteren. Daarnaast is met behulp van deze interpretatiemethode een aantal belangrijke algemene relaties tussen eigenschappen van lijnverbreding en eigenschappen van atoomverplaatsingen rond kristalfouten gevonden.

CURRICULUM VITAE

Jurgen van Berkum

Born September 4, 1967 in Oss, The Netherlands

August 1979 -	May 1985	Secondary education, Kruisheren Kollege, Uden.
August 1985 -	November 1989	Materials Science study, Delft University of Technology. Graduated *cum laude* in the group Physical Chemistry of the Solid State of Prof. E.J. Mittemeijer.
December 1989 -	March 1994	Ph.D. research at the Laboratory of Materials Science, Delft University of Technology, under supervision of Dr. R. Delhez and Prof. E.J. Mittemeijer.
August 1987 -	January 1993	Sociology study, Erasmus University Rotterdam. Graduated in the field of Sociology of Education.
March 1994 -	May 1994	Research fellow, Laboratory of Materials Science, Delft University of Technology.
May 1994 -		Military Service.